UNIVERSITY OF SOUTHAMPTON

FACULTY OF ENGINEERING AND THE ENVIRONMENT

Institute of Sound and Vibration

Measurement and prediction of nonlinear acoustic liners in the presence of high level multiple tones

by

Pablo G. Serrano

Thesis for the degree of Doctor of Philosophy

17th September 2018

UNIVERSITY OF SOUTHAMPTON

ABSTRACT

FACULTY OF ENGINEERING AND THE ENVIRONMENT
Institute of Sound and Vibration

Doctor of Philosophy

MEASUREMENT AND PREDICTION OF NONLINEAR ACOUSTIC LINERS IN THE PRESENCE OF HIGH LEVEL MULTIPLE TONES

by Pablo G. Serrano

Aircraft noise is a problem near airports all around the world. As a result, aircraft certification requirements are becoming more stringent over time. The engine fan is one of the most prominent noise sources that produces high amplitude blade passing frequency tones, their harmonics, and engine order buzz tones. Acoustic panels, consisting of resistive layers backed by honeycomb cells and a reflective hard wall, are used to line the engine nacelle in order to attenuate both broadband and annoying tonal noise. The acoustic impedance of single layer perforate liners (SDOF) show greater sensitivity to high sound pressure levels and grazing flow in comparison with wire mesh liners. The focus of the work reported here is to understand the physical loss mechanisms of SDOF perforate liners under high SPL multiple tones. This has been realised through measurements, modelling, and semi-empirical prediction of perforate liner impedance. Two harmonically related tones with varying combinations of amplitude and frequency were used as excitation signals. Punched Aluminium perforates, along with rapid 3D printing prototyped samples composed of ABS and Stainless Steel, were tested. A sample holder was designed to allow simultaneous *in situ* and traditional TMM measurements. A grazing flow test rig developed and commissioned by the author and others at the LVA/UFSC (Laboratory of Acoustics and Vibration at the Federal University of Santa Catarina), in Brazil, used TPM, MMM, and SFM impedance eduction techniques and the *in situ* method, which were cross validated. The semi-empirical 1D impedance models of Rice, Cummings, Boden, and Maa, were implemented numerically using MATLAB, and a proposed 1D impedance model with a frequency-dependent discharge coefficient was developed. Also, 2D Multiphysics numerical models in time domain, based on FEM, were developed and validated using the MATLAB & COMSOL Multiphysics 5.2a livelink. The COMSOL code reproduces high SPL experimental conditions, allowing direct comparisons with measurements and published data. These studies have aided the development of an improved semi-empirical 1D impedance model for pure tone excitation, and a resistance correction for multiple tone excitation.

Contents

List of Figures

List of Tables

Declaration of Authorship

I, Pablo G. Serrano , declare that the thesis entitled *Measurement and prediction of non-linear acoustic liners in the presence of high level multiple tones* and the work presented in the thesis are both my own, and have been generated by me as the result of my own original research. I confirm that:

- this work was done wholly or mainly while in candidature for a research degree at this University;
- where any part of this thesis has previously been submitted for a degree or any other qualification at this University or any other institution, this has been clearly stated;
- where I have consulted the published work of others, this is always clearly attributed;
- where I have quoted from the work of others, the source is always given. With the exception of such quotations, this thesis is entirely my own work;
- I have acknowledged all main sources of help;
- where the thesis is based on work done by myself jointly with others, I have made clear exactly what was done by others and what I have contributed myself;
- parts of this work have been published as: [87] and [88]

Signed:.....

Date:.....

Acknowledgements

I would like to acknowledge people that helped me during the journey. Dr. Paul Murray is an incredible person, technical, easygoing and funny. Thank you Paul for all the support, guidance and encouragement you gave me. Dr. Jeremy R. Astley thank you very much for the friendship, guidance, patience and valuable insights during the research period. You are a great person! Gislene Vieira dos Santos, you have been the person that understands me and give me strength to go even further, so I would like to thank you so much to be with me during the good and bad moments. Thank you Terezinha Regina Giordani Serrano and Alan Indio Serrano, my mother and my father, for always support me and for providing me the best study you could afford. Dr. Julio A. Cordioli gave me the first opportunity in this field of acoustics, and continued to believe in my work as I collaborated with him. Thank you Julio for your guidance, attention to details and for opening doors that I would not be able to open without you! André Spillere is an example of professionalism and proficiency. Thank you for helping me get flow rig results and discussing them. We are a good team and you will go much further than me because of your focus, drive and excellency, so thank you for showing me how to apply these values. Zargos Masson, during our period of development of our tool to control the test rig you showed yourself to be an excellent team driven professional. Thank you for your friendship and excellent opinions and discussions. Thank you Anderson Proença for the friendship and technical discussions when I needed. Thank you very much Martin Dawson for reading my thesis and for suggesting several changes. I would like to thank the EDMC technicians Kevin, John and Richard for helping me to manufacture 3D printed samples and for teaching me how to use the machines. The current research was funded by CNPq the Conselho Nacional de Desenvolvimento Científico e Tecnológico - Brasil.

Nomenclature

c	Sound Speed of air in normal pressure and temperature conditions [m/s]
b	Liner sample position in the x direction [m]
C_D	Discharge coefficient [-]
C_{Df0}	Discharge coefficient at the resonant frequency [-]
d	Diameter of the hole [m]
h	Cavity depth [m]
f	Frequency [Hz]
H_{bf}	Frequency response function, (b) back, (f) face sheet microphones [-]
H_{12}	Frequency response function between signal 1 and signal 2 [-]
K	Perforate constant [-]
k	Wave number [1/m]
k_x	Wave number in the x direction [1/m]
k_y	Wave number in the y direction [1/m]
k_z	Wave number in the z direction (axial) [1/m]
l	Liner face-sheet thickness [m]
l_0	One side end correction [m]
L	Effective face sheet thickness [m]
L_j	Jet length [m]
M	Grazing flow average velocity in the cross section of a test rig tube [-]
m_f	Face sheet mass inertance, frequency dependent [m]
m_{f0}	Facing sheet mass inertance at the resonance [m]
m_{f1}	Facing sheet mass inertance at the fundamental tone [m]
m_{f2}	Facing sheet mass inertance at the harmonic tone [m]
n	Enesimal frequency component [-]
P	Pressure excitation on the liner surface [Pa]
P_b	Pressure on the liner's back sheet, inside the honeycomb cavity [Pa]
P_f	Pressure on the liner's face sheet [Pa]
p^+	Incoming pressure (positive direction of z axis) [Pa]
p^-	Outgoing pressure (negative direction of z axis) [Pa]
σ	Porosity (Open area divided by sample area) [-]
R_o	Total orifice resistance [Rayl]
R_{os}	Steady flow orifice resistance [Rayl]

R_{on}	Face sheet nonlinear resistance [Rayl]
R_{ol}	Face sheet linear resistance [Rayl]
R_{os}	Face sheet steady flow linear resistance [Rayl]
R_{of}	Face sheet grazing flow linear resistance [Rayl]
S	Orifice area [m^2]
S_{vena}	*Vena contracta* area [m^2]
S_b	Backing plate area [m^2]
St	Strouhal number [-]
t_c	Critical thickness [m]
V	Cavity volume [m^3]
v_∞	Grazing flow velocity [m/s]
v_s	Particle velocity on the liner surface [m/s]
v_0	Particle velocity in the liner orifice [m/s]
v_x	Particle velocity in the x direction [m/s]
v_y	Particle velocity in the y direction [m/s]
x_0	Particle displacement in the orifice [m]
v_{rss}	Root sum square velocity [cm/s]
Z	Acoustic impedance [Rayl]
Z_0	Characteristic impedance [Rayl]
δ	Delta function [-]
γ	Phase of pressure wave [rad]
ϕ	Velocity phase relative to pressure, both on the liner surface [rad]
λ	Wave length [m]
λ_0	Characteristic wave length [m]
ϵ	End correction [m]
ϑ	Fluid damping [-]
ω	Angular frequency [rad/s]
ρ	Air density in normal pressure and temperature conditions [kg/m^3]
σ	Liner porosity [-]
μ	Dynamic viscosity of the medium [Pa.s]
η	Dimensionless velocity on the hole v_0/M [-]
ν	Kinematic viscosity [m^2/s]
θ	Normalized resistance of the liner [-]
θ_0	Normalized resistance in the perforate hole [-]
θ_{on}	Normalized nonlinear resistance component [-]
θ_{ol}	Normalized linear resistance component [-]
θ_1	Normalized resistance of the fundamental tone [-]
θ_2	Normalized resistance of the harmonic tone [-]
χ	Normalized reactance of the liner [-]
ζ	Normalized impedance of the liner [-]
ABS	Acrylonitrile Butadiene Styrene

BPF	Blade Passage Frequency
EHR	Extended Helmholtz Resonator model
EO	Engine Order
$EPNL$	Effective Perceived Noise Level in dB (reference $2E-5$ Pa)
FEM	Finite Element Method
$ICAO$	International Civil Aviation Organization
LVA	Laboratory of Acoustics & Vibration
MMM	Mode Matching Method
$MDOF$	Multiple Degrees of Freedom
MPP	Micro Perforate Plate
MT	Multiple tone
$NASA$	National Aeronautics and Space Administration
NIT	Normal Impedance Tube
ODE	Ordinary Differential Equation
PT	Pure Tone
POA	Percentage of Open Area [%]
POA_{eff}	Effective Percentage of Open Area [%]
$UFSC$	Federal University of Santa Catarina
$SCAPLR$	Software de Controle Aquisição e Processamento de sinais Liner Rig
$SDOF$	Single Degree Of Freedom
SFM	Straightforward Method
SPL	Sound Pressure Level in dB (reference $2e^{-5}$ Pa)
TMM	Two Microphone Method
TPM	Two Port Matrix

Chapter 1

Introduction

Aircraft noise is a problem all over the world, causing community annoyance and restricting commercial flight operations at many airports. As air travel is becoming more popular, noise exposition near airports is increasing significantly. All aircraft must be certified to meet international noise criteria. Effective Perceived Noise Level (EPNL) is the certification parameter used to evaluate aircraft community noise, and to regulate the use of airports. Other requirements may also be applied at individual airports, for example the A-weighted level at a given flight point [30]. Despite the technical aspects, public pressure to avoid the construction of new runways is common these days, for instance at Heathrow Airport in London.

The International Civil Aviation Organization (ICAO) published a report in 2014 [2] describing the status of noise reduction technology. The report also established medium- and long-term noise reduction goals. This report was written by specialists in the field, who stated that a reduction in fuel burn and emissions is desirable as well as the reduction of aircraft noise. To achieve the goals they summarized the status of technological advances over the last 10 years and defined 20 year goals which must be supported by current and future research. The report assessed the possibility of noise reduction and recommends updated mid-term and long-term technology goals. There are three primary approaches to reduce aviation noise exposure:

1. Reducing the noise at the source;
2. Noise abatement operational procedures;
3. Land use planning.

The first approach enumerated above is the driver of the current research. It is a prevention procedure that requires technological effort and research in order to get results.

1.1 Motivation

Aerospace, automotive and the building services industries are some of the sectors where acoustic liners are heavily used to reduce noise levels. The possibility of having acoustic absorption by using lightweight materials without using conventional fibrous or porous material, as commonly used in the automotive and building services industry, is particularly important to the aerospace industry. Fibrous materials are unsuitable as acoustic material in turbofan engines because they retain water, unburned fuel, and other engine fluids. The solution commonly found on nacelles of turbofan aircraft is a liner composed of a perforated sheet over a honeycomb core, backed by a rigid sheet. The main concern of this work is related to the aerospace industry. However, the technologies, techniques and methods could be applied to other industry sectors that use this type of liner.

1.1.1 Aircraft inlet noise source

The turbofan engine is a well known propulsion technology used in most civil aircraft. The bypass ratio is the proportion of the mass flow through the bypass duct compared to that through the core. An increased bypass ratio reduces jet noise due to increased mixing of the slower colder bypass air with the core air. Bypass ratio is predicted to increase in the mid-term and long-term, depending on the aircraft type, size and number of engines. The effect of increasing the bypass ratio is to make fan noise as important as the other noise sources in commercial turbofan engines. The fan noise contribution is, therefore, a critical issue in large bypass ratio engines, and characterization of fan noise and noise control techniques in the nacelles is required to face this challenge.

Fan noise is composed of tone and broadband components. The Blade Passing Frequency (BPF) is defined by the number of blades times the rotation velocity of the fan in rotations per minute (RPM) divided by 60, and it is given in Hertz. The BPF of an aircraft engine is perceived as a tonal noise that causes annoyance in humans. Engine orders are integer multiples of shaft rotational frequency [71]. Multiple tones occur due to non-linearities caused by supersonic speed at the tip of the blades. These phenomena create shock waves composed of several tonal frequency components that propagate non-linearly [35]. This noise source couples with the duct acoustic modes in the nacelle intake, where it then propagates along the nacelle duct and radiates to the far field. As tone levels tend to dominate, tonal noise attenuation, especially at the BPF and its harmonics, must be maximized in order to minimise certification EPNL levels. However, broadband noise also contributes to the Overall Sound Pressure Level (OASPL) and must also be reduced, particularly for modern engines where tone protrusion levels are lower.

Blade design parameters such as sweep, thickness, blade count, blade shape and fan diameter influence the amplitude of fan noise [55]. The high amplitude multiple tones generated have levels well above 130 dB, and propagate non-linearly through the duct. A

simulation of the spectrum at engine order amplitudes close to the fan face [59] is shown in Figure 1.1.(a) for a mean relative blade tip Mach number of M=1.2; it is possible to identify the BPF peak at EO (Engine Order) 22 and subsequent harmonics with SPLs (Sound Pressure Level) approximately 5 to 10 dB lower than the BPF. Also shown are "Buzzsaw" tones at multiples of the shaft rotation frequency, which are multiple tones that occur because of fan blade space, angle and size irregularities. Figure 1.1.(b) shows the same simulation near the end of the inlet duct (front of the engine) for the same condition, without a liner (white bars) and with a liner (gray bars) [59].

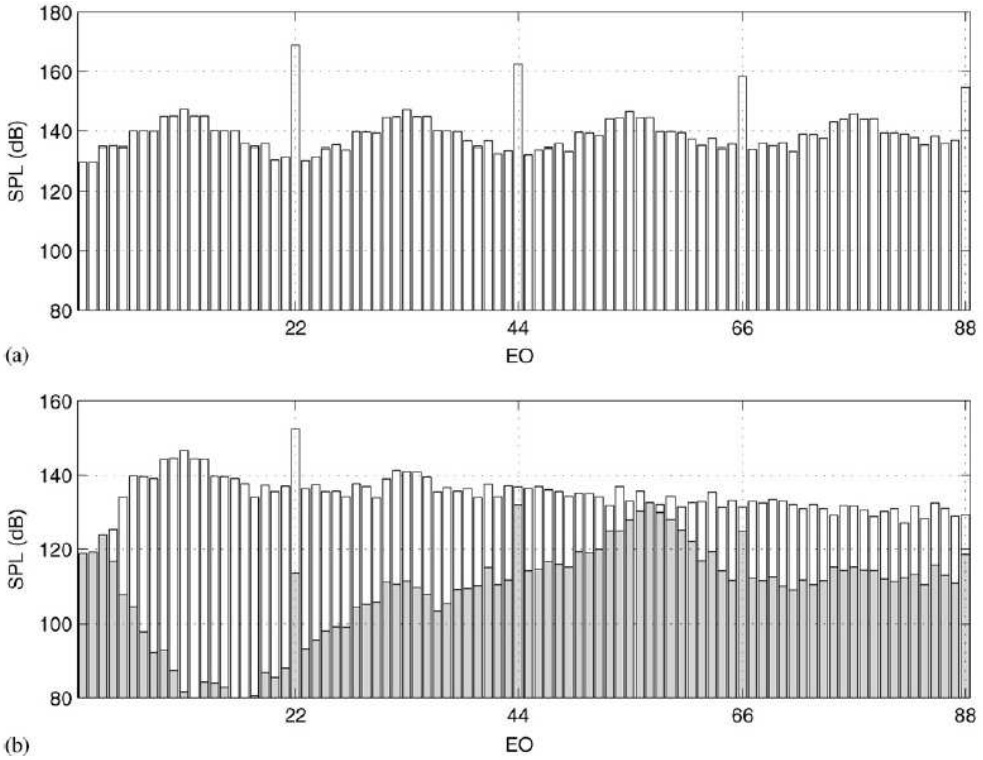

Figure 1.1: Fan noise example for a relative tip Mach number M=1.2 at the fan face (a), and near the end of the inlet (b) with and without liner. From: McAlpine, 2013 [59].

1.1.2 Liners

Acoustic materials are used to attenuate the noise sources described above. These materials partially line the inlet internal walls, along with the rest of the nacelle walls. They are usually made of aluminium, composite, or titanium. They act as Helmholtz resonators, and they are typically tuned to give maximum absorption for a given source spectrum and for a specific flight condition. Liners typically used have a single honeycomb layer, Single degree of freedom (SDOF), or multiple layers, Double degree of freedom (2DOF) or Multiple degrees of freedom (MDOF). Some liners are covered with a mesh. These are called linear liners because the resistance is not so dependent on the incident SPL and grazing flow speed. Linear liners have fiber metal meshes and woven wire, usually

overlaid on a perforate support plate [4]. A sketch of a typical SDOF liner section is shown in Figure 1.2.

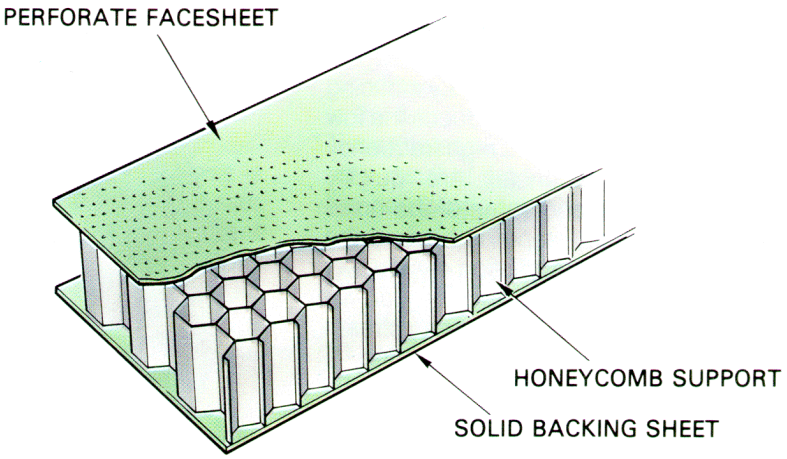

Figure 1.2: SDOF perforate liner. From: Rienstra, 2006[80].

Liner degrees of freedom are defined as the number of layers of resonators, each of which is made up of a sandwich of resistive sheets and honeycomb[4]. A SDOF perforate liner has one resistive layer composed of a perforated plate backed by a honeycomb structure and a reflective solid backing sheet. The SDOF liner typically attenuates sound over one octave bandwidth. On the other hand, MDOF liners are used to target a broader range of frequencies [66]. There are several conditions to be analysed in order to obtain maximum fan noise sound attenuation, such as:

1. Spectrum of the incident sound on the liner surface;
2. Mean grazing flow velocity near the liner surface;
3. Boundary layer at the liner surface;
4. Temperature of the fluid and equivalent sound speed;
5. Amplitude of the sound field impinging the liner.

The key acoustic parameter that combines all of the conditions above and characterizes the liner performance is the acoustic impedance, the time averaged and frequency dependent ratio of acoustic pressure and acoustic velocity at the sample surface. As the latter quantities are not always in phase for a given frequency, the impedance is a complex number. This parameter can be divided into a resistive part, which is responsible for the attenuation, and a reactive part, which defines the frequency response (inductance + capacitance). Liners are usually assumed to be locally reacting [38] because the resonator honeycomb cells do not interact. The locally reacting assumption allows liner modelling without requiring sound incident angle information. The cell widths are narrow enough

to allow only plane wave propagation in the liner resonator cavity. Some liners have drainage slots, that are small holes on the honeycomb structure used to drain water from the cavities. Drainage slots may influence liner impedance but the slot dimensions and orientation should be controlled to maximise attenuation [68]. If no drainage slots are present, the liner is locally reacting. However, if drainage slots are present significantly large, the liners are non-locally reacting.

1.1.3 Technological challenges

Tonal sources, such as BPF harmonics and buzz tones at departure, are important because they can lead to tone protrusion penalties in EPNL. Consequently, liners are used to attenuate tonal noise. The liner tuning frequency depends on the noise signature of the fan which varies with power setting and from engine to engine. Fan noise and airframe noise are the main sources of aircraft noise when compared to other sources at approach (arrival) condition, as shown in Figure 1.3. Fan noise is also a dominant source during take-off, together with jet noise. These noise distributions (e.g. Figure 1.3) vary depending on the aircraft and the technologies used to attenuate noise. It is expected that high bypass ratios will probably increase the importance of acoustic treatment for fan noise.

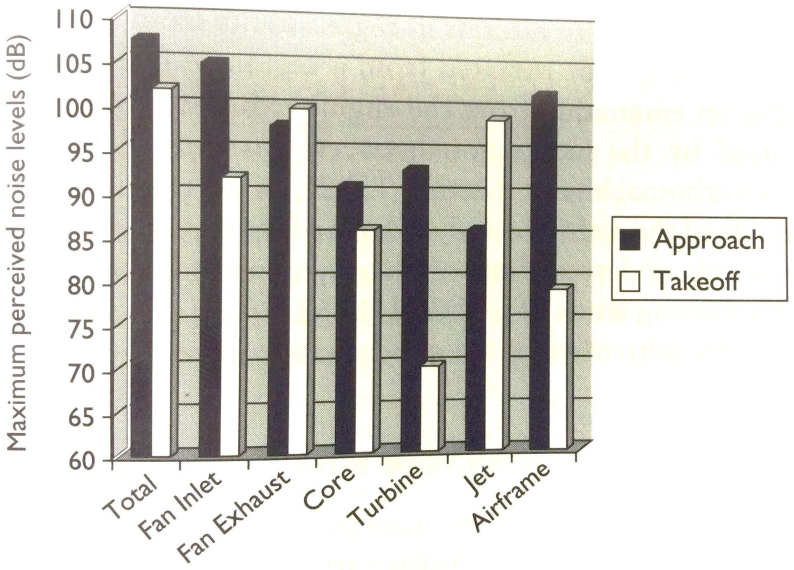

Figure 1.3: Sources contribution to aircraft total noise under departure (take-off) and arrival (approach) conditions. From: Fahy & Walker, 2004 [31].

Existing experimental techniques use pure tone and broadband signals to extract or educe liner impedance (see 2.7). These techniques are called impedance eduction methods and provide reasonable results for subsonic grazing flow and low SPLs using pure tone excitation. However, results for broadband excitation can show dramatically different

impedance values when compared to pure tone excitation. The effect of different excitation is evident at high SPL where the interaction of frequency components is intensified. Consequently, the interaction of frequency components [78][20][7] as well as the design of efficient broadband liners [37][73] are important current technological challenges.

To summarise, aircraft noise is a global issue of growing importance due to the increase in air travel and population growth in communities surrounding airports. These communities are affected by higher exposure to aircraft noise pollution. This can cause annoyance and health problems, such as stress and sleeping disorders. The ICAO established medium and long term noise reduction goals to deal with this problem [2]. Consequently, the aerospace industry has been working on technologies to reduce aircraft noise directly at the source. Liner technologies are also crucial in order to reduce fan noise and meet noise reduction goals. More acoustic material usually means more weight and drag. The trend towards increasing bypass ratio to reduce fuel burn will increase the nacelle duct area and weight. To offset this, ducts are being shortened, reducing the available area in which liners can be installed. So, more effective liner technologies are needed in order meet the requirements in the available area of the nacelle.

1.2 Objectives

The main objective of this research is to develop a robust liner model to predict impedance in the presence of high SPL multiple tone excitations, when grazing flow is not present. It is proposed to explore the impact of high amplitude multiple tones on liner impedance, realised through numerical modelling and experiments. The main outcome is an improved understanding of the physical phenomena underlying the acoustic response of typical liners to multi tone excitation, in order to create design tools and flexible models that address these issues. The main objective is to be achieved via the following steps:

1. Review relevant literature including: time and frequency domain liner impedance models, experimental techniques to educe the impedance or measure it *in situ*, for single and multiple tone excitations, at high SPLs;

2. Implement Rice and Cummings impedance models and use them as the starting point for future development of a new model;

3. Plan and run experimental campaigns using a portable impedance meter and a grazing flow test rig to measure low porosity typical liners and 3D printed samples;

4. Develop a numerical Finite Element Method (FEM) model using COMSOL Multiphysics & MATLAB in order to visualise and quantify the behaviour of nonlinear regimes in the facing sheet holes of a perforated liner.

5. Understand, describe and model the physical phenomena caused by pure tone and multiple tone excitation on liners;

6. Investigate the best acoustic velocity description for the liner, according to the type of excitation, in order to predict liner impedance;

7. Propose an improved semi-empirical correction for multiple tone excitation based on the observations from the experimental and numerical studies.

1.3 Methodology

The research methodology is divided into three main phases.

- Firstly, a literature review is undertaken, which includes the physical fundamentals and provides a description of liner models validated by analytical and numerical methods. There are several liner impedance models and eduction techniques in the literature [78][20][26][48][100][43][98], however the assumptions made usually underestimate the physical complexity of the problem and the models often do not include all the parameters necessary to characterize the liner at all flight conditions. So a comparison between different approaches is necessary, guided by experimental results.

- Secondly, measure the impedance of liner samples by using different experimental techniques. A measured database obtained by using the Portable Impedance Meter (PIM) and the grazing flow test rig will be analysed, in order to develop hypotheses regarding the physical mechanisms that describe the acoustical behaviour of the liner samples. The PIM was used to investigate 3D printed samples and a typical SDOF perforate liner by using the Two Microphone Method (TMM) and *in situ* technique [24]. Concurrently, a grazing flow test rig was used to measure acoustic data of the punched aluminium perforate liner only. All the no flow and grazing flow data was post-processed using computer codes, written in MATLAB, to educe the impedance and to directly extract it using the *in situ* technique, Two Port Matrix (TPM), Mode Matching Method (MMM), and Straightforward Method (SFM). Different relative amplitudes of two harmonically-related tones with the same initial phase were chosen, in order to generate signals and compare the liner impedance results using these multiple tone signals against broadband and pure tone excitations. The experimental conditions range from no flow to 0.26 Mach grazing flow conditions, at high OASPLs (130-150 dB), using signals in a frequency range from 500 to 6400 Hz, which encompasses the typical Approach environment conditions and BPFs of large and small engines.

- Thirdly, develop a numerical axi-symmetric FEM model for one resonator. A commercial FEM tool called COMSOL, that allows different physical descriptions in the same transient model, is used to create a simplified and high-fidelity description of a slit liner and an axi-symmetric liner with one cylindrical aperture. Straight, chamfered and conical edges on the facing sheet hole will be modelled, along with a convergent-divergent hole shape, evaluated and discussed in order to fully understand the effect of high SPL on the velocity and vorticity profiles near the hole edges. Furthermore, changes in the excitation signals used on the numerical model mimic the experimental conditions and also are discussed in terms of validation to explore how it changes the liner impedance.

- Fourthly, develop a semi-empirical 1D model for multiple tones. This model will be based on previous models with experimental semi-empirical fitting of coefficients and further observations based on 2D FEM high-fidelity models.

Chapter 2

Literature Review

This chapter introduces the concepts and techniques used in this research and already covered by other authors. The main topics include: the impedance definition, the effect of various factors on liner impedance, such as high-level excitation, multiple tone excitation, geometric design of features, and grazing flow. Subsequently, a section about different experimental techniques cover the normal impedance tube Two Microphone Method (TMM) [42], *in situ* Dean's method [24], and three eduction techniques used in test benches: the Two Port Matrix (TPM) [83], the Mode Matching Method (MMM) [28], and the Straightforward Method (SFM) [43]. A basic description of the fundamental equations for compressible flow is presented in order to introduce the concepts used on the two dimensional models. And, finally, semi-empirical one dimensional impedance models as well as two dimensional models are introduced [5][54][78][20][8].

2.1 Circular orifice impedance

The ultimate goal of the study is to obtain a generalized impedance value over the surface of liners used in the aerospace industry, rather than for a single resonator in an array. However, it is possible to address this problem by studying the response of a single resonator and calculating the impedance of the whole liner surface. Lord Rayleigh [77] was the pioneer of orifice impedance modelling. Rayleigh elaborated a general theory for acoustical Helmholtz resonators. He simplified the problem, using the hypothesis of an infinite plane and uniform velocity distribution across the orifice. In practice these conditions are not fully satisfied because the orifices may interact and the velocity profile at the orifice entrance is not uniform [92].

Several authors, for instance Bolt [12], performed experiments in order to determine the impedance of orifices. The steel plate of his samples had holes with diameters above 10 mm and no more than a few millimetres thick. His predictions included an analytical

description of the resonator, though unfortunately the geometry is outside the liners range of values, for aeronautical liners.

Discrepancies between theory and experiments have been reported by Ingard [41]. He showed that, for low acoustic velocities, the pressure and velocity had a linear relation in the orifice [38][40][39]. Nonetheless, the relation becomes quadratic for higher acoustic velocities as a consequence of high level excitations. Ingard used an impedance tube, stroboscopic illumination and a smoke generator to observe the behaviour of the air near the orifice opening [41]. Air displacement near the orifice showed different regimes depending on the ratio between the orifice plate thickness and the particle velocity, l/v_0, due to acoustic excitation.

The first region identified by Ingard, in Figure 2.1.(a) for low Reynolds number, showed that air entered in the orifice on the edges and exited the cavity in the middle zone of the orifice, which is shown by a vertical white line. The second region identified in Figure 2.1.(b), shows vortex structures causing recirculation on the edges of the orifice. A third region, illustrated in Figure 2.1.(c), was characterized by a superimposed steady circulations and pulsations. Finally, the fourth region shown in Figure 2.1.(d), was characterized only by a jet. The jet pulsations over the excitation period creates vortex rings travelling out from the orifice, as can be seen in Figure 2.1.(e). Ingard concluded that the non-linear losses at all levels could be explained by the energy required to drive the circulation currents and the vortex rings. Later on, Tam [92] used Direct Numerical Simulation (DNS) to study the same problem by observing the flow behaviour in a computer model. Tam stated that total energy losses are divided into basically two main mechanisms: viscous losses, at the boundary layer and at the shear layers near the resonator aperture; and vortex shedding that transforms the acoustical energy in kinetic energy, to be dissipated into heat.

Impedance is defined for a time harmonic sound field as the ratio of complex acoustic pressure amplitude, $\widetilde{p}(\omega)$, and complex acoustic velocity amplitude in a specific direction, $\widetilde{u}(\omega)$, at a certain point in space. The symbol $\widetilde{Z}$ over the quantity Z means that it is complex. The general expression for the acoustic impedance is given by,

$$\widetilde{Z}(\omega) = Re(\widetilde{Z}) + Im(\widetilde{Z}) = R + iX = \frac{\widetilde{p}(\omega)}{\widetilde{u}(\omega)}, \tag{2.1}$$

The liner impedance is the value of this parameter calculated in the liner surface, where the velocity, $\widetilde{u}$, is in the normal direction in respect to the surface and it is the spatially averaged normal velocity at the liner surface. The resistance, R, is related to the acoustic losses of the liner, and the reactance, X, is related to the stiffness, which is non dissipative. When the reactance is zero, the liner is in resonance and the maximum absorption is experienced in the absence of grazing flow for the normal incidence impedance tube. Usually, the absolute values of impedance are normalized by the characteristic impedance of the air, $Z_0 = \rho c$, where the density, ρ, and the sound speed, c, are calculated for a

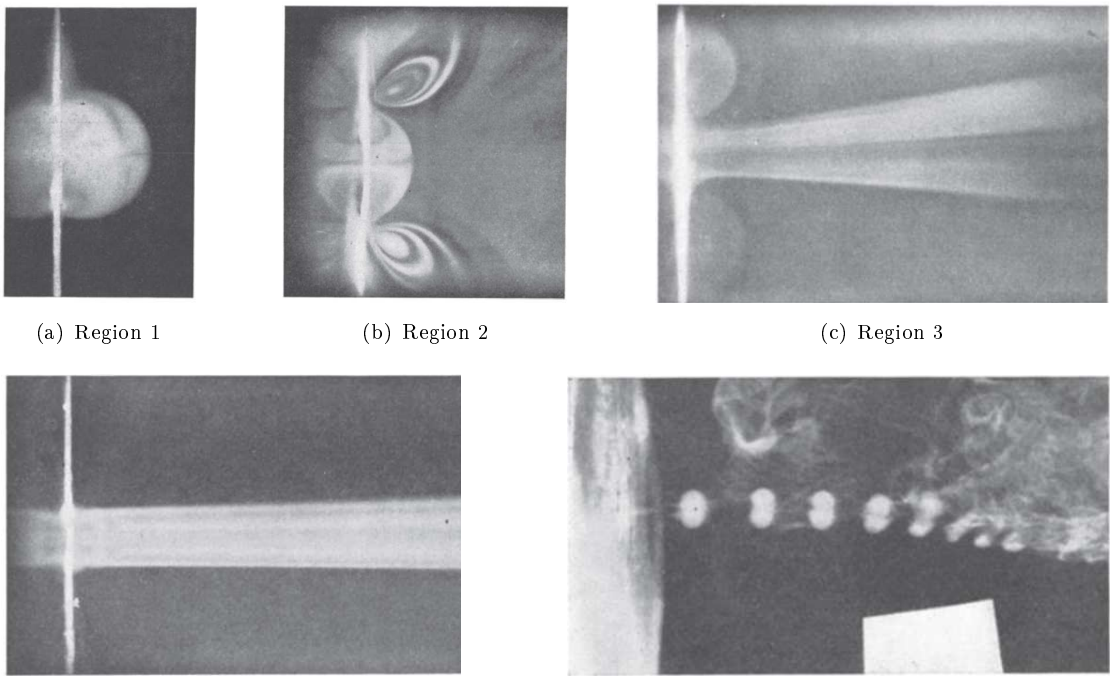

(a) Region 1 (b) Region 2 (c) Region 3

(d) Region 4 (e) Region 4 - Vortex rings

Figure 2.1: Air displacement using stroboscopic illumination in an orifice diameter of 5 mm excited by a pure tone at 234 Hz. From: Ingard, 1950 [41].

reference temperature and atmospheric pressure. The normalized impedance is described as,

$$\zeta = \frac{\widetilde{Z}(\omega)}{Z_0} = \theta + i\chi = \frac{R}{Z_0} + i\frac{X}{Z_0}, \tag{2.2}$$

where θ is the real part of the normalized impedance, called specific resistance, and χ is the imaginary part, called specific reactance [67]. The resistance R can be divided into different components, and may be interpreted as the summation of linear resistance terms R_{ol} and the non-linear resistance terms R_{on}. Similarly, we can interpret the liner reactance as a summation of the mass reactance, and the cavity reactance. The mass reactance is caused by the mass of air in the holes of a perforated sheet, and the cavity reactance is caused by the fluid inside the liner resonator cavity.

The first linear term of resistance is due to the effect of viscosity on the side walls of the orifice neck [36]. A second linear term is related to heat conductivity, however, it has been shown by Ingard [38] that these losses are smaller than the effect of viscosity and can usually be neglected. In addition, the surface resistance, R_s, can be defined if the boundary layer thickness of the acoustic perturbation through the orifice is smaller than the orifice radius, which is typically the case for aeroengine applications. It is given by,

$$R_s = \frac{1}{2}\sqrt{2\mu\rho\omega}, \tag{2.3}$$

where μ is the dynamic viscosity [38]. The total orifice resistance R, in the absence of grazing flow, is expressed by

$$R = \frac{R_s}{d}(l + \Delta l + \Delta_{nl}), \tag{2.4}$$

where l is the plate thickness, d is the orifice diameter, Δl is the linear resistance end correction found experimentally as $\Delta_l \simeq d$ and Δ_{nl} is the non-linear resistance term, due to the high level excitation, that will be explained in the Section 2.2. When the particle displacement in the orifice, x_0, is smaller than the plate thickness ($x_0/l << 1$) the linear resistance term is dominant. The non-linear resistance term becomes important when $x_0/l \simeq 1$, so the linear and non-linear components have approximately the same order of magnitude $\Delta_l \simeq \Delta_{nl}$. The critical thickness of the plate was defined by Ingard as,

$$l_c = \frac{V_c}{\omega}, \tag{2.5}$$

where V_c is the critical velocity, when non-linear and linear contributions have the same order magnitude. When the air displacement is lower than the critical thickness of the plate $x_0 < l_c$, non-linear resistance is dependent on x_0/l. For air displacement greater than the critical thickness of the plate, where $x_0 > l_c$, the non-linear resistance becomes dominant and the other terms may be neglected [38].

Hersh [36] studied the problem in more detail and elaborated a frequency domain model for liner impedance. The normalized liner resistance was composed of semi-empirical parameters strongly dependent on the ratio of plate thickness and orifice diameter, l/d. Hersh expressed the resistance as,

$$R = \frac{\nu}{d\sigma c}\frac{l}{d}\left[K_{ss} + \sqrt{(\omega d^2/\nu)}K_{ac}\right], \tag{2.6}$$

where σ is the liner porosity, that is related to the Percentage of Open Area (POA), which is the ratio between the area of the perforated sheet holes by the area of the backing sheet of the resonator cavity. The steady flow coefficient is defined by Hersh as $K_{ss} = 13 + 10.23(l/d)^{-1.44}$ and the viscosity coefficient as $K_{ac} = 3 + 2.32(l/d)^{-1}$. Usually, a typical liner shows the ratio $0.5 < l/d < 1$, and frequently the values of these parameters are simplified to $K_{ss} = 32$ and $K_{ac} = 6.6$ in order to obtain simple semi-empiric models.

Motsinger [66] modelled the reactance of a single degree of freedom Helmholtz resonator, as

$$\chi = \frac{k(l + \epsilon d)}{\sigma} - \cot(kh) \tag{2.7}$$

where k is the wave number and ϵ is the end correction which for a flanged condition is $\epsilon = 0.85$. The first term is the face sheet mass reactance and the second is known as the cavity reactance, which corresponds to a quarter wavelength resonator.

Some 1D semi-empirical liner impedance models are discussed in Section 2.6. There are several liner impedance models described in time and frequency domain. They all show limitations to fully describe the physical mechanisms of dissipation analytically. The main assumptions of these models normally include the linear regime of excitation, single tone excitation, and uniform grazing flow. 1D models are fast and produce reasonable liner impedance predictions. However, precise prediction models are needed in order to optimize sound attenuation in combustion engines.

2.2 High-level excitation

Sound Pressure Level (SPL) is defined as

$$SPL = 10log(\frac{p_{rms}^2}{p_{ref}^2}), \tag{2.8}$$

where $p_{ref} = 2.10^{-5}$ Pa is the reference threshold of hearing and p_{rms} is the root mean squared pressure at a given point in space calculated as

$$p_{rms} = \sqrt{\frac{1}{T}\int_0^T p(t)^2 dt}, \tag{2.9}$$

for a time period T that is sufficiently greater than the pressure fluctuation period of the lowest frequency component of interest. Depending on the sound signature, the integration time can be changed in order to obtain a representative and meaningful SPL. If the pressure wave is composed from several frequency components, the SPL is frequently called Overall Sound Pressure Level (OASPL). The SPL will be treated in the text as the level at a specific frequency component. For a pure tone excitation, the OASPL and the SPL are the same, however, for a multiple tone signal the values diverge depending on the amplitude and phase of the tones. Low SPLs cause linear response of liners, where the pressure and velocity ratio is easily predictable at the liner surface. However, the non-linear responses of liners to high excitation levels are important because they can occur during normal operational conditions of aeronautical turbofan applications close to the fan. Kurze [52] defined two different types of non-linearity. The non-linearity of the medium (air) creates distorted waves, such as sawtooth and buzzsaw noise. Also there is the non-linearity of the liner response, where the relation between pressure and velocity is no longer linear. Above around 140 dB SPL non-linearity of the propagating wave is observed, causing distorted sound waves in the medium. On the other hand, liners can produce non-linear responses when excited by sound waves at

levels lower than that required to create non-linearities in the medium [39]. Only the non-linear response of the liner will be discussed in this thesis as we are evaluating the material response to high SPLs and not sound propagation in the medium.

If a liner behaves linearly, it means that the sound attenuation per unit of length is constant, irrespective of the sound field magnitude. In the case of a non-linear liner, the liner behaviour changes in a way which is complicated to predict. Pressure on the surface is proportional to the square of the particle velocity, $p \simeq \rho v_0^2$ [41]. An increase of resistance and a decrease in mass reactance (facing sheet reactance) are consequences of liner non-linearities when Region 2 is reached - see Figure 2.1.(c). The transfer of acoustic energy, of the oscillating mass around the orifice, into kinetic energy to the vortex rings is irreversible due to the elongation of the moving mass on the resonator neck and consequent separation. This energy is later dissipated by viscosity, explaining the increase in liner resistance [40].

Rice [78] and Cummings [20] formulated 1D impedance models describing this high SPL behaviour by considering a lumped parameter system. Unidirectional velocity v_0 is obtained by an Ordinary Differential Equation (ODE) in the opening of the liner resonator. The effect of the high-level excitation is strongly related to a v_0 times $|v_0|$ contribution in the damping resistance term into their equations. Tam suggests that kinetic energy and vortex shedding are strongly related as v_0 times $|v_0|$ creates high velocity and vorticity near the hole [96]. The numerical implementations and validations of the Rice model and the Cummings model are detailed in sections 4.1 and 4.2 respectively.

Recently, Zhang and Bodony discussed several aspects of high-level excitations in the presence of grazing flow [102][103] and for different turbulent boundary layers over the liner surface by using a DNS model [104]. Acoustic pressure waves at 130 dB have the same order of magnitude as hydrodynamic pressure oscillations caused by the grazing or bias flow, but at higher SPLs the acoustic pressure is the main component of the pressure fluctuations. By bias flow it can be understand as the fluid motion through the perforated plate of the resonator caused by a steady flow or by a large sound pressure difference between each side of the perforate. DNS results were compared with analytical expressions showing that the instantaneous pressure fluctuations, p, for high SPLs above 140 dB are closely approximated by

$$p = 10^{(SPL/20-9.701)} e^{i\omega t}. \tag{2.10}$$

Forner et al. [34] also studied high level acoustic excitations over a symmetric Helmholtz resonator (straight edge on the facing sheet holes), asymmetric Helmholtz resonator (hole with a chamfer on one side), and a quarter wave length resonator. The scattering of the single tone acoustic waves to higher harmonics was around 2%. It was observed that the odd harmonics only (OHO) pattern was present at low SPLs but vanished for high SPLs where all the harmonics showed the same order of magnitude in the scattered wave.

The asymmetric resonator showed vortex shedding patterns at lower SPLs in comparison with symmetric resonators at the same excitation level, as also evidenced by Tam [92]. As stated earlier, vortex shedding is an effective acoustical dissipation mechanism, which corroborates to the use of beveled liners in aircraft engines. Both, Forner et al. [50] and Tam, used three dimensional DNS simulations to observe the microfluid dynamics near the micrometric holes in detail.

Usually just one hole is simulated by DNS, and the impedance is calculated on the liner surface for a given porosity. Near the hole the full Navier-Stokes equations are solved for compressible flow, however, away from the hole incompressible assumption can be used to reduce the computational effort as will be covered in Section 5. A piston like boundary condition is set at the inlet of the computational domain in all the literature cases, away from the facing sheet hole. Also no-slip condition was also applied to facing sheet orifice walls [96][34][102].

Tam et al. [95] elaborated benchmark models using DNS that were validated by experimental results obtained at NASA Langley. It was observed that the direction of the impinging sound wave had no impact on liner absorption, as already stated by other authors, thereby confirming the typical aeronautical liner as a locally reacting material. Ferrari [33] validated his high fidelity simulations using the results of this benchmark model presented by Tam in order to find coefficients to describe the discharge coefficient. The approach consists of comparing the ratio of shed vortex kinetic energy to the incident energy over a period of time as also suggested by Tam [96]. Tam et al. [92] also showed that is reasonable to use the complex reflection coefficient or complex impedance as a parameter to compare DNS and experimental data.

2.3 Multiple tone liner response

In previous studies, each frequency component had been considered independent in liner modelling, by assuming that non-linear effects due to frequency interactions are negligible. In fact, the relative amplitude and phase of pressure of each tone changes the overall root mean square pressure at the liner surface, and consequently the OASPL. This also holds for the particle velocity. In other words, high-level acoustic excitation at one frequency can change the impedance at other frequencies, thereby affecting the boundary condition on the liner surface, as discussed by Bodén [7].

Liner impedance is determined by liner features, such as: orifice diameter, plate thickness, porosity, and the resonator cavity depth. Also signal characteristics change liner impedance, such as: multiple tones, positions of tones in the frequency domain (such as near each other, harmonically related or not), phase of each tone component, SPL of each tone, and acoustic velocity produced by each tone. Various authors have addressed this topic by using semi-empirical curve fits to model the liner impedance in the presence

of pure tones, but the impact of all these parameters is not sufficiently well understood in terms of the physics and the complex interaction of different frequency components at high-levels of acoustic excitation. Also, the effect of phase differences between tones is not well understood [6]. No single parameter which controls the impedance for an arbitrary combination of tones has been proposed to date[7].

Rice [78] was the first to observe this issue in the context of his pure tone impedance model. However, Rice's impedance predictions for multiple tones did not satisfactorily match his impedance measurements. His attempt to include a contribution to the steady flow resistance which included all the frequency components did not produced meaningful results.

Cummings [20] proposed an improvement on Rice's equation by allowing the mass end correction to vary with time through the wave cycle. He tested liner samples by measuring the time response and compared this with a model that included a non-linear term based on the discharge coefficient and the instantaneous particle velocity. The results again give only limited understanding of the physics underlying the effect of multiple tone excitation at high level excitation. Cummings observed that different impedance values were measured at the same frequency for cases with and without the presence of a second tone of similar amplitude. Luong [53] rewrote Cummings' equations and analysed the problem of a perforated plate under bias flow for varying amplitudes of the excitation. He suggested the use of his model for noise control engineering, and for the estimation of the acoustic losses in the vocal tract. However, multiple tone modelling was not part of his work.

Bodén [6][10][7][8] performed experiments on four perforated sheet samples and predicted their impedance using Cummings model with the Luong end correction. He defined some semi-empirical constants, adjusted to fit the experimental data. Bodén's samples had orifice diameters from 1.0-3.0 millimetres, face sheet thicknesses between 1.0-2.0 millimetres and porosities from 2.0-28.0%. The samples were excited by several combinations of tones at different relative levels and frequencies. A single tone was usually maintained with its frequency and level fixed. There was no grazing flow or bias flow during the experiments. The impedance results for two, three and four tone combination were compared, while varying the level of each tone at a time. Both resistance and reactance were evaluated as a function of total particle velocity (all frequency components summed) and single frequency particle velocity.

The main conclusions of Bodén were:

1. The Cummings model, with semi-empirical constants adjusted, gives sufficiently good simulation results compared to experimental data for single tone excitation;
2. Harmonically related tones (odd multiples) strongly interact, changing the impedance results, compared to other combinations of tones not harmonically related;

3. Tones at neighbouring frequencies, e.g. 110 Hz and 120 Hz, have a strong interaction causing a higher degree of non-linearity in the resistance;

4. A change in phase between tones produces significant impedance changes at high excitation levels;

5. Impedance results plotted against acoustic velocity for a given frequency component collapse the data better, especially for the resistance.

Bodén [11] also proposed a scattering matrix determination in order to predict harmonic interactions of tones. He assumed that non-linear energy transfer only occurs from lower frequency components to higher frequency tones, and only to odd harmonics. These assumptions will be investigated further in this thesis. However, higher energy transfer between odd harmonics was studied by various authors [34][50][37]. In a more recent study, also by Bodén [9] a pure tone excitation was included in a broadband signal. The impedance spectra was evaluated for different amplitude ratios between the pure tone pressure level and the broadband overall pressure level. It was shown that a pure tone of high amplitude generally causes a resistance increase and reactance decrease in all the spectra in comparison with the impedance values of a broadband excitation without the tone. However, if the tone analysed has a level within 0 to 10 dB higher than the broadband level, the non-linearity was difficult to assess. This data was unfortunately also questionable, however, because the non-linearity evaluated might be caused by the loudspeaker as it is difficult to obtain a perfect sound source with non-linearity that reproduces exactly the desired frequency content.

In conclusion, more experiments including a broader range of frequencies (from 600Hz to 6kHz), combining broadband and multiple tones are needed in order to correctly understand liner responses to multiple tone excitation.

2.4 Design of acoustic resonators

The basic acoustic liner designs used in the aerospace industry are SDOF or MDOF liners. An SDOF liner is composed of a perforated plate over a honeycomb structure. An intermediate porous sheet (or septum) is present in the case of multiple degrees of freedom liners. A cylindrical hole or a slit can be used [96], however, new technologies are emerging, such as beveled holes, narrow tubes with different lengths and spiral cavities[2]. Ingard [38] proposed a theory to design acoustic resonators where the end correction is a function of the liner's porosity. He used geometrical features of the liner to calculate the resistance and the reactance in order to optimize the design and tune the liner for maximum absorption. Figure 2.2 shows resonators with the same cavity volume and the same orifice open area, however, each one has a different resonant frequency and different

resonant wave length. The first four on the top of the Figure 2.2 are represented in a free field and the ones on the bottom are confined in a tube.

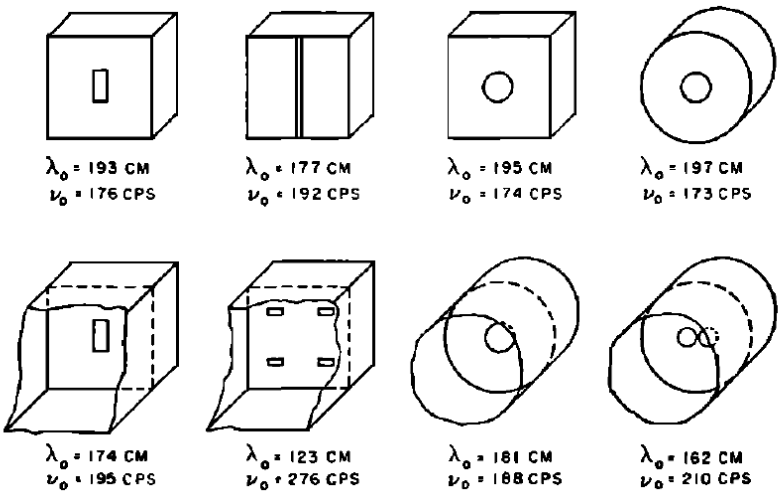

Figure 2.2: Resonators with different geometries but same cavity volume and orifice open area, where λ_0 and ν_0 denote the characteristic wavelength and fundamental resonant frequency for each configuration respectively. From: Ingard, 1953 [38].

The impedance of the resonator on the bottom right, which has two apertures, was calculated analytically by considering the air in the neck of the resonator to act as a piston in a cylindrical tube. The combined mass reactance when the orifices merge in just one orifice is higher than when the orifices are separated. This increases further if the single aperture is in the center of the tube. These observations suggest that using only one perforation is more effective to obtain maximum acoustic reactance for the same open area and volume [38]. This is attractive if a low frequency design is desired with a limited liner depth. However, aero engine liners typically require mass reactance to be minimised in order to maximise bandwidth.

Ingard showed that $\lambda_0/(2\pi)^{1/2}$ is approximately the limiting separation distance above which the apertures can be treated independently of each other. However, usually these separations (hole pitches) are not representative of the perforated facing sheets used in liners, which will probably experience interactions between orifices depending on the porosity and distance between them. Normally there is a fixed space in a nacelle in which to insert a liner and this determines the maximum depth of the liner's cavity. Consequently, the facing sheet porosity and the hole diameter are used to tune the liner to a specific frequency and to target the installed resistance for a given engine operating condition.

Another conclusion drawn by Ingard for resonators confined in a tube, as in the bottom of Figure 2.2, is that the exterior end correction equals the interior end correction (without grazing flow), causing a higher resonance frequency than for the corresponding resonators

in an infinite wall. This must be taken into account when comparing impedance tube data with test rig data, because the sample is positioned in the termination of the impedance tube in the first instance and on a large rectangular duct wall when a grazing incidence test rig is used. Furthermore, the addition of grazing flow serves to reduce the exterior end correction, and increase the resonance frequency, even further [66].

Jones [46] presented impedance data for ranges of geometrical values characteristic of those used in liners for commercial aircraft. The POA of the face sheet was between 6.4 and 13.2%. The orifice diameters were between 1.0-2.4 mm. The face sheet thicknesses were between 0.5-1.0 mm. Cavity depth, which is the honeycomb cell depth, varied from 38.1 mm to 76.2 mm. Various liners were measured using an impedance tube with normal incidence pure tone excitation set to 120 dB at one reference microphone. One geometrical parameter was varied at time, using different samples, to evaluate the effect of each geometrical feature alone. The geometric features of eight liners used in Jones' experiments are listed in Table 2.1. The impedance values measured by the Normal Impedance Tube (NIT) used normal incidence sound waves at the National Aeronautics and Space Administration (NASA), in Langley, USA, are shown on Table 2.2.

Table 2.1: Geometrical features of eight liner samples typically used on commercial aircraft. From: Jones, 2002 [46].

Config (#)	POA (%)	d (mm)	τ (mm)	τ/d	D (mm)
1	6.4	0.99	0.64	0.65	38.1
2	8.7	0.99	0.64	0.65	38.1
3	13.2	0.99	0.64	0.65	38.1
4	15.0	0.99	0.64	0.65	38.1
5	13.0	2.36	0.81	0.34	38.1
6	7.3	1.27	0.51	0.40	38.1
7	7.3	1.27	1.02	0.80	38.1
8	8.7	0.99	0.64	0.65	76.2

Liner resistance was found to be inversely proportional to the POA, showing little variation for values above 13.2 %. At the same time, reducing POA leads to a reduction in the resonant frequency, as the mass reactance is increased. This effect was also observed with grazing flow, where resistance values increase with increasing grazing flow velocities (from 0.0 to 0.5 Mach) as well as for lower POA. Murray, Ferrante and Scofano [70] found similar trends, however, effective POA was shown to vary considerably with manufacturing process depending on whether the perforated plate is punched or drilled, how much hole blockage there is after bonding to the honeycomb core.

In terms of facing sheet thickness, Murray *et al* [70] suggest that: "there is negligible impact on resistance for large diameter holes. However, the facing sheet thickness must

Table 2.2: Impedance values for eight samples under 120 dB, pure tone excitations without flow. From: Jones, 2002 [46].

(a) Acoustic Resistance, θ

	Frequency, kHz				
Liner #	1.0	1.5	2.0	2.5	3.0
1	0.25	0.23	0.20	0.23	0.23
2	0.10	0.15	0.14	0.16	0.16
3	0.08	0.09	0.08	0.09	0.12
4	0.08	0.12	0.08	0.08	0.11
5	0.08	0.11	0.08	0.09	0.11
6	0.10	0.16	0.12	0.15	0.15
7	0.12	0.15	0.19	0.24	0.23
8	0.12	0.14	0.41	0.38	0.18

(b) Acoustic Reactance, χ

	Frequency, kHz				
Liner #	1.0	1.5	2.0	2.5	3.0
1	-0.73	0.10	0.81	1.44	2.07
2	-0.89	-0.13	0.48	1.00	1.53
3	-1.02	-0.28	0.23	0.71	1.22
4	-1.00	-0.29	0.23	0.70	1.23
5	-0.87	-0.07	0.50	1.03	1.64
6	-0.78	-0.02	0.63	1.21	1.80
7	-0.66	0.23	0.93	1.49	2.18
8	0.16	1.12	3.64	-1.95	0.38

be minimised in order to optimize the panel reactance"[1]. Lower ratios of plate thickness to orifice diameter, l/d, increase resistance in flow cases and for all tones evaluated by Jones [46]. Simon [89] coupled narrow tubes made of PolyMethyl Methacrylate on the facing sheet and septum holes and explored the effect of the resonator neck size. He used SDOF and MDOF liners with variable tube lengths. In general, the presence of a narrow tube on the resonator neck causes low frequency absorption changing the resonant frequency of the resonator, which is dependent on the tube length. As the main mechanism of dissipation is based on the boundary layer created in the narrow tubes, the non-linearity due to high SPL is negligible. Narrow tube impedances were first modelled by Zwikker and Kosten [3, p. 45]. Also, ceramic liners having POA=57% were also used by Jones *et al* [45] to evaluate narrow tubes and potentially develop a broadband liner [44].

The cavity depth has a strong influence on the resonant frequency with a cotangent dependence. Deeper cores provide lower panel resonance frequencies and "j" shape cavities have been studied by Sugimoto *et al* [91] in order to minimize the liner depth and obtain low frequency absorption. In addition, Jones [46] observed a noticeable resistance increase at the anti-resonant frequency for samples having higher cavity depths, for both cases with and without grazing flow. Parrot [74] studied multi-layer liners and variable depth liners in order to obtain broadband attenuation. Recently, broadband liners designed using software tools have been studied in order to maximize attenuation, optimizing the available area of the liner using different depth channels [37]. Examples of novel designs proposed recently for broadband liners are shown in the Figure 2.3 where different depth channels are used to tune the liner to various frequencies.

Recent studies show the importance of facing sheet hole shape on the liner impedance.

[1] Private discussion with the author in 30/05/2018.

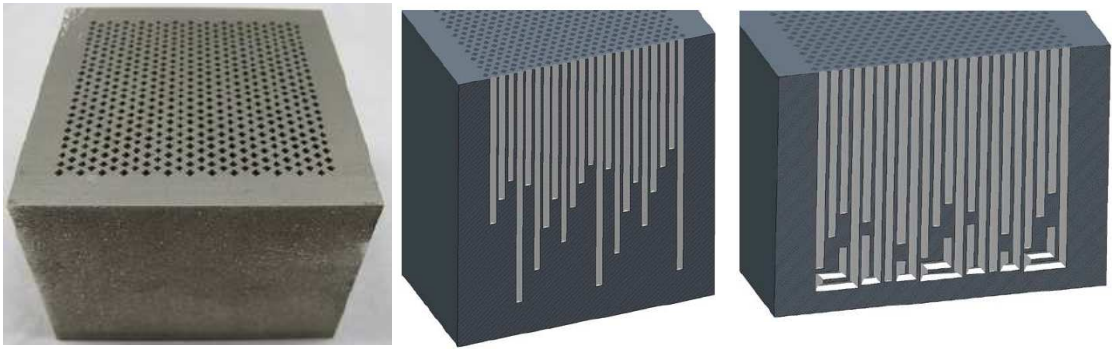

Figure 2.3: Broadband liners, top view on the left, quarter wave length tubes cross-section on the middle and complex shape tubes cross-section on the right. From: Howerton, 2012 [37].

Caiero *et al* [17] developed an adjoint method to optimize the hole edge shape of a resonator in order to promote higher acoustic attenuation at low SPL. Despite the practicalities of producing such precise geometric features, it was shown by Forner & Polifke that asymmetric holes with chamfered edges produce slightly lower resistances than straight and symmetric holes [34].

2.5 Grazing flow effect

The presence of grazing flow alters a liner impedance when compared with the case without grazing flow. Both resistive and reactive components are affected. A 2-D approach was used by several authors in order to isolate the grazing flow effect from other effects on the acoustical performance of the liner [52][21][56][69][47]. The mean Mach number of the tangential flow is a simple parameter that can be used, however the boundary layer developed and, in particular, its skin friction velocity provides an improved correlation for the grazing flow effect [51] [70].

Munjal [67] described the dispersion relation for the no flow case, assuming the continuity of the particle displacement in a closed tube with a rectangular cross section. In the absence of flow Cartesian wave numbers are given by

$$k_0^2 = k_x^2 + k_y^2 + k_z^2, \tag{2.11}$$

where $k_0 = \frac{2\pi f}{c_0}$ is the wave number; k_x, k_y and k_z are the wave numbers in each direction of a Cartesian system and z is the axial direction of the duct. For the flow case, we have

$$k_x^2 + k_y^2 + k_z^2 = (k_0 \pm M k_z)^2, \tag{2.12}$$

where $M = v_z/c$ is the average Mach velocity in the axial direction of the duct. The wave number of a plane wave propagationg in the axial direction can be written as

$$k_z^{\pm} = \frac{k_0}{1 \pm M}, \tag{2.13}$$

where k_x and k_y have been set to zero [1]. In this case, the cut-on frequency for higher order modes of a rectangular duct, with h as the largest side of the cross section, can be defined as

$$f_c = \frac{c_0}{2h}\sqrt{(1 - M^2)}. \tag{2.14}$$

Kurze [52] has shown that increasing Mach number decreases the liner attenuation when the sound waves are in the same direction as the flow, but increases the attenuation when the sound waves propagate against the flow in a duct. The attenuation is also a consequence of the optimum impedance in a duct, so in real engines the direction of the flow and the sound waves are important. Recent studies demonstrated the differences between downstream and upstream impedance eduction results [11]. Murray[70] observed that: "grazing flow increased acoustic resistance and decreased reactance, with the acoustic resistance under grazing flow decreasing with increasing frequency"[2]. Murray also observed a significant increase in resistance for high SPL, for highly non-linear SDOF perforate panels [69].

Kooi & Sarin [51] considered skin friction velocity as the parameter that better represents grazing flow effects, because a resistance decrease was observed for lower values of skin friction velocity at the same centerline Mach number. By using Mach number as the grazing flow correlating parameter, Murray [69], following on from the work of Kooi and Sarin [51], suggests a semi-empirical resistance due to grazing flow term to sum with the linear viscous resistance and non-linear resistance terms, which is

$$R_{gf} = \frac{k_2 M\,[5 - l/d]}{4\sigma} - \frac{k_3 df}{\sigma c_0}, \tag{2.15}$$

where k_2 and k_3 are empirical constants.

Cummings [21] developed a rectangular cross section test rig fed by a silenced air supply that developed the boundary layer on a duct until the flow reaches the liner sample with just one orifice. The acoustic source was upstream the orifice, so the sound waves travelled in the same direction of the flow. The velocity profile inside the duct could be measured using a Pitot tube. Cummings found that friction velocity partially masks the true nature of mean flow effects at the orifice. Rice [78] and Montsinger [66] modelled grazing flow effects based on the average Mach number of the grazing flow profile. The

[2] Private discussion with the author in 30/05/2018.

resistance, θ, and end correction, ϵ, were defined as

$$\theta = \frac{0.3M}{\sigma}, \tag{2.16}$$

$$\epsilon = \frac{0.85d\,(1 - 0.7\sqrt{\sigma})}{1 + 305M^3}. \tag{2.17}$$

Murray suggests a small change to Equation 2.17, representing the end correction as

$$\epsilon = \frac{0.85d\,(1 - 0.7\sqrt{\sigma})}{1 + 200M^3}. \tag{2.18}$$

Hersh, taking the discharge coefficient, C_D, as the ratio between the *vena contracta* area and the perforated plate hole area [36]. The ratio can be obtained applying the conservation of mass in a control volume. Hersh suggests that the discharge coefficient approaches $C_D = 0.64$ at the resonance at high SPL and it is independent of the hole diameter. However, Hersh suggested that $C_D \longrightarrow 1$ above the resonance, where the particle velocity magnitude is smaller.

Zhang & Bodony [104] used high-fidelity DNS models to study the effect of different boundary layers on perforated liners in the presence of high SPL. The discharge coefficient, C_D, simulated using DNS, was found to be highly dependent on the ratio of the acoustic velocity in the hole divided by grazing flow mean Mach number over the perforated sheet during the inflow, $\frac{v_{in}}{M}$, and outflow, $\frac{v_{out}}{M}$, regimes. The C_D calculated in both regimes and high SPL followed the equation,

$$C_{Din} = 0.76 \tanh\left[1.57\left(\frac{v_{in}}{M}\right)^{0.47}\right], \tag{2.19}$$

$$C_{Dout} = 0.76 \tanh\left[6.32\left(\frac{v_{out}}{M}\right)^{0.65}\right], \tag{2.20}$$

where C_{Din} and C_{Dout} are the discharge coefficients during the inflow and the outflow regimes respectively. The mean value of the discharge coefficients during these two regimes can be used to describe the effective discharge coefficient for a complete cycle. The same authors also suggest exploring additional simulations and experiments which target the near-liner interaction. This approach would be preferable to using impedance eduction results, in order to design the liners more efficiently [102].

To summarise the main hypotheses regarding grazing flow:

- The grazing flow effect is important for aero engine liner impedance predictions, and it is dependent on skin friction velocity, Mach number, SPL, frequency and geometric parameters such as POA, sheet thickness and hole diameter. Nevertheless, physical explanations are required to improve the existing models [70][104];

- The average Mach number can be used instead of friction velocity with minor discrepancies for ducts with small pressure gradients. This simplifies the impedance modelling as skin friction velocity is not always available [51][70].

2.6 1D Impedance Models

Several semi-empirical, numerical and experimental models have been developed to predict liner impedance. Frequency domain semi-empirical methods include these of Kooi & Sarin[51], Montsinger & Kraft[66], Maa[54], Hersh [36], Elnady[26] and Murray[69]. Rienstra & Singh[82] developed an analytical frequency domain impedance model for the resistance of a Helmholtz resonator that shows good agreement with the Montsinger & Kraft model. The Maa model is used to design micro perforated plates of typical interest as liner manufacture processes are developing to allow manufacture of micrometric hole diameters, which may show broadband attenuation if they are well designed and manufactured. However, it was studied to show the limitations of this approach during the liner impedance modelling. Rice [78], Cummings [20], Richter [79] and Tam [94] developed time domain models which are discussed in this section.

Most impedance models for perforate plates depend upon the same fundamental design parameters. If a lumped-parameter model is used, the coefficients may have physical interpretation and the system may be derived as an ODE (Ordinary Differential Equation). For most practical geometries, $\lambda \mathbf{a} \ll 1$, where λ is the characteristic wavelength and $\mathbf{a}$ is a characteristic dimension of the perforate, typically the hole radius or diameter. The wavelength is generally some orders of magnitude larger than the characteristic dimension of the resonator. So, this problem can be treated essentially as being one dimensional, by considering plane waves inside the resonator.

Although, micro fluid interaction is important for the case of sound incident upon a perforated sheet, it is computationally expensive if a 3D numerical simulation is used to solve the problem in time domain [102]. Engineering models for impedance use average fluid dynamic values, which subsequently need to be described carefully [81]. Analytical solutions are impractical for most cases because the time domain differential equations have non-linear terms and the nature of the incident pressure is complex. So, numerical solutions are needed to evaluate the influence of non-linear terms [20].

A convention of symbols, parameters, regions and geometry components based on a Helmholtz resonator model is defined here and used for different impedance models in the following sections.

Figure 2.4 illustrates a generic Helmholtz resonator, where facing sheet thickness is represented by l, cavity depth is h, cavity backing plate area is S_b. The region between "A" and "B" is the air cylinder, in case of a circular hole, represented as the resonator neck

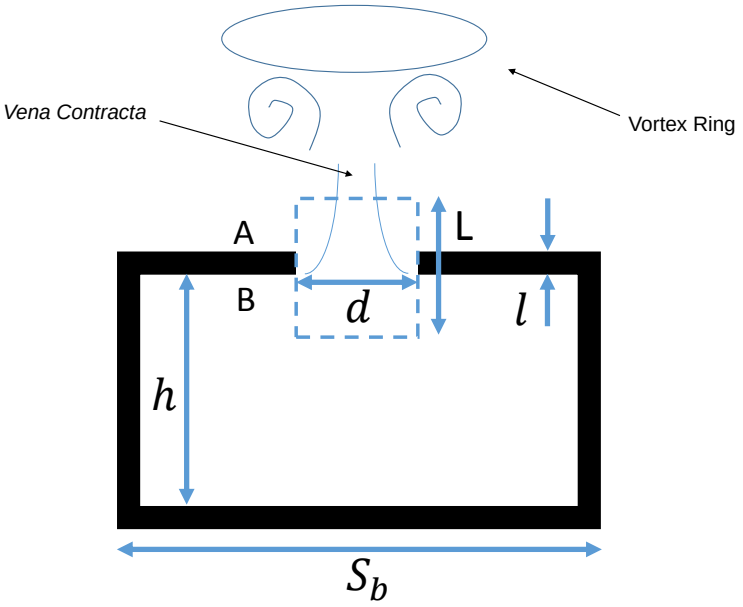

Figure 2.4: Helmholtz resonator simplified model.

with diameter d and the properties in this region are represented using the subscript zero. The effective thickness L is the sum of plate thickness, l, and the end correction, ϵ, which is dependent on the mean acoustic velocity, v_0, across the orifice area. The area of this air cylinder can be obtained by $S = \pi d^2/4$. The porosity of the liner is obtained from $\sigma = S/S_b$ and the POA is obtained from $POA = 100\sigma$. The cavity volume depends on the geometry of the cavity and typically, a commercial aircraft liner has honeycomb hexagonal structures dividing the cavities. But if POA is used as a parameter in a 1-D model, the shape and width of the cavity is irrelevant.

It is important to understand the acoustic velocity profile inside the orifice region to correctly predict the dissipation mechanism. Most engineering models use an assumption of uniform flow through the hole. If the plug of air contained in the hole oscillates at small amplitudes, the jet will not fully develop and the main dissipation mechanism is due to the interaction of the air with the walls of the hole [81]. A boundary layer is developed on the hole walls, which causes a laminar velocity profile on the hole cross section along the facing sheet thickness. This velocity profile contracts the mass of fluid in a narrow channel, also called *vena contracta*, during each acoustic cycle that causes pressure difference between inside and outside the liner cavity. The *vena contracta* is the area where the stream lines are parallel in the hole. The *vena contracta* represents a irrotational flow that is the core of the jet. The discharge coefficient can be calculated as the ratio of cross section area of this jet core S_{vena} by the area of the hole S, obtaining $C_D = S_{vena}/S$.

The discharge coefficient is one of the key parameters required to evaluate liner impedance, because it is a function of the dimensional properties of the plate, frequency and

flow properties. Cummings [20] used fixed value of $C_D = 0.76$ based on experimental data. Some years later, Murray [69] showed the dependence of C_D on frequency. Zhou [105] studied the effect of bias flow in perforated plates and considered the discharge coefficient as a product of acoustic oscillating flow and bias flow coefficients, that together influence the *vena contracta*. Zhou also suggests that the jet is unsteady and symmetric on both sides of the liner orifice for high SPL without flow. Furthermore, Elnady [25] proposed numerically simulated values of C_D based on geometrical parameters of the liner, as showed in Table 2.3.

Table 2.3: Numerical values proposed for the discharge coefficient. From: [25].

		Diameter, mm										
		0.6	**1**	**1.3**	**1.6**	**2**	**2.5**	**3**	**3.5**	**4**	**4.5**	**5**
Thickness, mm	**0.5**	0.855	0.832	0.80	0.78	0.76	0.74	0.725	0.724	0.72	0.72	0.72
	0.8	0.86	0.84	0.82	0.80	0.78	0.761	0.753	0.741	0.737	0.736	0.736
	1	0.87	0.85	0.83	0.815	0.80	0.78	0.77	0.765	0.762	0.761	0.761
	1.25	0.88	0.865	0.85	0.83	0.82	0.81	0.8	0.795	0.793	0.792	0.792
	1.5	0.89	0.875	0.865	0.855	0.84	0.83	0.825	0.82	0.818	0.817	0.817
	2	0.90	0.895	0.89	0.885	0.88	0.875	0.872	0.87	0.869	0.868	0.868
	2.5	0.91	0.91	0.91	0.91	0.91	0.91	0.91	0.91	0.91	0.91	0.91

Elnady also defined the effective discharge coefficient in the case of grazing flow, presented by an empirical equation,

$$C_D = \frac{1}{2.1 - 0.332/\eta + 0.0566/\eta^2}, \tag{2.21}$$

where $\eta = v_0/M$ is the ratio of bias flow through the hole, v_0, and grazing flow Mach number outside the liner, M.

For high SPLs near the resonant frequency of the liner, vortex rings are shed as shown in Figure 2.1.(e). The vorticity is random in both space and time, and exhibits a wide and continuous distribution of length and time scales that are related to the sound excitation [22]. The acoustic energy is transformed into kinetic energy of the vortex structures as the sound wave reaches the liner facing sheet. It is redistributed from large length scales to small length scales until it is dissipated in the form of viscosity. This mechanism of dissipation, or destruction, of kinetic energy is known as the energy cascade [22].

In conclusion, the interaction between the zero grazing and bias flow discharge coefficient, grazing flow Mach number, and bias flow velocity profile are key to modelling and predicting liner impedance. The selection of the best liner for a given application depends on the engine noise signature, the magnitude of the grazing flow, and the optimum wall impedance for the duct in question. So, numerical sound propagation models and experiments are needed to find the optimum liner impedance values for a given duct and consequently the liner geometry to best meet this requirement. The models described in

the next sections consider such parameters and are partially accepted by the scientific community to predict liner impedances.

2.6.1 Basic and Extended Helmholtz Resonator Model

The Helmholtz resonator model is known as a typical Lumped Parameter Model, because it obeys four principles:

- Limited number of time-dependent aggregate variables;
- Described by an ODE;
- The coefficients (lumped-parameter elements) have physical interpretation;
- Usually $ka < 1$, where a is a characteristic dimension, such as orifice diameter or radius.

Morse [65] states that typical liners may be modelled as an array of Helmholtz resonators, where the inertance of the system is the mass of air in the orifice, which is interpreted as the neck of the resonator. On the other hand, the compliance of the system is the volume of air inside the cavity, which is typically delimited by a honeycomb structure. This volume of air is compressible so it is interpreted as a spring effect. The force exciting the system is caused by the external pressure oscillation of a sound wave impinging upon the system at the facing sheet. The resistance represents the damping from hole friction and the creation of vortices at high SPLs.

A Helmholtz resonator model is straightforward and gives a good estimate of the resonant frequency of a single cell of the liner without flow. The impedance of the Helmholtz resonator may be split in two parts: neck impedance and cavity impedance[5], where

$$Z_{HR} = Z_{HR}^{neck} + Z_{HR}^{cavity}, \tag{2.22}$$

or

$$Z_{HR} = i\frac{\omega\rho L}{S} + \frac{\rho c k^2}{2\pi} + \frac{\rho c^2}{i\omega V}, \tag{2.23}$$

where ω is the frequency in radians, $L = l+\epsilon$ is the effective neck length, S is the open area of the orifice, k is the wave number and V is the cavity air volume. The end correction ϵ for a flanged termination can be approximated using $\epsilon = 0.85d$. The first two terms of Equation 2.23 correspond to the neck impedance and the third is related to the cavity impedance. When the system shows zero imaginary impedance, particle displacement and velocity are 90°out of phase, hence the system is at the resonant frequency; which is given by,

$$f_0 = \frac{c}{2\pi}\sqrt{\frac{S}{LV}}, \tag{2.24}$$

where f_0 is the resonant frequency of a single Helmholtz resonator in Hz.

There are some issues which arise if the model complexity increases, depending on the order of magnitude of some phenomena. For example:

- Flow profile inside the resonator neck;
- Reynolds number for the steady flow (bias flow) through the orifice;
- Wall heat exchange;
- Turbulence;
- Flow separation on sharp edges;
- Grazing flow outside the liner.

Usually the flow is considered adiabatic for small pressure oscillations and without flow separation, which means only linear losses and low damping. Instead, non-linear losses occur when the acoustic particle displacement has the same order of magnitude as the hole diameter. The Strouhal number, St, provides a measure for this effect, where

$$St = \frac{\omega d}{|v_0|}. \tag{2.25}$$

Forner [50] suggests a different definition of Strouhal number based on the spatially average particle velocity over the liner surface,

$$St = \frac{\omega d POA}{\langle \overline{v_s} \rangle}. \tag{2.26}$$

It was observed that non-linearity is observed at $St < 1$ for typical liners [50].

The impedance of the Helmholtz resonator can be also described as

$$Z(\omega) = R + i\omega m - i\cot(kh), \tag{2.27}$$

where ωm is the face plate mass reactance, and $-\cot(kh)$ is the cavity reactance, with h being the cavity depth. This model is called EHR (Extended Helmholtz Resonator) and it is used to represent the impedance of an array of Helmholtz resonators. This basic liner model can be expressed in the time domain by using the z-transform [80], considering that:

1. Damping is greater than zero, $\vartheta > 0$, at the cavity;
2. Cavity reactance is positive, $\beta > 0$;

3. Cavity depth is at multiples of the time step: $2h/c = \nu\Delta t$.

The EHR equation becomes,

$$Z(\omega) = R + i\omega m - i\beta \cot\left(\frac{1}{2}\omega\nu\Delta t - i\frac{1}{2}\vartheta\right). \tag{2.28}$$

This model satisfies the reality condition, is causal and can be transformed to the time domain, giving

$$\frac{\zeta(t)}{2\pi} = R\delta(t) + m\delta'(t) + \beta\delta(t) + 2\beta\sum_{n=1}^{\infty} e^{-\vartheta n}\delta(t - n\nu\Delta t), \tag{2.29}$$

where δ is the delta function. The complete derivation is given by Rienstra [80], who suggests the use of this analytical solution as a test case for numerical implementations.

Subsequently, Richter [79] compared the EHR with another time domain model proposed by Tam [94]. The model can be incorporated into computational aeroacoustic codes using the Myers boundary condition [72], as well as for single frequency excitation, producing fairly good predictions except when flow instability occurs. Five parameters of the model are obtained by a non-linear optimization procedure that neither deals with non-linearities nor multiple tone excitations.

2.6.2 Maa Model

A simple analytic model for MPP (Micro Perforated Plates), proposed by Maa, is described as the sum of resistance components due to friction loss and high SPL non-linear components. Non-linearities are related to jet formation and end correction changes [54]. It is a frequency domain impedance model which provides good representation of sub-millimetre orifices in a surface. The comparison of the Maa model with the Rice model, Cummings model and experimental data is included in the scope of the current thesis, despite the fact that there are several other time and frequency domain models.

The normalized impedance of the perforate plate can be described by the Maa model as,

$$\zeta = \theta + i\chi. \tag{2.30}$$

The resistance θ is given by

$$\theta = \frac{32\mu l}{\sigma\rho c d^2}\left[\sqrt{1 + K^2/32} + \frac{\sqrt{2}Kd}{8l}\right] + \frac{v_0}{\sigma^2 c}. \tag{2.31}$$

where K is the perforate constant given by,

$$K = \frac{d}{2}\sqrt{\omega/\nu}, \tag{2.32}$$

where $\nu = \mu/\rho$ is the dynamic viscosity. The velocity in the hole v_0 can be calculated using experimental data or using an asymptotic procedure.

Equation 2.31 shows two linear terms. The third term is the non-linear, because it depends on the particle velocity, v_0 which usually is modelled as the root-mean-square (calculated from the velocity in the time domain), root-sum-square (used for broadband noise, calculating an average of the velocity spectrum) or the peak value (calculated from the velocity in the time domain). However, there is no agreement among researchers regarding the best velocity description [10].

The reactance χ is described by Maa as

$$\chi = \frac{\omega l}{\sigma c}\left[1 + \left(1 + K^2/2\right)^{-1/2} + 0.85\frac{d}{l}\left(1 + \frac{v_0}{\sigma^2 c}\right)^{-1}\right]. \tag{2.33}$$

Equation 2.30 is used either to design MPP absorbers, or to compare and validate other models [10][18]. Unfortunately, the Maa model can be used to predict liner impedance behaviour only in the presence of a single tone excitation. Bodén [10] compared the Maa model, the Elnady Model [26] and experimental data using random, multiple or pure tone excitations. Both models showed inconsistent results, and provide limited frequency ranges. This observation reinforces the hypothesis that signal frequency content should be included in the impedance models, to represent the linear and the non-linear velocity regions. The experimental data collected in the current work aims to test this hypothesis.

Recently, Carbajo [18] compared the Maa model with numerical simulations. Visco-thermal terms were taken into account and the tube had no flow in order to perform the FEM calculation using the Linearized Navier Stokes equation. The geometry of an impedance tube with a perforated panel coupled with a backing cavity was analysed. The results of the FEM simulation agreed better with experimental data than with the Maa model for Carbajo's samples. Carbajo simulated all the holes of the perforated plate, which was computationally costly so only low SPL was simulated.

2.6.3 Rice Model

Rice [78] suggested an one-dimensional model to describe the behaviour of a single resonator with one orifice. The impedance of one orifice can be used to calculate the impedance of the surface of the liner by dividing by the POA. The model combines linear and non-linear terms to describe the system response over a wide range of sound pressure levels. It also considers the excitation as either a single pure tone or a combination of

multiple tones, however the impedance results for multiple tone does not produce meaningful values. This section includes the description of the Rice model. The numerical implementation and validation will be covered in section 4.1.

The differential equation of the Rice model uses the absolute particle displacement in the hole as the variable to be calculated for a given pressure signal. The effective thickness (plate thickness + end correction) is not time dependent but varies with the hole diameter, POA and grazing flow Mach number. It is given by

$$L = l + \epsilon, \tag{2.34}$$

where

$$\epsilon = \frac{0.85d\,(1 - 0.7\sqrt{\sigma})}{1 + 305M^3}. \tag{2.35}$$

The grazing flow is given by $M = v_\infty/c$, where v_∞ is the velocity of the flow outside the boundary layer. When the flow is confined in a duct, v_∞ could be represented as the average value over the analysed cross section of a tube. The definition of the end correction of Equation 2.35 has been used by other authors [66]. However, the end correction varies with acoustic particle velocity and frequency. This dependency will be further investigated during the analysis of the experimental results reported in this thesis.

The total resistance of a single resonator, R_o, can be separated into a non-linear component R_{on}, related to the acoustic velocity, and a linear component R_{ol}. Moreover, the non-linear term is described as highly dependent on the level of excitation. The linear term is composed of the steady flow resistance R_{os} and the frequency-dependent orifice resistance, R_{of}, which arises from the viscous boundary layer.

Hence, the total resistance R_o is expressed by

$$R_o = R_{on} + R_{ol}, \tag{2.36}$$

where the linear resistance is composed of the orifice and steady flow resistances, $R_{ol} = R_{os} + R_{of}$. The Rice model defines the orifice resistance, R_{of}, differently depending on the frequency and on the excitation signal. For single tone excitation, R_{of} is defined as,

$$R_{of_{pure}} = \rho c \theta_{of_{pure}} = \rho\sqrt{8\nu\omega}\,(1 + l/d + \Delta_{NL}/d)\,. \tag{2.37}$$

where Δ_{NL}/d is the non-linear resistive end correction.

Ingard [40] found good correlations of the non-linear resistive end correction with measured data for diameters varying from 7 to 90 mm. His experimental data was collected in the presence of a steady bias flow having the same magnitude as the particle velocity caused by a sound wave. It was found that a quadratic relation between pressure and velocity exists for high SPLs, where $p \backsimeq \rho v_0^2$. In addition, Rice suggests that a loss of

acoustic-radiation efficiency is due to the rotational velocity field in the vicinity of the orifice, which creates a jet and does not contribute to the sound field. Rice excludes the term Δ_{NL}/d for low excitation levels, which is sensible. The argument is that viscous drag dominates the absorption mechanism for low SPL without grazing flow.

For multiple tones, when k frequency components are present, the orifice resistance is defined by Rice as

$$R_{of_{multiple}} = \rho c \theta_{of_{multiple}} = \rho\sqrt{8\nu}\left(\frac{\sum_k P_k}{\sum_k P_k/\sqrt{\omega_k}}\right), \tag{2.38}$$

where P_k is the pressure peak amplitude value of the k^{th} frequency component. This definition is considered unsatisfactory by Rice, and require further studies [78]. Rice states that non-linear resistance terms are larger than linear terms for high SPL. Consequently, the term in the Equation 2.38 would be considerably smaller than the R_{on} term. For this reason no attention was given by Rice to the effect of the multiple tone responses, especially when grazing flow was considered.

The steady flow resistance, R_{os}, presented by Rice is based on a derivation by Nelsen [78, p.7]. Alternatively, Motsinger [66] defines the linear steady flow resistance by,

$$R_{os} = \frac{32\mu l}{C_D d^2}, \tag{2.39}$$

by considering just the bias flow generated by the acoustic field and assuming the flow is incompressible inside the orifice. Bias flow is defined as the flow through the liner perforated plate hole, differently from the grazing flow caused by a steady or an unsteady flow outside the liner sample. The non-linear resistance is defined as,

$$R_{on} = \rho|v_0|, \tag{2.40}$$

and when normalized by the characteristic impedance of air this gives,

$$\theta_{on} = \frac{R_{on}}{\rho c} = \frac{|v_0|}{c} = M_0, \tag{2.41}$$

where M_0 is the acoustic Mach number of the air particle in the neck of the resonator. At high SPL, the relationship of pressure and particle velocity is quadratic, with a subsequently linear resistance-particle velocity relationship above certain values of velocity [40].

In order to validate this method by using impedance tube measurements, no grazing flow terms were included in the formulation. The particle velocity v_0 caused by the sound excitation might interact with the grazing flow velocity, v_∞, to form the jet, depending on the magnitude and direction of both velocities. The non-linear resistance in the presence

of grazing flow is defined by Rice as

$$\theta_{on} = Q, \ for \ Q > \frac{|v_0|}{c}, \tag{2.42}$$

$$\theta_{on} = \frac{|v_0|}{c}, \ for \ Q < \frac{|v_0|}{c}. \tag{2.43}$$

where Q describes the grazing flow influence, defined as,

$$Q = 0.3M\left(\frac{3.15 \times 10^{-2}}{\sigma} + 1.77\sigma + 0.3\right). \tag{2.44}$$

When the acoustic jet is outward from the cavity, Equation 2.42 is used as the grazing flow contribution dominates, or Equation 2.43 is used when acoustic particle velocity in the orifice dominates.

When the jet is acting into the cavity, both non-linear and grazing flow components are important, depending on the relative magnitudes of SPL and M, so the following equation is used,

$$\theta_{on} = \frac{|v_0|}{c} + Q. \tag{2.45}$$

The facing sheet non-linear resistance, θ_{on}, is usually much bigger than the linear component, θ_{ol}, for perforated plate liners in the presence of high SPL. Therefore, Rice suggests linear terms may be discarded if the objective is to describe the perforate liner impedance at high SPLs. Observe that it is difficult to establish a fixed value for the grazing flow Mach number contribution because the event is cyclic and the jet occurs in both directions.

The differential equations of the Rice model are given by,

$$\rho L\frac{d^2x_0}{dt^2} + R\frac{dx_0}{dt} + \frac{\rho c^2\sigma}{h}x_0 = P(t), \tag{2.46}$$

$$v_0 = \frac{dx_0}{dt}. \tag{2.47}$$

where $P(t)$ is the incident pressure in Pascal on the liner surface [78]. The porosity, σ, can be replaced by the Effective Percentage of Open Area (POA_{eff}) if experimental data is available.

Following manipulation of Equation 2.46, by isolating the acceleration term, and dividing the whole equation by ρL to transform it into a first order ODE, the Rice model for pure tones can be expressed using Equation 2.41, Equation 2.39 and Equation 2.37 as,

$$\frac{d^2x_0}{dt^2} = \frac{P(t)}{\rho L} - \left[\frac{|v_0|}{L} + \frac{32\mu l}{C_D d^2 \rho L} + \frac{\sqrt{8\nu\omega}}{L}(1 + l/d)\right]\frac{dx_0}{dt} - \frac{c^2\sigma}{hL}x_0. \tag{2.48}$$

For multiple tone excitation, Rice model is given by,

$$\frac{d^2x_0}{dt^2} = \frac{P(t)}{\rho L} - \left[\frac{|v_0|}{L} + \frac{32\mu l}{C_D d^2 \rho L} + \frac{\sqrt{8\nu}}{L}\left(\frac{\sum_{k=1}^{k=\infty} P_k}{\sum_{k=1}^{k=\infty} P_k/\sqrt{\omega_k}}\right)\right]\frac{dx_0}{dt} - \frac{c^2\sigma}{hL}x_0. \quad (2.49)$$

2.6.4 Cummings Model

Cummings proposed a model [20] to deal with both high SPL and multiple tone excitations in 1984. It is essentially the same equation as the Rice model with some improvements on the time variable end correction and the introduction of the discharge coefficient in the non-linear damping term. First, the effective orifice thickness L of a perforated plate is defined as the sum of the physical thickness l and the end correction ϵ defined in Cummings model as,

$$\epsilon = \epsilon_r \epsilon_m, \quad (2.50)$$

where

$$\epsilon_r = \epsilon_a/\epsilon_m, \quad (2.51)$$

which is the ratio of the actual end correction ϵ_a divided by the maximum possible end correction ϵ_m. This parameter essentially depends on the shape of the orifice and the flow velocity through it. For low SPL, the velocity in the orifice is also low and the end correction can be assumed to be equal on both sides of the perforated plate, if the attached mass of both adjacent orifices do not interact [64].

Lord Rayleigh [77] found that for flanged orifices in infinite walls the end correction at each side is $l_0 = 4d/3\pi \approx 0.425d$, which was proved later by Ingard [38]. Consequently, Cummings proposed the effective thickness for low SPL (linear region) as

$$L = l + \epsilon = l + 2l_0. \quad (2.52)$$

The ratio ϵ_r applies when there is a non-linear response, which occurs, as defined empirically by Cummings [20], as a function of the jet length L_j, formed outwards from the orifice. The effective thickness of the perforated plate decreases as the jet length increases because the inertia of the potential flow through the orifice is progressively replaced by that of the jet. The ratio ϵ_r is defined by Cummings as,

$$\epsilon_r = \left(1 + \frac{L_1^{1.585}}{3}\right)^{-1}, \quad (2.53)$$

where,

$$L_1 = \frac{L_j}{d} = \frac{\int_0^{\tau} |v_0| dt}{d}, \quad (2.54)$$

and the period of time from $t = 0$ to $t = \tau$ comprises a half cycle in which the flow ejection process occurs. This means that the period between the beginning and the end of flow ejection on one side of the plate is used to calculate the integral of Equation 2.54 [53].

The transient velocity response, represented in the first milliseconds of the excitation process, occurs at the beginning of the physical process, when the pressure wave hits the perforate plate. The velocity response can be represented as a sum of sine and cosine waves, where just a half cycle is extracted to calculate L_1 and the end correction ratio ϵ_r, after considering enough time to obtain a permanent regime solution. The effective thickness of the facing sheet, considering the end correction in the non-linear regime without flow was represented by Luong[53] as,

$$L = l_0 + (l + l_0)\epsilon_r. \tag{2.55}$$

Bodén [10] also implemented the Cummings model by using different values of the end correction ratio, where

$$\epsilon_r = \left(1 + \frac{L_1^{1.2}}{24}\right)^{-1}, \tag{2.56}$$

for perforate plates with porosities, σ, from 2.0 % to 28 %. The constants used to calculate L_1 were obtained by comparing the numerical implementation of Cummings model with his experimental data [7][8].

Having defined the end correction, the differential equation that models the problem of a perforate plate with a cavity attached for high sound pressure levels is given by

$$\rho L \frac{d^2x_0}{dt^2} + \left[\frac{\rho|v_0|}{2C_D^2}\right]\frac{dx_0}{dt} + \frac{\rho c^2 S}{V}x_0 = P(t). \tag{2.57}$$

It can be observed that Equation 2.57 has non-linear damping only in the second term, because it is assumed that the linear terms are negligible for high level acoustic excitations and the equation will be used only for high SPL. However, the linear terms defined in Equation 2.37 and Equation 2.39 can also be included to represent the behaviour of the liner in all the SPL range.

2.6.5 Model Comparisons

Although same similarities exist, both the Rice and Cummings time domain impedance models use distinct approaches to calculate the end correction and use different non-linear terms to describe damping of the system.

The Rice model gives,

$$\rho L\frac{d^2x_0}{dt^2}+\left[\rho|v_0|+Q+\frac{32\mu l}{C_D d^2}+\rho\sqrt{8\nu\omega}\,(1+l/d)\right]\frac{dx_0}{dt}+\frac{\rho c^2\sigma}{h}x_0=P(t). \tag{2.58}$$

where

$$L=l+\frac{0.85d\,(1-0.7\sqrt{\sigma})}{1+305M^3}. \tag{2.59}$$

The Cummings model is given by

$$\rho L\frac{d^2x_0}{dt^2}+\left[\frac{\rho|v_0|}{2C_D^2}\right]\frac{dx_0}{dt}+\frac{\rho c^2 S}{V}x_0=P(t). \tag{2.60}$$

where

$$L=l_0+(l+l_0)\left[1+\left(\frac{\int_0^\tau|v_0|dt}{d}\right)^{1.585}/3\right]^{-1}. \tag{2.61}$$

The Bodén model, based on Cummings is given by

$$\rho L\frac{d^2x_0}{dt^2}+\left[\frac{\rho|v_0|}{2C_D^2}+\frac{32\mu l}{C_D d^2}+\rho\sqrt{8\nu\omega}\,(1+l/d)\right]\frac{dx_0}{dt}+\frac{\rho c^2 S}{V}x_0=P(t). \tag{2.62}$$

where

$$L=l_0+(l+l_0)\left[1+\left(\frac{\int_0^\tau|v_0|dt}{d}\right)^{1.2}/24\right]^{-1}. \tag{2.63}$$

Recently, another time-domain model was proposed by Zhang [103], given by

$$\rho L\frac{d^2x_0}{dt^2}+\left[\rho\frac{1-C_D|v_0|}{C_D}\right]\frac{dx_0}{dt}+\frac{\rho c^2 S}{V}x_0=PSe^{i\omega t}+\sum_j T_j\,(\omega_j)\,Se^{i(\omega_j t+\phi_j)}, \tag{2.64}$$

where T_j in the last term represents the amplitude of the turbulent boundary layer fluctuation at frequency ω_j, S is the orifice area and ϕ_j is a random phase. This expression was used to predict the discharge coefficient, C_D, using different grazing flow boundary layers. This model won't be implemented and compared with the others, but it shows the importance of flow effects on liner modelling. Another description of the non-linearity shown in the second term on the left hand side of the Equation 2.64 can be tested in the evaluated models in order to evaluate the effect of the discharge coefficient.

The first terms of both the Rice and the Cummings models are different because Cummings considers L varying with time. On the other hand, Rice includes the grazing flow effect that is not described by Cummings. The second terms consider differently the non-linearities and Cummings does not consider the linear terms at high SPL. The linear terms were included in the Bodén model. The ratio S/V, which is the neck resonator

area divided by the cavity volume, can be written as the POA divided by the cavity depth,

$$\frac{S}{V} = \frac{\sigma}{h}, \tag{2.65}$$

so essentially the stiffness is the same in both models and is represented on the third term of the equations. The Rice, Cummings and Bodén models represent one single orifice of the liner, so it is necessary to divide the impedance by POA to have representative values on the liner surface.

The Maa frequency domain model is given by

$$\zeta = \frac{32\mu l}{\sigma\rho c d^2}\left[\sqrt{1+K^2/32} + \frac{\sqrt{2}Kd}{8l}\right] + \frac{v_0}{\sigma^2 c} + \tag{2.66}$$

$$i\frac{\omega l}{\sigma c}\left[1 + \left(1+K^2/2\right)^{-1/2} + 0.85\frac{d}{l}\left(1+\frac{v_0}{\sigma^2 c}\right)^{-1}\right], \tag{2.67}$$

where

$$K = \frac{d}{2}\sqrt{\omega/\nu}. \tag{2.68}$$

Table 2.4 compares some of the key features between the cited models. It can be seen that Cummings model is the only one which does not consider the linear terms as damping components. Bodén used the Cummings model, including the linear terms, and experimental data to obtain better correspondence with measured data.

Table 2.4: Comparison of Maa, Rice, Cummings and Bodén model's characteristics

Comparison	Rice	Cummings/Bodén	Maa
Solving Domain	Time	Time	Frequency
End correction	Constant	Variable	Do not consider
Grazing Flow	Include	Do not include	Do not include
C_D	On linear term	On linear and non-linear	Do not consider

2.7 Experimental techniques

There are several experimental techniques to measure the liner's impedance. Some comparisons have been made over recent years [49][16][98][63]. The most simple one uses a normal incidence plane wave in an impedance tube, which is a good approximation for linear liners under grazing flow. However, "for perforates, an impedance tube can extract the effective open area, but grazing flow facility is needed to derive the flow effect" [3] [70].

Typical aircraft engine liners have apertures and cavity widths smaller than the wavelength of interest, and the sound incidence has little effect on the liner impedance. Consequently,

[3] Private discussion with the author in 30/05/2018.

these liners are called locally reacting and may be evaluated in ducts with normal incidence. The TMM [42] using an impedance tube and the *in situ* method [64][24] were performed and will be covered in this section.

Grazing flow is impossible to realize in such normal incidence tubes, so eduction techniques were developed for grazing flow facilities. The *in situ* method may also be used under grazing flow. To extract the impedance an iterative process using experimental data is used on the eduction techniques to "guess" and adjust the impedance until the predicted acoustic field matches the measured acoustic field. In other words, the estimated impedance changes at each iteration in an algorithm which simulates the acoustic field until it minimizes the difference and matches the measured pressure field in each microphone of the test rig. The impedance eduction techniques TPM [83], MMM [27] and SFM[43] are discussed in this section. The eduction techniques were implemented in the UFSC test rig, and the results will be discussed in section 3.2. Other eduction and numerical techniques can be found in the literature but they will not be discussed in this document [97][100][99][75].

2.7.1 Normal incidence impedance tube

The impedance tube is a standardized experimental assembly used to characterize the impedance using normal incidence sound excitation. ISO-10534 [42] is the international standard that explains how the impedance tube works and how the TMM is used to calculate the normal impedance. The sample is positioned at the end of a tube of circular cross-section, as shown on Figure 2.5. Its diameter defines the maximum frequency, while the spacing between the flush mounted wall microphones determines the accuracy as a function of frequency. Small diameter tubes operate to higher frequencies than larger diameter tubes, because plane waves are assumed and the cross mode cut-on frequency determines the maximum frequency of operation.

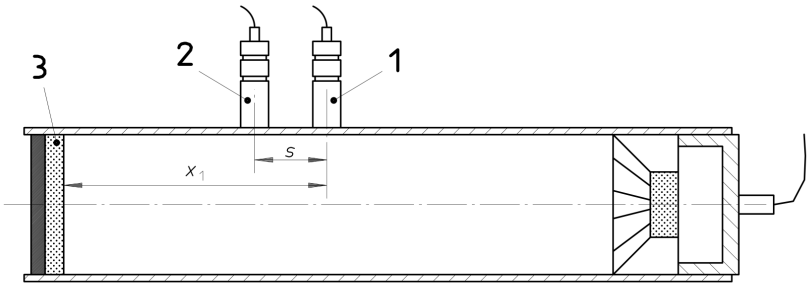

Figure 2.5: Impedance Tube. Extracted from: ISO-10534 [42].

It is possible to obtaining the transfer function

$$H_{12} = \frac{P_2(\omega)}{P_1(\omega)}, \tag{2.69}$$

where $P_1(\omega)$ and $P_2(\omega)$ are the frequency domain complex pressures at position 1 and position 2 respectively. The reflection factor on the liner surface position is given by [42]

$$\Gamma = |\Gamma| e^{i\theta_r} = \frac{H_{12} - e^{-ik_0 s}}{e^{-ik_0 s} - H_{12}} e^{2ik_0 x_1}, \tag{2.70}$$

where x_1 is the distance from the closest microphone to the liner surface $x = 0$, s is the distance between microphones ($s = x_1 - x_2$) and k_0 is the wave number. The transfer function H_{12} can also be substituted by a corrected transfer function H_c that is obtained by interchanging the microphone position in the impedance tube experimental setup, in order to correct the experimental mismatch of phase between microphones.

The impedance at the liner surface is calculated based on the reflection coefficient [42]

$$z_L = \frac{1 + \Gamma}{1 - \Gamma}. \tag{2.71}$$

The Bruel & Kjaer portable impedance meter system, type 9737, built according to ISO-10534 was used for no flow experiments reported in the Chapter 3. The data-sheet can be found in Annex A. The system with all accessories is illustrated on the Figure 2.6.

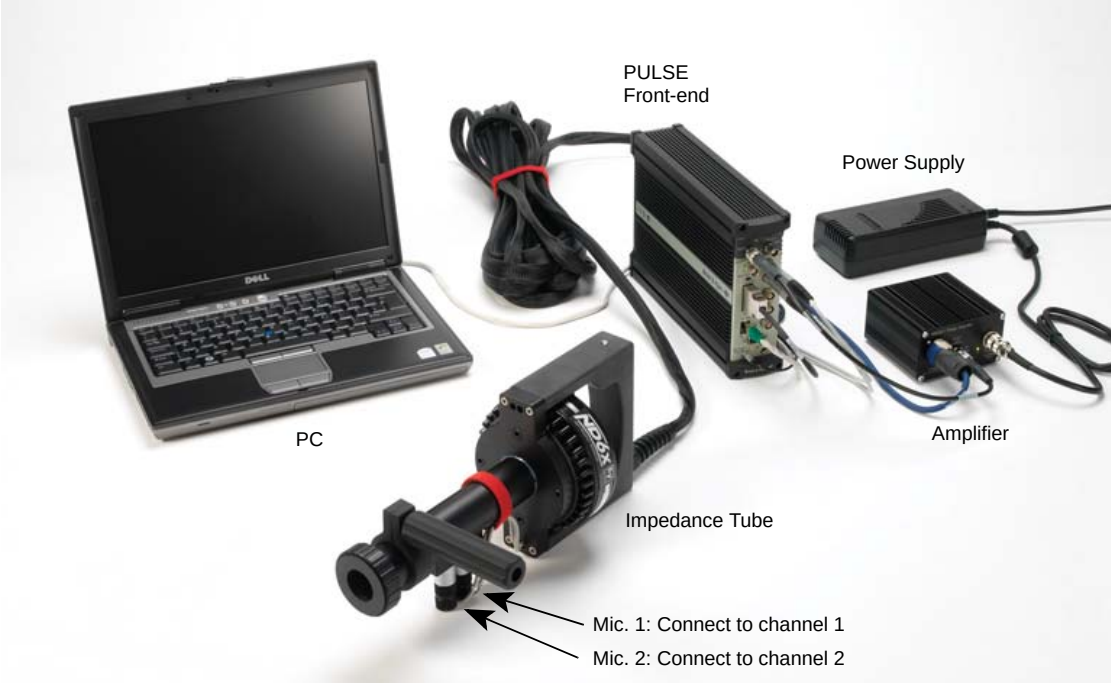

Figure 2.6: Portable Impedance Meter System, type 9737. Extracted from: Bruel & Kjaer [14]

2.7.2 *In situ* Method

The so called Dean's method [24], considers the case where two microphones are instrumented in a single liner cell, one at the face sheet and other at the back sheet for a single layer liner. A further microphone is added in the septum for a 2DOF design. The walls of the honeycomb cell are assumed to be rigid and impervious to sound. The cell width is small enough to assume only plane wave propagation within the honeycomb cell. The acoustic pressure inside the cavity causes standing waves, and is given by

$$P = |P_b| e^{i\omega t} \cos(ky), \tag{2.72}$$

where $|P_b|$ is the magnitude of the pressure measured at the back sheet of the liner's cavity, and y is the cavity depth position. So, by measuring the pressure at the face sheet, where $y = h$, and the pressure on the back sheet, where $y = 0$, the normalized impedance can be calculated using the expression [24][64][84]

$$\zeta = \frac{-i|P_f|}{\sin(kh)\,|P_b|} e^{i\gamma_{fp}} \tag{2.73}$$

where $|P_f|$ is the magnitude of the face sheet pressure wave and γ_{fp} is the relative phase between both, back and face sheet, pressure waves. The $sin(kh)$ refers to the quarter wave length difference caused by the microphone positions. If we apply a DFT (Discrete Fourier Transform) on two time domain pressure signals, $p_f(t)$ and $p_b(t)$, it is possible to calculate the impedance of each ω frequency component individually. Schuster [84] discussed different ways of using this equation, and referenced some authors that used FRFs (Frequency Response Functions) between microphones to obtain impedance results. If Ensemble-Averages are used to calculate the impedance there are four options, each one considering different references for the noise which degrades the FRF. Instantaneous impedance values can be computed using the DFT of both signals, but the particular combination of bandwidth, window and averaging method (overlapping) can compute different auto-spectra and cross-spectra values used to calculate the FRF. The expression that was considered the most consistent by Schuster is giving by,

$$\zeta = \frac{-i}{\sin(kh)} \frac{\langle P_b^* P_f \rangle}{\langle P_b^* P_b \rangle}, \tag{2.74}$$

where $\langle P_b^* P_f \rangle$ denote the ensemble-averaged frequency domain signal of the complex conjugated pressure on the back sheet P_b* times the pressure on the face sheet P_f. This is also the method employed by NLR to perform the same type of measurements [76]. H_{bf} is the FRF of the back and face sheet pressures, calculated by the expression,

$$H_{bf} = \frac{S_{bf}}{S_{bb}} = \frac{\langle P_b^* P_f \rangle}{\langle P_b^* P_b \rangle}, \tag{2.75}$$

where S_{bf} is the cross-spectra of the back sheet and the face sheet signals, and S_{bb} is the auto-spectra of the back sheet signal. This expression was recommended when there is noise at the face sheet signal [84]. It is therefore possible to calculate the normalized impedance, using the expression

$$\zeta = \frac{-i}{\sin(kh)} H_{fb}. \tag{2.76}$$

2.7.3 TPM (Two Port Matrix)

The TPM considers the liner as an unknown box, **T**, with two parameters on each side, pressure and particle velocity in the axial direction (z axis), as the Figure 2.7 illustrates. The incoming and outgoing wave in the tube are measured by microphones on the sections 1 and 2, away from the liner sample. The liner section T, can be a rectangular duct, where one wall of the cross section is acoustically treated with the liner material, and the other three walls are rigid.

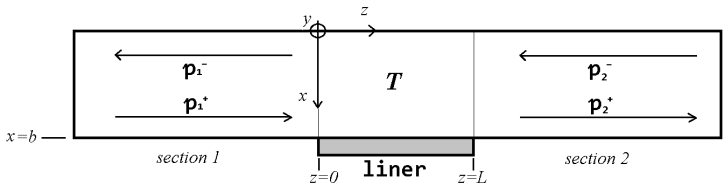

Figure 2.7: Two Port Matrix. Adapted from: Santana, 2011 [83].

Plane waves must be assumed in the duct cross section in order to perform this technique. If the pressure and particle velocity are determined outside of the box, the transfer matrix inside the box can be determined. On the inlet side, the pressure is p_1 and the velocity v_1. On the outlet side, the pressure is p_2 and the velocity is v_2, so the system of equations with matrix T in brackets is given by

$$[T] = \begin{bmatrix} \frac{Z^+ e^{-ik_z^+ L} + Z^- e^{ik_z^- L}}{Z^+ + Z^-} & \frac{Z^+ Z^- \left(e^{-ik_z^+ L} - e^{ik_z^- L}\right)}{Z^+ + Z^-} \\ \frac{e^{-ik_z^+ L} - e^{ik_z^- L}}{Z^+ + Z^-} & \frac{Z^- e^{-ik_z^+ L} + Z^+ e^{ik_z^- L}}{Z^+ + Z^-} \end{bmatrix} \tag{2.77}$$

where Z^+ is the liner impedance calculated from the inlet side and is equal to Z^-, which is the liner impedance calculated from the outlet side.

$$\begin{Bmatrix} p_2 \\ v_2 \end{Bmatrix} = [T] \begin{Bmatrix} p_1 \\ v_1 \end{Bmatrix}, \tag{2.78}$$

Equation 2.78 is a system of two equations and two variables. The matrix T contains k_z^+ and k_z^-, which are the wave numbers of the waves travelling downstream and upstream respectively in the axial direction z. The liner impedance, represented as the unknown

box, is a function of these wave numbers. It can be determined if the system of equations expressed in Equation 2.78 is solved. The pressure field is composed of an incoming wave and an outgoing wave in each side of the unknown region, given by

$$p_1 = p_1^+ + p_1^- \tag{2.79}$$

$$p_2 = p_2^+ + p_2^-, \tag{2.80}$$

where p_1 is the pressure on the section upstream the liner (left hand side of the Figure 2.7), and p_2 is the pressure on the section downstream the liner (right hand side of the Figure 2.7). The wave numbers of both incoming and outgoing waves are iteratively adjusted using an optimization algorithm, and consequently the impedance values Z^- and Z^+ are calculated. The optimization procedure runs until the guessed wave numbers match the measured two-port experimental data.

The solution for the pressure field split into the incoming and outgoing waves can be determined by considering the position (x,y) in the rectangular cross section of a duct. The solution for the acoustic pressure is,

$$p^+(x,y,z,t) = C_z^+ e^{-jk_z^+ z}\left(e^{-jk_x^+ x} + C_x^+ e^{jk_x^+ x}\right)\left(e^{-jk_y^+ y} + C_y^+ e^{jk_y^+ y}\right)e^{j\omega t}, \tag{2.81}$$

$$p^-(x,y,z,t) = C_z^- e^{jk_z^- z}\left(e^{-jk_x^- x} + C_x^- e^{jk_x^- x}\right)\left(e^{-jk_y^- y} + C_y^- e^{jk_y^- y}\right)e^{j\omega t}. \tag{2.82}$$

A hardwall boundary condition $\partial p/\partial y = 0$ is used at $y = h$ and $y = 0$ for the entire duct, setting y as the height of the cross section. The wave numbers in the y direction of the n acoustic modes are defined as $k_{y,n}^+ = k_{y,n}^- = n\pi/h$. The solution of the pressure can be represented mathematically as an infinite sum of cosines. Imposing the same hard wall boundary condition at $x = 0$, it is possible to find the constants $C_x^+ = C_x^- = 1$, using Equation 2.82. Appling the resulting equation to the conservation of momentum equation, it is possible to obtain the particle velocity expressions in the x direction, as shown in Equation 2.83 and Equation 2.84 [23], given by

$$v_x^+ = \frac{C_z^+}{Z_0}\frac{k_x^+}{k_0}\frac{1}{\left(1 - M_1\frac{k_z^+}{k_0}\right)}\left(e^{-ik_x^+ x} - e^{ik_x^+ x}\right)\sum_{n=0}^{\infty}\cos\frac{n\pi y}{h}e^{-ik_z^+ z}e^{i\omega t}, \tag{2.83}$$

$$v_x^- = \frac{C_z^-}{Z_0}\frac{k_x^-}{k_0}\frac{1}{\left(1 - M_1\frac{k_z^-}{k_0}\right)}\left(e^{-ik_x^- x} - e^{ik_x^- x}\right)\sum_{n=0}^{\infty}\cos\frac{n\pi y}{h}e^{-ik_z^- z}e^{i\omega t}. \tag{2.84}$$

The dispersion relation then becomes

$$k_x^{\pm} = \sqrt{(k_0 \pm M_1 k_z^{\pm})^2 - k_z^{\pm 2}}. \tag{2.85}$$

The particle displacement, η, in the fluid and on the lined wall are identical (no slip condition as given by Munjal [67]). The particle velocity in the x direction and the impedance are related to the particle displacement by

$$\frac{p}{Z} = \frac{\partial \eta}{\partial t} \tag{2.86}$$

$$v_x = \frac{D\eta}{Dt}. \tag{2.87}$$

The Myers condition is obtained when Equation 2.86 and Equation 2.87 are combined eliminating particle displacement [72], giving the impedance on the lined section from $z = 0$ to $z = L$

$$\frac{Dp(b, y, z, t)/Dt}{-\partial v_x(b, y, z, t)/\partial t} = Z. \tag{2.88}$$

where b is the position of the liner as shown in the Figure 2.7. Finally, evaluating Equation 2.88 by differentiating Equation 2.84 and Equation 2.82 for the wave in one direction, and differentiating Equation 2.83 and Equation 2.81 for the wave in the other direction, it is possible to obtain two expressions for the impedance. They must be consistent [83] and are given by,

$$\begin{aligned} Z^+ &= iZ_0 \frac{k_0}{k_x^+} \left(1 - M\frac{k_z^+}{k_0}\right)^2 \cot(k_x^+ b), \\ Z^- &= iZ_0 \frac{k_0}{k_x^-} \left(1 + M\frac{k_z^-}{k_0}\right)^2 \cot(k_x^- b), \\ Z &= Z^- = Z^+. \end{aligned} \tag{2.89}$$

Concluding, the liner's impedance can be calculated using Equation 2.89. To solve this equation the wave numbers in the z (axial) direction are needed in order to calculate the wave numbers in the x direction. At least two independent measurements are necessary in order to obtain the wave numbers in the z direction. There are three different techniques to do this: with two sources, two loads, or using a combination of both techniques. Two sources technique places the acoustic sources in two different positions, usually upstream and downstream the liner sample. Alternatively, the two load technique uses two different boundary conditions at the duct termination [83].

These two sets of pressure data, using the two source technique for instance, can be split into the incoming and outgoing pressure waves by applying the pseudo-inverse operation on the Moore-Penrose matrix [61, p. 114]. Thus, the measured pressure waves can be compared with those calculated using a “guessed" impedance input into Equation 2.78.

The code can be optimized to search for the impedance value that minimizes the error of this comparison, to finally educe the liner impedance.

There are some issues regarding the impedance transition which occurs at the beginning, $z = 0$, and at the end, $z = L$, of the liner section. To solve this issue a transition matrix is used on both sides of the matrix T. The solution of these matrices begins by supposing that they are the identity matrix. Also, the transition matrices T_+ and T_- are assumed to be the same. Six transducers are required in order to solve these transition matrices [60][61, p. 51], but further details can be obtained in the literature.

2.7.4 MMM (Mode Matching Method)

The MMM uses a single transfer matrix with two sections and the liner in the middle. The matrix is fed with the pressure and the particle velocity in each section. The method is mathematically complex to implement. However, it uses just four microphones and provides flexibility because it represents the pressure field with all of the propagating modes included. Its assumptions include no vorticity in the flow, so that the potential velocity equation can be used. The potential velocity is divided into two components, x and y, which are both perpendicular to the rig duct axis and define the cartesian position of the cross section. The problem is solved in two dimensions describing the pressure field in the lined region as

$$p_2 = \sum_{q=1}^{Q} A_+^{(q)} \cdot \Psi_{2i}^{(q)}(x,y) \cdot e^{-jk_{z2i}^{(q)} z} + \sum_{q=1}^{Q} A_-^{(q)} \cdot \Psi_{2r}^{(q)}(x,y) \cdot e^{-jk_{z2r}^{(q)}(z-L)}, \tag{2.90}$$

where q is the acoustic mode index; Q is the number of modes considered; A is the amplitude of pressure for each mode and direction; the incoming wave is represented by A_+ and the reflected (outgoing) wave is represented by A_-. $\Psi(x,y)$ represents the modal shape, z is the position of the pressure measurement and L is the length of the lined section. [25]

The solution is calculated in each of the three regions: upstream, downstream and within the lined region. With these solutions, the coefficients of the transfer matrix can be calculated by matching the values for each mode.

Figure 2.8 illustrates a longitudinal section of a rectangular duct with the liner in one of the walls in the central section. Ψ_{1i} represents the summation of modal shapes of the incident wave in the z direction of the upstream section. On the other hand, Ψ_{1r} represents the summation of modal shapes of the reflected wave going in the opposite direction. This nomenclature pattern is extended to the other sections 2 (with the liner in one wall) and 3 (rigid walls), having z as the axis direction with or without flow, x the liner surface normal direction and y the transverse direction, out of the paper, perpendicular to the others. The boundary conditions are the continuity of pressure and

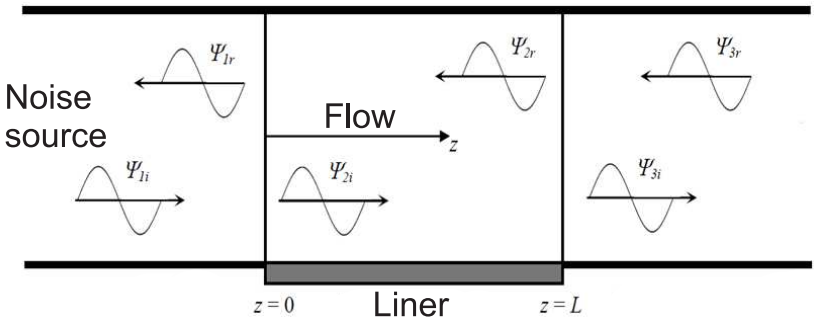

Figure 2.8: Decomposition of the acoustic field. Adapted from: Elnady, 2004[27].

particle velocity on all of the section interfaces and a hard wall for areas other than the liner wall. In order to match the acoustic field at the intersect of the sections we need to have,

$$p_1 = (x, y, 0) = p_2(x, y, 0), \tag{2.91}$$

$$p_2 = (x, y, L) = p_3(x, y, L), \tag{2.92}$$

$$\sum_{q=1}^{Q} \frac{\partial p_1^{(q)}/\partial z}{(k \mp M k_{z1}^{(q)})}|_{z=0} = \sum_{q=1}^{Q} \frac{\partial p_2^{(q)}/\partial z}{(k \mp M k_{z2}^{(q)})}|_{z=0}, \tag{2.93}$$

$$\sum_{q=1}^{Q} \frac{\partial p_2^{(q)}/\partial z}{(k \mp M k_{z2}^{(q)})}|_{z=L} = \sum_{q=1}^{Q} \frac{\partial p_3^{(q)}/\partial z}{(k \mp M k_{z3}^{(q)})}|_{z=L}. \tag{2.94}$$

Applying the boundary conditions in the Linearised Euler Equations (LEE), it is possible to obtain a system of equations with $4Q$ unknowns. These are the amplitudes of the pressure waves for each mode under consideration. It is necessary to calculate the reflection coefficient in one of the hard wall sections and find the plane wave amplitudes at the interface of the liner in that section. The same thing is done in the other hardwall section, thereby providing the incoming and outgoing pressure on each side of the liner using the TMM [28].

The MMM gives an initial estimation of the liner impedance using the pressure measurements and the calculated pressure field. The calculated pressures are compared with the measurements and the impedance is iterated until an error criteria is reached. Elnady created the method and used the function “fminsearch" of Matlab to do the iteration process [27]. Later on, Elnady proved that shear flow effects may be neglected and a uniform grazing flow profile with mean Mach number across the cross section can be used, considering just low order modes present in the duct [28].

The TPM, and the MMM were validated against a numerical model using the FEM commercial code, Actran, and evaluated in references [62][61][86][98]. TPM is more expensive computationally for Mach numbers lower than 0.2. MMM presents instabilities

in the optimization algorithm and does not give stable results for impedance at high frequencies. On the other hand, MMM represents the pressure field analytically, and it is fast computationally. It is noted that this method cannot be applied to ducts with complex geometries.

2.7.5 SFM (Straightforward Method)

The TPM and the MMM rely on pressure measurements in the hard-wall sections of the test rig duct. The MMM uses them to calculate the incident pressure and the reflection coefficient, and the TPM to calculate the pressure and the velocity at the liner's leading and trailing edges. The Straight-Forward Method (SFM) uses pressure measurements along the lined section on the opposite hard wall. If N equally-spaced microphones are positioned on the wall opposite the liner sample, the pressure at the $n-th$ microphone may be written as a sum of exponentials, where

$$p(z_n) = \sum_{q=1}^{k} A^q e^{\mu^q z_n} \tag{2.95}$$

where $k = 2Q$, Q is the number of modes considered in the solution, and A^q is the product of the wave amplitude times its mode-shape at the measured duct height, $\mu^q = -jk_z^q$ are the complex wave numbers for downstream (q odd), and $\mu^q = jk_z^q$ for upstream (q even) travelling waves, and z_n is the axial position of the $n-th$ microphone [61]. If $z_n = n - 1 = 0,\ 1,\ 2,\ ...,N$ - 1, the exponentials in Equation 2.95 can be written as $e^{\mu^q n} = \left(e^{\mu^q}\right)^n = (\alpha^q)^n$. Jing [43] observed that each of these exponentials satisfy a fixed, $k-th$ order linear differential equation

$$y(n+k) + C_{k-1}y(n+k-1) + C_{k-2}y(n+k-2) + ... + C_0 y(n) = 0. \tag{2.96}$$

The characteristic equation is

$$\alpha^k + C_{k-1}\alpha^{k-1} + C_{k-2}\alpha^{k-2} + ... + C_0 = 0, \tag{2.97}$$

with roots α^q. If any individual term satisfies the linear, homogeneous equation, then linear combinations of them also satisfy it. In particular, the pressure function, Equation 2.95, satisfies it, so,

$$p(n+k) + C_{k-1}p(n+k-1) + C_{k-2}p(n+k-2) + ... + C_0 p(n) = 0, \tag{2.98}$$

for $n = 1, 2, ..., N-k$. Since $p_{(z_n)}$ is known from measurements at n points corresponding to the microphones, Equation 2.98 can be used to construct a system of k equations from which the coefficients $C_i\ (i = 0, 1, ..., k-1)$ can be found. Knowing the C_i, we can substitute them into the Equation 2.97, to find the roots $\alpha^{(q)}$, which in turn give the exponents μ^q and thus the wavenumbers k_z^q. It is necessary to have at least $2k$ measurement

points (microphone positions), i.e., $n \geq 2k$, for a determined or overdetermined system of equations. Using the obtained axial wave numbers, the same procedure outlined in the TPM is followed: calculate k_x and then the impedance from Equation 2.89. To avoid aliasing, the distance between microphones should be chosen in order to have at least 2 points per wavelength at the highest frequency of interest. The hard-soft wall transition effects might be important in Prony's method [43], so a limited length of the liner sample may contaminate the measurements using a small array of microphones. Good practice when designing the microphone array is to leave at least a few wavelengths of distance from the transitions to the closest microphones in order to avoid this problem [61].

2.8 Fundamental equations of compressible flow

Near field effects on perforated panels due to high SPLs are not fully understood. Fluid motion due to hydrodynamic instabilities caused by large particle displacements near perforates should be described correctly. Viscous effects near the perforates are also important, due to low Reynolds numbers. This section will introduce the fundamental flow equations in order to explain the main assumptions used in the numerical 2D models implemented. The equations and hypothesis are common knowledge on this field.

Each hole on a perforated plate can be studied alone, if a reasonable distance between holes is considered [38]. So, each hole can be represented as a short flanged tube containing a finite quantity of air subjected to an oscillatory motion caused by the sound pressure field. If the mass of air is subjected to a small displacement during the motion, the end correction will be minimal, due to the flanged termination. On the other hand, large fluid displacement and flange interaction can cause vortex shedding and nonlinearities in the liner response [34]. This can be observed when the resonator is subjected to high SPLs. The phenomena is intensified at the resonant frequency of the resonator, increasing the velocity magnitude at the orifice. The fundamental equations of mass, momentum and energy apply in a control volume. The unknowns of this equations are the velocity, thermodynamic pressure and absolute temperature that defines the sound speed.

2.8.1 Conservation of mass

For an Eulerian description, the rate of change in mass is equivalent to the variation in density and volume of a particle, as described by White [101]. Conservation of mass gives,

$$\frac{D\rho}{Dt} + \rho \nabla \cdot \mathbf{u} = 0, \tag{2.99}$$

where the material total derivative $\frac{D}{Dt}$ denotes $\frac{\partial()}{\partial t} + u \cdot \nabla()$. For low Mach numbers, usually the fluid is considered incompressible, meaning that $\frac{D\rho}{Dt} = 0$, so $\nabla \cdot \mathbf{u} = 0$ too.

However, the flow velocity on the liner facing sheet holes can be high, around 0.1 to 0.3 Mach, depending on the OASPL at the liner surface. Consequently, to obtain better precision on the model, a compressible flow condition should be considered.

2.8.2 Navier-Stokes Equations

Newton's second law expresses the proportionality between applied forces and the resulting acceleration of a particle of mass m, where $\mathbf{F} = ma$. In a fluid in motion, as described by COMSOL [19], this gives

$$\rho\frac{D\mathbf{u}}{Dt} = \mathbf{f} = \mathbf{f}_{body} + \mathbf{f}_{surface}, \tag{2.100}$$

where $\mathbf{f}$ is the force applied per volume a given set of fluid particles. The following equations of the section up to Equation 2.107 are defined by White [101]. The forces can be normal or create shear stresses on the fluid element due to the pressure field and viscosity, giving,

$$\rho\frac{D\mathbf{u}}{Dt} = \rho\mathbf{g} + \nabla\cdot\tau_{ij}, \tag{2.101}$$

where g is the acceleration due to gravity, and the tensor τ_{ij} is expressed in terms of the velocity $\mathbf{u}$ by assuming viscous shear proportional to the deformation rate. This is satisfied by all cases and most common fluids, the tensor τ_{ij} can be expressed as

$$\tau_{ij} = -p\delta_{ij} + \mu\left(\frac{\partial u_i}{\partial x_j} + \frac{\partial u_j}{\partial x_i}\right) + \delta_{ij}\lambda\nabla\mathbf{u}, \tag{2.102}$$

where μ is the dynamic coefficient of viscosity and λ is the coefficient of bulk viscosity. Combining the Equation 2.101 with the Equation 2.102 gives Navier-Stokes equation

$$\rho\frac{D\mathbf{u}}{Dt} = \rho\mathbf{g} - \nabla p + \frac{\partial}{\partial x_j}\left[\mu\left(\frac{\partial u_i}{\partial x_j} + \frac{\partial u_j}{\partial x_i}\right) + \delta_{ij}\lambda\nabla\mathbf{u}\right]. \tag{2.103}$$

The gravitational effect is negligible for acoustic problems and Equation 2.103 becomes

$$\rho\frac{D\mathbf{u}}{Dt} = -\nabla p - \rho\mathbf{u}\cdot\nabla\mathbf{u} + (\lambda + 2\mu)\nabla(\nabla\cdot\mathbf{u}), \tag{2.104}$$

where $\lambda = -\frac{2}{3}\mu$ for perfect gases, and μ is the dynamic viscosity. So, it is also possible to write the equation as

$$\rho\frac{D\mathbf{u}}{Dt} = -\nabla p - \rho\mathbf{u}\cdot\nabla\mathbf{u} + (\frac{4}{3}\mu)\nabla(\nabla\cdot\mathbf{u}), \tag{2.105}$$

The non-dimensional parameter used to identify the transition between a laminar and turbulent regime in an orifice of diameter d can be defined by the Reynolds number given

by

$$Re = \frac{\rho u d}{\mu}, \tag{2.106}$$

where the characteristic length is d, the diameter of the hole, and u a characteristic velocity magnitude. If the Reynolds number is low, considering a Poiseulle Flow in a duct, it means that the fluid is laminar. In this condition, computational fluid dynamics (CFD) can be applied to solve the Navier Stokes equation with some accuracy for a variety of flows and geometries [101]. At high Reynolds numbers, empirical relations are needed to define the turbulent stresses. However, the range of velocities in the liner model is not sufficient to warrant a turbulent model. So the compressible flow Navier Stokes Equations can be written as

$$\rho \frac{D\mathbf{u}}{Dt} = -\nabla p + \mu \nabla^2 \mathbf{u}. \tag{2.107}$$

2.8.3 Thermodynamic equation of state

By considering acoustic waves as an isentropic mechanism, no heat transfer and viscosity can be neglected, so it is possible to affirm that the acoustic pressure is only dependent on the density. The following equations of section 2.8.3 and 2.8.4 are defined by Blackstock [5]. For ideal gases,

$$p = R\rho T, \tag{2.108}$$

and the internal energy is only dependent on the temperature, $\varepsilon = \varepsilon(T)$, so that

$$d\varepsilon = C_v dT, \tag{2.109}$$

where $R = (\gamma - 1)C_v$ is the universal constant for air, and $\gamma = C_p/C_v$ is a constant ratio. Finally, it is possible to solve the energy equation and obtain

$$\frac{p}{p_0} = (\frac{\rho}{\rho_0})^{\gamma}. \tag{2.110}$$

An infinitesimal variation in pressure corresponds to an infinitesimal linear variation in density. Consequently, it is possible to write the following equation for a local sound speed c,

$$c^2 = \frac{\partial p}{\partial \rho}. \tag{2.111}$$

Observe that the ratio of the acoustic pressure and the acoustic variation of density is proportional to c^2, so the sound speed can also be written using the Equation 2.108, as

$$c = \sqrt{\gamma RT}, \tag{2.112}$$

and finally it is possible to say that for small amplitudes of pressure

$$\frac{\partial \rho}{\partial t} = \frac{1}{c^2}\frac{\partial p}{\partial t}. \tag{2.113}$$

Observe that for high SPLs, γ varies, so the ratio of pressure and density is not constant anymore. This means that there is a local change in temperature and viscous dissipation, varying the sound speed locally and causing distortions in the propagating wave. Concluding, if the particle velocity is comparable to the sound speed (high SPLs), it is not reasonable to assume an incompressible mechanism.

2.8.4 Acoustic Wave Equation

By substituting Equation 2.113 into Equation 2.99 it is possible to obtain the wave equation

$$\frac{\partial p}{\partial t} + c^2 \rho \nabla \mathbf{u} = 0, \tag{2.114}$$

and considering that the acoustic variations of pressure are small and around the equilibrium value of the atmospheric pressure, so that p represents the acoustic pressure. Also, the Navier Stokes equation from Equation 2.107 can be linearized considering that the viscosity terms are small for acoustic waves, so it can be expressed by

$$\rho \frac{\partial \mathbf{u}}{\partial t} + \nabla p = 0. \tag{2.115}$$

It is possible to derivate the Equation 2.114 in respect of time and apply the ∇ operator on the Equation 2.115 obtaining the system of equations

$$\frac{\partial p}{\partial t} + \rho c^2 \frac{\partial}{\partial t}(\nabla \cdot \mathbf{u}) = 0 \tag{2.116}$$

$$\rho \frac{\partial}{\partial t}(\nabla \mathbf{u}) + \nabla^2 p = 0. \tag{2.117}$$

The last step is to multiply Equation 2.117 by c^2 and subtract Equation 2.116 from Equation 2.117, in order to obtain the first order wave equation, given by

$$\nabla^2 p - \frac{1}{c^2}\frac{\partial^2 p}{\partial t^2} = 0. \tag{2.118}$$

The wave equation can be used in linear acoustic problems without flow. It is used in the multiphysics model in Chapter 5 in order to describe the sound propagation away from the liner surface, where the pressure is fairly constant over the simulated tube cross-section. This tube is used as a plane wave guide between the inlet and the liner surface.

2.8.5 2D Impedance Simulations

The majority of the 2D or 3D impedance models use Direct Numerical Simulation (DNS) models that solve the full Navier Stokes equations. The meshes used in such problems are extremely refined and the computational cost is high. Solutions for narrow channels or single cells can take days but they can provide valuable visualization insights about the microfluid dynamics of the problem. Tam explored a slit resonator using 2D DNS in order to predict the fluid dynamics and acoustic behaviour of a straight and beveled slit[92]. He observed the vortex shedding formation for different SPLs and frequencies, and found strong vortices had been generated at lower frequencies and higher SPLs. He compared the reflection coefficients and the impedance results against experimental data, and demonstrated that DNS can be used as a tool to predict liner impedance for pure tone and broadband excitations at a reasonable cost [93].

When the incident sound wave reaches a high pressure outside the resonator, fluid is forced into the cavity through the slit. The stream lines create a narrow flow area with high velocity that diverges abruptly after passing through the aperture. It causes vortex shedding at the two corners on the cavity size. The phenomena is symmetric for a straight edge liner hole. Depending on the excitation frequency and SPL, the vortex may be shed or not. It will also depend on the ratio of plate thickness to the aperture diameter. Large vortex shedding is followed by random shedding of smaller vortices. They either merge into large vortices or simply dissipate slowly by molecular viscosity[92]. Figure 2.9 shows two different slit liners with straight and bevelled shapes. The vortex formation at the beginning of a cycle is illustrated, where smaller vortices are formed on the bevelled liner. For the bevelled slit liner, most of the shedding occurs at the sharp edge and the behaviour is highly asymmetric.

The time-average dissipation rate must be addressed in order to understand the microfluid dynamics and the dissipation mechanism of resonant liners [96]. For a given point in a 2D domain the time-average dissipation rate, $\bar{D}$, is defined as,

$$\bar{D}(i,j) = \frac{1}{T}\int_0^T \sigma_{ij}\frac{\partial u_i}{\partial x_j}dt, \tag{2.119}$$

where T is the period of oscillation and σ_{ij} is the stress tensor. Observe that σ_{ij} for a 2D axisymmetric problem can be represented by the radial, r, and the axial, z, components

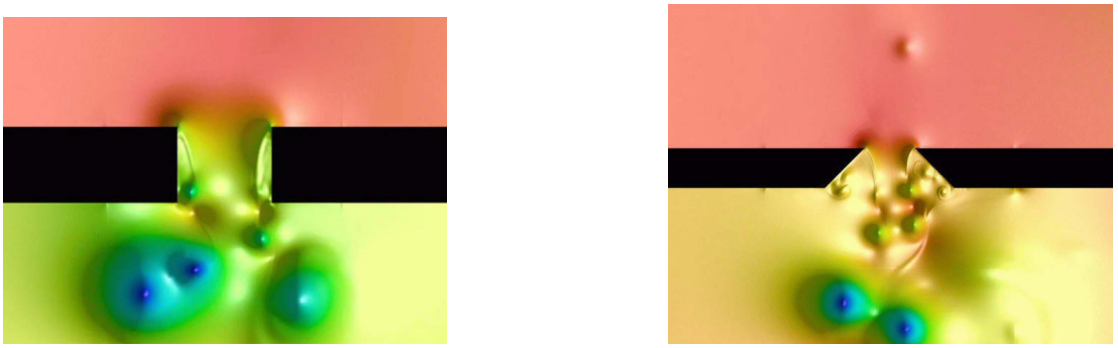

(a) Straight slit liner

(b) Bevelled slit liner

Figure 2.9: DNS results of pressure, showing the vortex shedding on a straight hole (a) and a beveled (b) slit liners at high SPLs. From: Tam, 2000 [96].

in a coordinate system. Since the velocity in the ϕ direction is zero, the stress can can be written in terms of the velocity gradients in the r and z directions, where

$$\sigma_{rz} = \mu(\frac{\partial u_r}{\partial z} + \frac{\partial u_z}{\partial r}). \tag{2.120}$$

It is also possible to infer from Equation 2.119 that most of the energy dissipation takes place adjacent to the walls of resonator aperture [96]. The shear gradient of the jetlike boundary layer flow at the walls is responsible for most of the energy dissipation, especially for frequency excitation away from the resonant frequency or at lower SPLs [96]. The total dissipation rate due to viscosity is obtained by integrating Equation 2.119 over resonator surface area, and it is more significant near the resonator aperture [96]. The total dissipation rate is given by

$$E_{viscous} = \int \int \bar{D}(r,z) dr dz, \tag{2.121}$$

and is summed over the shed vortices [96]. The ensemble averages of the kinetic energy of a single vortex per unit span can be used to calculate the acoustic energy transformed into vortices and later dissipated into heat per period, where

$$E_{shedding} = \frac{N}{T} < \pi \int_0^R \rho(r) V_\theta^2(r) r dr >, \tag{2.122}$$

considering R the radius of the vortex, V_θ the rotational velocity of the vortex and N the number of vortices created during the period T [96]. The total energy dissipation rate due to viscous and shedding mechanisms can be calculated summing Equation 2.121 and Equation 2.122, obtaining

$$E = E_{viscous} + E_{shedding}. \tag{2.123}$$

The energy flux of the incident acoustic waves at the resonator aperture can be defined as

$$E_{incident} = \frac{\bar{p^2} d}{\rho c}, \tag{2.124}$$

where the pressure amplitude squared is a time average, d is the aperture diameter, and it is normalized by the characteristic impedance ρc [96]. The ratio of the dissipated energy to the incident energy, $E/E_{incident}$, gives the energy fraction dissipated by the resonator.

The vortex shedding mechanism is an effective sound dissipation mechanism, as observed by Tam, and shown in Figure 2.10.

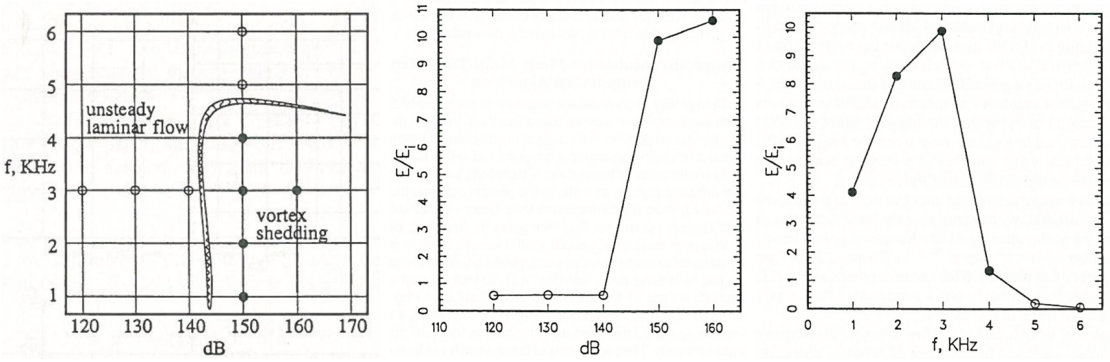

(a) Vortex shedding regions (b) Energy ratio with SPL (c) Energy ratio with frequency

Figure 2.10: Effect of vortex shedding into energy dissipation. From: Tam, 2000[96].

Tam varied the SPL and the excitation frequency of a liner tuned on 3kHz and observed the vortex shedding appearance, calculating the energy ratio presented above. Two distinctive areas were delimited showing that the energy dissipation due to the vortex shedding is significant and happens only for a limited bandwidth, and above 140 dB SPL for the modelled liner geometry, as observed in Figure 2.10.(a). Figure 2.10.(b) shows the threshold of vortex shedding at 3kHz due to SPL increase, and Figure 2.10.(c) shows the energy ratio for different excitation frequencies at 150 dB. So, it is possible to infer that vortex shedding occurs above a certain SPL and for frequencies lower or around the resonant frequency of the liner in question. This shows that it is difficult to obtain high frequency attenuation (without grazing flow) using this type of liner because the vortices are not shed as effectively as they are at lower frequencies. The simulated cases in Chapter 5 will explore the particularities of this behaviour.

Chapter 3

Experiments

This chapter includes a description of impedance tests on liner samples during the course of this research project. The main goal was to understand the differences between experimental methods used to calculate liner impedance and also to evaluate different geometries, manufacturing techniques, and signals affecting the liner impedance. The focus was to fully understand the pure tone excitation liner impedances and exploit the multiple tone excitation using different combinations of harmonically-related tones.

A comprehensive amount of data obtained by varying the relative amplitude of two harmonically-related tones will be presented by using different experimental techniques and samples to assess the precision and reliability of the results. Experimental data collected during this study showed that the impedance of a specific frequency component is highly dependent on the relative amplitude of pressure for the frequency analysed and that for the other frequency components present in the impinging sound field.

Table 3.1 provides the dimensions of the conventional flat SDOF punched aluminium liner sample and a flat wire mesh liner. The wiremesh liner is used to calibrate the portable impedance meter, as it shows linear response at high SPL. The punched aluminium liner sample was experimented in different conditions, with a flanged impedance tube, with a cylindrical sample extracted and inserted in a sample holder, and also in a grazing flow rig [85].

The first is a typical SDOF perforated liner composed of a punched aluminium facing sheet with a honeycomb core and an aluminium backing sheet. This sample was experimented in three different conditions, using a flanged impedance tube, using a sample holder in the impedance tube and at the duct wall of the grazing flow test rig. The second sample is a wire mesh liner composed of a support sheet with a large POA over 30%, which shows an almost linear response to high SPLs. The latter sample was used to calibrate the flanged normal impedance tube system, so the impedance results of this liner will not be discussed in details. A sample with 29 mm diameter was extracted from

Table 3.1: Nominal sample geometry.

Sample information	1 - Punched Aluminium SDOF liner	2- Wiremesh	Unity
Diameter of perforated sheet holes	0.991	-	mm
Thickness of face plate	0.635	-	mm
Length	210	210	mm
Width	182	158	mm
Face sheet Area	38220	33180	mm^2
POA	5.20%	-	%
Eff POA @ resonance ($C_D = 0.76$)	5.18%	-	%
Hexagonal wall dimension (cell size)	5.00	5.00	mm
Height of honeycomb	19.05	30.00	mm
Honeycomb volume	1.24E-06	1.95E-03	mm^3

the perforated liner in order to be measured in the impedance tube sample holder, while the large perforated sample also had one cell instrumented to allow in-situ measurements in the grazing flow facility.

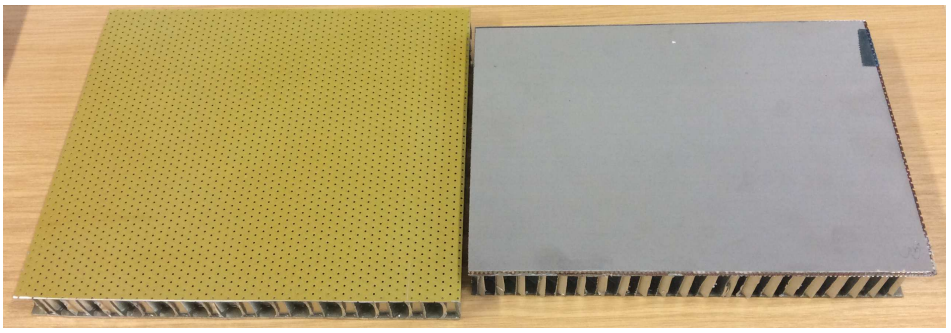

Figure 3.1: Perforated SDOF liner on the left, and wire mesh liner on the right.

The samples shown in Figure 3.2 were produced using two different 3D printing techniques. The S1M sample is made of stainless steel, manufactured by laser sintering 3D printing; the others are made of ABS (Acrylonitrile Butadiene Styrene), manufactured by photopolymerization 3D printing.

3.1 Portable impedance tube measurements

This section reports on the portable impedance tube measurement results. Two distinct measurements were performed; using a flanged tube and applying the Flanged Two Microphone Method (FTMM), or using a sample holder using either the TMM or the *in situ metho* as shown on the left and middle pictures in Figure 3.3. The sample holder was designed in order to contain the sound excitation inside the tube and also corrects the mismatch between the facing sheet and the backing sheet areas of the liner, causing the edge effect[68] illustrated on the right hand side of the Figure 3.3.

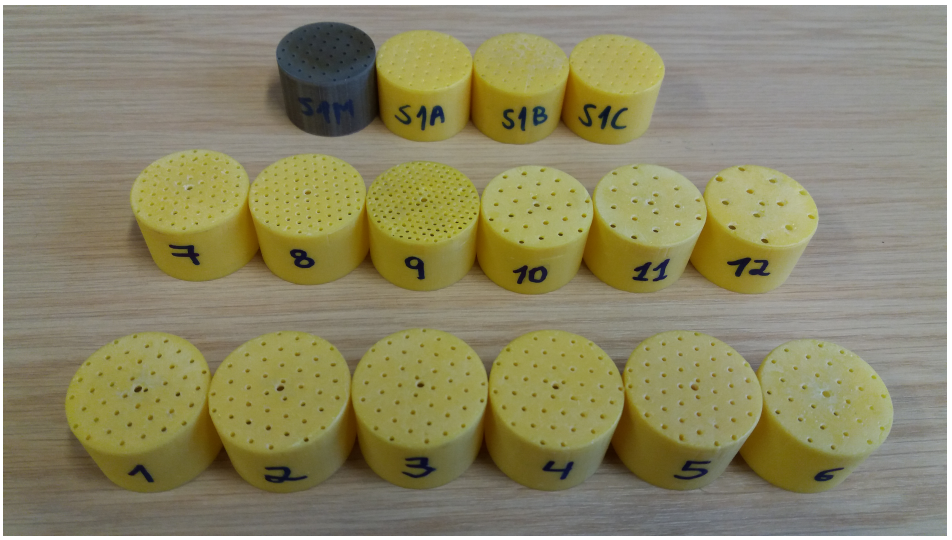

Figure 3.2: 3D printed samples.

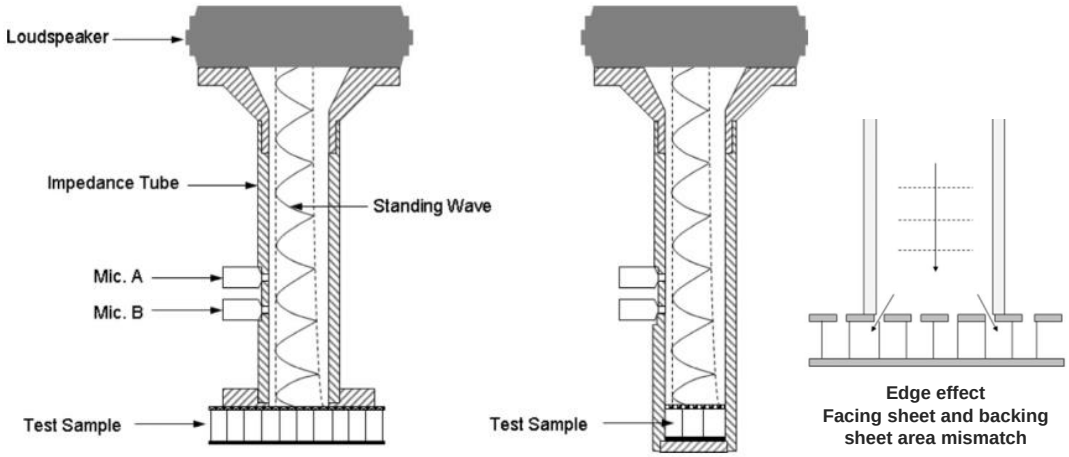

Figure 3.3: Portable impedance meter cross section. Left - flanged setup, Center - sample holder setup, Right - edge effect. Adapted from Ferrante, 2016 [32].

The *in situ* instrumentation assembly was developed to be used in the sample holder setup and is illustrated in Figure 3.4.

The goal was to acquire simultaneously the time domain signals from the capacitive microphones "Mic. A" and "Mic. B" using TMM, illustrated on the left hand side of Figure 3.3, and signals of the high intensity microphones at the liner surface and backing plate using Dean's Method. Kulite microphones named "Mic. 1" and "Mic. 2" were used to perform the *in situ* measurements on the 3D printed samples which were drilled in order to fit the microphones as shown on the exploded view of the assembly in Figure 3.4. Two microphone holders (also 3D printed) were used to fix the microphone in place in

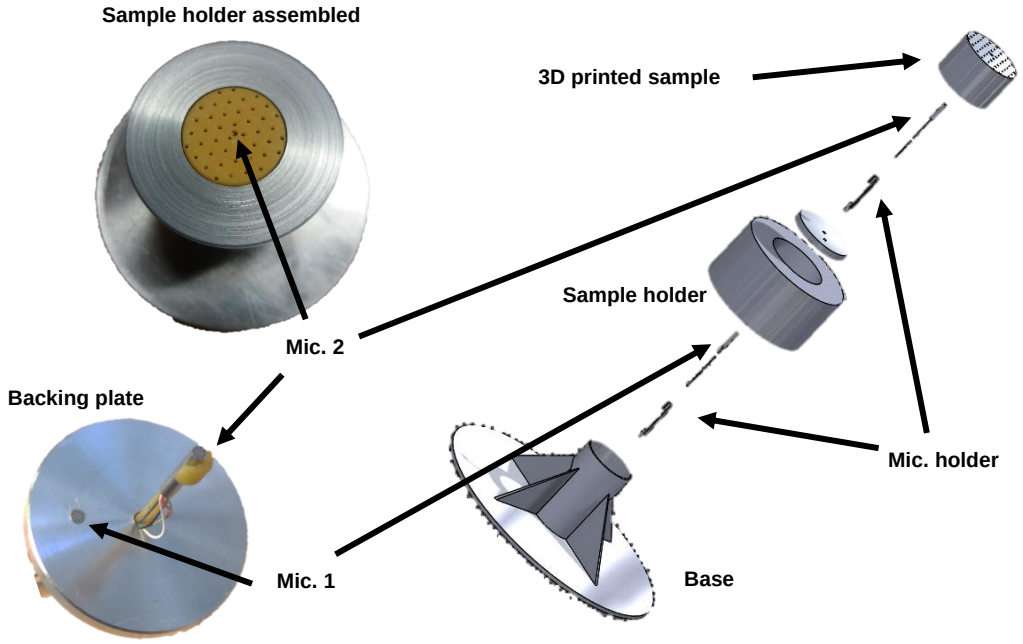

Figure 3.4: *In situ* assembly using the sample holder setup for portable impedance meter simultaneous measurements.

order to avoid any sound leakage. Also, a high performance silicon sealant was applied between the edges of the sample cavities and the backing sheet.

Table 3.2 contains the list of instrumentation used for the no flow experiments.

Table 3.2: Instrumentation used for no flow measurements

Type of Equipment	**Brand**	**Model**
Laptop	Sony	Vaio PCG-31311M
Acquisition system	Bruel & Kjær	3560-B-130
Power Amplifier	Bruel & Kjær	WB3541
Ambient Monitor	Testo	622
Microphone calibrator	Bruel & Kjær	4231
Impedance meter	Bruel & Kjær	WA-1599-W-005
Capacitive microphones (2)	Bruel & Kjær	4187
Preamplifiers (2)	Bruel & Kjær	2670-W-007
Measurement software	Bruel & Kjær	Pulse Labshop v.19.0.0.128
Microphone 1.6 mm diameter	Kulite	Mic-062
Kulite pre-amp	Customized	-
10V Power Supply	Hameg Instruments	HM8040-3

3.1.1 Test conditions and calibration procedures

A calibration of the system was performed before each set of measurements. Each capacitive microphone was calibrated using the acoustic calibrator once in the beginning of the campaign. A signal to noise ratio was checked and a transfer function calibration was also performed once and stored in a template. The wire mesh sample was measured during this calibration procedure as its impedance is well known. Pure tone and white noise measurements were performed on the wiremesh sample that is used to check the calibration. After the measurements on the desired sample, another measurement on the wiremesh sample confirm that the system was correctly calibrated during the entire experiment. The acoustic center calibration used a rigid metal sample, to ensure the correct distance between the sample surface and microphone acoustic center used in the calculation of the impedance. The TMM calculates the impedance based on the reflection coefficient measured.

In terms of signal processing, broadband signals were measured using 800 lines and 8 Hz resolution (0 to 6400 Hz) in the frequency domain while the pure tone measurements used 6400 lines and 1 Hz resolution. During the measurement 4 time averages were taken for pure tone cases. This is sufficient when using the impedance meter as the signals are very deterministic. However, 40 averages were used for broadband signals such as white noise, square, sawtooth and pink noise. The Hanning window was applied to perform the Fast Fourier Transform (FFT) on the acquired signal.

The environmental data of absolute pressure, relative humidity and temperature were monitored continuously and reported in the signal acquisition software. The environmental data allow the calculation of the characteristic impedance, which was used to extract the normalized impedances calculated. The environmental conditions did not vary much during the experimental campaigns remaining around 25 $\pm$ 3°C, and 1015 $\pm$ 1 hPa. The temperature and ambient pressure were used to calculate the normalized impedance for each set of measurements.

3.1.2 Punched Aluminium SDOF liner results

As the liner shows different number of apertures per cell, the liner impedance is an average value that varies locally. Five different positions were measured on the punched aluminium SDOF sample placing the flanged tube on the top of different cells. Broadband, multiple tone and pure tone signals were used to excite the sample and obtain the impedance at different liner cells. Data from five measurement locations show deviations, which suggests that the flange position adds variability due to the number of cells excited and partial blockage of some holes, which change the effective porosity ($POAeff$) of the sample.

The pressures in each microphone of the impedance tube allow the calculation of the spatial average pressure at the liner surface, p_0. Consider the microphone "A" at the position x_1 and the microphone "B" at the position x_2 as shown in Figure 3.3. The pressure of the incident and reflected waves along the impedance tube can be be written as

$$p_I = \hat{p}_I e^{ik_0 x}, \tag{3.1}$$

$$p_R = \hat{p}_R e^{-ik_0 x}, \tag{3.2}$$

where $\hat{p}_I$ and $\hat{p}_R$ are the complex magnitudes of the incident and reflected waves at the reference plane which corresponds to the liner surface.

The complex pressures measured in both microphones can be represented as p_1 and p_2 for the microphone "A" and "B" respectively, in order to maintain the same notation as in the standard and given by

$$p_1 = \hat{p}_I e^{ik_0 x_1} + \hat{p}_R e^{-ik_0 x_1}, \tag{3.3}$$

$$p_2 = \hat{p}_I e^{ik_0 x_2} + \hat{p}_R e^{-ik_0 x_2}. \tag{3.4}$$

Transfer function between those microphone is given by

$$H_{12} = \frac{p_2}{p_1} = \frac{\hat{p}_I e^{ik_0 x_2} + \hat{p}_R e^{-ik_0 x_2}}{\hat{p}_I e^{ik_0 x_1} + \hat{p}_R e^{-ik_0 x_1}}. \tag{3.5}$$

The reflection factor is the ratio of the reflected wave to that of the incident wave and can be obtained in different positions x on the impedance tube considering plane wave propagation, where

$$\Gamma = \frac{p_R}{p_I} = \frac{\hat{p}_R e^{-ik_0 x}}{\hat{p}_I e^{ik_0 x}} = \frac{\hat{p}_R}{\hat{p}_I} e^{-2ik_0 x}. \tag{3.6}$$

At the liner surface $x = 0$ the reflection factor is given by $\mathit{\Gamma} = \frac{\hat{p}_R}{\hat{p}_I}$. So, the pressures at the microphone positions can be written as a function of the reflection coefficient, that can be substituted in the Equation 3.5. The transfer function can be written as

$$H_{12} = \frac{e^{ik_0 x_2} + \mathit{\Gamma} e^{-ik_0 x_2}}{e^{ik_0 x_1} + \mathit{\Gamma} e^{-ik_0 x_1}}. \tag{3.7}$$

Isolating the reflection factor, factorizing by $e^{ik_0 x_1}/e^{ik_0 x_1}$ and substituting $s = x_1 - x_2$ it is possible to calculate the reflection coefficient in terms of the transfer function [42]

as shown in section 2.7.1, where

$$\Gamma = |\Gamma|e^{i\theta_r} = \frac{H_{12} - e^{-ik_0 s}}{e^{-ik_0 s} - H_{12}} e^{2ik_0 x_1}. \tag{3.8}$$

From Equations 3.3 and 3.4 it is possible to isolate the reflected wave magnitude and equate both equations [15],

$$\hat{p}_R = \frac{p_1 - \hat{p}_I e^{ik_0 x_1}}{e^{-ik_0 x_1}} = \frac{p_2 - \hat{p}_I e^{ik_0 x_2}}{e^{-ik_0 x_2}}. \tag{3.9}$$

Solving for the incident wave it is possible to obtain

$$\begin{aligned}
(p_1 - \hat{p}_I e^{ik_0 x_1})e^{-ik_0 x_2} &= (p_2 - \hat{p}_I e^{ik_0 x_2})e^{-ik_0 x_1}, \\
p_1 e^{-ik_0 x_2} - \hat{p}_I e^{ik_0(x_1 - x_2)} &= p_2 e^{-ik_0 x_1} - \hat{p}_I e^{-ik_0(x_1 - x_2)}, \\
\hat{p}_I(e^{ik_0(x_1 - x_2)} - e^{-ik_0(x_1 - x_2)}) &= p_1 e^{-ik_0 x_2} - p_2 e^{-ik_0 x_1}, \\
\hat{p}_I &= \frac{p_1 e^{-ik_0 x_2} - p_2 e^{-ik_0 x_1}}{e^{ik_0(x_1 - x_2)} - e^{-ik_0(x_1 - x_2)}}, \\
\hat{p}_I &= \frac{p_1 e^{-ik_0(x_1 - x_2)} - p_2}{e^{ik_0(x_1 - x_2)} - e^{-ik_0(x_1 - x_2)}} e^{-ik_0 x_1}, \\
\hat{p}_I &= \frac{p_1 e^{-ik_0 s} - p_2}{e^{ik_0 s} - e^{-ik_0 s}} e^{-ik_0 x_1},
\end{aligned} \tag{3.10}$$

where the transfer function can be substituted to obtain

$$\begin{aligned}
\hat{p}_I &= \frac{e^{-ik_0 s} - \frac{p_2}{p_1}}{e^{ik_0 s} - e^{-ik_0 s}} p_1 e^{-ik_0 x_1}, \\
\hat{p}_I &= \frac{e^{-ik_0 s} - H_{12}}{e^{ik_0 s} - e^{-ik_0 s}} p_1 e^{-ik_0 x_1}.
\end{aligned} \tag{3.11}$$

In the same way from Equations 3.3 and 3.4 it is possible to isolate the incident wave magnitude and obtain a similar equation to the reflected wave [15],

$$\hat{p}_R = \frac{H_{12} - e^{-ik_0 s}}{e^{ik_0 s} - e^{-ik_0 s}} p_1 e^{ik_0 x_1}. \tag{3.12}$$

Both Equations 3.11 and 3.12 can be used to calculate the pressure on the liner surface where $x = 0$, given by

$$\begin{aligned}
p_0 &= \hat{p}_I e^{ik_0 x_0} + \hat{p}_R e^{-ik_0 x_0}, \\
p_0 &= \hat{p}_I + \hat{p}_R, \\
p_0 &= \frac{e^{-ik_0 s} - H_{12}}{e^{ik_0 s} - e^{-ik_0 s}} p_1 e^{-ik_0 x_1} + \frac{H_{12} - e^{-ik_0 s}}{e^{ik_0 s} - e^{-ik_0 s}} p_1 e^{ik_0 x_1}.
\end{aligned} \tag{3.13}$$

The pressure on the liner surface will vary accordingly to the position of the flanged impedance tube. This technique will be called as Flanged Two Microphone Method

(FTMM). The average pressure can also be obtained by several measurements at different positions n on the liner surface, given by

$$\bar{P} = \frac{1}{n}\sum_{n}(P_0)_n, \tag{3.14}$$

where n is the number of measurements taken in each different flanged tube position on the liner surface and $(P_0)_n$ is the frequency domain root mean squared pressure on the liner surface for the n^{th} measurement obtained by the Equation 3.13. The impedance was calculated based on the TMM that uses the reflection coefficient from the Equation 2.71.

The results will be shown in the following subsections by type of acoustic excitation in order to elucidate the signal implications on the measured liner impedance. The discharge coefficient and face sheet mass reactance were also calculated for pure tone excitation.

3.1.2.1 White noise

Figure 3.5 shows the impedance results measured at five different positions at the perforated liner sample facing sheet. The broadband test at 130 dB OASPL in each measurement was performed with the impedance meter flange resting over the sample, partially sealing excited resonator cells. A statistical variability in the results caused by the meter position is frequency dependent. The results have small variations below 0.1 for the resistance within a certain frequency band 2.5-5.0 kHz. The results above 5.0kHz and below 2.5kHz shown uncertainties on liner's impedance that are caused by the limitations of the flanged tube at low frequencies, where the edge effect dominates. The flanged tube impedance results are more accurate above the resonance frequency. A mean curve was calculated for each OASPL in order to obtain a single value for the liner impedance based on the pressure given by Equation 3.14 and mean velocity acquired by the same procedure used for the pressure.

Figure 3.6.(a) shows the mean impedance curves over the five measurement positions on the perforated liner facing sheet using the flanged impedance tube. Each curve shows the impedance results over a range of OASPLs from 130 to 155 dB in 5 dB steps. The oscillation of the curves suggest statistical variability in the results, where more oscillation is observed for the curves at higher OASPLs, meaning that more averages are needed to perform precise measurements at higher OASPLs. An increase of resistance, and a decrease of reactance is observed as the OASPL increases.

Figure 3.6.(b) shows the impedance results of a small sample cut from the original perforated liner sample, and inserted into a sample holder, for various OASPLs and white noise signals. The differences between the results in Figure 3.6.(a) and Figure 3.6.(b) are mostly related to the different POA. The flanged sample has $POAeff = 5.2$ % and the

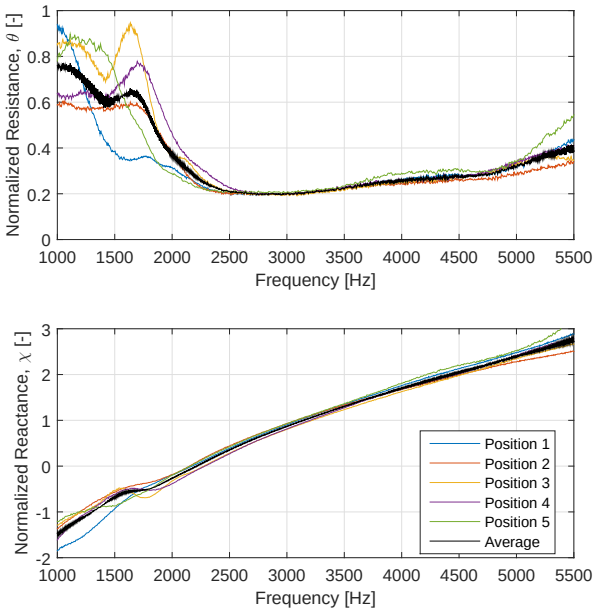

Figure 3.5: Punched aluminium SDOF liner impedance for white noise excitations at 130 dB, on different physical positions using FTMM.

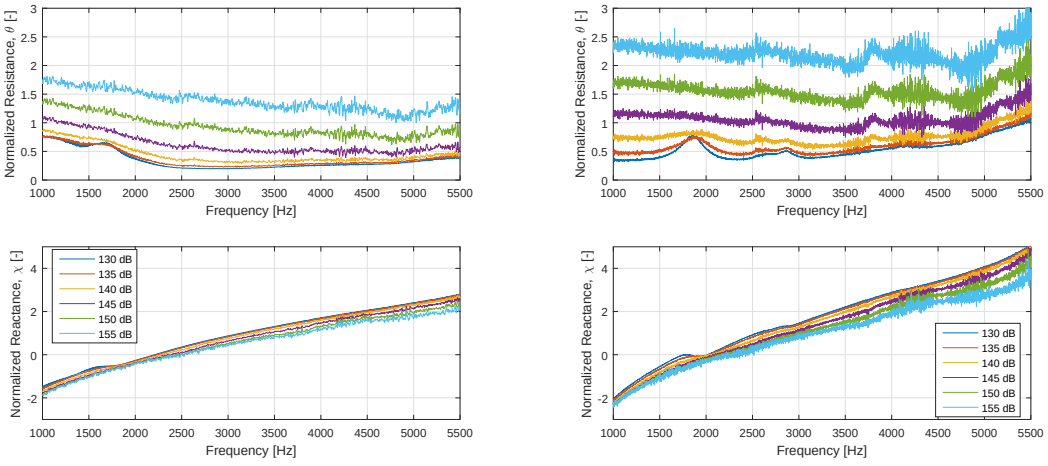

(a) Flanged.

(b) Sample holder.

Figure 3.6: Mean impedance results calculated using FTMM on five different positions of the punched aluminium SDOF liner and using TMM for the same liner in the sample holder for white noise excitation from 130-155 dB OASPL.

small sample on the holder has $POAeff = 3.5$ %. This large difference is caused because the extracted sample area was slightly smaller than the impedance tube diameter and some holes were blocked by the sealant on the edges of the sample holder. As expected the in tube results using TMM are better at lower frequencies.

Figure 3.7 shows the average particle velocity magnitude and phase over the sample holder liner surface for OASPL values from 130-150 dB. The velocity magnitudes at high

SPLs showed in logarithmic scale behave likewise the velocity magnitudes at low SPLs. The phase at around 1800 Hz shows a phase-wrapping that might be associated with the edge effect bump observed on the resistance curve.

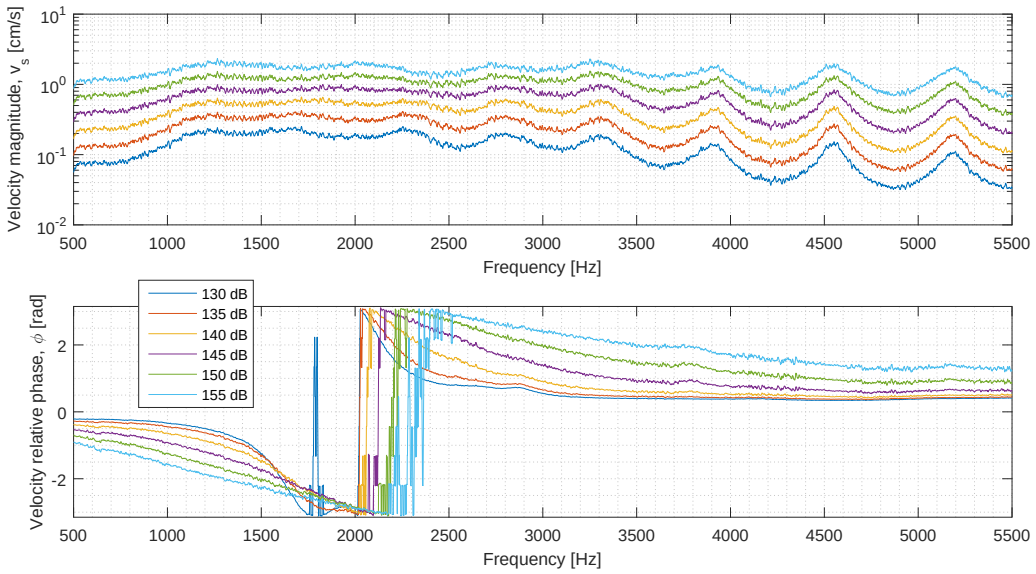

Figure 3.7: Punched aluminium SDOF liner in the sample holder average particle velocity over the liner surface calculated using TMM for white noise excitations from 130-155 dB OASPLs, using seven points moving average.

Figure 3.8 shows the absorption coefficients of the sample holder liner for 130-155 dB OASPL using white noise excitation. Efficient liner absorption occurs over a specific frequency band and it is SPL dependent. The absorption frequency band increases as the OASPL increases, however the absorption coefficient varies, reaching a peak of 1.0 around 2100-2150 Hz for 145 dB OASPL and showing values below 0.85 for 155 dB OASPL. The peak occurs when the normalized impedance is closest to 1+0j, which is the characteristic impedance of the air.

The peak in absorption around 1.5-2.0 kHz suggests that non-linearities can occur near the resonant frequency using a broadband signals at 130 and 135 dB. However, the velocity magnitudes are low and does not provide significant non-linearities at this SPLs. Resistance increase at this frequency range and oscillations also appears for reactance as showed in Figure 3.6.(b). This sudden increase in resistance diminishes as the OASPL increases, so as the peak absorption also shifts to higher frequencies. Also, Figure 3.5 shows significant variations depending on the flanged measurement position. The edge effect could be observed for flanged measurements as reported by Murray as an "unrealistic" increase in resistance at low frequency because of an area mismatch between the facing sheet and the backing sheet areas [68]. This can also occur in small scale using the sample holder, as the sample is slightly smaller than the tube diameter.

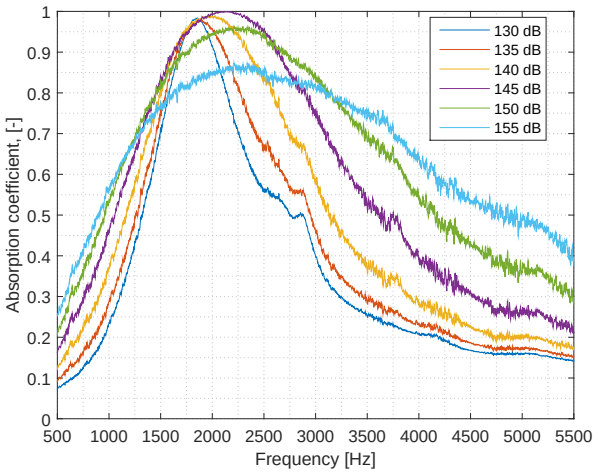

Figure 3.8: Absorption coefficient results on the surface of the perforated liner in a sample holder for white noise excitations at different OASPLs, using a seven point moving average.

Figure 3.9: Punched aluminium SDOF sample extracted from the panel and inserted on the sample holder.

3.1.2.2 Flanged tube - Pure tone

Pure tone measurements were performed using a waveform signal. Pure tones from 1.1-5.1 kHz in 500 Hz steps were used to excite and measure the flanged impedance on the large punched aluminium sample using the Flanged Two Microphone Method (FTMM). The same five physical positions used to perform the broadband excitation experiment were used to perform the pure tone excitation experiment. The same OASPL as the broadband excitation experiment was target at the liner surface during the pure tone excitation experiments.

Figure 3.10 shows the average impedance of the punched aluminium sample measured by a flanged tube in five positions at 130 dB OASPL. Similar statistical variations were observed for pure tone excitation in comparison with Figure 3.5 for a broadband signal. Large dispersion and consequently less confidence is expected below approximately 2.0 kHz in both cases.

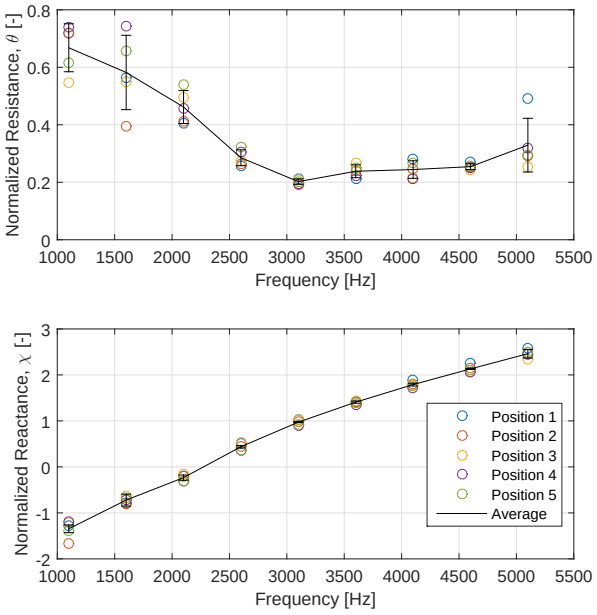

Figure 3.10: Punched aluminium SDOF liner impedance results using FTMM for pure tone excitations at 130 dB, at different physical positions and the arithmetic average of results.

Figure 3.11 contains the average curves of impedance, based on the results of 5 different physical positions on the punched aluminium liner sample using FTMM. Each curve was obtained for a fixed OASPL value and contains the standard deviation for each excitation frequency represented as the error bars. The average impedance curves were calculated for 130-150 dB SPL at the liner surface using 5 dB steps in order to assess the non-linearity progression.

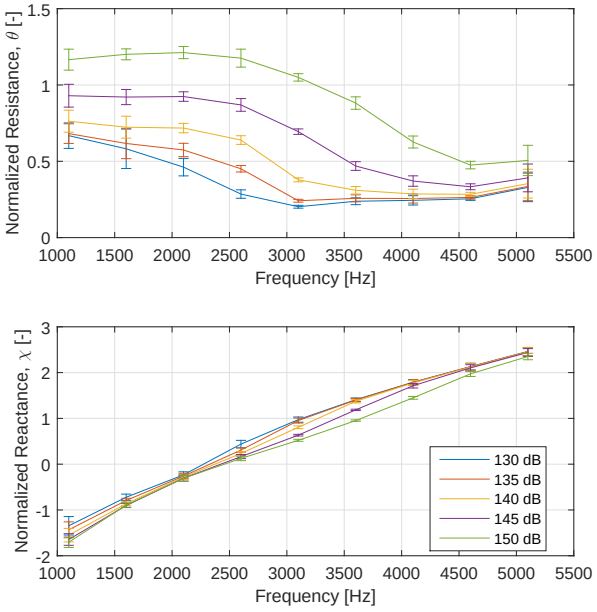

Figure 3.11: Punched aluminium SDOF liner average impedance results for pure tone excitations at different OASPLs using FTMM.

The error bars represent the standard deviation of the impedance values, placing the flanged tube in five distinct face sheet positions. Resistance standard deviations higher than 0.1 were calculated below 2.0 kHz and above 5.0 kHz. The resistance also increases at low frequencies due to the edge effect. These results shows the same trend as the white noise results, where higher uncertainty is expected at low frequencies. Thus, the sample holder results will be studied in more detail.

3.1.2.3 Sample holder - Pure tone

The sample holder measurements were performed using more tones from 0.6-5.1 kHz in 250 Hz steps. The same OASPLs as the previous experiments were target at the liner surface to performed the experiments. Figure 3.12 shows the impedance, SPL and velocity results measured on the perforated liner in the sample holder.

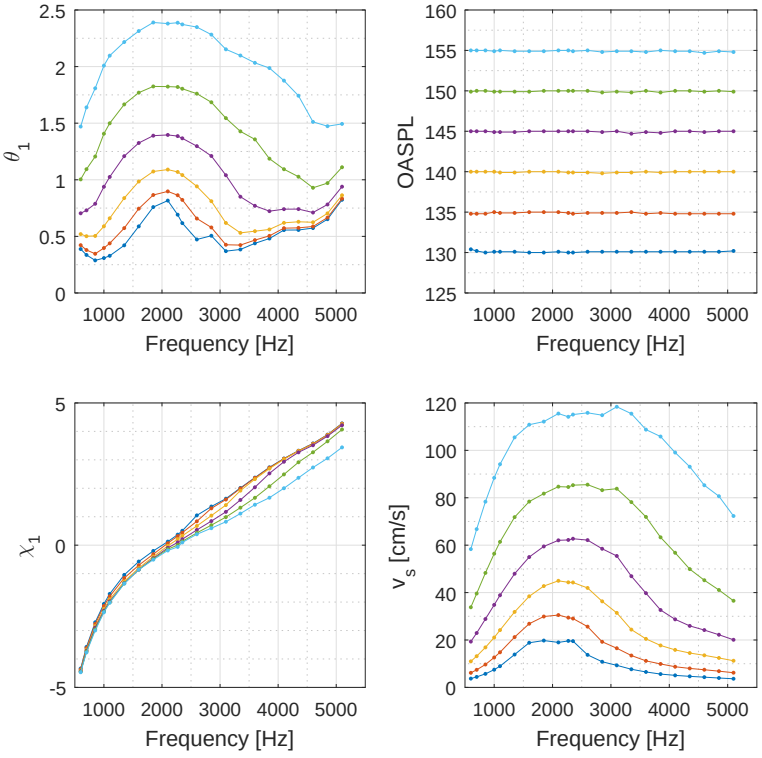

Figure 3.12: Impedance, SPL and velocity results for pure tone excitation on the perforated liner in a sample holder.

The resistance and reactance results are larger using the sample holder, shifting the resonant frequency to lower values than the flanged set-up. The POA_{eff} is the main reason why the results diverge, as there are fewer open holes in the sample holder facing sheet. The results show more reliable data for low frequencies when using the sample holder as the edge effect is partially removed. However, normal incidence experimental data is not enough to describe the liner impedance under real engine noise excitation, as the grazing flow influence is absent.

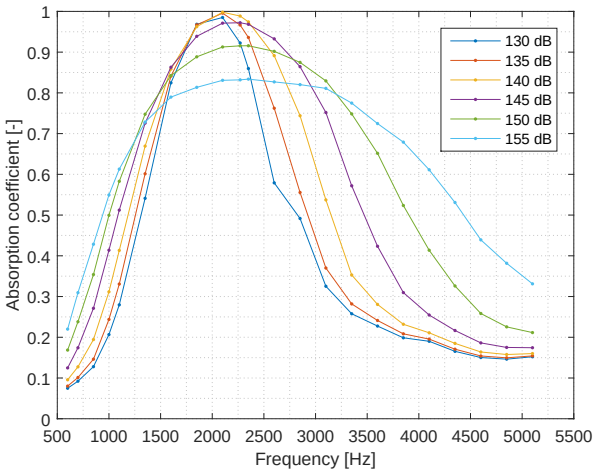

Figure 3.13: Absorption coefficient for 130-155 dB SPL range using the sample in the holder at different pure tone frequencies.

Figure 3.13 shows the absorption coefficient calculated on the surface of the sample inserted in the sample holder and excited by pure tones at 130-155 dB OASPL. Comparing the absorption curves for pure tones and for white noise, in Figure 3.8, it is possible to observe that higher absorption peaks occur at lower OASPLs for pure tones. Both excitations shows narrow band absorption at low OASPL and broader band at high OASPL, as well as the absorption coefficient peak reduces above 150 dB OASPL achieving around 0.85 at 155 dB OASPL at 2250 Hz.

Figure 3.14.(a) shows the resistance change due to the increasing Root Mean Squared (RMS) velocities measured in the perforated liner surface using pure tones at various frequencies and OASPLs. Different slopes for each line represents the nonlinear behaviour of the liner at that specific frequency. Every pure tone shows some degree of nonlinearity as the velocity increases. Pure tones at low frequencies show the greatest non-linearities with the non-linear slope remaining almost constant up to around 2 kHz. As the excitation frequency increases above around 2 kHz progressively lower degrees of nonlinearity are shown, suggesting that the vortex shedding energy dissipation mechanism is more effective at lower Strouhal numbers that correlate the frequency and velocity components.

Figure 3.14.(b) shows the resistance at the same frequencies as shown in Figure 3.14.(a) in terms of the Strouhal number, as defined in Equation 2.26. It can be seen that this higher non-linearity reported in terms of the frequency and velocity occurs for lower Strouhal numbers than approximately $1 < St < 2$. Above such values there is nonlinearity too, but not so intense as it is at lower Strouhal numbers. As the curves do not collapse with frequency, it is suggested that some factor is missing. This factor may be the discharge coefficient as it varies with frequency.

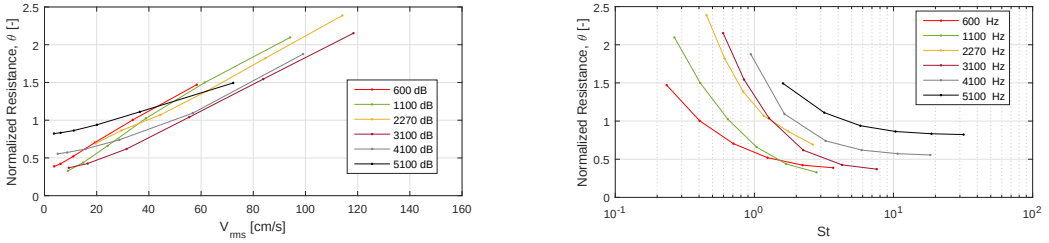

(a) Nonlinearity varying with velocity.

(b) Nonlinearity varying with St.

Figure 3.14: Resistance dependence on the spatial average RMS velocity measured for 130-155 dB OASPL at different frequencies in the sample holder and versus Strouhal number.

3.1.2.4 Discharge coefficient

The resistance θ versus v_{rms} data of Figure 3.14.(a) was linearly regressed in order to calculate the non-linear slope and consequently the POA_{eff}. Velocities below approximately 25 m/s were excluded during the curve fitting in order to isolate the non-linear components. The POA_{eff} of the sample can be determined at the resonant frequency of the liner using the well accepted value $C_D = 0.76$, using

$$POA_{eff} = \frac{100}{C_D}\sqrt{\frac{10^{-3}\rho}{2\psi}}, \tag{3.15}$$

where ψ is the slope of the straight line given in cgs $\frac{Rayls}{cm/s}$ and ρ is the density in g/cm^3 [70].

For a constant POA_{eff} calculated at the resonant frequency, the discharge coefficient C_D can be isolated using Equation 3.15 and calculated using the slope ψ found at the frequency of interest. Velocities below 25 cm/s were excluded during the curve fitting in order to obtain the same slope obtained at lower Strouhal numbers for all SPLs.

The resulting discharge coefficients calculated for the flanged measurements on the perforated sample are displayed in Figure 3.15. The calculated C_D approaches unity as the frequency increases (i.e. the acoustic boundary layer thickness reduces as frequency increases).

The same procedure was used to calculate the discharge coefficient for the aluminium perforated sample inside the holder, using a large number of pure tones, as shown in Figure 3.16. Results similar to the sample outside the holder were obtained at the same frequencies, but at this time the discharge coefficient is progressively increasing so a polynomial curve was fitted to extract $C_D(f)$. The polynomial equation of $C_D(f)$ was used in the 1D numerical implementation of different impedance models in order to obtain the impedances corrected by this frequency dependent discharge coefficient.

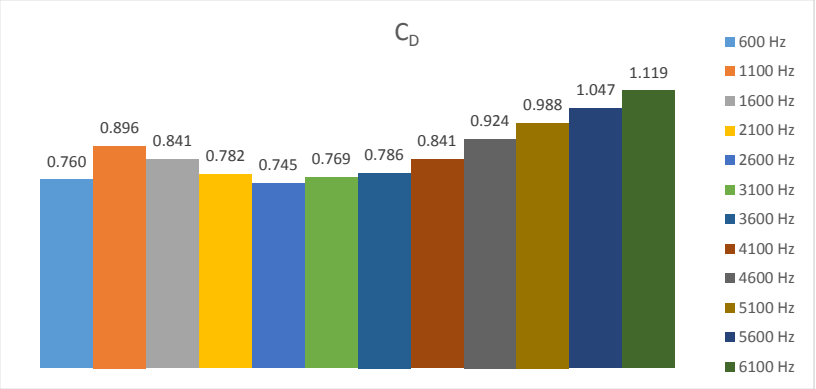

Figure 3.15: Discharge coefficient calculated for the punched aluminium SDOF liner using the flanged impedance tube ($POA_{eff} = 5.2\%$).

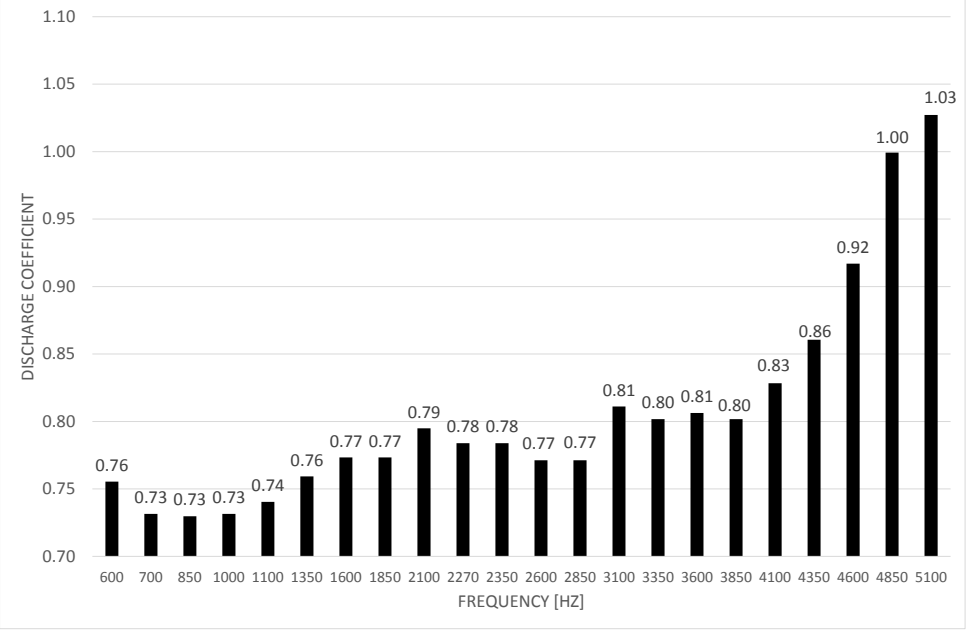

Figure 3.16: Discharge coefficient calculated for the punched aluminium SDOF liner contained in the holder ($POA_{eff} = 3.5\%$.

3.1.2.5 Face sheet mass reactance

One way to interpret the reactance is to divide it into two main components, the cavity reactance and the face sheet mass reactance. The cavity reactance can be determined analytically from $-cot(kh)$, where k is the wave number and h is the cavity depth. The face sheet mass reactance m_f is time dependent, because the mass volume that oscillates in the neck of the resonator varies over time, altering the end correction. The non-linearity observed at high OASPL affects the end correction so the mass reactance term is the most important reactance term to fully characterize the liner reactance. Defining the normalized frequency in terms of the resonant frequency as,

$$\omega_0 = f/f0, \tag{3.16}$$

where f_0 is the resonant frequency of the liner and f is the frequency component evaluated. The face sheet mass reactance can be calculated at the resonant frequency of the liner f_0 knowing that,

$$\chi_0 = m_{f0}k - cot(kh), \tag{3.17}$$

where m_{f0} is the face sheet mass reactance at the resonant frequency. Knowing that $\chi_0 = 0$ at the resonant frequency, it is possible to isolate m_{f0}, obtaining

$$m_{f0} = \frac{cot(kh)}{k}. \tag{3.18}$$

Assuming that the discharge coefficient is frequency dependent and it is strongly related to mass reactance, the values of m_f are also frequency dependent. Using the experimental $C_D(f)$ obtained previously for the sample in the holder is was possible to calculate m_f using the following equation

$$m_f = m_{f0}\frac{C_D}{C_{Df0}}, \tag{3.19}$$

where C_{Df0} is the discharge coefficient at the resonant frequency given by 0.76. The new semi-empirical curve obtained for the reactance is given by $\chi = km_f - cot(kh)$ using a frequency dependent mass reactance.

The graphs in Figure 3.17 show the reactance using the sample holder configuration.

Experimental and numerical curves using frequency dependent mass reactance m_f show good agreement for both pure tone and broadband experimental data from 130-150 dB. Observe that for a non frequency-dependent mass reactance m_{f0} that uses a fixed value of discharge coefficient, the agreement is not good at higher frequencies. The numerical model used on this validation is the one proposed in the section 4.3 and it is based on Rice model, and Cummings model with Bodén´s corrections that were covered on section 2.6 and it´s implementation is covered in the Section 4.2.

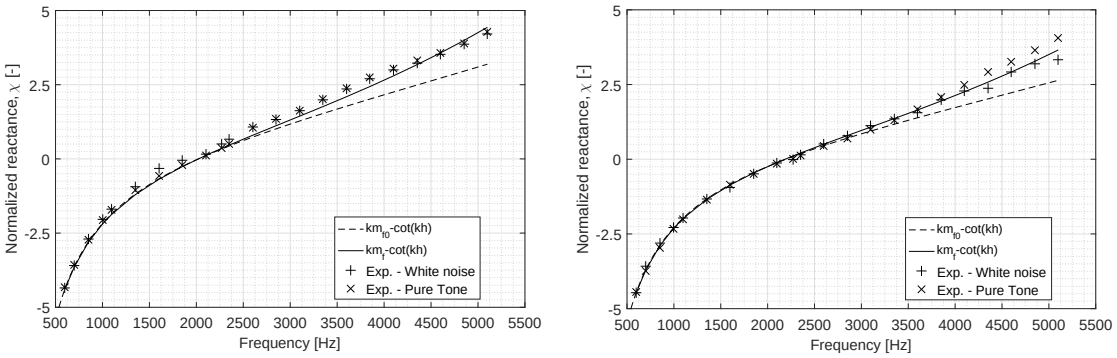

(a) 130 dB OASPL (b) 150 dB OASPL

Figure 3.17: Reactance curve using the sample holder and the calculated frequency dependent mass reactance against experimental results for pure tone and broadband excitation at 130 dB and 150 dB OASPL.

3.1.2.6 Other broadband signals

Four different broadband signals were evaluated to check if there is any correlation between the number of frequency tones and the associated resistance. Figure 3.18 illustrates the resistance comparison using broadband signals and pure tones to excite the sample in the holder at the same OASPL. The signals used were the white noise, pink noise, sawtooth and square waves.

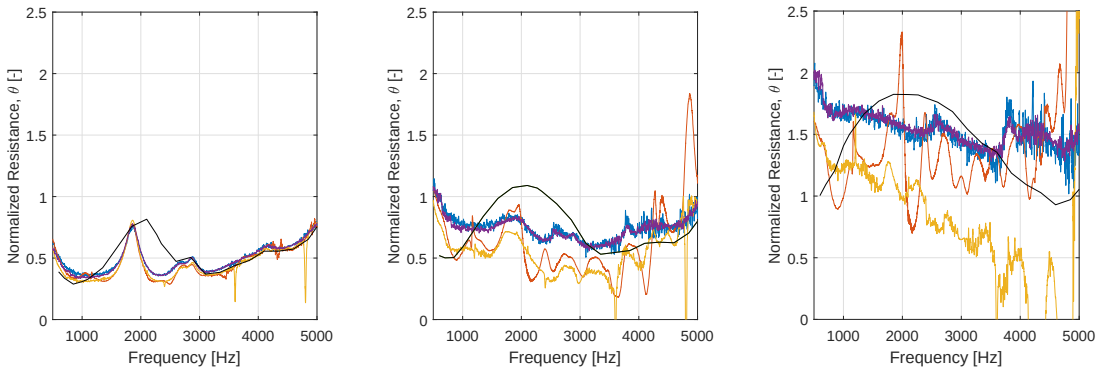

(a) OASPL=130 dB (b) OASPL=140 dB (c) OASPL=150 dB

Figure 3.18: Broadband resistances compared with pure tone for the sample in the holder using TMM. Black line - Pure tones, Purple line - White noise, Red line - Sawtooth, Blue line - Pink noise, Yellow line - Square.

The OASPL was kept constant in each graph, however, each frequency component has a different SPL, depending on the signal signature. The black line corresponds to the pure tone resistance, already shown in the Figure 3.12. Each of the broadband signals was smoothed using a moving average composed of 10 adjacent frequency component resistances. It is possible to observe a very good agreement between the pink noise and

white noise signal resistances, as both have several frequency components in the same bandwidth.

The Sawtooth signal is composed of several even and odd harmonically related tones from 600 Hz onwards. However, the impedance spectra is captured in each 1 Hz bandwidth. In the case of Square signal, only the odd harmonics are present, and also the fundamental frequency chosen was 600 Hz. Both sawtooth and square wave resistance spectra are calculated for each 1 Hz frequency bandwidth. Despite the fact that square and sawtooth signals have only few frequency components in the frequency range shown, it is possible to observe that the loudspeaker used to excite the system cannot just work in this specific frequencies and there is a significant sound pressure level in frequencies other then the harmonics. However, it is possible to observe the differences in resistance caused by broadband signals in comparison to pure tone signals.

The broadband signals showed lower resistances than the pure tone excitation within the liner resonant frequency octave. On the other hand, the pink noise and white noise cause higher resistances away from the resonant frequency octave. This resistance increase also is shown when using the sawtooth, however, it is shown by the square signal only at lower frequencies. More non-linearity is observed as the OASPL increases, suggesting that the entire frequency spectra of the incident pressure should be taken into account during liner modelling at high levels. Also, the resistance spectra change of the square wave from 140 dB to 150 dB suggests that the odd harmonic non-linearity vanishes at high SPLs, apart the fact that the entire spectra of the square signal response, composed by only a couple of odd harmonics, and considering the graphs in the Figures 3.18.(b) and 3.18.(c).

It is possible to conjecture that there is a relationship between liner resonant frequency and the relative amplitude between frequency components of the excitation signal. This effect potentially causes higher resistances away from the resonant frequency octave, and also lower resistances within the resonant frequency octave. The next analysis uses two harmonically related tones, the fundamental and first even harmonic, in order to simplify the analysis and observe only the effect caused by these two frequency components.

3.1.2.7 Multiple tone results

The impedance depends on the time history of the acoustic particle velocity at the liner surface. If the incoming sound wave contains only a single tone, the impedance will be controlled by the acoustic particle velocity at that frequency for a given SPL. On the other hand, random or periodic acoustic excitations with multiple tones may contain several frequency components and consequently, complex velocity history on the resonator aperture.

Two tone signals were generated with three different combinations of amplitudes, in order to analyse the impedance of each frequency component in the presence of a second tone. The low frequency tone, will be presented as "fundamental" or by the index "1", and the high frequency tone will be presented as "harmonic" or by the index "2". Considering the input signal, pressure amplitude ratios between tones in decibels was kept fixed for each set of measurements. The OASPL was changed by changing the voltage applied on the loudspeaker of the impedance tube only. Keeping the pressure amplitude ratio between tones constant, it could be particularly interesting to observe the energy transfer between frequency components as the OASPL increases. This was not carried, but the experimental results provide a good understanding about the differences in impedance due to the presence of multiple tones. The following acronyms will be used to identify each type of input signal analysed:

- Pure tone signal, where the pressure amplitude ratio between tones is much larger than 10 dB (PT);
- Fundamental tone sound pressure level is 10 dB higher than the harmonic tone sound pressure level (F>H);
- Two tones present in the signal have the same sound pressure level (Same);
- Harmonic tone sound pressure level is 10 dB higher than the fundamental tone sound pressure level (H>F).

The tones are harmonically related and the frequencies of the fundamental tone were chosen in order to obtain the fundamental tones near of below the resonant frequency of the liner. The harmonic tone remains within the frequency range measured by the impedance meter. The complex impedance of the liner was calculated at each frequency component, and only the excited frequencies were analysed.

Figure 3.19.(a) shows the fundamental tone resistance values, θ_1, for the liner inserted into the sample holder. The resistance was calculated at the liner surface using four different signals with the same OASPL. Each signal had a different pressure amplitude ratio between the fundamental and the harmonic tones. The pure tone signal (PT) contains the majority of the energy in the fundamental tone, whereas the (H>F) signal contains the majority of the energy in the harmonic signal.

It is possible to observe in the Figure 3.19.(a) that the pressure amplitude ratio between tones strongly influences the impedance at the evaluated tone. The peak of resistance occurs around 2100 Hz for the pure tone case, as observed by the yellow bars. However, the peak shifts to lower frequencies as more incident energy is placed in the harmonic frequency, as the maximum resistance for H>F is at 1100 Hz. Exciting the same sample at higher OASPLs produce essentially the same behaviour as the results at lower sound pressure levels, where the peak of resistance shifts from the resonant frequency to lower

frequencies as the incident energy increases in the harmonic tone. This can be seen analysing the peaks in the bars of Figure 3.19.(b) where the presence of equal energy in the harmonic both increases the fundamental resistance and lowers the peak frequency.

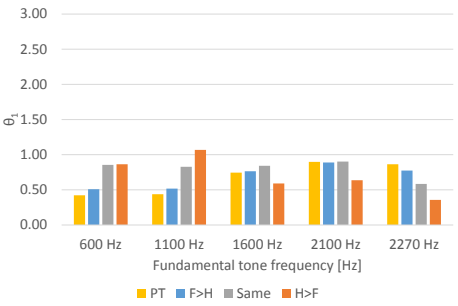

(a) Resistance, 135 dB OASPL

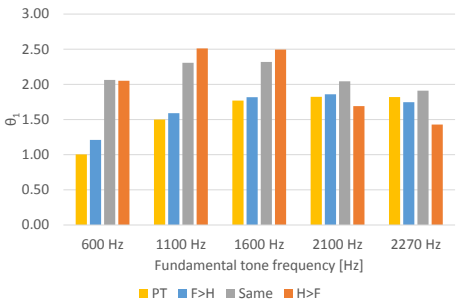

(b) Resistance, 150 dB OASPL

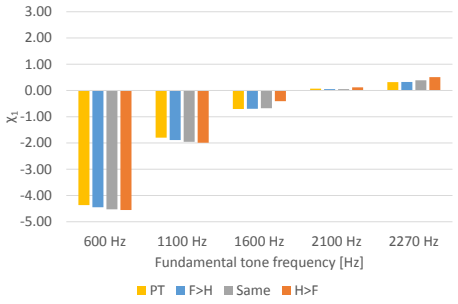

(c) Reactance, 135 dB OASPL

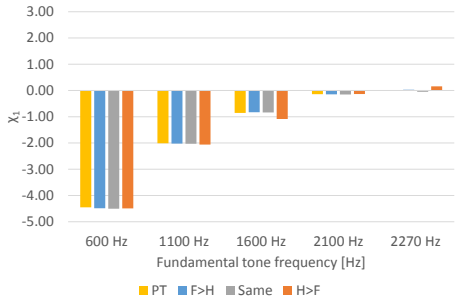

(d) Reactance, 150 dB OASPL

Figure 3.19: Impedance of the fundamental tone calculated at the punched aluminium SDOF liner surface inserted in the sample holder for incident signals with varying pressure amplitude ratios between frequency components using TMM.

A reactance decrease is observed as the OASPL increases from Figure 3.19.(c) to Figure 3.19.(d), especially at frequencies around the resonance, where the resonant frequency increases from 2100 Hz to 2270 Hz. However, no significant reactance changes were observed at each fundamental frequency when the frequency content of the signal was modified, see Figure 3.19.(d).

In other words, for a fixed OASPL, the resistance at an specific frequency component using pure tones differs from the impedance using multiple tones. The pressure amplitude ratio between tones in a given incident wave determines the liner response and consequently the resistance at a given tone. This behaviour is frequency dependent and is likely to be correlated with the resonant frequency of the liner, as the resistance increases for $w_0 < 1$ and decreases for $w_0 \approx 1$ when the level of the second tone is greater than the evaluated tone.

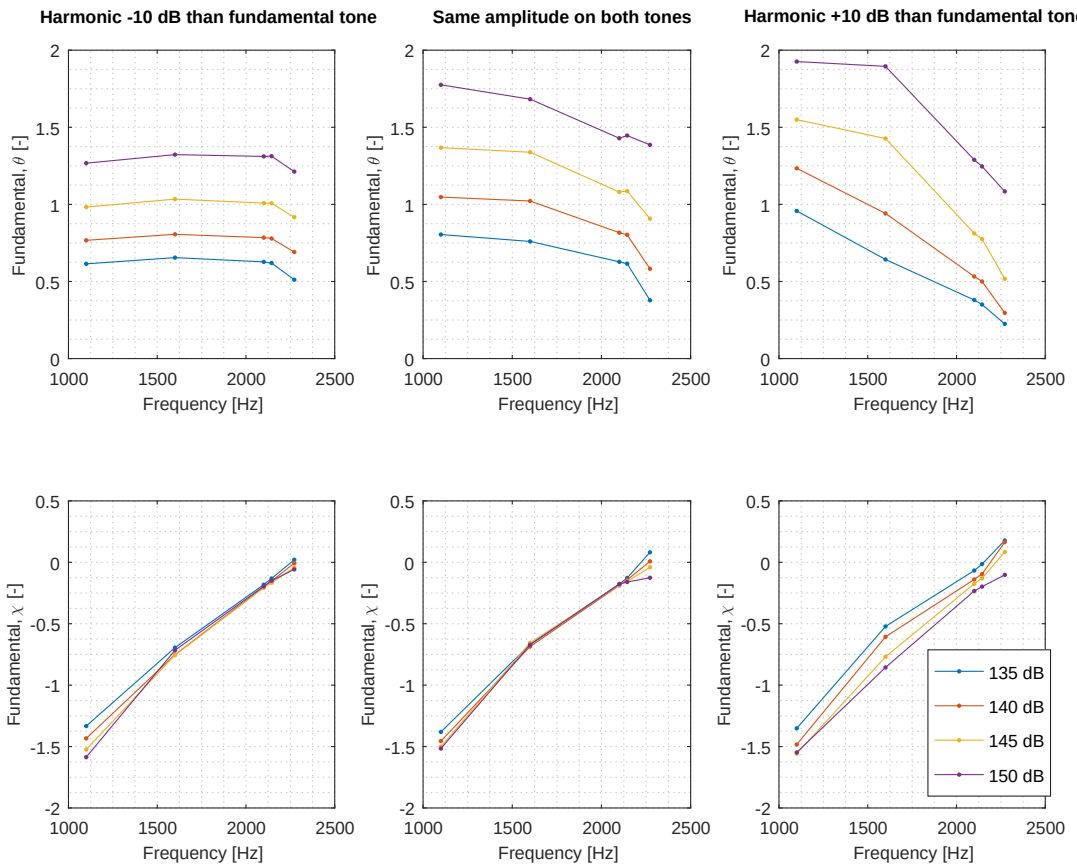

Figure 3.20: Impedance results of the fundamental tone, using two tones with different incident relative amplitudes measured in the punched aluminium SDOF liner using FTMM. On the left hand side incident fundamental tone pressure is 10 dB higher than the harmonic tone pressure. In the middle both tones have the same pressure amplitude. On the right hand side the harmonic tone pressure amplitude is 10 dB higher than the fundamental tone.

The trends are also seen for tests with flanged tube using FTMM as shown in Figure 3.20. Even with the edge effect, it is possible to observe the same behaviour as measured on the sample holder. The impedance of the fundamental tone, using a multitone signal, was plotted as a trend line for different frequencies at the same OASPL. Each dot corresponds to the impedance of the fundamental tone during one measurement. The graphs on the left hand side show the results of signals that contain incident fundamental tone pressure 10 dB higher than the harmonic tone pressure. The graphs in the middle show the impedances using signals that contain both tones with the same pressure amplitude. The graphs on the right show the impedances using signals that contain the harmonic tone pressure amplitude 10 dB higher than the fundamental tone. The legend shows the OASPL of each group of measurements.

Incident waves that contain higher harmonic tone pressure amplitudes are shown to

induce higher resistances at the fundamental tone frequencies below 2 kHz and lower resistances around 2 kHz for different OASPLs. The reactance behaviour is also sensitive to OASPL but only when the signal contains higher pressure amplitudes in the harmonic tone.

On the other hand, Figure 3.21 contains the same measurement results as Figure 3.20 but from the perspective of the harmonic tone. The impedance data plotted is calculated at the frequency of the harmonic tone using a multitone signal.

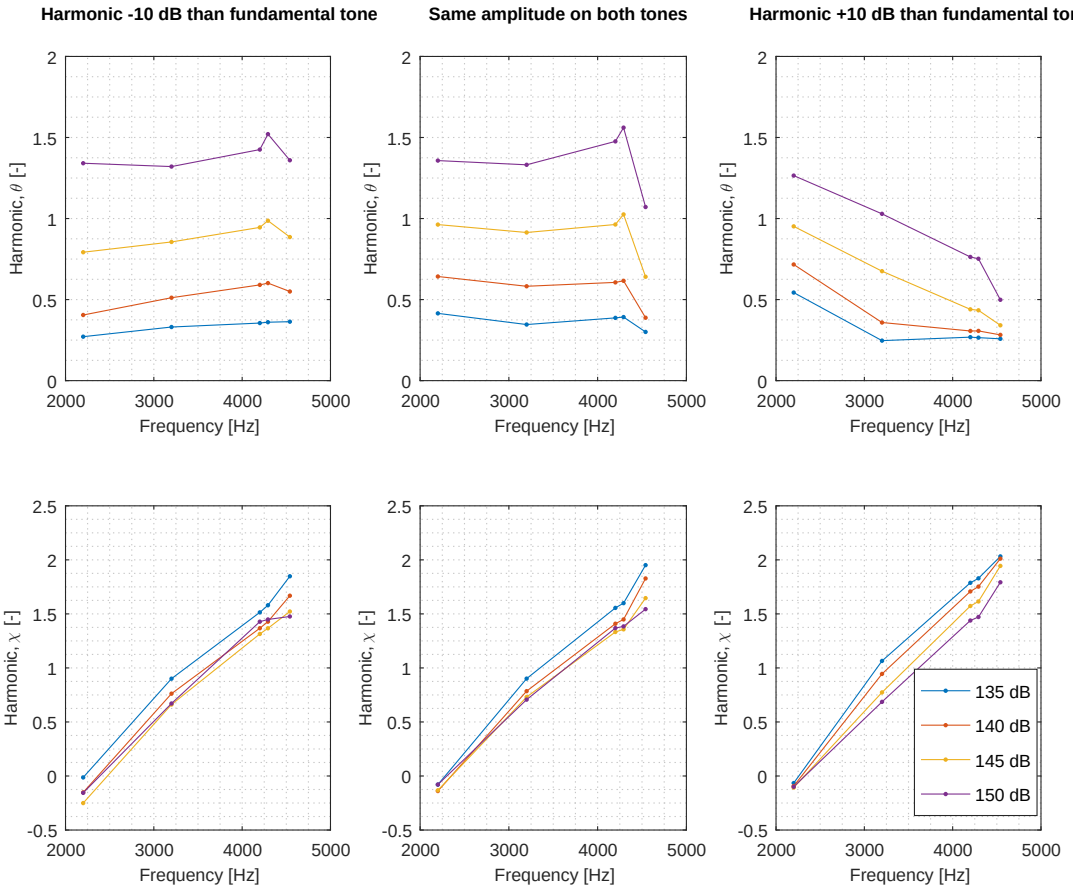

Figure 3.21: Impedance results of the harmonic tone, using two tones with different relative amplitudes measured in the punched aluminium SDOF liner sample using FTMM.

It was observed that a signal with higher pressure amplitudes at the harmonic behaves similarly as a pure tone at the same frequency. However, when the incident wave contains more energy in the fundamental tone than in the harmonic, the liner impedance shows higher resistances at the harmonic tone frequency above 3 kHz as observed on the left hand side graphs in Figure 3.21, in comparison with the graphs on the right hand side. Hence, in this case, losses are increased at the harmonic frequency when energy is

added to the fundamental. Near the resonant frequency $w_0 \approx 1$ the effect reversed, as increasing the energy in the fundamental reduces the resistance at the harmonic (resonant frequency).

Furthermore, a resistance peak was observed around 4300 Hz when the magnitude of the fundamental tone is high and greater than the level at the harmonic. This frequency is double the resonant frequency of the liner, which is around 2150 Hz at moderate to high OASPL. Perhaps the energy transfer to the harmonic is increased for the enhanced liner response at the resonance frequency.

The reactance calculated at the harmonic suggests that the liner has reduced inertance when the fundamental tone has increased pressure amplitudes.

3.1.3 3D printed liners results

It is evident that more data is needed in order to fully characterize the physical behavior involving multiple tone excitations in liners. Therefore, additional measurements were conducted using 3D printed samples in order to check if the multiple tone characteristics are similar for a different liner geometry. The 3D printed samples also incorporate in cell measurements of the impedance, for comparison with TMM. Table 3.3 illustrates the geometric average manufacturing errors in respect to the nominal values for the 3D printed samples.

3.1.3.1 Manufacturing process evaluation

Different 3D printing techniques were used in this study in order to evaluate the differences in impedance caused by slight changes in geometry due to the manufacturing process. A replica of the sample S1 was produced by photopolymerization using the original honeycomb geometry, the same as the perforated liner produced by conventional methods, and it was called S1A. A laser sintering process was also used to produce one sample having the same nominal geometric features as the sample S1, and it was called S1M.

The photopolymerization process, used to build the samples, works with ultraviolet light that solidify the photopolymeric solution and construct the sample in several stages. A base containing the photopolymer moves in order to fill the chamber with the solution. Each layer is constructed one over the other, using the ultraviolet light to solidify each layer. The base plate usually needs a dedicated construction structure to be placed below the part in order to allow the sample extraction without damaging it. The machine used to manufacture the samples is the EnvisionTec Ultra that allows up to 50 μm layers.

The influence of each geometric feature on liner impedance can be evaluated by a parametric analysis, where several samples are needed in order to obtain sufficient data to

formulate a liner model. Three sets of samples were produced in order to perform such analysis. Samples S1A, S1B, S1C and S1M are copies of the SDOF perforated sample showed in Figure 3.1. They were produced to assess the influence of material and manufacturing repeatability. On the other hand, samples S1 to S12 have a single cavity and variations in the hole diameter, the facing sheet thickness and the POA. The range of values for each parameter were chosen in order to mimic the typical geometries found on commercial liners used in the aerospace industry. The geometric features of the 3D printed samples are tabulated in Table 3.3.

Table 3.3: Geometric features of the 3D printed samples

Parameter	Hole diameter	Plate thickness	Cavity depth	Sample diameter	POA	Number of holes
			S1			
Nominal	1.00	0.64	19.05	29.00	5.2%	44
Mean	1.03	0.85	18.93	28.95	5.5%	
Std. Deviation	0.02	0.01	0.04	0.04	0.3%	
Error from nominal	3.0%	34.0%	0.7%	0.16%	6.0%	
			S2			
Nominal	1.00	1.00	19.05	29.00	5.2%	44
Mean	1.02	1.19	18.99	28.94	5.5%	
Std. Deviation	0.03	0.02	0.02	0.03	0.3%	
Error from nominal	2.5%	19.5%	0.3%	0.21%	5.6%	
			S3			
Nominal	1.00	1.25	19.05	29.00	5.2%	44
Mean	1.01	1.41	19.04	28.93	5.4%	
Std. Deviation	0.01	0.01	0.05	0.03	0.1%	
Error from nominal	1.4%	12.6%	0.1%	0.24%	3.3%	
			S4			
Nominal	1.00	1.50	19.05	29.00	5.2%	44
Mean	1.06	1.69	19.09	28.97	5.9%	
Std. Deviation	0.05	0.01	0.03	0.06	0.6%	
Error from nominal	6.1%	12.5%	0.2%	0.12%	13.0%	
			S5			
Nominal	1.00	2.00	19.05	29.00	5.2%	44
Mean	1.01	2.17	18.98	28.78	5.4%	
Std. Deviation	0.01	0.01	0.02	0.40	0.1%	
Error from nominal	0.7%	8.6%	0.4%	0.75%	3.1%	
			S6			
Nominal	1.00	0.64	19.05	29.00	3.6%	30
Mean	1.05	0.87	18.94	29.01	3.9%	
Std. Deviation	0.02	0.02	0.02	0.04	0.1%	
Error from nominal	5.1%	37.0%	0.6%	0.03%	10.3%	
			S7			
Nominal	1.00	0.64	19.05	29.00	7.1%	60
Mean	1.13	0.95	18.96	29.03	9.0%	
Std. Deviation	0.02	0.03	0.05	0.07	0.3%	
Error from nominal	12.7%	49.4%	0.5%	0.09%	26.8%	
			S8			
Nominal	1.00	0.64	19.05	29.00	10.0%	84
Mean	1.10	0.86	18.95	29.02	9.4%	
Std. Deviation	0.07	0.01	0.06	0.09	1.4%	
Error from nominal	10.0%	36.1%	0.5%	0.06%	5.5%	
			S9			
Nominal	1.00	0.64	19.05	29.00	19.3%	162
Mean	1.14	0.86	18.83	28.72	25.4%	
Std. Deviation	0.03	0.01	0.04	0.39	1.4%	
Error from nominal	13.7%	36.1%	1.2%	0.95%	31.8%	
			S10			
Nominal	1.27	0.64	19.05	29.00	5.2%	27
Mean	1.36	0.81	18.94	29.00	5.9%	
Std. Deviation	0.03	0.01	0.01	0.06	0.2%	
Error from nominal	6.7%	27.5%	0.6%	0.01%	13.9%	
			S11			
Nominal	1.56	0.64	18.42	29.00	5.2%	18
Mean	1.51	0.85	18.91	29.06	4.8%	
Std. Deviation	0.01	0.01	0.04	0.09	0.1%	
Error from nominal	3.5%	33.4%	2.7%	0.20%	7.2%	
			S12			
Nominal	1.91	0.64	19.05	29.00	5.2%	12
Mean	2.01	0.82	18.93	29.08	5.7%	
Std. Deviation	0.02	0.01	0.05	0.14	0.2%	
Error from nominal	5.1%	29.2%	0.6%	0.28%	9.8%	
Average error	**5.9%**	**28.0%**	**0.7%**	**0.3%**	**11.4%**	

The "mean" values are the averages of four measurements taken on each parameters selected in random locations. The Moore & Wright Digitronic Micrometer 200 series with $\pm$ 0.001 mm precision from 0-25 mm was used to measure the facing sheet thicknesses, and

the cavity depth. The hole diameters were measured using Alicona optical microscopy images that provided precision of ± 0.01 μ m. Samples S1, S2, S3, S4 and S5 have progressively larger facesheet thicknesses. Samples S6, S7, S8 and S9 have progressive larger porosities (POA). Samples S10, S11 and S12 have progressive larger hole diameters keeping the other parameters constant.

The technical drawings of each sample and the impedance meter sample holder assembly, used to perform *in situ* measurements are given in Annex B. A ribbed structure with just 4 mm depth from the facesheet was printed on the samples S1 to S12, instead of using a complete honeycomb structure, in order to give rigidity to the facesheet but avoid difficulties to insert *in situ* microphones. Only the experimental results using the perforated liner, S1, S2, S1A and S1M are reported in this chapter in order to illustrate the comparisons between manufacturing processes, measurement methods, and signal excitation responses of the evaluated samples.

The photopolymerization does not provide a rigorous geometry control of the samples. On average a 28% error was obtained on the facing sheet thickness of the liner sample produced by this technique as observed in Table 3.3. However, the liner cavity depth of the sample show lower geometric errors of 0.7% in respect to nominal values. The holes needed to be re-drilled after the 3D printing process, so the precision of the hole diameter was controlled by the bench drill used, showing average errors of 5.9% in terms of the nominal values. The deviations caused on the $POAeff$ were calculated based on the precision of two measurements, the hole diameter and the diameter of the entire sample. The propagated average error of the whole set of samples is 11.4% in respect the nominal values.

The metallic sample produced by laser sintering in Stainless Steel had the same manufacturing challenges as the ones produced by photopolymerization. The base of the powder bed also needs a dedicated construction structure in the laser sintering 3D printer. This allows the sample to be removed and cleaned easily. A strong interaction between the technicians and engineers is needed in order to guarantee the best results of the auxiliary structure so that doesn't affect the sample geometry. The nominal facing sheet thickness of 0.64 mm was not possible to achieve due to the method used to extract the laser sintered 3D printed sample (S1M) from the support base. Fortunately, the sample S1M has $l = 1.30mm$ which is similar to sample S2 and some comparisons can be performed between these samples. Figure 3.22 shows the different roughness of samples S1M and S1C. It is also possible to see that the photopolymer sample in ABS has holes with round edges and the S1M has holes with sharp edges.

Figure 3.23 shows the impedance comparisons between samples S1M ($POAeff$ =5.68%, l =1.3 mm) and S2 ($POAeff$ =6.89%, l =1.19 mm) for 130 dB and 150 dB OASPL, using pure tone excitation. Similar reactances were measured by both samples for all the range of OASPLs measured. Similar resonant frequencies were measured on the sample's

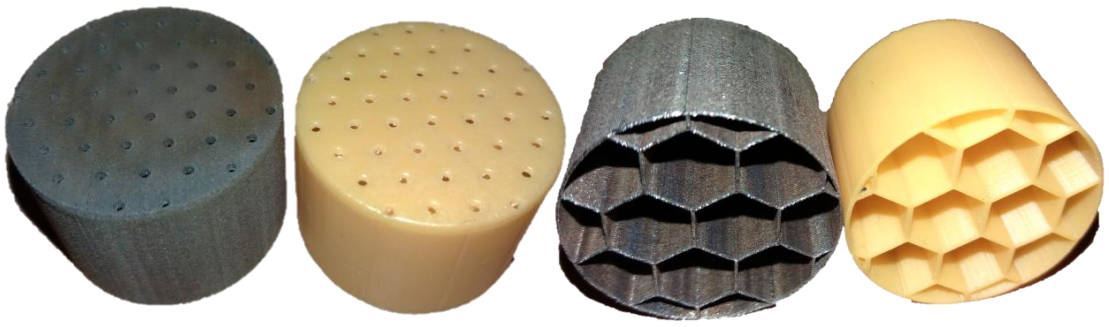

Figure 3.22: Laser sintered sample S1M on the left of each pair, and photopolymerized sample S1C on the right.

surfaces causing higher resistances on that frequency range as the OASPL increases. The S1M shown higher resistances at high OASPLs in comparison with the S2. The $POAeff$ was evaluated at 2100 Hz for both samples and the $POAeff$ of the sample S2 is higher than the one of S1M. Higher $POAeff$ is consistent with lower resistances and the experiment shows the sensitivity of the results due to small geometry changes and non-linearity. The ratio of the facesheet thickness by the diameter l/d is 1.21 for the S1M and 1.16 for the S2. Surface roughness is possibly causing a larger boundary layer, and lower discharge coefficients in the holes of S1M that culminate in higher resistances. Another possible cause of deviation is due to the hole shape, as the S1M shows straight edges and the ABS sample shows round edges.

The hole shape of each sample facing sheet was measured by an optical microscope called Alicona that has precision of 10 nm, at the national Center for Advanced Tribology (nCATS) located in the University of Southampton. The differences of the hole shape are more evident on the following pictures in Figure 3.24. From the top view of the sample S2 shown in the Figure 3.24.(a) it is possible to observe the shape of the holes, including the bigger ones used to fit the Kulite microphones in order to perform the *in situ* experiments. It is apparent that the photopolymerization samples shows holes with chamfered edges on the top surface that is exposed to the impinging sound wave, as the picture Figure 3.24.(b) shows dark colours near the hole edges of the sample S2 facing sheet, as seen from the cavity. This hole was scanned to check the roughness of the sample surface, so an angled image is shown in the Figure 3.24.(c) in which it was also possible to evaluate the facing sheet thickness. As the scanning process was performed from the back side of the facing sheet, it is possible to observe that the hole edge is quite sharp, suggesting that a rounded edge occurs only in one side of the hole. Figure 3.24.(d) shows the S1M facing sheet hole, where the hole walls looks rougher than for sample S2. The laser sintered sample S1M was not drilled, unlike S2, showing that the metal 3D

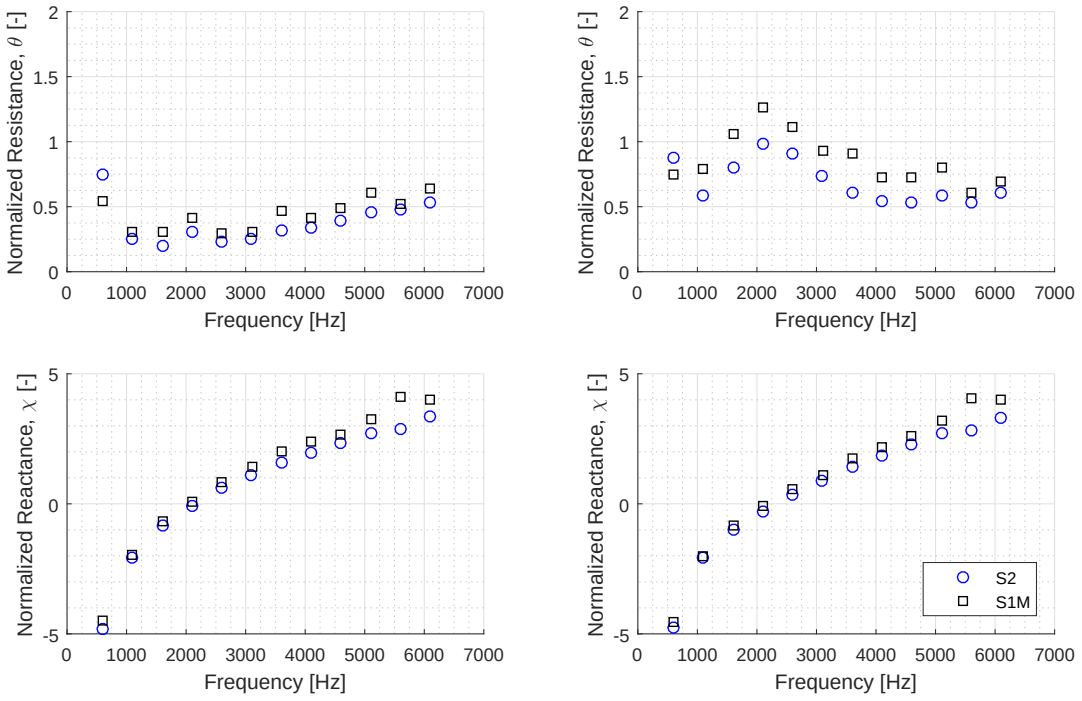

(a) OASPL=130 dB

(b) OASPL=150 dB

Figure 3.23: S1M and S2 pure tone impedances measured by TMM method using the portable impedance meter and the sample holder.

printing process can produce holes around 1 mm with reasonable accuracy, but with rough inner walls.

The second comparison is made between S1 and S1A, two samples with the same nominal geometry produced by photopolymerization 3D printing technique. The pure tone results are also compared with the perforated liner measured using both the flanged impedance tube and the TMM method, which is the standard method using the two microphones of the tube. Geometric features vary by up to 15% between the samples where l/d ratio is 0.64, 0.82 and 0.79 for the perforated liner using the flanged tube, S1 and S1A samples respectively. The respective precision of each geometrical measurement is provided in Table 3.4. Nominal geometry values of the perforated liner sample that are made of a punched aluminium sheet where obtained from the supplier, Alenia Aermacchi. Geometry values of the samples are averages of at least four measurements on the actual 3D printed samples and the precision is given by one standard deviation.

The samples S1 and S1A show good agreement in terms of the resistances for different OASPLs in all the bandwidth experimented, however the large flat liner (non-destructive) impedance doesn't agree with the other samples at lower frequencies because of the edge effect. The statistical variations of the hole diameters might cause POA differences that can be significant in terms of the resistance. Nonetheless, while the high frequency

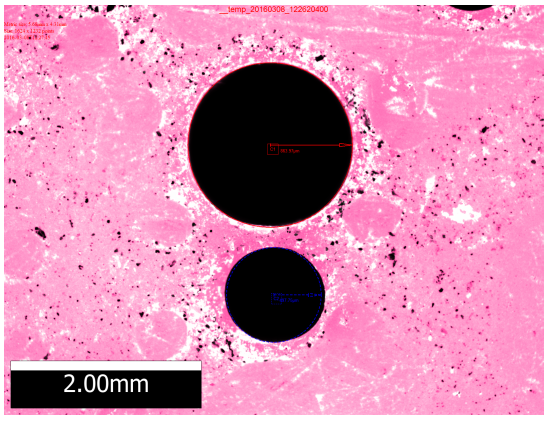

(a) S2 facing sheet hole and microphone hole (top surface)

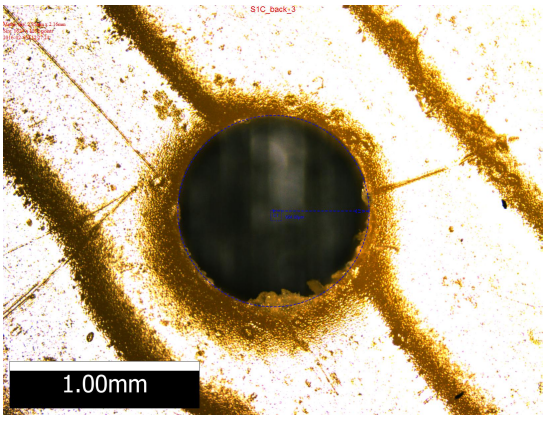

(b) S2 facing sheet hole shape (bottom surface)

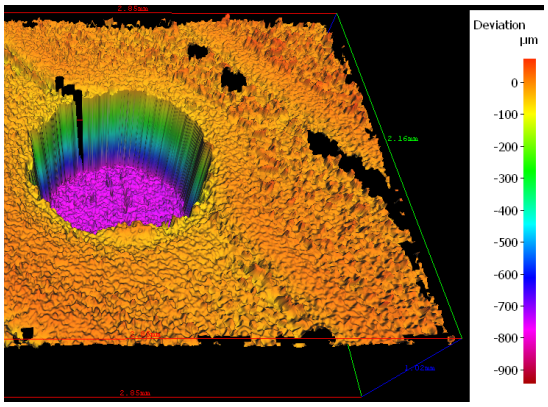

(c) S2 roughness

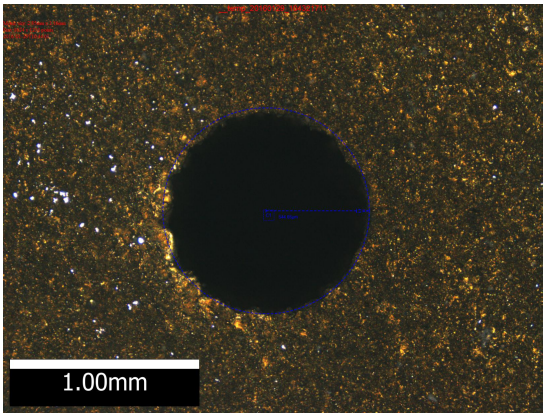

(d) S1M hole shape

Figure 3.24: S1M and S2 impedances measured by TMM method using the portable impedance meter and the sample holder.

Table 3.4: Geometry evaluation of the samples compared

			Sample		
Parameter	**Liner**	**S1**	**S1A**	**S2**	**S1M**
Diameter [mm]	0.99 ± 0.02	1.03 ± 0.02	1.04 ± 0.02	1.02 ± 0.03	1.07 ± 0.02
Thickness [mm]	0.64 ± 0.05	0.85 ± 0.02	0.83 ± 0.16	1.19 ± 0.04	1.30 ± 0.06
Cavity depth [mm]	19.05 ± 0.05	18.93 ± 0.04	19.09 ± 0.05	18.99 ± 0.02	19.28 ± 0.05
POA [%]	5.2 ± 0.5	5.5 ± 0.3	5.7 ± 0.3	5.5 ± 0.3	6.0 ± 0.3
Material	Al	ABS	ABS	ABS	Stainless Steel

agreement is good, it can be affirmed that an statistical variation is expected between samples and also between 3D printing processes.

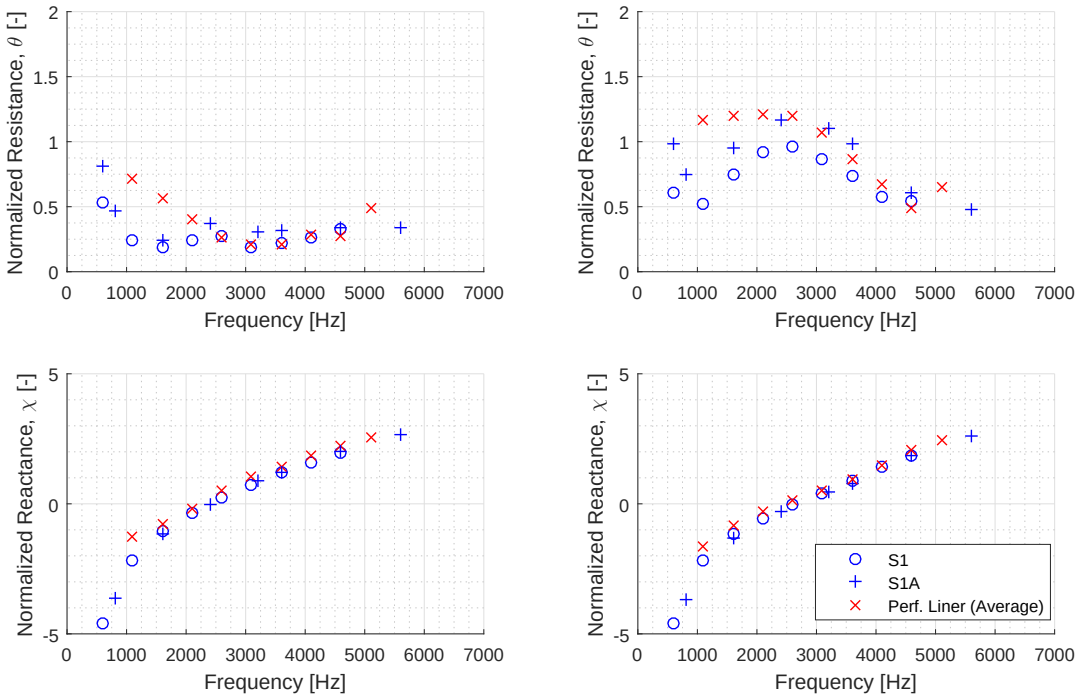

(a) OASPL=130 dB

(b) OASPL=150 dB

Figure 3.25: S1 and S1A impedances measured by TMM method using the portable impedance meter and the sample holder, compared with the perforated flanged liner measured by the same method.

3.1.3.2 *In situ* and TMM comparisons

In situ measurements are possibly the most accurate impedance measurement procedure that permits the validation of non invasive methods and numerical predictions. Figure 3.26 shows impedance results of S1 sample placed in the sample holder, excited by white noise using *in situ* and TMM methods simultaneously. The *in situ* technique results in the frequency domain were smoothed using a moving average window of 50 points and is represented by the red solid line. The TMM results are also averaged using overlapping in order to calculate the ensembled-averages and then transforming the results to the frequency domain. By overlapping we understand the signal processing technique that creates averages based on a sequence of two samples that contain almost the same points in time domain, varying only a few of them as established by a percentage of overllaping.

It is possible to observe a good agreement as the OASPL increases. For lower frequencies, below 2000 Hz and higher frequencies, above 5000 Hz, it is clear that the TMM measured higher resistances than *in situ* technique. At lower frequencies still some edge effect is present, due to the sample wall thickness of the sample, and consequently mismatch of areas, even inside the sample holder. The portable impedance tube used has 208.2

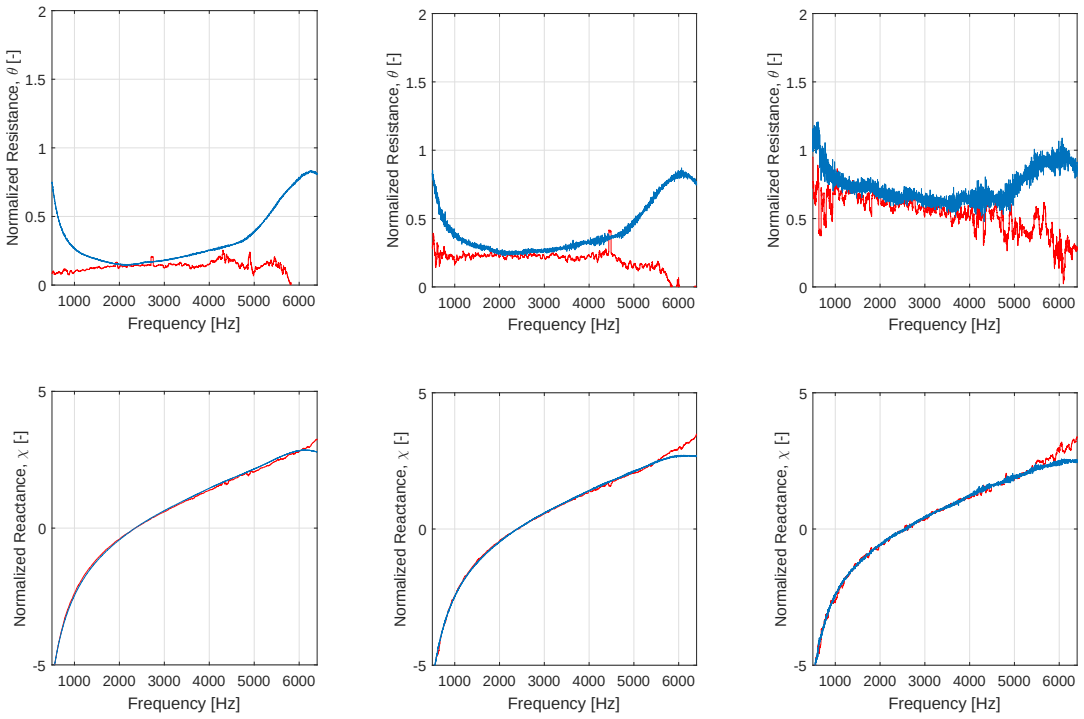

(a) OASPL=130 dB (b) OASPL=140 dB (c) OASPL=150 dB

Figure 3.26: Broadband impedance results using the S1 sample in the sample holder. *In situ* - red solid line, TMM - blue solid line.

mm length, so wave lengths larger than the tube length does not create a complete standing wave in a tube reducing the measurement precision for the TMM at lower frequencies. It is notable that, in the mid frequency range, where both methods agree, the resistance increases with frequency at low OASPLs and reduces with increasing frequency at high OASPLs. At higher frequencies the liner behaviour shows anti-resonances that are also hard to predict accurately via TMM. The particle velocity shows small magnitudes and consequently the liner surface acts as a reflecting surface at the anti-resonance. Consequently, the resistance increases and becomes difficult to measure. The microphone spacing and correct acoustic centre of the microphones in the tube also influences the measurement precision. The reactance results are in good agreement, except for higher frequencies where TMM shows higher resistances than *in situ* technique.

The same observations apply for the pure tone excitation results, where *in situ* and TMM agrees only in a limited frequency range due to the limitations of the TMM method when using a short impedance tube and the sample holder. Figure 3.27 contains the comparisons between *in situ* and TMM for different OASPLs measured simultaneously on the S1 sample placed in the sample holder. Resistances measured by the *in situ* technique are lower than the TMM results in general. Again the methods show good

agreement around the resonant frequency of the liner, the most important frequency range in terms of liner design.

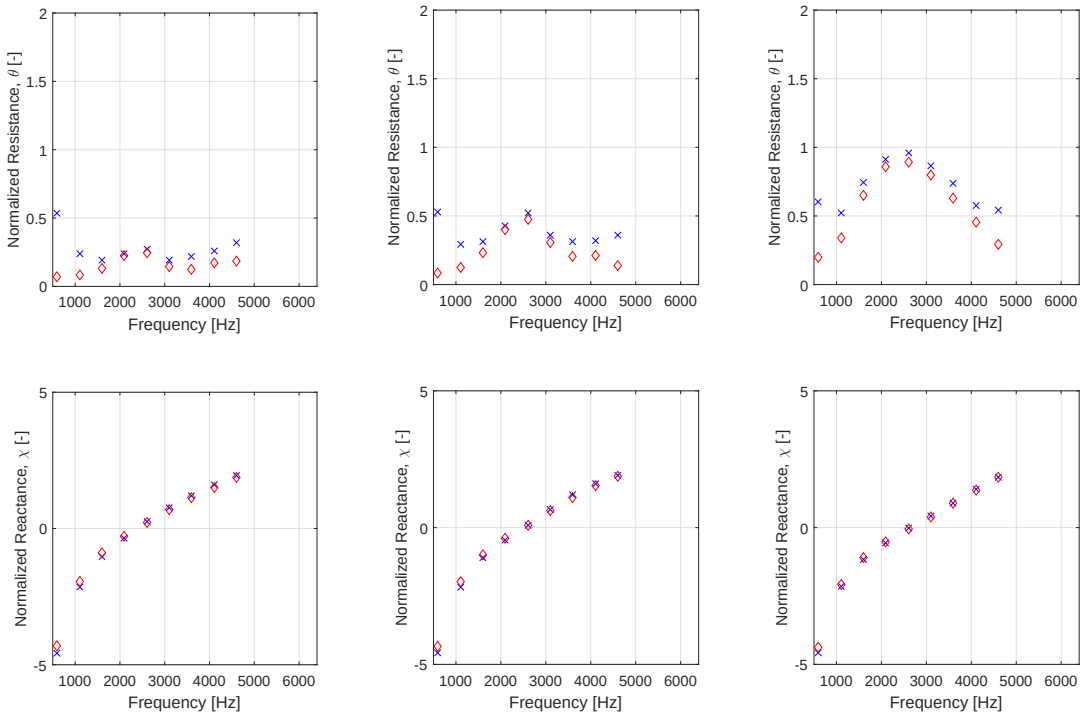

(a) OASPL=130 dB (b) OASPL=140 dB (c) OASPL=150 dB

Figure 3.27: Pure tone impedance results using the S1 sample. *In situ* - red Diamond (◇), TMM - blue X-mark (×).

The second 3D printed sample, S2, that has a thicker facing sheet (1.19 mm) was also instrumented for *in situ* measurements in the sample holder. The comparisons for three different pure tone OASPLs between TMM and *in situ* technique is shown in the Figure 3.28. Again, a limited frequency range around the resonant frequency for the liner contains better agreement between both experimental techniques. The TMM and in-situ method results diverge for lower and higher frequencies, where the *in situ* method produces lower resistances than TMM. In the same way as with S1, *in situ* reactances are higher than TMM reactances at high frequencies. In comparison with the sample S1, sample S2 shows slightly lower resonant frequency as shown by the peak of resistance and also the null reactance. Differences between the results can also be caused by microphone phase calibration and/or by the precision of microphone positions in both pairs of microphones. Also the cavity depth estimation used to calculate the *in situ* results is a cause of uncertainty.

On the next section using the grazing flow test rig the results of the *in situ* were calibrated for the microphone presence which leads to a cavity volume loss and honeycomb cell wall blockage. Sample S1 has a plate thickness of 0.85 mm and the same hole diameter (1.03

mm) as the S2 (1.02 mm), and both have one large cell containing all the sample holes. This does not affect the TMM measurement as the cell is narrow enough to allow only plane waves to propagate on the sample holder cavity. A calibration curve obtained by Ferrante [32] was used in the grazing flow *in situ* measurements in order to correct the pressure measured by the Kulite microphones on the surface and on the backing sheet of the instrumented liner cell. The corrections in pressure magnitude and phase are around ±0.02 dB and ±2 degrees respectively. The sensibility of the Kulite microphones was obtained comparing the measured pressure on the liner surface with the calculated pressure using the TMM method for 2 kHz. This calibration procedure is not ideal but it is feasible as the Kulites are very small to be placed in a conventional sound calibrator used for capacitive microphones.

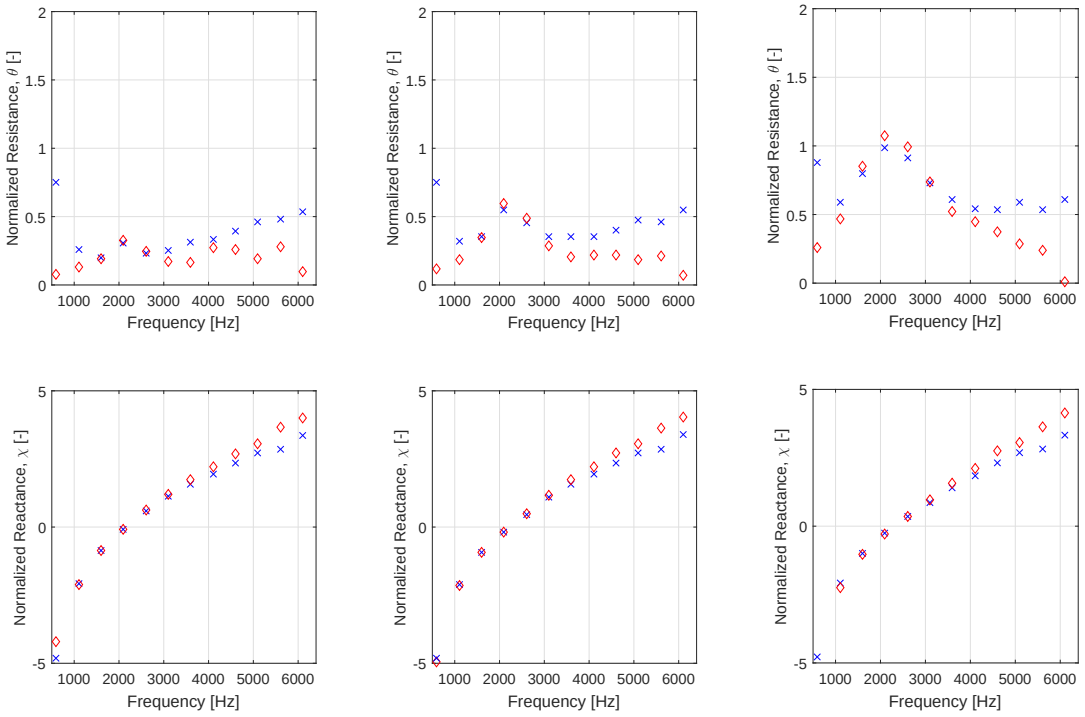

(a) OASPL=130 dB (b) OASPL=140 dB (c) OASPL=150 dB

Figure 3.28: Pure tone impedance results using the S2 sample. *In situ* - red Diamond (◇), TMM - blue X-mark (×).

3.1.3.3 Multiple tone results

As explored earlier with the liner in the sample holder, the presence of another frequency component on the excitation signal strongly influences the impedance response of the liner in the nonlinear regime. Figure 3.29 contains the impedance results of the S1 sample placed in the sample holder, using four different excitation signals. The solid lines are the

pure tone resistances and reactances measured using the TMM method at 130 dB, 140 dB and 150 dB OASPL. The dashed lines represents the impedance of each frequency component of a multiple tone excitation. Each measurement using two tones together, generates two values of impedance, one for each tone that are plotted in different graphs. The top graph in each pair contains the impedances of the fundamental frequency. The bottom graph of the pair contains impedances of the first even harmonic component, which corresponds to double the fundamental frequency. The resistance of the first tone, the fundamental, is identified by θ_1, and the mass reactance of this frequency component is $m_{f1}k$. Similarly, the resistance and mass reactance of the harmonic are identified as θ_2 and $m_{f2}k$ respectively. The normalized reactance had the cavity effect removed so that $m_{f1}k = \chi_1 + cot(kh)$. The trend lines highlight the impedance differences of each excitation signal in comparison with the pure tone excitation. In addition to the pure tone, three different multiple tone signals were applied at the impedance tube inlet, in which the amplitude ratio between the tones was kept constant. The signals had:

- Fundamental tone 5 dB higher than the harmonic (F>H)
- Two tones with the same amplitude (F=H)
- Harmonic tone 5 dB higher than the fundamental (H>F)

Impedance results of the sample S1 shown in Figure 3.29 folow the same trend as the impedance results of the perforated sample in the holder, shown in Figure 3.20.

The presence of a second tone excitation generally increases the resistance of a tone for frequencies away from the resonant frequency defined in the Equation 3.16, $\omega_0 > 1$ or $\omega_0 < 1$, and decreases the resistance of a tone near the resonant frequency, $\omega_0 \approx 1$. The resistance change is proportional to the amplitude ratio between frequency components. For instance, for a fundamental tone at 600 Hz up to 2000Hz, $\omega_0 < 1$, 5 dB higher than the harmonic (F>H), the resistance is similar or slightly higher than the pure tone excitation as observed in the top graph of Figure 3.29(a). When the harmonic is 5dB higher (H>F), using the same combination of tones, the resistances measured at the fundamental tone are higher than the pure tone case, as observed in the top graph of Figure 3.29(c). The same trend is observed in the bottom graphs of the Figure 3.29(a), (b) and (c), but this time the harmonic resistance exceeds that of the pure tone for $\omega_0 > 1$.

These results again show that the impedance at a specific frequency changes in the presence of an even harmonically related tone at lower or higher frequency, especially away from the resonant frequency bandwidth. The impedance of a tone is strongly dependent on the signal frequency content and also on the liner resonant frequency (determined by the OASPL and the geometry). The greater the OASPL the greater is the change in resistance arising from multi-tone signal.

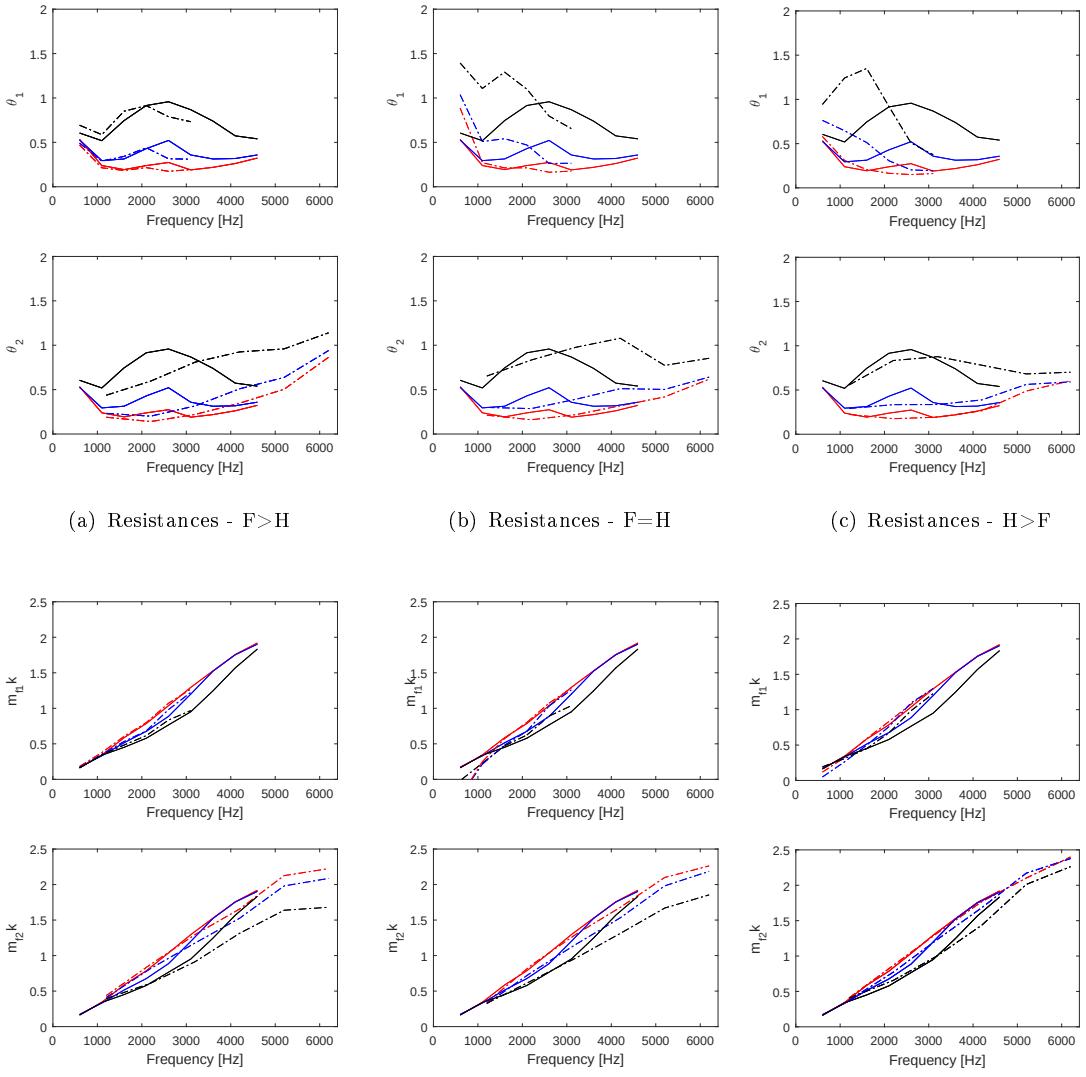

(a) Resistances - F>H (b) Resistances - F=H (c) Resistances - H>F

(d) Reactances - F>H (e) Reactances - F=H (f) Reactances - H>F

Figure 3.29: S1 sample impedances at different OASPLs for each frequency component of multiple tone signals (dashed lines) in comparison with pure tone signals (solid line) using TMM. Red - 130 dB, Blue - 140 dB, Black - 150 dB.

In terms of the reactance, as the pressure amplitude ratio between tones changes, different behaviours are observed. The top graphs of Figure 3.29(d) shows that the fundamental tone reactance does not change significantly in the presence of a harmonic 5 dB lower in comparison with the pure tone excitation. However, as the energy (pressure amplitude) of the harmonic increases, as shown in the top graph of Figure 3.29.(f), the reactance of the fundamental tone increases, approaching the linear response for $\omega_0 \approx 1$ and it slightly decreased for $\omega_0 < 1$, maintaining the same OASPL. The same behaviour happens analysing the harmonic tone mass reactance, showing a slight increase for $\omega_0 \approx 1$, and considerable decrease for $\omega_0 < 1$ as the low frequency component shows significant or higher amplitude than the harmonic observed in the bottom graph of Figure 3.29.(d).

In conclusion, nonlinearity is caused in both resistance and reactance results at frequencies away from the resonant frequency octave $\omega_0 \approx 1$ if a second harmonically related tone has significant energy. The nonlinearity happens in both ways, from lower to higher frequencies and vice-versa, confirming that liner modelling demands previous knowledge of the whole frequency content and amplitude ratios between significant tones present in a multitone signal that impinges the liner surface.

Figure 3.30 shows the sample S2 impedance results (d=1.02 mm, l=1.19 mm and POA= 5.5%) using TMM and varying the type of excitation keeping the total OASPL constant in each graph.

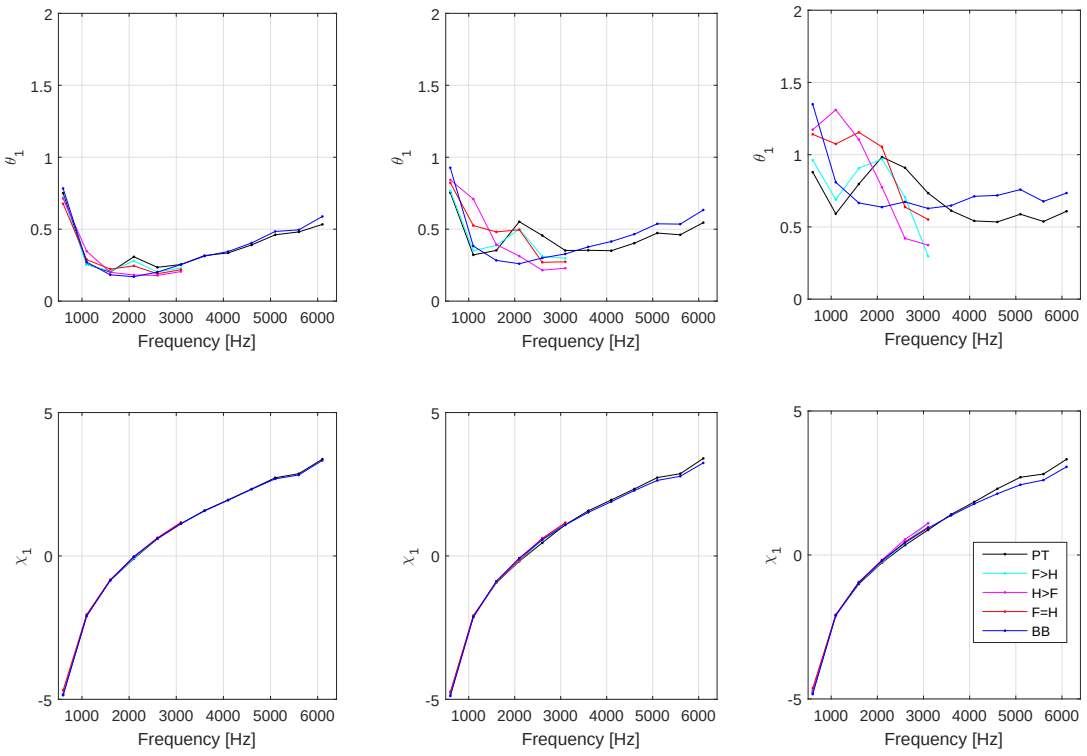

(a) OASPL = 130 dB (b) OASPL = 140 dB (c) OASPL = 150 dB

Figure 3.30: S2 sample fundamental tone impedances at progressive OASPLs for distinct signal excitations using TMM. Black - Pure tone, Cyan - Fundamental 5 dB higher than the harmonic tone, Magenta - Harmonic 5 dB higher than the fundamental tone, Red - Same level in both tones, Blue - Broadband white noise signal.

The OASPL is based on the root mean square pressure of the signal, which can have several frequency components. The SPL of each tone is the root mean square pressure magnitude calculated at the specific frequency, after post processing the signal in the frequency domain. The acronyms PT, F>H, H>F, F=H and BB stand for pure tone, fundamental higher than the harmonic, harmonic higher than the fundamental, same

amplitude and white noise excitations respectively. Each dot corresponds to impedance results at the fundamental tone, θ_1 and χ_1, where multitone excitation signals have the same set of relative amplitude as the previous case for S1 (max delta = 5 dB). It is possible to observe that nonlinear effects are more evident at higher OASPLs in terms of resistance changes, however, the reactance is not strongly affected. Probably the cavity reactance is not much affected, but the mass reactance is, as shown on the Figures 3.29.(d),(e) and (f). The bell shape curve of resistance obtained for pure tone excitation moves it's peak as more energy is applied on the other tone. For $\omega_0 < 1$ the peak of the fundamental tone resistance shifts to lower frequencies as the harmonic tone amplitude increases. As seen for sample S1, the peak of the harmonic tone resistance shifts to higher frequencies as the fundamental tone amplitude increases. This last case can be observed for sample S1 in terms of θ_2 in the Figure 3.29.(a),(b) and (c) for the dashed line.

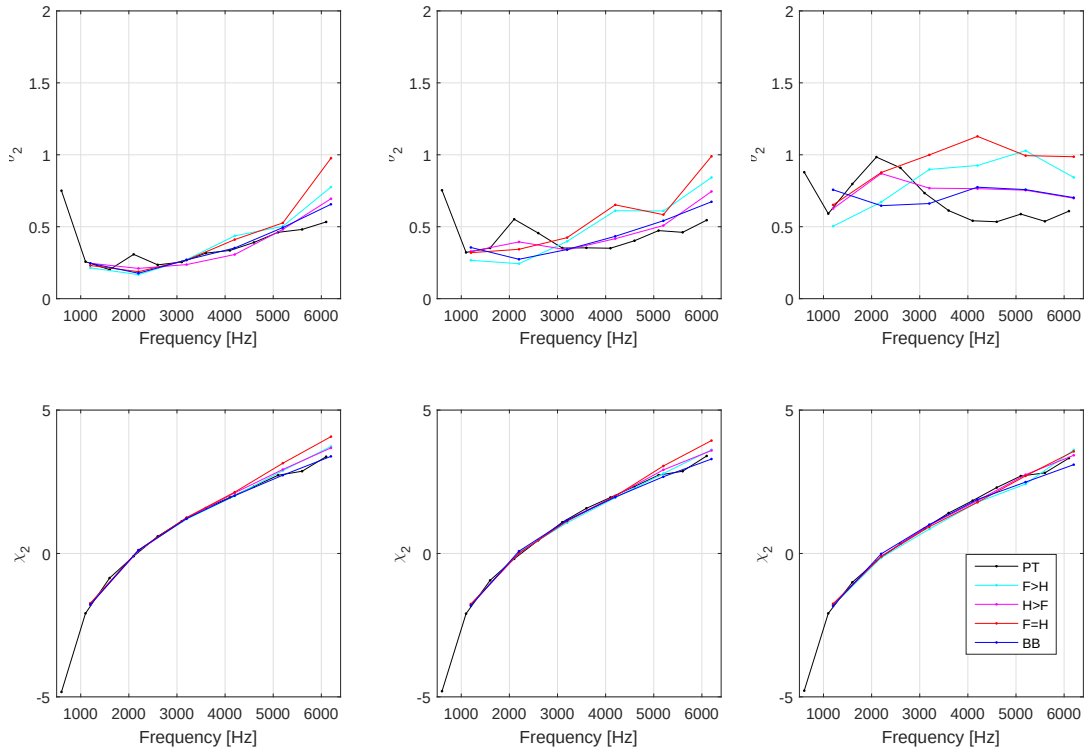

(a) OASPL = 130 dB (b) OASPL = 140 dB (c) OASPL = 150 dB

Figure 3.31: S2 sample harmonic tone impedances at progressive OASPLs for distinct signal excitations using TMM. Black - Pure tone, Cyan - Fundamental 5 dB higher than the harmonic tone, Magenta - Harmonic 5 dB higher than the fundamental tone, Red - Same level in both tones, Blue - Broadband white noise signal.

Figure 3.31 shows sample S2 impedance results using TMM at different OASPLs and using various excitation signals, where resistance results at the harmonics, θ_2, for multiple

tone and broadband signals are illustrated with pure tone resistance in Figure 3.31.(a),(b) and (c). The same behaviour observed for sample S1 is also observed for sample S2, where around the resonance, $\omega \approx 1$, the resistance of the harmonic reduces for increasing energy on the fundamental. However, the harmonic resistance increases above the resonance $\omega_0 > 1$ as the fundamental tone increasing energy. The peak of resistance shifts to higher frequencies as more energy is applied on the fundamental.

3.2 Grazing flow test rig

The UFSC (Universidade Federal de Santa Catarina) grazing flow impedance test rig was developed to evaluate typical aero engine liners using impedance eduction techniques [85]. Future plans include mounting the test section in an anechoic chamber built in the LVA (Laboratório de Vibrações e Acústica - part of mechanical engineering department of UFSC). The effect of grazing flow is important to characterize the liner in operation conditions but full scale engine tests are expensive. In this context, grazing flow test rigs are an inexpensive approach to characterize the liners in similar flow conditions.

3.2.1 Rig Overview

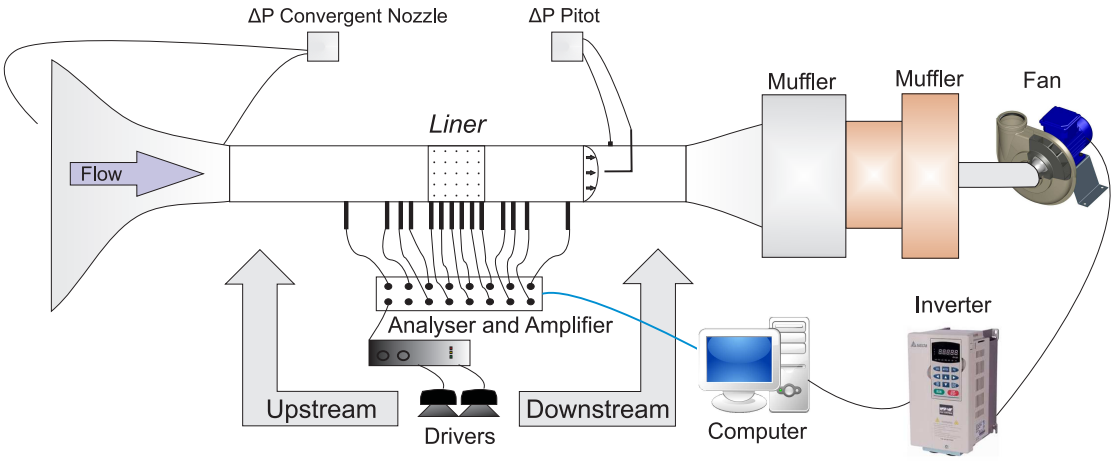

Figure 3.32: UFSC impedance test rig scheme. From: Serrano, 2014 [86]

Figure 3.32 illustrates the scheme used in the first version of the UFSC impedance test rig built in 2014. The rig comprises of a tube connecting one chamber to a nozzle that accelerates the fluid through a 40x100 mm rectangular tube. After the test section the cross section expands via a diffuser, which terminates at the inlet to a centrifugal fan connected to resistive mufflers that avoid unwanted noise from the fan to the test section.

The rig has several transducers connected to the tube and signals are acquired by a National Instruments PXI industrial data acquisition system. The input signal goes to an output of the analyser and is sent to power amplifiers connected to acoustic compression

drivers. The position of the drivers can be changed in the test section to an upstream or downstream portion of the test section as shown by the arrows in Figure 3.32. The software, called SCAP LR (Software de Controle Aquisição e Processamento de sinais Liner Rig)[57], programmed for this application was written using the LabVIEW programing language and controls the analyser. The application was validated using the Bruel & Kjær acquisition system, Pulse [57].

In terms of the grazing flow, a Pitot tube can be used to measure the velocity profile in the test section. It is manually manipulated and may be removed if necessary. The differential manometer connected on both sides of the convergent nozzle reads the differential pressure and sends the information to the analyser, which collects the signals of all the microphones connected to the walls of the test section. The positions of the microphones are pre-defined. There are up to 4 microphones upstream, 4 downstream and up to 10 on the wall opposite to the liner sample. This fan is controlled by SCAP LR which has a calibrated curve that allows an estimation of the grazing flow speed into the test section using the pressure difference measured at the nozzle. The user can set up the desired mean air velocity in the test section using a signal that is sent to an inverter connected to the fan. The velocities range from 0 to 0.29 Mach in the current configuration. The noise generator is another module of the software specially implemented for this application.

Figure 3.33 illustrates six photos of the rig during a campaign of experiments. The convergent nozzle connected to a chamber and eight acoustic drivers with the power amplifiers on a metallic trolley are shown in the first photo on the top left. The drivers produce sound through thick rubber tubes that are connected to the main test section duct, which is made of acrylic (see top middle photo). The downstream source position and the metallic diffuser can be seen in the top right photo. Microphones with 1/4 inch diameter are connected to the acrylic section through metallic couplers and may be seen in the bottom left and right photos. Finally, an insertion thermometer connected to the test section through a nylon coupler can be seen on the bottom middle photo. The temperature for use of the acoustic flowmeter technique that will be explained on Section 3.2.2 is important for precisely measuring the grazing flow.

3.2.2 Grazing flow calibration procedure

Grazing flow velocity measurements were performed using two different techniques. A cross validation procedure was used to evaluate the mean Mach number generated in the UFSC test rig. The Pitot tube technique was used to measure differential pressures in various cross section points to obtain the arithmetic mean Mach number. This velocity is an average value of 16 velocities measured at a cross section of the rectangular duct and it was evaluated against the centerline Mach number [85]. The other technique, the so-called “acoustic technique", uses three microphones and a random signal of acoustic

Figure 3.33: UFSC impedance test rig in operation. Nozzle and compression drivers on the top left, rubber tubes connected to the upstream section on the top center, diffuser and rubber tubes connected to the downstream section on the top right. Couplers with the microphones upstream, thermometer and microphones downstream are shown on the bottom left, center and right respectively.

excitation with flow to calculate the mean Mach number using an analytical formulation and optimization procedures [61, p. 125].

In the following analysis conducted by Medeiros [60] and Serrano [85], the Pitot tube technique was used with a spatial average of 16 points. The velocities were evaluated for different flow speeds using a centrifugal fan with speed control based on the frequency applied on the motor. The acoustic technique used a pure tone excitation in the presence of grazing flow for the same fan speed in a different measurement campaign. The acoustic technique was first validated with numerical simulations and obtained 0.5% maximum error. The acoustic technique showed a 1.48% average relative difference in relation to Pitot technique, using the latter technique as the reference. The data in Table 3.5 shows the fan rotation frequency in the first column and the Mach velocity calculated in the test section (where the liner is measured) using both of the techniques mentioned above.

In Table 3.5 it is possible to observe that the maximum velocity in the test section for the frequency range of the fan operation is 0.290 Mach using the Pitot tube technique and 0.2928 Mach using acoustic technique. The maximum absolute relative difference between the techniques is 5.82%. In conclusion, both techniques provided similar results with small differences, cross validating both techniques. The Pitot tube technique takes more time to complete and required a dedicated test section with a Pitot tube mounted. The position of such a duct section was substituted later by a lined test section containing the samples to be evaluated. On the other hand, the acoustic technique is practical and fast, offering results with relative little variation compared with the Pitot tube technique. Therefore, the acoustic technique was incorporated into the TPM (Two Port Matrix)

Table 3.5: Comparison of grazing velocity measurement techniques. From: Serrano, 2014 [85].

Frequency [Hz]	Pitot [Mach]	Acoustic [Mach]	Relative difference
5	0.02430	0.02472	1.72%
10	0.0503	0.0503	0.03%
15	0.0760	0.0774	1.87%
20	0.103	0.1043	1.23%
25	0.120	0.1272	5.82%
30	0.150	0.1499	0.14%
35	0.178	0.1752	1.44%
40	0.200	0.1989	0.54%
45	0.221	0.2230	0.90%
50	0.245	0.2455	0.20%
55	0.273	0.2651	2.90%
60	0.290	0.2928	0.95%

impedance eduction technique, which was described in section 2.7.3, in order to obtain impedance results at the UFSC test rig with grazing flow. The pressure drop measured at the convergent nozzle was linearly correlated with to the pitot and acoustic techniques in order to monitor and set the desired grazing flow Mach number on the liner position, as shown on Figure 3.32.

3.2.3 Pure tone excitation with grazing flow

The liner sample used in the experimental campaign is illustrated on the left hand side of the Figure 3.1. Table 3.6 provides the geometrical properties of the liner sample and the instrumented cell. One of the facesheet holes was increased in diameter to introduce a 1.6 mm microphone, for the *in situ* measurement. The microphone with its holder reduced the percentage of open area (POA) to 3.74% and cavity volume to 1447 mm^3. The wall thickness of the honeycomb structure was taken into account to obtain an estimate of the acoustic impact of the facesheet and the backing sheet areas. Only the effects of the honeycomb walls (ε_w) and the cavity volume (ε_m) were corrected, using equation[32],

$$z_c = \frac{z_m}{1 - \varepsilon_w - \varepsilon_m} + i\frac{\varepsilon_m}{tan(kh)}, \tag{3.20}$$

where z_c is the normalized *in situ* corrected impedance; z_m is the normalized *in situ* measured impedance; ε_w is the ratio of half the cross-sectional area of the surrounding cell walls to the area of the liner cell (i.e. the percentage of cell wall blockage); ε_m is the percentage of cavity volume loss due to the presence of the microphone and the holder.

Two different set-ups were used to acquire the data. Figure 3.34 shows the first set-up, and the numbered microphone positions used to educe the impedance by the TPM and MMM methods. The TPM method needs two different flow/propagation combinations to calculate the impedance. Up to eight loudspeakers were positioned upstream and

Table 3.6: Instrumented liner geometric features

Feature	Value
Honeycomb cavity volume $[mm^3]$	1497
3D printed holder volume in the cavity $[mm^3]$	33
Microphone volume in the cavity $[mm^3]$	18
Cavity volume without the holder and the microphone $[mm^3]$	1447
Cavity volume loss due to microphone presence ε_m	3.4%
Area of cavity with walls $[mm^2]$	84
Area of cavity without walls $[mm^2]$	79
Area of walls $[mm^2]$	5.8
Cell wall blockage, ε_w	7.4%
POA *in situ* cell	3.74%
POA liner (Average)	5.18%
Facesheet hole diameter $[mm]$	0.991
Facesheet thickness $[mm]$	0.635
Cell cavity depth $[mm]$	19.050
Number of facesheet holes over the *in situ* cell	4

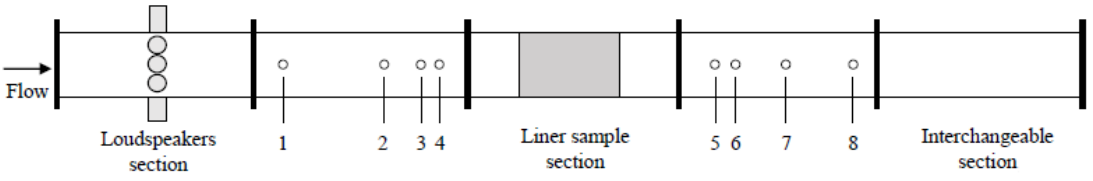

Figure 3.34: Impedance Eduction Setup for TPM and MMM [90].

downstream of the liner sample, in order to acquire adequate measurements for these two conditions. The loudspeakers section and the interchangeable section of Figure 3.34 were placed on the left hand side of the rig, when in the upstream and downstream configurations respectively [11].

The second set-up, illustrated in Figure 3.35, shows the positions of the microphones used to perform the SFM technique, in Figure 3.35.(a), and how the Kulite *in situ* microphones were mounted at the back of the sample, in Figure 3.35.(b). The same test section length and upstream loudspeakers position were used in both the first and second set-ups. More information about the rig construction and grazing flow calibration and measurement can be found in Serrano, 2014[85].

The experiments were conducted using SCAP LR to control the rig [57]. The OASPL at the entrance plane of the microphone array (upstream) was controlled in order to try to obtain the same value of acoustic pressure at each frequency. However, it was not possible to obtain the same OASPL for all frequencies and grazing flow conditions, due to the sound power limitations of the sources and the varying impedance of the sample. The results for low SPLs (below 130 dB) were compared for the impedance eduction and *in situ* techniques described in section 2.7. The *in situ* transfer functions were multiplied

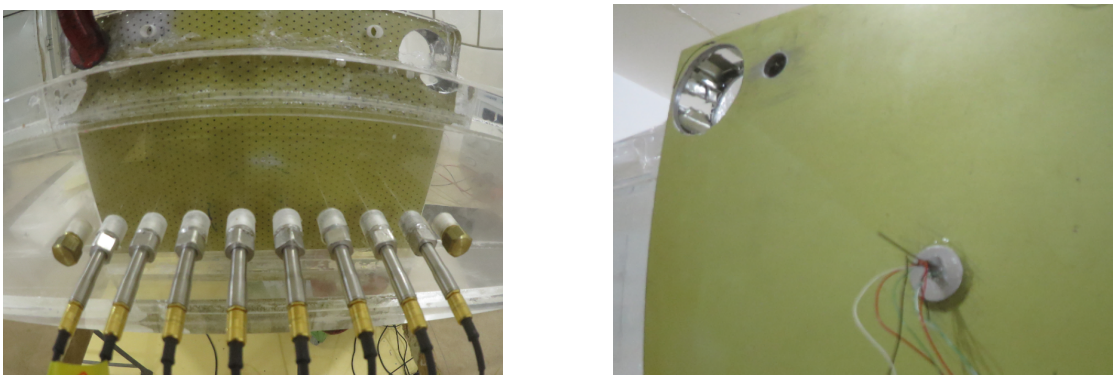

(a) Array of microphones in front of the liner

(b) Kulite microphones mounted at the back

Figure 3.35: *In situ* and SFM setup.

by an amplitude and phase correction factor, in order to compensate for the microphone response at different frequencies[32]. After this calibration, the measured impedance was corrected using Equation 3.20.

Pure tones were used as the source for all of the measurements, using different frequency steps dependent on the experimental method. The impedance was calculated separately at each frequency. A minimum of 120 averages, using RMS linear averaging, were taken using 95% overlapping. A sampling rate of 12800Hz, with a 1 Hz frequency step, was used to acquire the microphone pressures. A flat top window was used to perform the FFT on the acquired signals. The test temperature was 20-25°C and acquired just once per day of measurement, and the atmospheric pressure was 1013 hPa. The appropriate ambient conditions were used to calculate the impedance for each test point.

The rig was implemented in a way that it was not able to search for an SPL target for these measurements. Therefore, the same level of voltage was applied to the drivers for the full set of pure tone frequency steps. The same input voltage leads to differing SPL magnitudes at the microphones for different frequencies. Large variations in impedance are seen at low frequencies, given the low source SPL (low SNR), and the low liner efficiency at these frequencies.

3.2.3.1 *In situ* Results

The results using the *in situ* technique for different grazing flow Mach numbers using the upstream condition (loudspeakers upstream the liner sample) are shown in Figure 3.36. Each point used pure tone excitations with a 250 Hz frequency step. The current rig capacity in terms of fan pressure head and the pressure drop of the rig tube limited the range of the current analysis. The flow was measured using the pressure drop at the nozzle to adjust the flow speed of the fan calibrated for this particular tube configuration with the same tube length as discussed in Section 3.2.2. The values measured were 0.1, 0.15, 0.20 and 0.25 Mach, which are not sufficient to characterize the aircraft take-off

condition. However, the maximum Mach number of 0.25 provides impedances sufficiently close to those seen at the aircraft approach condition.

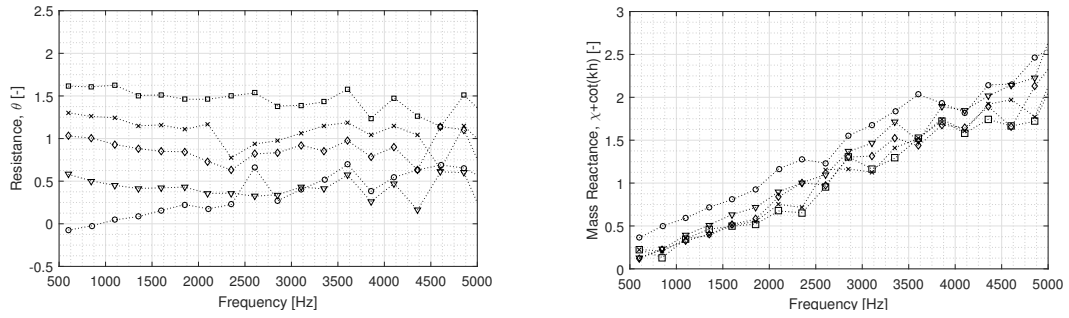

(a) *In situ* Re(ζ) (b) *In situ* Im(ζ)

Figure 3.36: *In situ* liner impedance upstream in the presence of grazing flow at moderate OASPL. Circles ($\circ$) - 0.00 Mach (no flow), Triangles ($\bigtriangledown$) - 0.10 Mach, Diamond ($\diamond$) - 0.15 Mach, X-mark ($\times$) - 0.21 Mach, Square ($\square$) - 0.26 Mach.

It is possible to observe the expected resistance increase, and reactance decrease respectively, for increasing Mach numbers. It is seen that the presence of grazing flow has a large impact on the impedance, which changes from a progressively increasing resistance with frequency without flow to an almost flat variation with frequency with flow. The amount of scatter in the resistance measurements increases with increasing Mach number and frequency. The reactance is expressed in terms of the mass reactance, by excluding the cavity reactance given by $-cot(kh)$ from the total reactance calculated, in order to graphically observe the grazing flow effects. The coherence of the *in situ* microphones in respect to two different signals, the backplate and the input signal sent to the compression drivers, is plotted in Figure 3.37. The coherence of the signals was considered satisfatory, above 0.8, at the microphone positioned on the entrance plane. The coherence between 2.1 and 3.1 kHz is lower than that for other frequencies. This can be explained by the fact that the liner resonant frequency is between 2.2 kHz and 2.6 kHz, causing lower signal to noise ratios (SNR) at these frequencies (lower facing sheet SPL), especially true at higher Mach numbers (higher flow noise). The background noise caused by the boundary layer at higher Mach numbers imposes a limitation on the current test configuration. Consequently, the SPL of the exciting acoustic signal needs to be high enough to avoid noise contamination of the results. The *in situ* impedance data may also not be completely clean of other sources of error, such as rig vibration boundary layer flow noise and the impact of the liner leading edge discontinuity. This effects were explored in other publications [85].

The set of graphs in figure 3.38 contain the rig *in situ* technique tonal results without grazing flow. In order to obtain the same exciting OASPL at the liner leading edge (entrance plane microphone - upstream), an algorithm was used to control the phases and amplitudes of the drivers. It consists of a three trial procedure that measures the OASPL at the entrance plane, which is the first capacitive microphone of the array in

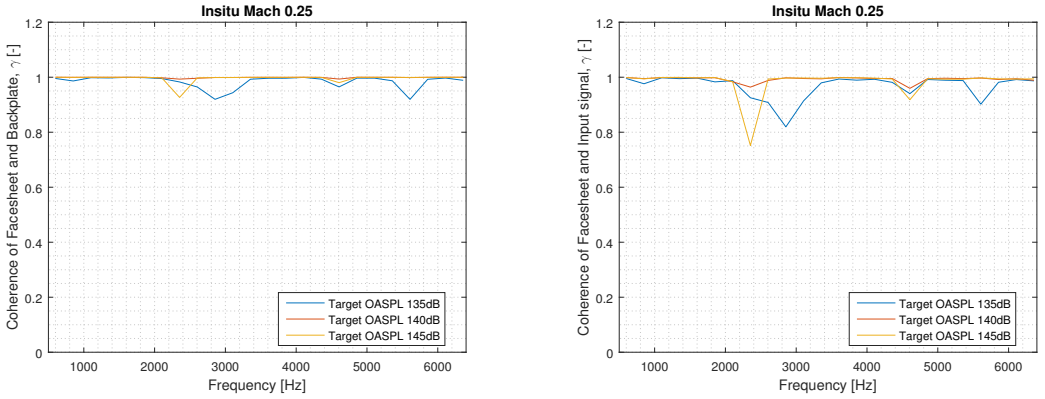

(a) Mach 0.25 - *In situ* microphones

(b) Mach 0.25 - Facesheet *in situ* and input signal

Figure 3.37: Coherence for different OASPL targets.

Figure 3.35.(a). This microphone is the one nearest to the cluster of 8 compression drivers. This acoustic source position is called as upstream configuration, in which the signal of the 8 compression drivers is directed to a section upstream the liner. It is called upstream configuration because the acoustic wave generated by the compression drivers travels in the same direction of the flow until impinges the liner. The upstream configuration reflects the situation seen in an aircraft engine bypass duct.

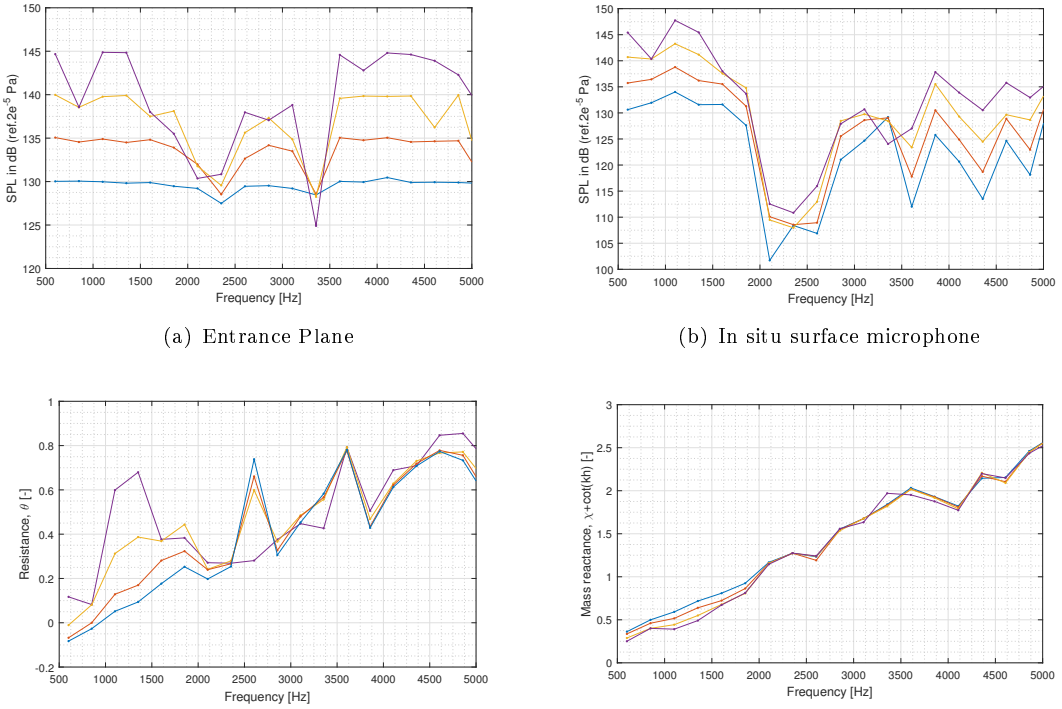

(a) Entrance Plane

(b) In situ surface microphone

(c) In situ Re(ζ)

(d) In situ Im(ζ)

Figure 3.38: *In situ* results without grazing flow using the following SPL targets at the entrance plane: Blue - 130 dB, Red - 135 dB, Yellow - 140 dB, and Purple - 145 dB.

The first two graphs on the top of the Figure 3.38 are the SPLs at the entrance plane on the opposite wall of the liner Figure 3.38.(a), and at the surface of the liner (*in situ* surface microphone) Figure 3.38.(b). It can be seen that the target SPL was not reached for all pure tone excitations, especially between the 1.5 kHz and 3.5 kHz. This range includes the liner resonance frequency, where most of the acoustic energy is dissipated due to the physical mechanisms of non-linear (and linear) dissipation. In other words, the presence of the liner sample causes sound absorption over certain bandwidths, requiring extreme gain amplitudes on the compression drives in order to obtain higher SPLs at the entrance plane. The gain and acoustic power limitations of the compression drivers installed on the rig lead to SPLs not sufficiently high enough to reach the target values specified by the algorithm.

It is noted that a safety limit was set on the root mean square voltage of the drivers to avoid damaging them. As a result of the voltage limit on the compression drivers, the SPL measured on the liner surface was relatively low. It was below the threshold, which is around 130 dB, needed to observe any non-linearities within the liner resonant frequency bandwidth, as can be seen on Figure 3.38.(b). The nonlinear effects can be observed in the range from 0.5-1.5 kHz though. The non-linearities caused by the high SPL excitations can be observed as a change in impedance. Figure 3.38.(c) illustrates the resistance increase, due to an increase in SPL in the range of 0.5-1.5 kHz. On the other hand, the liner reactance decreases, due to an increase in SPL, as shown on Figure 3.38.(d). Non-linear effects cannot be fully evaluated for higher frequencies, from 3.5-5.0 kHz, because the SPL measured at the liner surface is not high enough in order to create vortex rings that are the non-linear mechanism of energy dissipation. At this frequency range and SPL, the air displacement is small. As a consequence, the linear losses, related to the boundary layer on the inner walls of the perforated plate holes, are the main mechanism of dissipation. Concluding, liner impedance can be adequately measured at low SPLs (up to approximately 130 dB), but larger incident SPLs are required in order to induce significant nonlinear losses, especially at the resonant frequency bandwidth. The drivers did not have enough power to generate sufficiently high SPLs for tones above 2.0 kHz at the liner surface, where the *in situ* microphone was located. As a consequence, no progressive change in both resistance and reactance could be obtained above 2.0 kHz among the experiments at the same frequency for different voltage applied to the drivers.

Figure 3.39 shows results with grazing flow, again with the array of drivers located upstream of the liner. The background noise, caused by the grazing flow, contributes to the OASPL measured at the entrance plane. However, the SPL measured at each tonal frequency was not high enough to reach the target OASPL, because the background noise was of the same order of magnitude as the pure tone signal, causing a low SNR, and consequently low fidelity measurements.

Figures 3.39.(a) and (b) show the SPL measured for each tone at the entrance plane, and at the *in situ* surface microphone, respectively. It can be inferred that only linear

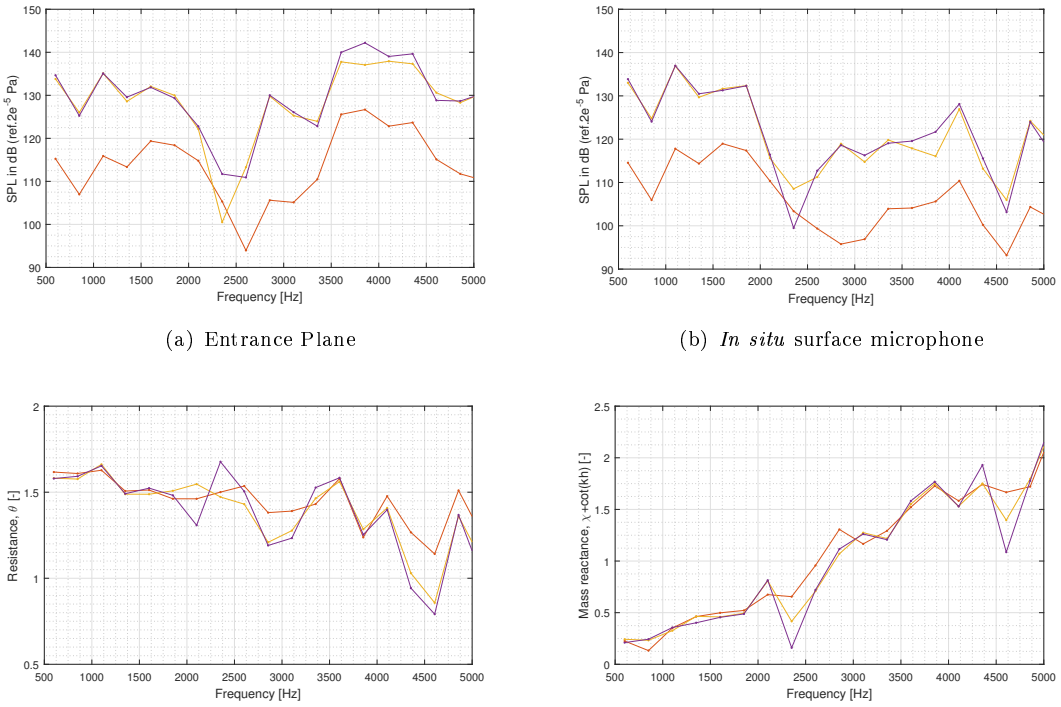

(a) Entrance Plane

(b) *In situ* surface microphone

(c) *In situ* Re(ζ)

(d) *In situ* Im(ζ)

Figure 3.39: Grazing flow 0.25 Mach *in situ* results using the following OASPL targets at the entrance plane: Red - 135 dB, Yellow - 140 dB, and Purple - 145 dB.

regimes of excitation could be attained at the liner surface with the current speaker set-up. Consequently, it was expected that the *in situ* method would return similar impedance results. This can be observed for frequencies from 0.5-1.85 kHz for both the resistance and reactance curves of Figures 3.39.(c) and (d), respectively. The grazing flow data show a fall-off with increasing frequency, consistent with that seen by Murray *et al* [69]. This reflects an increase in effective discharge coefficent with increasing frequency. The variations in impedance seen at higher frequencies are random, due to the generally poor signal to noise ratio at high frequencies.

3.2.3.2 TPM Results

The impedance eduction technique called TPM, described in the Section 2.7.3, was used to extract the experimental data and run the algorithm to calculate the real and imaginary parts of the liner impedance [83]. Due to the SPL limitations of the rig, the excitation level was below 130 dB for all pure tone frequencies measured at the microphones used for this technique. This means that the results correspond to a linear response of the liner. The pure tones were measured independently. Each point in the graphs of Figure 3.40 corresponds to one measurement and one run of the TPM algorithm. Due to the optimization process implemented in the algorithm, some points did not converge.

As a consequence, the result of the impedance values were set to zero, and can be neglected. Figure 3.40 contains the resistance and reactance graphs for differing grazing flow Mach numbers in the test section. An average Mach number was used, considering the upstream and downstream configurations. More details about the set-up and the measurement procedure can be found in the authors' publications [85][61][90][11].

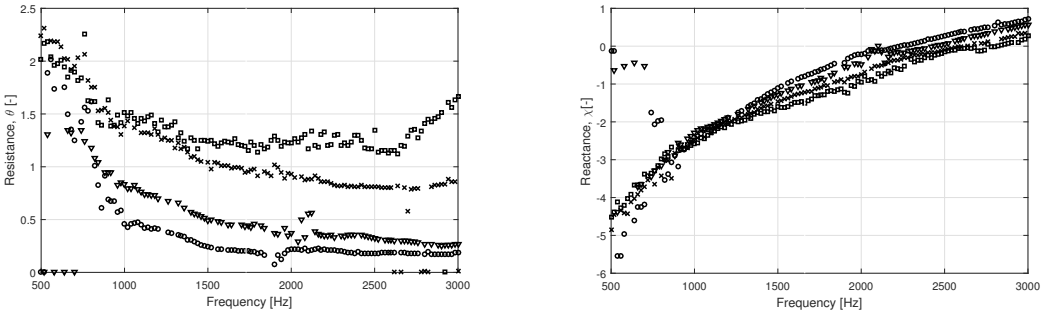

(a) TPM Re(ζ). (b) TRM Im(ζ).

Figure 3.40: Liner impedance calculated using TPM technique, in the presence of grazing flow. Circles ($\circ$) - 0.00 Mach (no flow), Triangles ($\bigtriangledown$) - 0.10 Mach, X-mark ($\times$) - 0.21 Mach, Square ($\square$) - 0.26 Mach.

The main finding from Figure 3.40 is the uncertainty at frequencies lower than 1.0 kHz, which causes oscillations in the impedance results at all Mach numbers. This is mainly caused by the poor SNR due to the power limitation of the drivers used to generate the acoustic field. The liner is also inefficient at low frequencies, further reducing the accuracy of the method because the liner acts as a reflecting surface. There are also some fluctuations at higher Mach numbers for both resistance and reactance, shown in Figure 3.40.(a) and Figure 3.40.(b) respectively.

The maximum frequency was limited to 3 kHz, in order to avoid the presence of high order modes in the duct. These high order modes could cause undesirable results using this method, as it considers only plane wave propagation. The microphones are positioned on a nodal point of the first transversal mode, thereby allowing the extension of the analysis from the cut-off frequency of 1.6 kHz to 3.0 kHz. However, this extended region needs be evaluated carefully. Some oscillations occur around 2.0 kHz, and can be seen on the circles and triangles of the Figure 3.40.(a) and (b), probably because of cut-on of the first transversal mode of the rig duct. As mentioned before TPM works well only with the plane wave mode not capturing the effect of high order modes. Although, this was reported by other authors [83], the general trends with frequency and Mach number are good. It is possible to observe the expected increase of resistance, and decrease of reactance, as a consequence of an increase in Mach number, again consistent with the trends measured by Murray *et al* [69].

3.2.3.3 MMM Results

The MMM techique is summarized in the Section 2.7.4 and was used to educe perforated liner impedance in the grazing flow test rig. As seen with the TPM results, the MMM results exhibit dispersion at frequencies lower than 1.0 kHz for both resistance and reactance, was shown in Figures 3.41.(a) and (b) respectively. As before, the resistance increases, and the reactance decreases, as the Mach number increases. However, the no flow resistance shows trends which are inconsistent with the other eduction, in-situ and flanged impedance tube measurements.

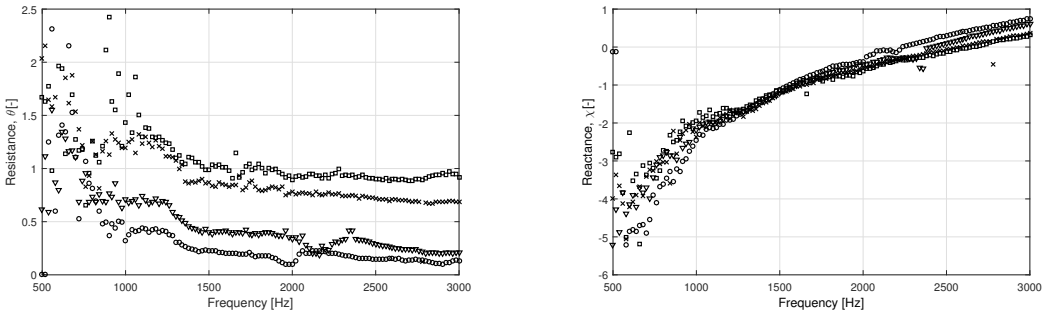

(a) MMM Re(ζ). (b) MMM Im(ζ).

Figure 3.41: Liner impedance calculated using MMM technique, in the presence of grazing flow with the acoustic source upstream the liner. Circles ($\circ$) - 0.00 Mach (no flow), Triangles ($\bigtriangledown$) - 0.10 Mach, X-mark ($\times$) - 0.21 Mach, Square ($\square$) - 0.26 Mach.

The background noise level at the highest Mach number is around 93-95 dB throughout the test section. As a consequence, if the liner attenuation is higher than a certain value at a certain frequency, the acoustic excitation is not sufficient to capture the true attenuation without background noise. This happens because the liner attenuation is higher than the difference between the acoustic excitation and the background noise. This leads to a poor SNR and uncertainties in the impedance results. This problem is present for the eduction techniques, because the microphones are located away from the sample and exposed to the boundary layer noise. This problem was minimized in the second version of the rig, reducing in up to 5 dB the background noise using specially designed microphone couplers to recess the microphones, which were flush mounted, including a grid in front of the membrane as shown by Spillere [90].

3.2.3.4 SFM Results

The SFM technique, described in the Section 2.7.5, was used in two experiments that were performed at different times. Both pure tones were measured in 20 Hz frequency steps using a fixed voltage applied to one driver. Four Mach numbers were measured in order to test the repeatability of the test rig. In addition, the second experiment used

the SPL control algorithm that will be explained in the Section 5.2, which calculates the pressure magnitude of the wave on a given microphone position and adjusts the input power of the noise source to reach a specific desired level.

The results for both experiments are shown in Figure 3.42, in order to compare the uncertainties of this procedure in the UFSC test rig. The SFM code, similar to the case with the other impedance eduction techniques, showed difficulty in converging at lower frequencies. Hence, the plots include only the frequency range between 1.0-3.0kHz. Better results were obtained at high Mach numbers, during the 2^{nd} experiment, in comparison with the first experiment for high frequencies. However, higher resistances were measured at low frequencies for the 2^{nd} experiment in Figure 3.42.(c), in comparison with the first experiment in Figure 3.42.(a) too. More dispersion on the second experiment can also be observed on the reactance results in Figure 3.42.(d) possibly because of temperature changes not accounted on the impedance calculations, or calibration issues.

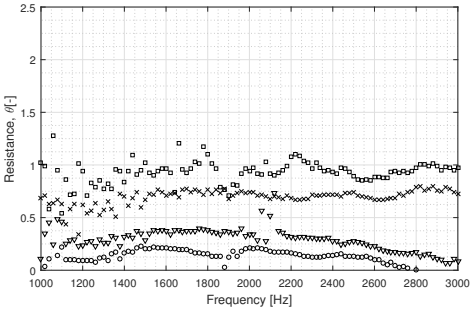

(a) SFM Re(ζ) - 1^{st} Experiment.

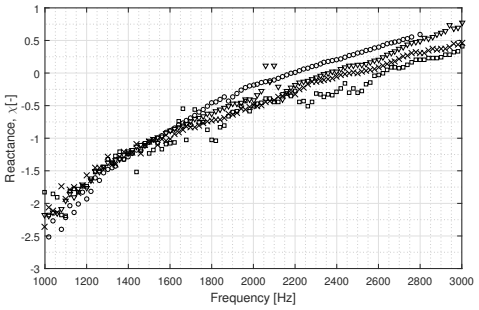

(b) SFM Im(ζ) - 1^{st} Experiment.

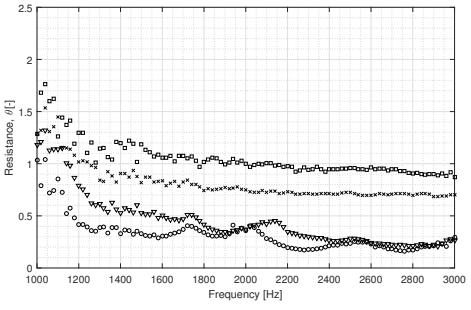

(c) SFM Re(ζ) - 2^{nd} Experiment.

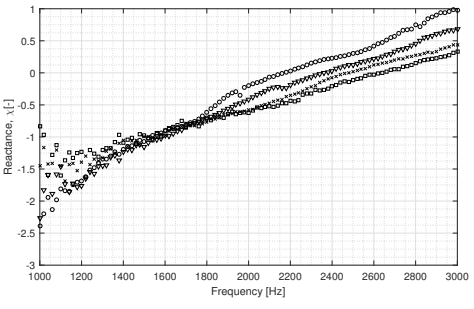

(d) SFM Im(ζ) - 2^{nd} Experiment.

Figure 3.42: Liner impedance calculated using SFM technique, in the presence of grazing flow with the acoustic source upstream the liner. Circles ($\circ$) - 0.00 Mach (no flow), Triangles ($\bigtriangledown$) - 0.10 Mach, X-mark ($\times$) - 0.21 Mach, Square ($\square$) - 0.26 Mach.

Despite the fact that it is difficult to obtain the same SPL on the liner resonant frequency bandwidth, the target SPL was in the linear regime of excitation for both experiments. In conclusion, there is reasonable agreement between experiments for both resistance and reactance, as observed in Figures 3.42. It is possible to identify the resonant frequency of the liner on the graphs shown at the Figure 3.42.(b) and (d), when the reactance values

reach zero. Both experiments shown similar resonant frequencies on 2.2 kHz, 2.4 kHz, 2.5 kHz and 2.6 kHz for 0.00, 0.10, 0.20 and 0.25 Mach numbers respectively. Notice that the Figure 3.42.(d) contains a point measured just above the cut-off frequency of the duct (1600 Hz), resulting in uncertainties. This cut-off frequency corresponds to the first transversal mode of the larger dimension (100 mm) and is dependent on the grazing flow Mach number. The SFM and the TPM both consider only a plane wave propagation, consequently, uncertainties are expected above the cut-off frequency because the energy of higher modes are not taken into a count on the impedance eduction technique algorithms.

3.2.3.5 Analysis and Conclusions

In conclusion, the impedance results show generally good agreement for all the different procedures, particularly between the frequency range of 1.4 kHz to 3.0 kHz. The dispersion in this frequency range may be due to variations in the effective Mach number used for each procedure. Below 1.4 kHz, the absorption of the liner sample reduces, leading to greater uncertainties in the the results from the eduction procedures, which rely on the liner attenuation. The *in situ* results also show increasing uncertainty with reducing liner absorption.

If only the liner resistance is required, a deeper cell depth is expected to increase the accuracy of the low frequency results. An increased number of averages may reduce the statistical uncertainty. The poor SNR is caused by relative low realisable SPL from drivers, vibration of the test section, and high background noise by the grazing flow at high Mach numbers [85].

The POA of the instrumented cell was chosen in order to be similar to the average POA of the liner sample. However corrections were needed for the *in situ* method to account for the change in the local effective POA, in order to compare the results with the impedance eduction techniques. Instrumentation of additional cells, without changing the effective POA, will provide more data and assess the differences of impedance along the liner sample, particularly at high incident SPLs, at frequencies were the liner is absorbing efficiently. It could be useful to compare the SPL decay along the instrumented cells and compare these levels with those on the opposite hard wall of the duct. Eversman,[29] investigated the impact of SPL variation along a liner, suggesting that the liner is generally designed to an SPL higher than it is actually exposed. Consequently, the impedance predictions should take into account the decay of the SPL along the liner sample.

The comparisons provided confidence intervals for the use of these procedures to develop semi-empirical models or to validate numerical methods to predict liner impedance. Normal incidence impedance measurements using an impedance tube can be used to compare the no flow results from the eduction techniques. The *in situ* and two microphone methods can be used simultaneously during the impedance tube measurements. These back

to back comparison using both the impedance tube and rig may be useful to check the effect of microphone installation, sound leakage on the instrumented cell, and the effect of the local POA on the impedance. The results can be useful for comparing the local cell impedance with the liner panel average impedance.

An analysis could be performed to assess the individual sensitivity of each method to the liner impedance (attenuation), and provide guidelines for the most efficient liner test geometries (cell depths). Finally, the extension of the test procedures to high frequencies, higher Mach numbers, and higher SPLs is recommended, along with the use of varying boundary layer profiles, to allow investigation of the full liner design space.

Eventually, multidimensional numerical models can be validated using the experimental results presented, leading to flow visualisation and the possibility of examining other liner geometric designs or impedance models for multiple tone excitations.

Chapter 4

Numerical implementations of 1D semi-empirical models

This chapter includes the numerical implementation of both Rice and Cummings models, their validation via comparison to analytical solutions and impedance predictions for the liners measured in the previous chapters. The chapter also includes a description of a proposed model based on Cummings and Bodén model with frequency dependent discharge coefficient that better agrees with Maa's reactance results and grazing flow term based on Rice and Murray models.

4.1 Rice numerical implementation

Equations 2.48 and 2.49 were solved by using the Runge-Kutta numerical method, implemented in an ODE45 solver of MATLAB [13]. The frequency domain values for impedance were obtained by using Rice's decomposition of the signal into sine waves which can be treated as components of a Fourier series [78]. The subscript n denotes that the value is taken on the n^{th} frequency, so the normalized impedance was given by

$$\zeta_n = \theta_n + i\chi_n, \tag{4.1}$$

$$\zeta_n = \frac{P_n}{\sigma\rho c U_n}\cos\left(\gamma_n - \phi_n\right) + \frac{P_n}{\sigma\rho c U_n}\sin\left(\gamma_n - \phi_n\right), \tag{4.2}$$

where P_n is the pressure amplitude of the incident wave, U_n is the amplitude of the particle velocity inside the orifice, $\gamma_n - \phi_n$ is the phase between the pressure and particle velocity.

The particle velocity U_n is defined as

$$U_n = \sqrt{S_n^2 + C_n^2}, \tag{4.3}$$

where S_n and C_n are Fourier coefficients that can be approximated as

$$S_n = \frac{2\int_{t_1}^{t_2} v_0(t)\cos(\omega_n t)dt}{t_2 - t_1}, \tag{4.4}$$

$$C_n = \frac{2\int_{t_1}^{t_2} v_0(t)\sin(\omega_n t)dt}{t_2 - t_1}. \tag{4.5}$$

The solution of the ODE45 solver is a numerical array of particle velocities, v_0, were obtained from the resolution of the Equations 2.48 or 2.49 for a given time interval. Then, v_0 was used on Equations 4.4 and 4.5 to find the Fourier coefficients S_n and C_n. The complex value of the particle velocity in the frequency domain V_n, calculated by using Equation 4.3, can be used in Equation 4.2 with the input pressure, in order to calculate the numerical value of impedance at a certain frequency. In section 4.1.1 this numerical implementation will be compared to an analytical solution that includes only linear resistance terms, for input signals with low SPL.

4.1.1 Linear analytic solution for pure tone excitation

The models of both Rice and Cummings models can be solved analytically for low SPL, which means that nonlinear terms were kept off the solution. Incident pressure can be described as a sum of sine and cosine waves and can be represented by $P(t) = \mathbf{P}e^{i\omega t}$, where $\mathbf{P} = \mathbf{P}(\omega)$ is the frequency dependent pressure amplitude. Consequently, the particle displacement at the surface of the material may be represented as $x_0(t) = \mathbf{X}e^{i\omega t}$, where $\mathbf{X} = \mathbf{X}(\omega)$ is the frequency dependent displacement amplitude. The time derivatives of the particle displacement are then given by

$$\begin{aligned} x_0 &= \mathbf{X}e^{i\omega t}, \\ \frac{dx_0}{dt} &= i\omega\mathbf{X}e^{i\omega t}, \\ \frac{d^2x_0}{dt^2} &= -\omega^2\mathbf{X}e^{i\omega t}. \end{aligned} \tag{4.6}$$

Substitution of Equation 4.6 into Equation 2.46 gives,

$$\left(-\omega^2\rho L + i\omega R + \frac{\rho c^2\sigma}{h}\right)\mathbf{X}e^{i\omega t} = \mathbf{P}e^{i\omega t}, \tag{4.7}$$

$$\mathbf{X} = \frac{\mathbf{P}}{\left(-\omega^2\rho L + i\omega R + \frac{\rho c^2\sigma}{h}\right)}. \tag{4.8}$$

We may write,

$$\mathbf{X}(\omega) = \mathbf{H}(\omega)\mathbf{P}(\omega), \tag{4.9}$$

where $\mathbf{H}(\omega)$ is the transfer function of the system, represented by the liner. The velocity of the system is the derivative of the displacement, and it is defined as,

$$\mathbf{V}(\omega) = i\omega\mathbf{H}(\omega)\mathbf{P}(\omega). \tag{4.10}$$

Finally, the analytical solution for the impedance of this system in the frequency domain is given by,

$$\mathbf{Z}(\omega) = \frac{\mathbf{P}(\omega)}{\mathbf{V}(\omega)} = \frac{\mathbf{P}(\omega)}{i\omega\mathbf{H}(\omega)\mathbf{P}(\omega)} = \frac{1}{i\omega\mathbf{H}(\omega)}, \tag{4.11}$$

$$\mathbf{Z}(\omega) = \frac{\left(-\omega^2\rho L + i\omega R + \dfrac{\rho c^2\sigma}{h}\right)}{i\omega} = R + i\left(\omega\rho L - \frac{\rho c^2\sigma}{h\omega}\right). \tag{4.12}$$

Although this solution is valid for a single resonator only, the liner impedance solution (considering the liner as an array of resonators which do not interact in terms of inertance) can be calculated by dividing $Z(w)$ by the porosity of the liner, σ, or POA_{eff} if available. Observe that the resistance R is not dependent on the velocity if only linear damping terms are considered. Also, observe that the reactance can be split into the mass reactance term $\omega\rho L$ and the cavity reactance term $\frac{\rho c^2\sigma}{h\omega}$. Equation 4.12 is a steady state frequency domain description of a resonator that is the base for all the semi-empirical models.

Alternatively, solving the problem directly in the time domain requires finding the homogeneous and particular solutions of the Equations 2.46, considering harmonic pressure input. The solution of the particle displacement in the hole is given by,

$$x_0(t) = x_h(t) + x_p(t) \tag{4.13}$$

where $x_h(t)$ is the homogeneous solution and $x_p(t)$ is the particular solution. To find $x_h(t)$ Equation 2.46 needs to be equal to zero to give the ODE,

$$\rho L\frac{d^2x_h}{dt^2} + R\frac{dx_h}{dt} + \frac{\rho c^2\sigma}{h}x_h = 0. \tag{4.14}$$

Changing the variables to

$$\frac{d^2x_h}{dt^2} = \lambda^2 x_h, \tag{4.15}$$

$$\frac{dx_h}{dt} = \lambda x_h, \tag{4.16}$$

it gives the characteristic equation

$$\rho L\lambda^2 + R\lambda + \frac{\rho c^2\sigma}{h} = 0. \tag{4.17}$$

Solving the polynomial equation two complex roots are obtained

$$\lambda_1 = \alpha + i\omega_0, \tag{4.18}$$

$$\lambda_2 = \alpha - i\omega_0, \tag{4.19}$$

where

$$\alpha = -\frac{R}{2\rho L}, \tag{4.20}$$

$$\omega_0 = \frac{\sqrt{|R^2 - \frac{4\rho^2 c^2 L\sigma}{h}|}}{2\rho L}. \tag{4.21}$$

The possible values for ω_0 are complex roots, so the homogeneous solution is an exponential function multiplied by the summation of sine and cosine waves with the undamped resonant frequency ω_0 as the argument

$$x_h(t) = e^{\alpha t}\left(C_1 \sin(\omega_0 t) + C_2 \cos(\omega_0 t)\right). \tag{4.22}$$

The particular solution x_p takes the form of the forcing function, P, which is sinusoidal

$$P(t) = A\sin(\omega t), \;\; for \; t > 0. \tag{4.23}$$

Hence $x_p(t)$ is a summation of sine and cosines

$$x_p(t) = C_3 \sin(\omega t) + C_4 \cos(\omega t). \tag{4.24}$$

Substituting the particular solution Equation 4.24 for x_0 in Equation 2.46 gives,

$$\begin{aligned}\rho L\left(-\omega^2 C_3 \sin(\omega t) - \omega^2 C_4 \cos(\omega t)\right) + R\left(\omega C_3 \cos(\omega t) - \omega C_4 \sin(\omega t)\right) + \\ + \frac{\rho c^2 \sigma}{h}\left(C_3 \sin(\omega t) + C_4 \cos(\omega t)\right) = A\sin(\omega t).\end{aligned} \tag{4.25}$$

Equating coefficients of sine and cossine terms leads to a linear system of equations which can be solved for C_3 and C_4. This leads to

$$C_3 = \frac{P}{-\rho L\omega^2 + \frac{R_0^2\omega^2}{\frac{\rho c^2\sigma}{h} - \rho L\omega^2} + \frac{\rho c^2\sigma}{h}}, \tag{4.26}$$

$$C_4 = \frac{-R_0\omega C_3}{\frac{\rho c^2\sigma}{h} - \rho L\omega^2}. \tag{4.27}$$

Finally, the solution for particle displacement in the orifice is given by

$$x_0(t) = e^{\alpha t}\left(C_1 \sin(\omega_0 t) + C_2 \cos(\omega_0 t)\right) + C_3 \sin(\omega t) + C_4 \cos(\omega t). \tag{4.28}$$

Particle velocity in the orifice is the first derivative of the particle displacement, given by

$$x_0'(t) = \alpha e^{\alpha t}\left(C_1 \sin(\omega_0 t) + C_2 \cos(\omega_0 t)\right) + \omega C_3 \cos(\omega t) - \omega C_4 \sin(\omega t) + \\ + e^{\alpha t}\left(C_1 \omega_0 \cos(\omega_0 t) - C_2 \omega_0 \sin(\omega_0 t)\right). \tag{4.29}$$

Applying the initial conditions that $x_0(0) = 0$ and $x_0'(0) = 0$, the coefficients C_1 and C_2 can be found,

$$C_1 = \frac{\alpha C_4 - \omega C_3}{\omega_0}, \tag{4.30}$$

$$C_2 = -C_4, \tag{4.31}$$

so the linear velocity response of the orifice can be analysed analytically in the time domain for a single tone excitation by using Equation 4.29.

The displacement and velocity time responses were calculated as a function of the incident pure tone SPL for a reference liner of a 5.2% perforate, with 0.991 mm diameter orifices, 0.635 mm face sheet thickness and 19.05 mm cavity depth. More data about the sample is available in Table 3.1 and it is illustrated on the left hand side of Figure 3.1. Figures 4.1 and 4.2 illustrate the time response of the Rice model to a pure tones with the analytical solution in blue and numerical solution in red. For excitations below approximately 100 dB, as in Figure 4.1, the numerical solution shows excellent agreement with the analytical solution, validating the numerical implementation in the linear regime of excitation.

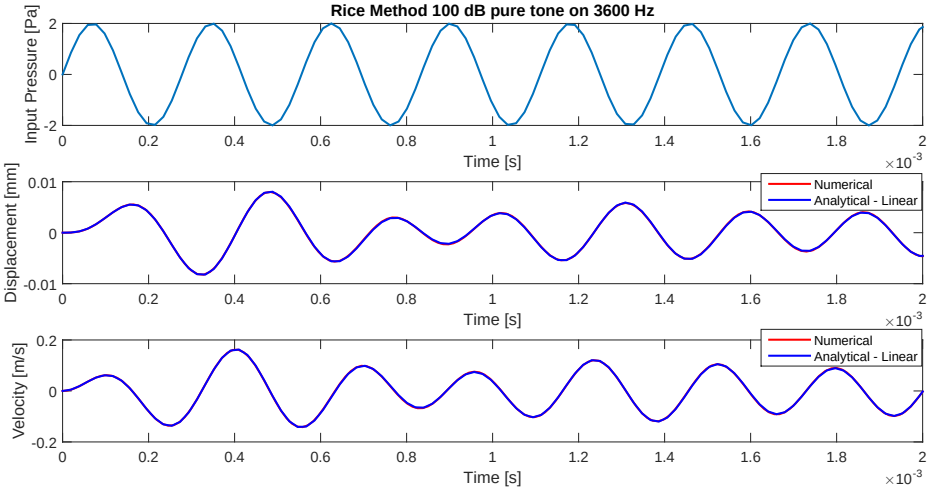

Figure 4.1: Rice model time domain solutions for a SDOF liner for pure tone of 3600 Hz at 100 dB OASPL. Analytical solutions in blue and numerical solutions in red.

On the other hand, the second term on the right hand side (nonlinear) of Equation 2.48 becomes more significant as larger pressure amplitudes excite the liner. As a consequence, there is a significant difference between the analytical response curves considering just

the linear terms and the numerical response curves in Figure 4.2. It is then, possible to observe the distortion in the numerical velocity response obtain by the numerical solution for 150 dB, as well as the difference in amplitude and phase caused by the nonlinear term modelled.

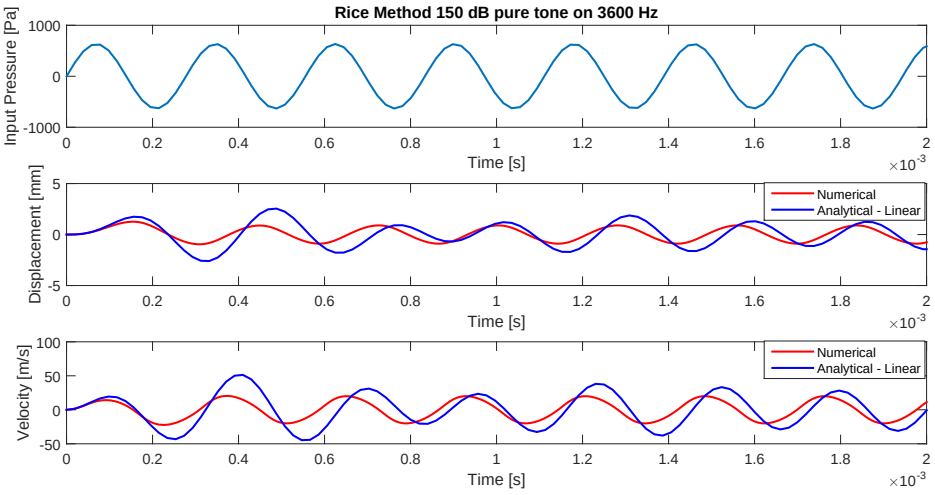

Figure 4.2: Rice model time domain solutions for a SDOF liner for pure tone of 3600 Hz at 150 dB OASPL. Analytical solutions in blue and numerical solutions by using nonlinear terms in red.

Figure 4.3 illustrates the effect of non-linearity on the numerical liner resistance calculated. For excitations below 100 dB the non-linear effect is minimal. For high excitation levels the resistance increases near the resonant frequency and becomes broader as the SPL increases. The resistance values shown in Figure 4.3 are the frequency domain results, after applying the FFT. The orifice resistance was divided by the porosity of the liner and normalized by the air impedance, so if the normalized resistance is 1, it means that the air and the liner surface have the same value of resistance.

Ideally, the incident pressure level and grazing flow velocity are known, for a specific engine operating condition, in order to design a liner, or during a measurement campaign in laboratory. However, the attenuation of the sound wave by the liner means that the incident pressure varies along the length of the liner. Consequently, impedance changes along the liner length. Possibly liner geometry should be modified or adaptive along its length for optimum attenuation.

Observe that only linear terms contribute to the reactance of the system in the Rice model. This means that the reactance values will be the same for all the SPLs simulated. Figure 4.4 shows the analytical solution for linear terms compared with simulated values, which are in perfectly agreement.

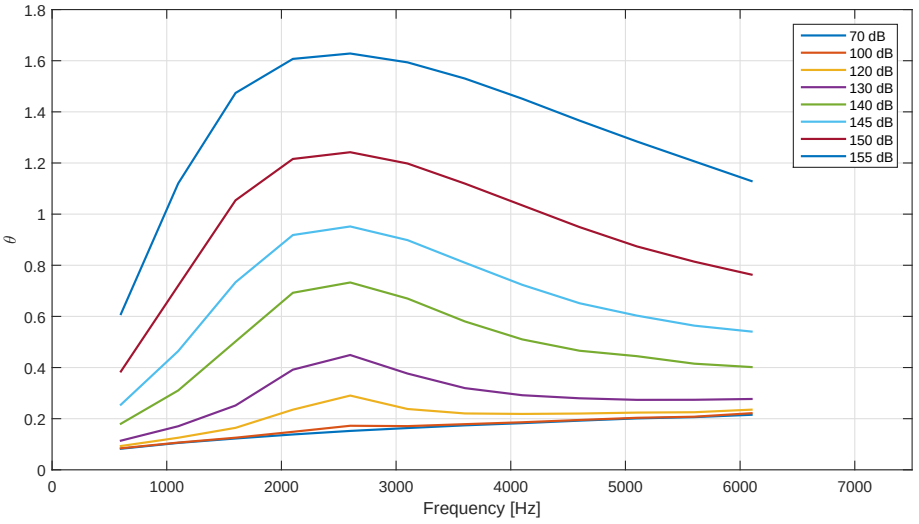

Figure 4.3: Numerical liner resistance simulation by using Rice model for pure tone excitation from 70 dB until 155 dB.

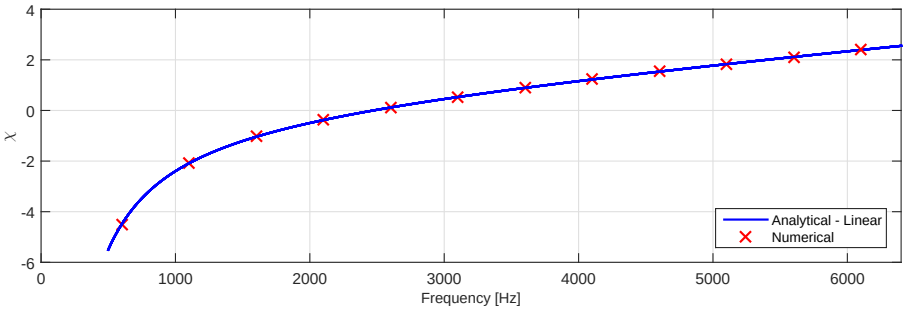

Figure 4.4: Liner reactance simulation by using Rice model for pure tone excitation.

4.1.2 Linear analytic solution for multiple tone excitation

The same principles applied to the pure tone can be used to model multiple tones by using the Rice model. The procedure is the same in order to solve Equation 2.46 considering two deterministic tones as the excitation signal and including the linear resistance terms: solve for the homogeneous solution, which is the same as for the single tone, and solve for the particular solution. Now the excitation is assumed to be a sum of two sine waves, which can be rewritten in exponential terms as

$$A\sin(\omega_1 t) + B\sin(\omega_2 t) = \frac{A}{2i}\left(e^{i\omega_1 t} - e^{-i\omega_1 t}\right) + \frac{B}{2i}\left(e^{i\omega_2 t} - e^{-i\omega_2 t}\right), \tag{4.32}$$

where A and B are the amplitudes of the tones; ω_1 and ω_2 are the angular frequencies of the tones in different frequencies; and t is the time variable.

Equations 4.22 and 4.21 give the homogeneous solution and the undamped resonant frequency. The particular solution, $x_p(t)$, could be reasonably assumed as a sum of exponentials. The $x_p(t)$ and its derivatives are

$$x_p(t) = C_3 e^{i\omega_1 t} + C_4 e^{i\omega_2 t} + C_5 e^{-i\omega_1 t} + C_6 e^{-i\omega_2 t}, \tag{4.33}$$

$$x_p'(t) = iC_3\omega_1 e^{i\omega_1 t} + iC_4\omega_2 e^{i\omega_2 t} - iC_5\omega_1 e^{-i\omega_1 t} - iC_6\omega_2 e^{-i\omega_2 t}, \tag{4.34}$$

$$x_p''(t) = -C_3\omega_1^2 e^{i\omega_1 t} - C_4\omega_2^2 e^{i\omega_2 t} - C_5\omega_1^2 e^{-i\omega_1 t} - C_6\omega_2^2 e^{-i\omega_2 t}. \tag{4.35}$$

Substituting Equations 4.33 to 4.35 into the left hand side of Equation 2.46 and Equation 4.32 into the right hand side, in the place of P; it is then possible to equate the coefficients of each exponential on both sides of the equation to calculate C_3, C_4, C_5 and C_6 as functions of A and B.

$$C_3 = \frac{A}{2i\left(-\rho L\omega_1^2 + iR_0\omega_1 + \frac{\rho c^2\sigma}{h}\right)}, \tag{4.36}$$

$$C_4 = \frac{-A}{2i\left(-\rho L\omega_1^2 - iR_0\omega_1 + \frac{\rho c^2\sigma}{h}\right)}, \tag{4.37}$$

$$C_5 = \frac{B}{2i\left(-\rho L\omega_2^2 + iR_0\omega_2 + \frac{\rho c^2\sigma}{h}\right)}, \tag{4.38}$$

$$C_6 = \frac{-B}{2i\left(-\rho L\omega_2^2 - R_0\omega_2 + \frac{\rho c^2\sigma}{h}\right)}. \tag{4.39}$$

The displacement and velocity responses in the orifice then become,

$$\begin{aligned} x_0(t) = {} & e^{\alpha t}\left(C_1\sin(\omega_0 t) + C_2\cos(\omega_0 t)\right) + \\ & + C_3 e^{i\omega_1 t} + C_4 e^{i\omega_2 t} + C_5 e^{-i\omega_1 t} + C_6 e^{-i\omega_2 t}, \end{aligned} \tag{4.40}$$

$$\begin{aligned} x_0'(t) = {} & \alpha e^{\alpha t}\left(C_1\sin(\omega_0 t) + C_2\cos(\omega_0 t)\right) + iC_3\omega_1 e^{i\omega_1 t} + iC_4\omega_2 e^{i\omega_2 t} - \\ & - iC_5\omega_1 e^{-i\omega_1 t} - iC_6\omega_2 e^{-i\omega_2 t} + e^{\alpha t}\left(C_1\omega_0\cos(\omega_0 t) - C_2\omega_0\sin(\omega_0 t)\right). \end{aligned} \tag{4.41}$$

Finally, the initial conditions can be applied to Equations 4.40 and 4.41, by using $x_0(0) = 0$ and $x_0'(0) = 0$, which then provides the values of the constants C_1 and C_2 as

$$C_1 = -C_3 - C_4 - C_5 - C_6, \tag{4.42}$$

$$C_2 = \frac{i(\omega_1 C_5 + \omega_2 C_6 - \omega_1 C_3 - \omega_2 C_4) - \alpha C_1}{\omega_0}. \tag{4.43}$$

The same methodology may be used for a combination of more than two tones. However the analytical solution is valid only for linear damping terms. In other words, the analytical response for linear regime is available only for low SPLs (approximately below 100 dB).

The analytical and numerical solutions agree for relatively low SPL, as shown on Figure 4.5.

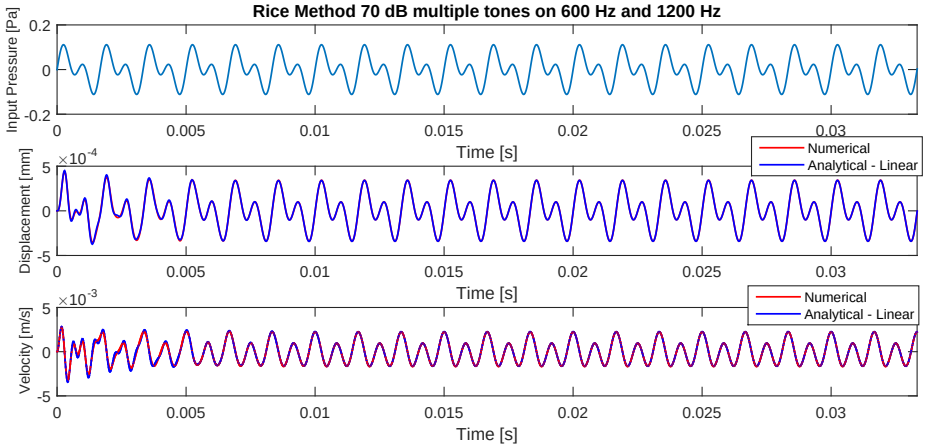

Figure 4.5: Time domain simulation of Rice model excited by two tones at 600 Hz and 1200 Hz having the same amplitude of 70 dB.

Figure 4.6 illustrates the solution for two tones together at 600Hz and 1200 Hz having the same amplitude of 140 dB each. The mathematical expressions in the analytical solution are very complex, so a numerical approach is needed, which is computationally fast and robust and can deal with non-linear terms. The numerical and the analytical results diverge significantly for both displacement and velocity, but it was expected that non-linear interactions could cause lower displacement and lower particle velocities, especially at the resonant frequency of the liner as just the linear terms were used on the analytical expression. Results suggest that non-linearities are dominant at this OASPL.

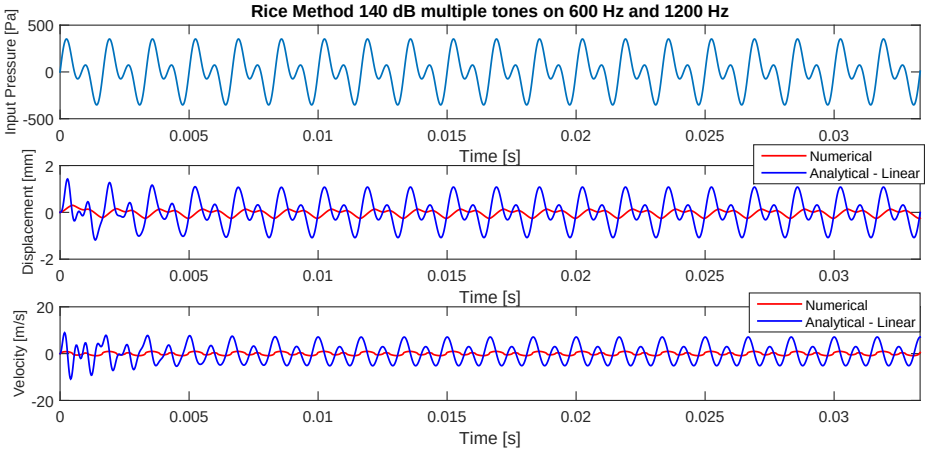

Figure 4.6: Rice model results by using two tones at 600 Hz and 1200 Hz having the same amplitude of 140 dB.

4.2 Cummings numerical implementation

The numerical method used to solve the Equation 2.57 has been implemented in MATLAB. The geometric features of the liner sample used are in Table 3.1 and are the same values used to validate Rice's numerical model. The discharge coefficient used was $C_D = 0.76$, based on Cummings, and the ϵ_r was calculated by using Equation 2.56. The code was written following the steps below:

1. An error control variable was established in order to evaluate the convergence of the plate effective thickness (physical thickness plus end correction) over the iteration process $E = \frac{|\epsilon(i)-\epsilon(i-1)|}{\epsilon(i)}$, where i is the iteration number;
2. The convergence criteria was chosen to find a fast solution with a low associated numerical error and few iterations (a 2% relative error required just 2 iterations and resulted in minor differences in the calculated impedance values);
3. Initial conditions of zero displacement, zero velocity and Rice's first estimate for the end correction (from Equation 2.35) were assumed;
4. The constants were defined: geometry of the liner, air temperature, atmospheric pressure, sound speed, time span for the solution, frequency range, and SPL.
5. Equation 2.57 was solved by using MATLAB's ODE45 differential equation solver;
6. The transient response for three to five cycles was rejected and a random half-cycle on the permanent solution was searched by incrementing the vector of time until the last value changed sign;
7. The first two and the last two points of the solution velocity vector were interpolated in order to have the exact values for the half-cycle integration;
8. The integral for the coefficient L_1 was performed on the selected half-cycle;
9. The end correction and effective thickness of this iteration was calculated;
10. The next period of jet formation was identified and the steps 5 to 9 were repeated, by using the new value of the end correction calculated as input to solve the ODE. The error control variable was monitored until the convergence criteria was reached.

Each iteration used a smaller time step because it was assumed that a better time-domain discretization would produce a reduced variation on the calculated end correction, converging the solution. The number of samples determine the computational effort, but it need to be sufficient to produce a steady state solution.

An analysis of the behaviour of some parameters (e.g. effective thickness) as a function of the inverse Strouhal number, defined in Equation 2.25, can be done as shown in

Figure 4.7. The simulated plate effective thickness reduces linearly with $1/St$ when different pure tones, one at time from 600 Hz to 2100 Hz, excite the liner at high levels from 130 to 155 dB. The effect of multiple tones and grazing flow may potentially change this behaviour.

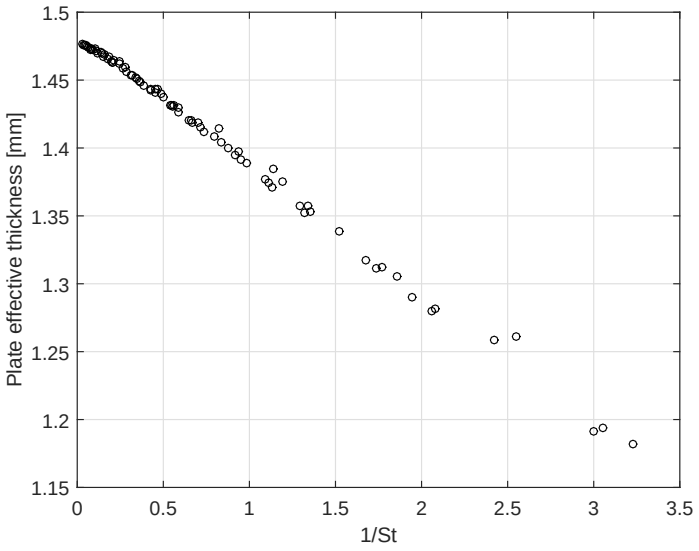

Figure 4.7: Numerical results of Cummings model for effective thickness correlated with 1/St.

Figure 4.8 shows the normalized resistance as a linear function of peak orifice velocity for simulated data by using the Cummings model. Each point on the graph corresponds to a different frequency in the range of 600-3000 Hz. The slope characterizes the non-linear behaviour of the typical liner simulated. Each curve corresponds to an SPL and shows a maximum resistance for the resonant frequency of the liner, where maximum orifice velocity is observed too.

Reactance values were simulated by using the Cummings model and are illustrated in Figure 4.9. The reactance is zero at the resonant frequency, at which the higher velocity is observed.

4.3 Proposal for an improved 1D impedance model

Based on the Cummings model and Boden's end correction of Equation 2.56, it is hypothesised that the discharge coefficient was mainly responsible for the lack of agreement between the existing models, because it is frequency dependent and proportional to the end correction, and consequently the velocity, as the SPL increases. An improved end correction is proposed by using the expression,

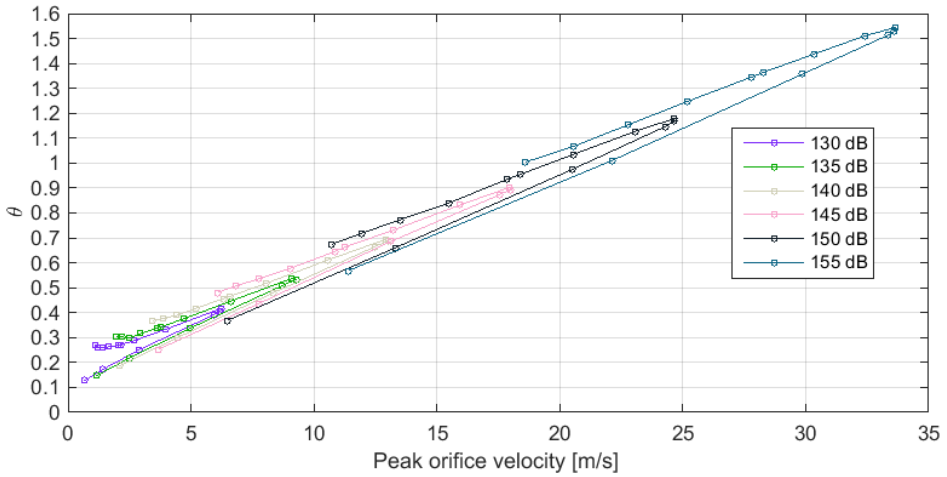

Figure 4.8: Normalized resistance over peak orifice velocity to various SPLs by using the Cummings model.

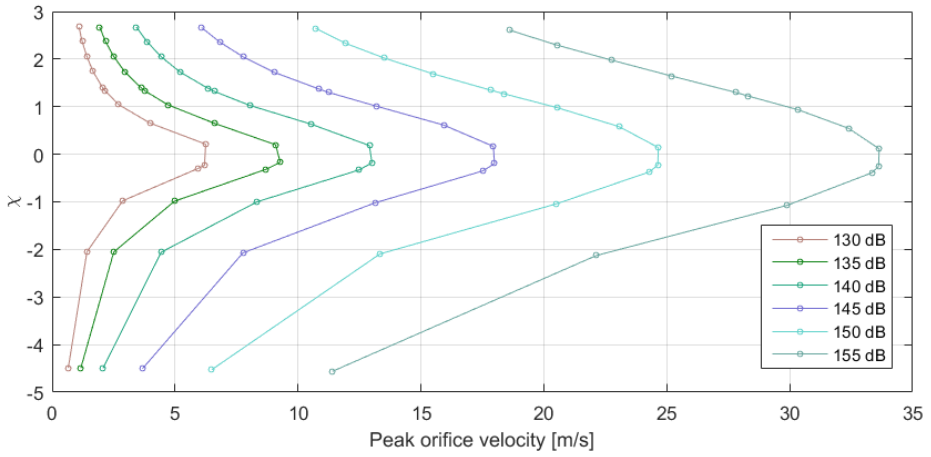

Figure 4.9: Normalized reactance over peak orifice velocity to various SPLs by using the Cummings model.

$$\epsilon_r = \frac{C_D}{C_{Df0}} \left(1 + \frac{(\frac{\overline{v_0}}{2fd})^{1.2}}{24} \right)^{-1}, \tag{4.44}$$

where C_{Df0} is the discharge coefficient at the resonant frequency. Usually this value is assumed to be 0.76 and allows the calculation of the POA_{eff} if a range of resistances is available at different SPL. After defining the POA_{eff} a frequency dependent discharge coefficient can be calculated, based on the non-linearity of the sample, as described in the section 3.1.2.4. The proposed model for a pure tone excitation by using a frequency dependent discharge coefficient can be obtained by the equation,

$$\rho L \frac{d^2 x_0}{dt^2} + \left[\rho |v_0| + Q + \frac{32 \mu l}{C_D d^2} + \rho \sqrt{8 \nu \omega} \, (1 + l/d) \right] \frac{dx_0}{dt} + \frac{\rho c^2 S}{V} x_0 = P \sin(\omega t), \tag{4.45}$$

where $L = l_0 + (l + l_0)\epsilon_r$ is the effective length for a frequency dependent end correction and $Q = 0.3M(3.15e - 2/POA + 1.77 * POA + 0.3)$. Observe that the velocity v_0 is the a solution of the equation. If the grazing flow is dominant in respect to the bias flow, the component Q is higher than the nonlinear term $\rho|v_0|$ which is vanished. So, the model is non-linear and it need to be iterated until the ϵ_r and the velocity v_0 converge. The discharge coefficient is also frequency dependent, which means that each pure tone excitation considering $P = Psin(2\pi ft)$ will be solved for f by using the correspondent value of the discharge coefficient for that frequency $C_D(f)$. The jet length was defined by Cummings and Boden as

$$L_1 = \frac{\int_0^{T/2} v_0 dt}{d}, \tag{4.46}$$

where half period corresponds to $\frac{T}{2} = \frac{1}{2f}$ if a single tone is considered. The Strouhal number can be written as

$$St = \overline{v_0}/2\pi fd. \tag{4.47}$$

So Equation 4.47 can be included into Equation 4.44 obtaining

$$\epsilon_r = \frac{C_D}{C_{Df0}} \left(1 + \frac{(\frac{\pi}{St})^{1.2}}{24}\right)^{-1}. \tag{4.48}$$

Observe that the plate effective thickness, and consequently the end correction, is linearly proportional to the $1/St$ simulated and presented in Figure 4.7.

4.3.1 Validation for pure tone excitation

Experimental and numerical predictions for different models are compared in this section, in order to validate the numerical implementations and also the proposed model for pure tone excitation. The models presented in section 2.6 were implemented in their complete form. The proposed model uses a frequency dependent discharge coefficient obtained from the procedure described in section 3.1.2.4. The Rice, Cummings and Boden models usually use a constant discharge coefficient $C_D = 0.76$, however a variable discharge coefficient was implemented in all models aiming to analyse only the ODE differences and not other semi-empirical effects. The discharge coefficient used on the models was shown in Figure 3.15 for the perforated sample in the holder and the root mean square velocities at the liner surface were used to feed the Maa model.

The following comparisons were also validated against experimental data by using TMM on the portable impedance meter. The predictions shown in Figure 4.10 were obtained for the perforated liner into the holder for the same input conditions, OASPL and excitation frequency at 130 dB OASPL.

At 130 dB OASPL the liner response is fairly linear and the majority of impedance models agree with experimental data in terms of resistance, except for the Cummings

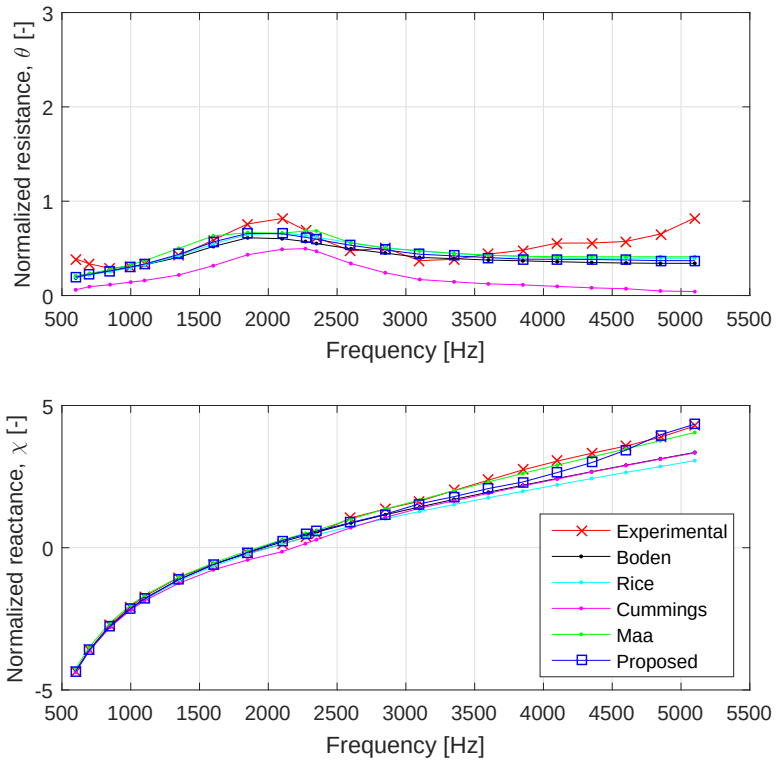

Figure 4.10: Experimental and numerical impedance predictions of a perforated liner in the holder having POA_{eff}=3.5 %, d=0.99 mm, h=19.1 mm, l=0.635 mm, by using the Rice, Cummings, Boden, Maa models and the proposed model at 130 dB OASPL.

model that does not include linear terms of dissipation into the ODE. The reactance simulated by the Maa model shows good agreement with experimental data, especially at higher frequencies as it uses the experimental velocities in order to obtain the reactances. All the other models underpredict the reactance at higher frequencies.

Figure 4.11 contains the experimental and numerical predictions of the perforated liner in the sample holder at 140 dB OASPL, where both the Rice model and the proposed model show excellent agreement with experimental data in terms of resistance. However, the Rice model does not show good agreement with the reactance. Although the Cummings model shows good agreement with experimental resistance data at a limited frequency band, it does not shows good agreement in terms of reactance. The Boden model slightly under predicts the resistance in the resonant frequency octave, around 2100 Hz, however, it follows the trend of the Rice and Cummings models mass reactance at higher frequencies, diverging from experimental data. It is worth notice that experimental data at higher frequencies shows higher uncertainties as they approaches the anti-resonance and also the TMM method diverges from *in situ* measurements.

As the OASPL increases to 150 dB, the agreement of Rice and the proposed model is maintained in terms of resistance within the resonant frequency octave. The proposed model also shows good agreement with experimental data and the Maa model in terms

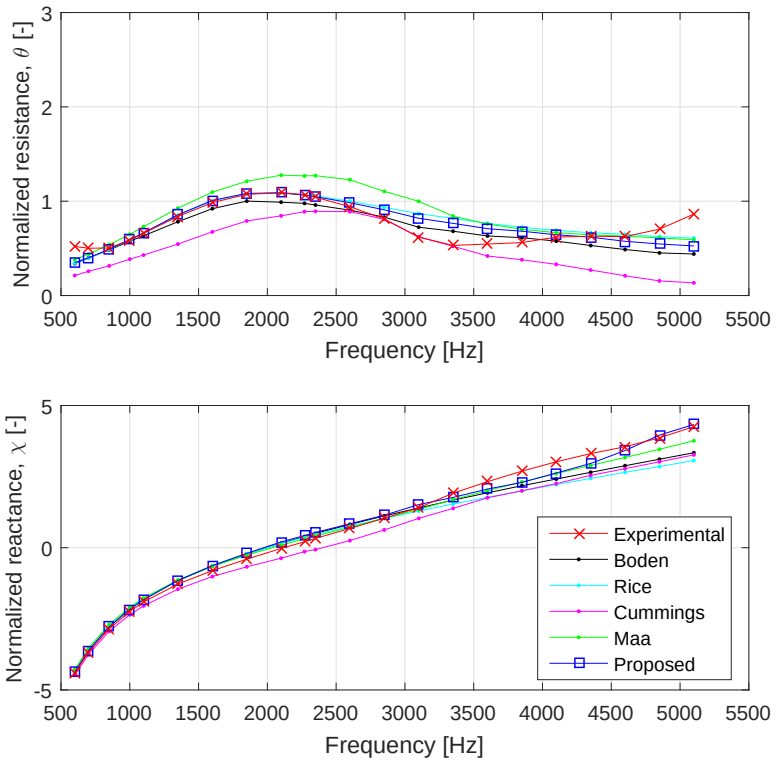

Figure 4.11: Experimental and numerical impedance predictions of a perforated liner in the holder having POA_{eff}=3.5 %, d=0.99 mm, h=19.1 mm, l=0.635 mm, by using the Rice, Cummings, Boden, Maa models and the proposed model at 140 dB OASPL.

of the mass reactance. The other models diverge from experimental results in terms of reactance, but the Boden and Cummings models show good resistance agreement from 2.5 kHz until 4.5 kHz.

The same analysis was performed for the sample S1M which was laser sintered. The pure tone resistances and velocities were measured by using TMM, and later the discharge coefficient was obtained based on the same approach as described in section 3.1.2.4. The POA_{eff} calculated for the S1M was 5.68% and the measured POA=6.0%. The diameter of the holes simulated are d=1.07 mm, the facing sheet thickness l=1.30 mm and the cavity depth h=19.28 mm. A second order polynomial function was used to obtain the discharge coefficient in terms of the frequency. The calculated values obtained from Equation 3.15 and the polynomial function are shown in Figure 4.13.

Figure 4.14 shows the S1M impedance predictions for the Rice, Cummings, Boden, Maa models and the proposed 1D semi-empirical model at 130 dB OASPL. Around the resonant frequency, at 2100 Hz, the majority of models agree with experimental data for both resistance and reactance, except for the Cummings model. However, at higher frequencies the models diverge in terms of mass reactance.

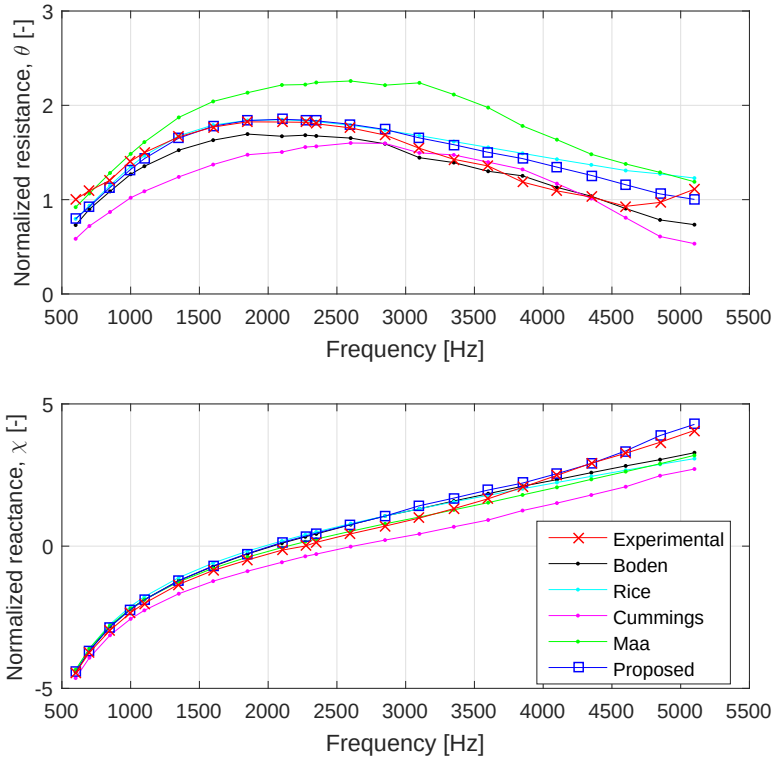

Figure 4.12: Experimental and numerical impedance predictions of a perforated liner in the holder having POA_{eff}=3.5 %, d=0.99 mm, h=19.1 mm, l=0.635 mm, by using Rice, Cummings, Boden, Maa models and the proposed model at 150 dB OASPL.

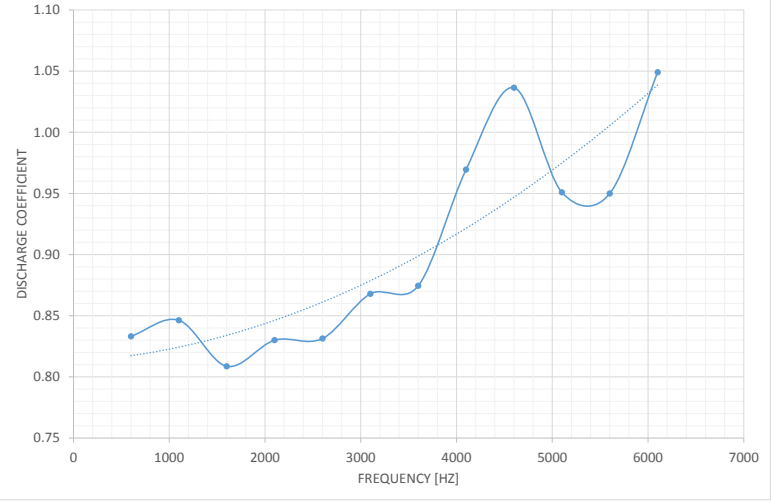

Figure 4.13: Discharge coefficient calculated from experimental data and the polynomial function used to simulate the impedance on the 1D models.

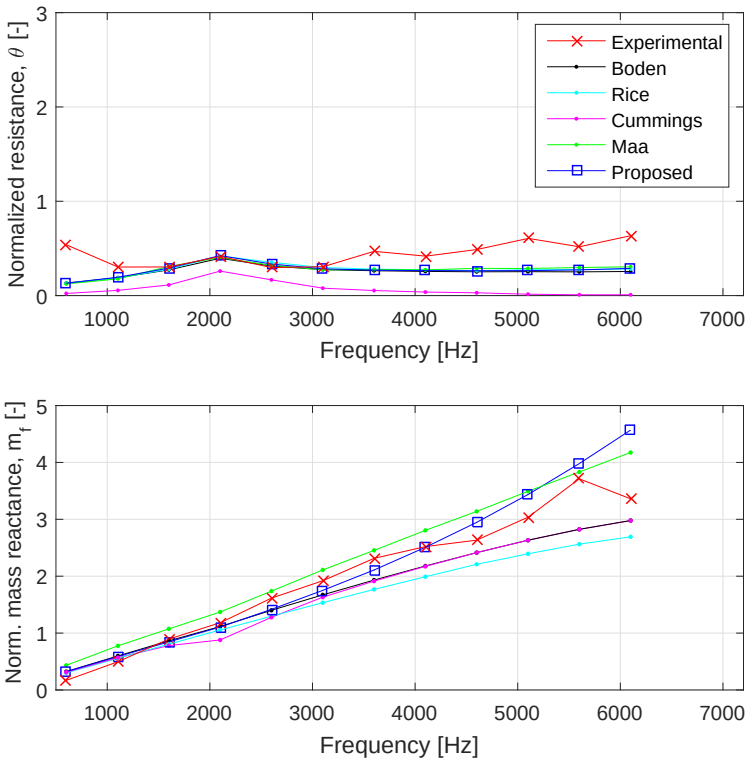

Figure 4.14: Experimental numerical impedance predictions of S1M having POA_{eff}=5.68 %, d=1.07 mm, h=19.28 mm, l=1.30 mm, for the Rice, Cummings, Boden, Maa models and the proposed model at 130 dB OASPL.

Figure 4.15 shows the impedance comparison by using the S1M sample at 140 dB OASPL. The Rice model and the proposed model show good agreement with the experimental resistance again. Mass reactance results at high frequencies varies depending on the model, but the proposed model shows good agreement, following the trend of the Maa model.

Figure 4.16 contains the S1M impedances measured and simulated by the 1D semi-empirical models at 150 dB OASPL. Whereas the Boden model shows good reactance agreement with experimental data, the resistance is under predicted. Rice and the proposed model agree with experimental resistance but the proposed model diverges shows slightly better mass reactance results.

In conclusion, five alternative impedance models were presented, implemented and compared at different OASPL, samples and frequencies. Impedance results of the 1D models are limited by the description of the root mean squared velocity on the liner surface and the discharge coefficient. The proposed model shown better agreement with experimental data for pure tone excitations by using the non-linear term description suggested by Rice, the time variant end correction proposed by Cummings, the experimental jet length coefficients proposed by Boden and a frequency dependent discharge coefficient proposed here to address the mass reactance mismatch of the previous models.

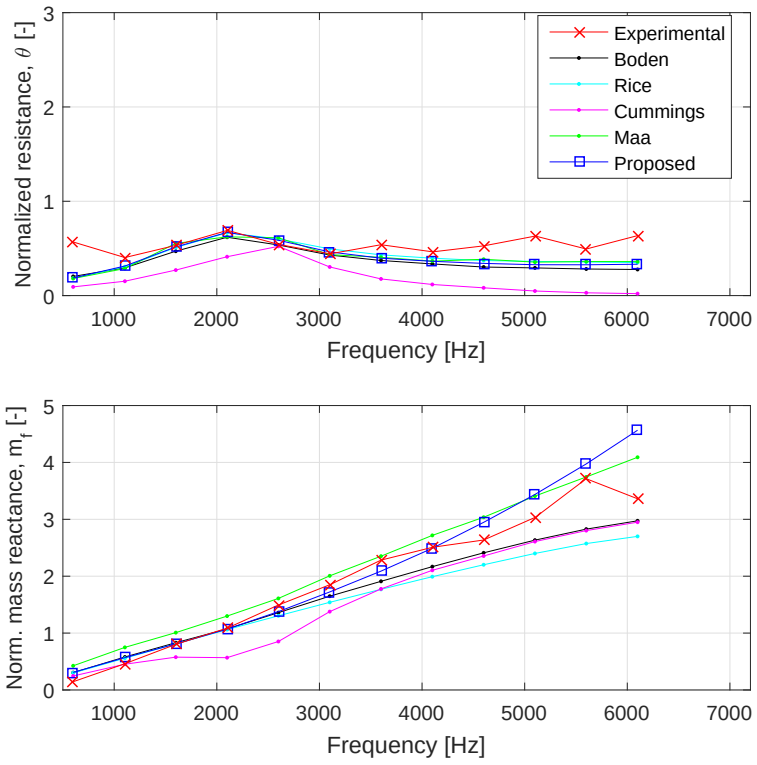

Figure 4.15: Experimental numerical impedance predictions of S1M having POA_{eff}=5.68 %, d=1.07 mm, h=19.28 mm, l=1.30 mm, by using the Rice, Cummings, Boden, Maa model and the proposed model at 140 dB OASPL.

4.4 Grazing flow, pure tone excitation

The proposed 1D semi-empirical model validation against *in situ* measurements on the grazing flow test rig is presented in this section, where the simulations were obtained considering the grazing flow factor Q and the non-linear term due to high SPL in Equation 4.45 for pure tone excitation. Figure 4.17 contains impedance results for the no flow configuration obtained by and by using the *in situ* and the 1D model for the punched aluminium SDOF liner sample. Since the *in situ* microphone was in the middle of the liner, away from the leading and trailing edges, and the OASPL was calibrated at the leading edge microphone on the opposite wall of the liner; the non-linearities were not well captured by the *in situ* microphones. This means that they were exposed to relatively low SPLs in a limited frequency bandwidth as showed in Figure 3.38.(b). The SPLs used in the 1D model were the experimental SPLs measured at the *in situ* surface microphone, which is positioned a few micrometres recessed from the liner facing sheet and exposed to the grazing flow. The case where high SPLs excited the sample and generated nonlinearities in the range of 0.6 kHz to 2.0 kHz was selected in order to show the agreement between by the prediction model developed and the *in situ* measurements without flow on the LVA/UFSC rig.

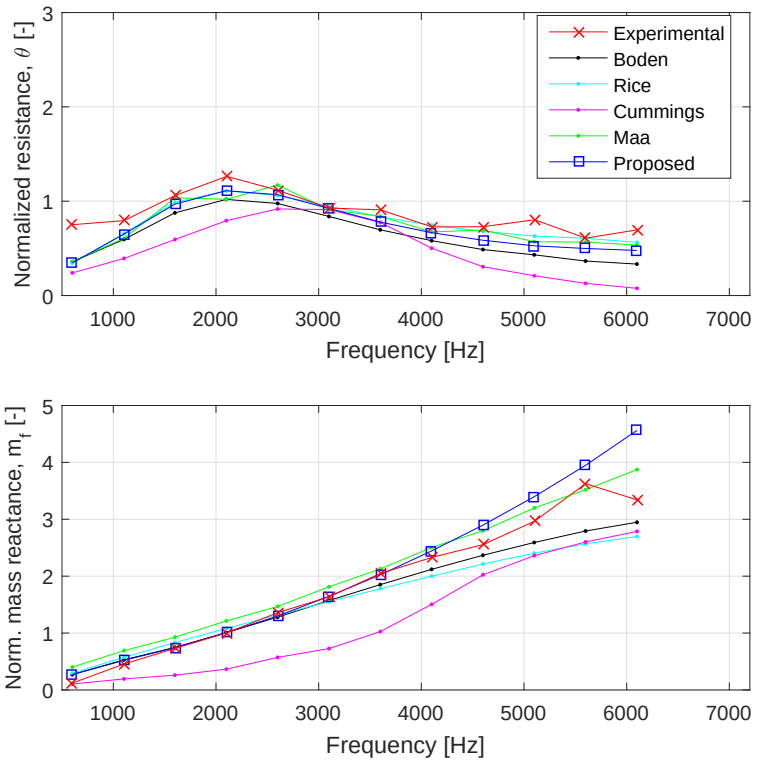

Figure 4.16: Experimental numerical impedance predictions of S1M having POA_{eff}=5.68 %, d=1.07 mm, h=19.28 mm, l=1.30 mm, by using Rice, Cummings, Boden, Maa models and the proposed model at 150 dB OASPL.

Given the limitations of the *in situ* approach and the maximum SPL achievable on the test rig, the numerical simulated impedances are in good agreement with experimental results, especially for the reactance. As the SPL is lower than 125 dB for the pure tones between 2.0 kHz and 3.0 kHz, it is expected that some deviation may occur at this frequency range. The experimental resistances at high frequencies are higher than the predictions, possibly because the duct termination is not perfectly anechoic and the rig vibration causes uncertainties on the pressures measured by the Kulite microphones. Also, the precision on the Mach number measuring varies 0.02 and the coefficients of the grazing flow contribution need to be adjusted on the model to account for this discrepancies.

Figure 4.17, Figure 4.18 and Figure 4.19 show the impedance comparisons between *in situ* upstream measurements by using Dean's method and the proposed model in the absence of grazing flow, at 0.15 Mach and at 0.25 Mach respectively.

The measurements and predictions in the absence of flow shown in Figure 4.17 show the non-linearities caused by high SPLs from 0.6 kHz until 2.0 kHz. Above this frequency the maximum SPLs measured at the *in situ* microphones were below 130 dB due to power limitations of the test rig drivers.

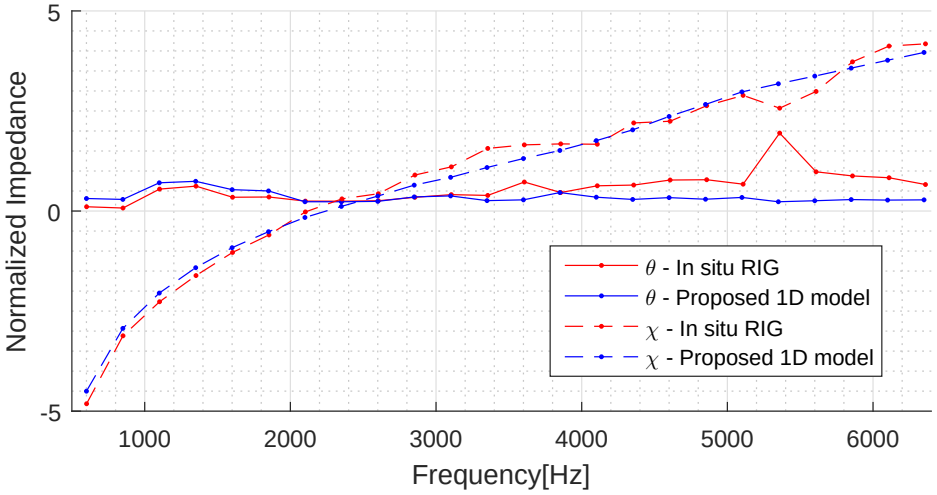

Figure 4.17: Experimental impedance predictions by using Dean's *in situ* method and the proposed 1D model for the punched aluminium SDOF liner in the grazing flow rig 0.00 Mach: POA_{eff}=4.74 %, d=0.99 mm, h=19.1 mm, l=0.635 mm.

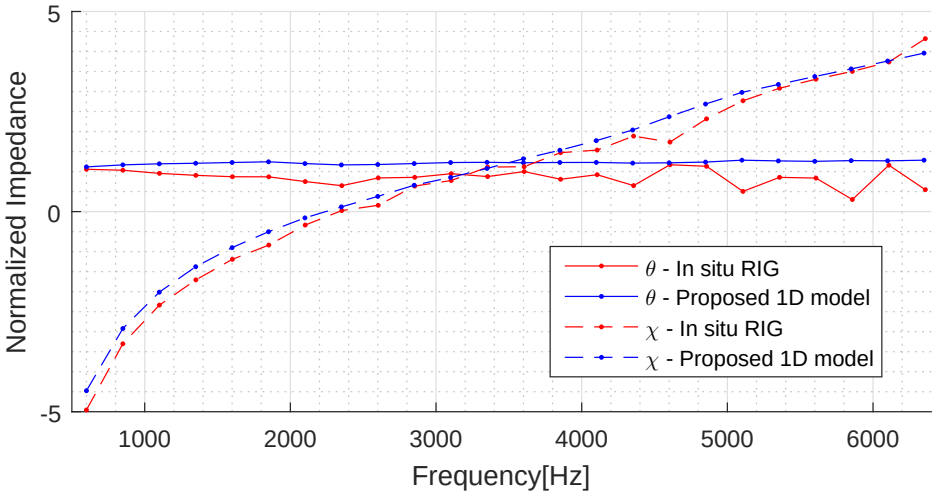

Figure 4.18: Experimental impedance predictions by using Dean's *in situ* method and the proposed 1D model for the punched aluminium SDOF liner in the grazing flow rig for 0.15 Mach: POA_{eff}=4.74 %, d=0.99 mm, h=19.1 mm, l=0.635 mm.

The model generally over estimate both resistance and reactance but the average errors are at the order of 0.4. At higher Mach numbers the signal to noise ratio is not ideal because it is contaminated by the boundary layer flow generated on the duct from the nozzle to the liner sample. Also the maximum voltage applied to the drivers was not sufficient to obtain high SPLs above 2.0 kHz, as was shown in Figure 3.39.(b). Consequently, the liner response is reasonably linear at this SPLs and the oscillation caused in the *in situ* results over frequency is due low SNR and calibration errors in terms of the Mach number, microphone amplitude and phase.

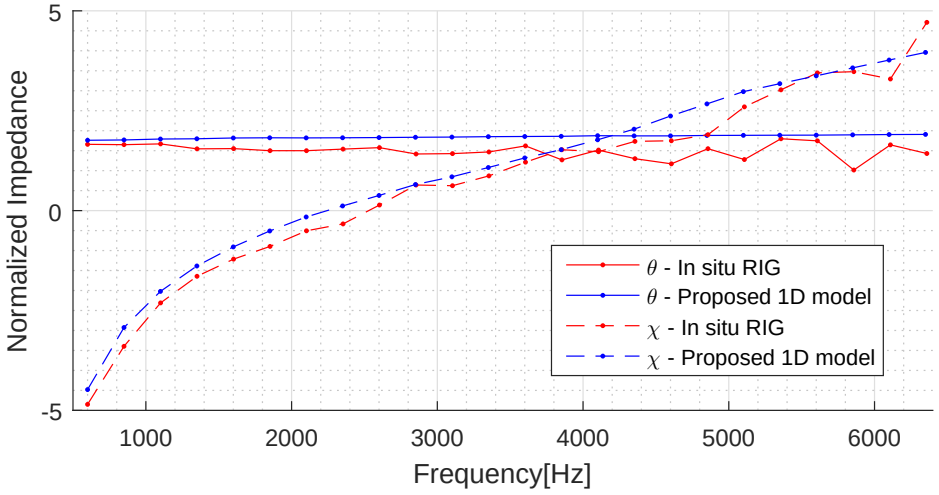

Figure 4.19: Experimental impedance predictions by using Dean's *in situ* method and the proposed 1D model for the punched aluminium SDOF liner in the grazing flow rig for 0.25 Mach: POA_{eff}=4.74 %, d=0.99 mm, h=19.1 mm, l=0.635 mm.

Chapter 5

2D numerical model

High fidelity 2D and 3D models can be used to explore liner impedance in the presence of high SPL and grazing flow. The level of the complexity of such models is related to the precision required to fully represent the flow features near the perforated plate holes. Simplifications may be applied to the Navier Stokes equations that describes the compressible flow, in order to reduce the time required to solve the equations. If low Reynolds numbers occur near the hole, a laminar flow hypothesis is practicable, and a turbulence closure model is not required to solve the problem. If there is no grazing flow on the liner surface, high intensity acoustic waves impinging the liner are the only cause of the local acceleration of fluid though the hole. Far from the perforated plate holes the waves can also be considered as plane waves, and can be represented by using the wave equation, in Equation 2.118. Note that linear propagation is assumed even at high SPLs.

This chapter includes the validation of two numerical models based on the COMSOL Multiphysics FEM code, version 5.2a[19] (with MATLAB version 2015b[58] livelink). The first model is a 2D slit liner model, and the second is a 2D axi-symmetric model. Four different impedance calculation methods are used to extract the pressure and velocity data from the numerical models. This section describes the models and the assumptions used. It also describes an SPL control algorithm implemented into the model solution routine. Finally, the model results will be presented and validated against data from other authors.

The FEM approach accommodates multiple pure tone simulations, and therefore extends the work of other authors, who used either pure tone, broadband or pseudo-random signals. Pure tone simulations are compared to experimental data acquired from the samples described in Chapter 3 in order to validate the models. Further analysis, including an assessment of the sensitivity to hole shape, will be covered in this chapter.

5.1 Impedance calculation methods

There are multiple ways to calculate the impedance at a physical or notional surface in a numerical model. One is to analyze the spectra of the time history of pressure and velocity at certain nodes or on planes of nodes in the FEM mesh. The liner surface is of greater interest in the current study. It corresponds to the outer surface of the perforated plate facing into the impedance tube. The impedance can be calculated from spatially averaged numerical data on the liner surface itself, or inferred from numerical data collected at transverse planes further up the impedance tube and perpendicular to the tube axis. That is to say, if the spatial average pressure and velocity is calculated on a plane away from the liner surface, the impedance can be calculated at that plane and subsequently transposed to the liner surface position.

For example, suppose an impedance tube as in Figure 5.1 has an speaker in one end and a liner sample on the other, in which x_n denotes the distance of the speaker to a generic position of the tube. If the reflection factor is unknown, but the impedance Z_n at a certain point distant x_n is known, it is possible to calculate the liner impedance Z_L at the duct end, $x = L$, by using the pressure and velocity extracted at x_n. If we substitute a microphone located at the generic position on this physical analogy by a node on the numerical model, it is possible to collect the spatially averaged pressure $\widetilde{p}$ and velocity $\widetilde{u}$ at that point in space and calculate the impedance at any other position in the model.

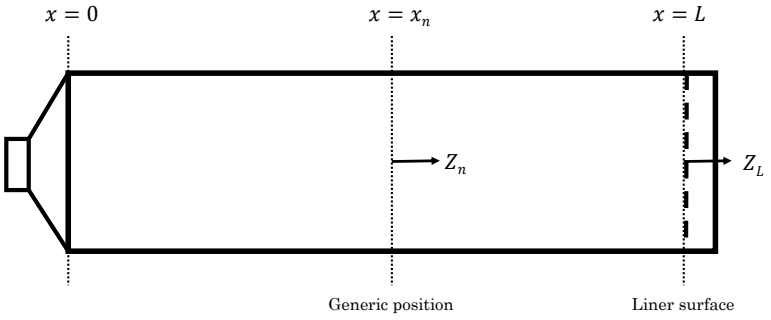

Figure 5.1: Impedance tube with a liner sample on the end.

A plane harmonic wave inside the impedance tube can be written as

$$\widetilde{p}(x,t) = \left(\widetilde{A}e^{ikx} + \widetilde{B}e^{-ikx}\right) e^{-i\omega t}, \tag{5.1}$$

where $\widetilde{A}$ and $\widetilde{B}$ are constants to be determined, k is the wave number and ω is the frequency.

By using the acoustic wave equation in Equation 2.118 it is possible to differentiate the pressure $\widetilde{p}(x,t)$ and obtain the velocity $\widetilde{u}(x,t)$ given by

$$\rho\frac{\partial\widetilde{u}(x,t)}{\partial t} = -\frac{\partial\widetilde{p}}{\partial x}, \tag{5.2}$$

giving,

$$\widetilde{u}(x,t) = \frac{\left(\widetilde{A}e^{ikx} - \widetilde{B}e^{-ikx}\right)}{\rho c}e^{-i\omega t}, \tag{5.3}$$

where $c = \omega/k$ is the speed of sound. At the liner sample surface $x = L$ the impedance is

$$Z_L = \frac{\widetilde{p}(L)}{\widetilde{u}(L)} = \rho c\frac{\left(\widetilde{A}e^{ikL} + \widetilde{B}e^{-ikL}\right)}{\left(\widetilde{A}e^{ikL} - \widetilde{B}e^{-ikL}\right)}. \tag{5.4}$$

Similarly, at the $x = x_n$ the impedance is given by

$$Z_n = \frac{\widetilde{p}(x_n)}{\widetilde{u}(x_n)} = \rho c\frac{\left(\widetilde{A}e^{ikx_n} + \widetilde{B}e^{-ikx_n}\right)}{\left(\widetilde{A}e^{ikx_n} - \widetilde{B}e^{-ikx_n}\right)}. \tag{5.5}$$

Normalized impedance at the generic position and at the liner position is defined as $z_n = Z_n/\rho c$ and $z_L = Z_L/\rho c$ respectively. Rearrange Equations 5.4 and 5.5 to give

$$\widetilde{A}\,(z_L - 1)\,e^{-ikx_L} - \widetilde{B}\,(z_L + 1)\,e^{ikx_L} = 0, \tag{5.6}$$

$$\widetilde{A}\,(z_n - 1)\,e^{-ikx_n} - \widetilde{B}\,(z_n + 1)\,e^{ikx_n} = 0. \tag{5.7}$$

Equations 5.7 have a non-trivial solution for $A, B \neq 0$ if

$$(z_n - 1)\,(z_L + 1)\,e^{-ik(x_n - L)} - (z_n + 1)\,(z_L - 1)\,e^{ik(x_n - L)} = 0. \tag{5.8}$$

The distance from the generic plane to the liner is defined as $x_n - L = x_1$. It is possible to rearrange terms above to give,

$$\begin{aligned}
& z_L\left[(z_n - 1)\,e^{ikx_1} - (z_n + 1)\,e^{-ikx_1}\right] = \left[(1 - z_n)\,e^{ikx_1} - (1 + z_n)\,e^{-ikx_1}\right] \\
\textit{or} \quad & z_L = \frac{\left[\left(e^{ikx_1} - e^{-ikx_1}\right) - z_n\left(e^{ikx_1} + e^{-ikx_1}\right)\right]}{\left[z_n\left(e^{ikx_1} - e^{-ikx_1}\right) - \left(e^{ikx_1} + e^{-ikx_1}\right)\right]} \\
\textit{or} \quad & z_L = \frac{\left[i\sin kx_1 - z_n\cos kx_1\right]}{\left[iz_n\sin kx_1 - \cos kx_1\right]} \\
\textit{or} \quad & z_L = \frac{z_n - i\tan(k_0x_1)}{1 - iz_n\tan(k_0x_1)}.
\end{aligned} \tag{5.9}$$

The following methods described in the next sections were used to calculate the normalized impedance z_n at a certain position in the numerical wave guide that simulates an impedance tube. They were compared for different windowing of the time traces of pressure and velocity calculated at distinct positions in the numerical models. The sampling

size was varied in order to optimize the total time required to solve the transient numerical model. Comparisons between methods for different sample sizes allowed precision and convergence assessments.

5.1.1 ISO 10.534-2 - ASTM

This method is based on the ASTM ISO 10.534-2 [42] international standard. It is used to calculate the impedance by using an impedance tube as described in Section 2.7.1. The data is collected from two different tube positions on the numerical model domain, simulating microphone centre positions. Consider the pressure history on each virtual microphone position as $p_1(t)$ for position x_1, and $p_2(t)$ for position x_2. Applying an FFT on both signals, it is possible to obtain the transfer function between the microphone signals given by,

$$\widetilde{H}_{12} = \frac{\widetilde{p}_2(\omega)}{\widetilde{P}_1(\omega)}, \tag{5.10}$$

where $\widetilde{P}_1(\omega)$ and $\widetilde{P}_2(\omega)$ are the Discrete Fourier Transforms of the pressure signal at position 1 and position 2 respectively, as the numerical model provides a limited sample containing discrete values in time. The reflection factor, Γ, at the sample position was obtained in Section 3.1.2 for the tube termination, which is given by [42]

$$\Gamma = |\Gamma| e^{i\theta_r} = \frac{\widetilde{H}_{12} - e^{-ik_0 s}}{e^{-ik_0 s} - \widetilde{H}_{12}} e^{2ik_0 x_1}, \tag{5.11}$$

where s is the distance between the virtual microphone positions ($s = x_1 - x_2$) and k_0 is the wave number. The transfer function $\widetilde{H}_{12}$ can also be substituted by a corrected transfer function $\widetilde{H_c}$ that is obtained by interchanging the microphone position on the impedance tube experimental set-up [42], in order to correct the amplitude and phase mismatch between microphones, but it is not required for a numerical model. Finally, the complex normalized impedance at the liner surface z_L on the numerical model can be calculated by using

$$z_L = \frac{1 + \Gamma}{1 - \Gamma}. \tag{5.12}$$

5.1.2 Incident and reflected waves - IRW

The normal impedance z_n at a certain position of a tube can be written as a function of the incident and reflected standing waves by,

$$z_n = \frac{Z_n}{\rho c} = \frac{p_I + p_R}{u_I + u_R}, \tag{5.13}$$

where p_I and p_R are the incident and reflected complex pressure wave contributions, and u_I and u_R are the incident and reflected complex particle velocity contributions. All of

these quantities are frequency dependent and complex values with real and imaginary parts . The pressure and velocity are related by

$$p_I = \rho c u_I, \tag{5.14}$$

$$p_R = \rho c(-u_R). \tag{5.15}$$

The reflected pressure wave may also be written as a function of the incident pressure wave and the reflection coefficient,

$$p_R = p_I \Gamma e^{i\theta}, \tag{5.16}$$

where θ is the phase angle between the incident and reflected pressure waves, and Γ is the reflection factor. Substituting Equations 5.14, 5.15 and 5.16 into Equation 5.13, it is possible to obtain the impedance in terms of the reflection factor by,

$$z_n = \frac{1 + \Gamma e^{i\theta}}{1 - \Gamma e^{i\theta}}. \tag{5.17}$$

Using the Fourier transforms of pressure and velocity calculated from a node of the FEM mesh, it is possible to calculate the reflection factor and the impedance at that node. Finally, the impedance at the node can be transposed to the sample surface using Equation 5.9.

5.1.3 Fourier Coefficients at 2 positions - FC

Consider two virtual microphone positions with pressures $P_1(t)$ and $P_2(t)$, at distances x_1 and x_2 from the sample position x_L. Considering plane wave propagation and standing waves in the tube, incoming and outgoing waves can be represented at each virtual microphone position as a series of sine and cosine waves with multiple frequency components. Truncating the series to obtain just the first frequency component ω, it is possible to express the pressures as

$$p_1(t) = A_1 \cos(\omega t) + B_1 \sin(\omega t), \tag{5.18}$$

$$p_2(t) = A_2 \cos(\omega t) + B_2 \sin(\omega t). \tag{5.19}$$

Numerical Fourier series can be used to extract the coefficients A_1, B_1, A_2 and B_2 from the time domain signals, and use those to calculate the impedance at the liner surface z_L. The complex form can be written as

$$P_1(x,t) = (ae^{ikx_1} + be^{-ikx_1})e^{-i\omega t}, \tag{5.20}$$

$$P_2(x,t) = (ae^{ikx_2} + be^{-ikx_2})e^{-i\omega t}. \tag{5.21}$$

Defining $x_1 = 0$, and $s = x_2 - x_1$ the distance between the two virtual microphones, so

$$P_1(x,t) = (ae^{ik0} + be^{-ik0})e^{-i\omega t} = a + b = A_1 - iB_1 = C_1, \tag{5.22}$$

$$P_2(x,t) = (ae^{ikx_2} + be^{-ikx_2})e^{-i\omega t} = ae^{iks} + be^{-iks} = A_2 - iB_2 = C_2, \tag{5.23}$$

where C_1 and C_2 are constants that can be calculated if A_1, B_1, A_2 and B_2 are known. Multiplying the Equation 5.23 by $-e^{-iks}$ and summing with Equation 5.23,

$$-ae^{-iks} - be^{-iks} = -C_1e^{-iks}, ae^{iks} + be^{-iks} = C_2, \tag{5.24}$$

it is possible to obtain

$$a(e^{iks} - e^{-iks}) = C_2 - C_1e^{-iks}. \tag{5.25}$$

By using the trigonometric identity $2i\sin(x) = e^{ix} - e^{-ix}$ it is possible to write

$$a2i\sin ks = C_2 - C_1e^{-iks}, \tag{5.26}$$

$$a = \frac{i(C_1e^{-iks} - C_2)}{2\sin ks} \tag{5.27}$$

The same approach is used to obtain b, given by

$$b = -\frac{i(C_1e^{-iks} - C_2)}{2\sin(ks)}. \tag{5.28}$$

Now, a and b can be used to calculate the impedance at any position in the impedance tube, for instance at $x = 0$. The impedance at the position x_2 can be written as

$$z_0 = \frac{p(0,t)}{u(0,t)} = \frac{ae^{ik0} + be^{ik0}}{ae^{ik0} - be^{ik0}} = \frac{a+b}{a-b}, \tag{5.29}$$

Also, rearranging the Equation 5.12 for a given impedance z_n is possible to isolate the reflection factor,

$$\Gamma = \frac{z_n - 1}{1 + z_n}, \tag{5.30}$$

The same approach can be used at the liner position x_L, considering the distance from the origin $x_1 = 0$, where

$$z_L = \frac{ae^{-ikx_L} + be^{ikx_L}}{ae^{-ikx_L} - be^{ikx_L}}, \tag{5.31}$$

$$z_L = \frac{e^{-2ikx_L} + \Gamma}{e^{-2ikx_L} - \Gamma}. \tag{5.32}$$

An alternative way to interpret the results is to obtain the time history of the average pressure, $\overline{p_L(t)}$, and velocity, $\overline{p_L(t)}$, over the FEM liner surface. The Fourier coefficients

of each signal are given by,

$$\overline{p_L(t)} = A_1 \cos(\omega t) + B_1 \sin(\omega t), \tag{5.33}$$

$$\overline{u_L(t)} = A_2 \cos(\omega t) + B_2 \sin(\omega t). \tag{5.34}$$

The Fourier coefficients (A_1, A_2, B_1 and B_2) can be obtained by fitting sine and cosine waves using the function "fit()" of MATLAB[58]. Then, from the complex form it is possible to directly calculate the normalized impedance as done in Equations 5.23 and 5.23,

$$\overline{z_L(t)} = \frac{\overline{p_L(t)}}{\overline{u_L(t)}} = \frac{A_1 - iB_1}{(A_2 - iB_2)}. \tag{5.35}$$

5.1.4 Fast Fourier Transform method - FFT

This approach is straightforward and can be used to calculate the impedance at a node in the numerical model or on a surface by using a spatially averaged value of pressure and velocity in a selected domain. The average impedance at a generic point or plane z_p can be expressed as

$$\overline{z_p(\omega)} = \frac{\int_{-\infty}^{\infty} \overline{P(t)} e^{i\omega t} dt}{\int_{-\infty}^{\infty} \overline{V(t)} e^{i\omega t} dt}, \tag{5.36}$$

$$\overline{z_p(\omega)} = \frac{FFT(\overline{P(t)})}{FFT(\overline{V(t)})}. \tag{5.37}$$

The sample size defines the frequency step, while the time step defines the maximum frequency that can be analysed. So, in practice the DFT is applied to the pressure and velocity signals. This approach limits the analysis in both precision and frequency range, as the duration and time step need to be optimized in order to minimize the computational cost to obtain the numerical solution of the Discrete Fourier Transform (DFT).

Having the impedance at a point or a plane, it may be transposed to any other position on the virtual impedance tube using the Equation 5.9.

5.2 SPL control algorithm

The experimental procedure implemented in the PIM, to obtain the impedance curves at desired non-linear SPLs, was implemented also in the numerical models. The basic procedure is summarized in Figure 5.2. The input parameters to the algorithm are:

- liner geometry - hole diameter, porosity (POA), cavity depth and face sheet thickness. These are needed to create the COMSOL model and calculate the parameters on the liner surface;
- desired SPL (SPLd) - the value at the liner surface to be targeted at each pure tone frequency calculated;
- number of cycles - dependent upon the fundamental frequency of the input signal, the sample size is determined by the number of cycles choosen to perform the FFT procedure;
- frequency - the pure tone frequency or frequencies used to generate a wave that excites the numerical model.

A code was implemented in MATLAB and linked with COMSOL to drive the numerical model, taking account of the boundary conditions and the frequency-dependent mesh criteria. The time step is frequency dependent and it is defined as $\delta_t = T_0/ppl$, where T_0 is the period of the lowest tone of the signal and ppl is the number of Points Per Wavelength. The chosen $ppl = 20$ was found to be sufficient to avoid aliasing and sufficiently precise to capture harmonics at twice the frequency of the fundamental pure tone exciting the system.

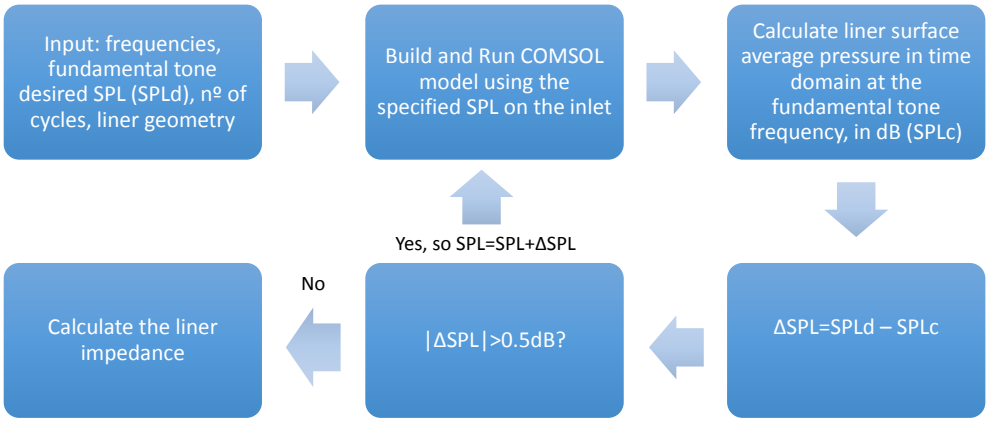

Figure 5.2: SPL control procedure.

The procedure in Figure 5.2 was implemented in order to compare experimental and numerical impedance results. The experimental OASPL measured at the liner surface was used as the desired value (SPLd) on the liner surface of the COMSOL model. The PIM uses the same approach, iterating the speaker OASPL until the desired OASPL is attained at the sample surface. This procedure takes 2 or 3 iterations to converge,

both for the experiment and for the numerical model. The experimental OASPLs were iterated to be within ±0.5 dB of deviation in respect to the desired values.

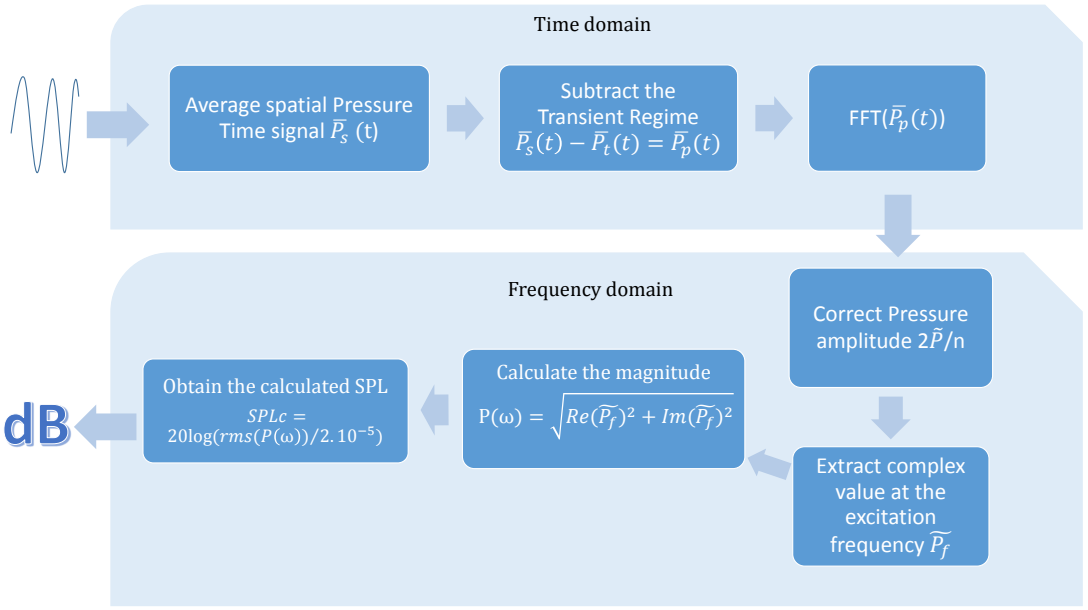

Figure 5.3: Signal processing used to calculate the spatial average SPL of a tone on the numerical liner surface.

The scheme presented in Figure 5.3 shows each step used to obtain the SPL of a frequency component or an OASPL and occurs within the top right box of the fluxogram in Figure 5.2. Firstly, a spatially averaged pressure over the liner surface $\overline{P_s}(t)$ is calculated from the model solution based on the combination of input parameters. Secondly, the time history of the average pressure is truncated, separating out the transient regime and the permanent regime solutions. This usually happens a couple of milliseconds after the wave impinges on the liner surface. This transient response takes no more than 2 to 5 complete cycles, depending on the period of the excitation frequency, or the period of the lowest frequency, in the case of multiple tones. The transient solution is excluded from the impedance calculation and only the steady state solution is post processed by using the FFT.

To calculate the steady state solution a DFT can be used instead of a FFT by using the fft function of MATLAB[58] on an vector of values of pressure or velocity. Magnitude corrections are needed depending on the number of points on the vector to obtain the correct value in each frequency component. The calculated SPL (SPLc) in dB corresponds to the RMS sound pressure level calculated in one specific frequency component. The OASPL corresponds to the sound pressure level of all the frequency components of the signal logarithmically summed.

The calculated pressure (SPLc) is compared with the desired pressure (SPLd), in order to check if the incident pressure amplitude reproduces the desired spatially averaged pressure on the liner surface. If the difference between SPLc and SPLd is smaller than

0.5 dB, the criteria is met and the impedance is calculated over the liner surface by using the impedance calculation methods described in the previous sections. If the pressure difference is larger then the criteria, the solution is recalculated by using a linear adjustment of the pressure excitation amplitude at the inlet.

For pure tone excitations, the impedance spectra is meaningful only at the excited frequency (the SPL of the pure tone is equivalent to the OASPL).

5.3 2D Slit liner - COMSOL model

A SDOF aero engine perforated liner is an array of locally reacting multiple Helmholtz resonators. The resonator facing sheet holes are also sufficiently far away from each other, that there is no interaction between the holes. Consequently, the impedance of each Helmholtz resonator will be the same as the impedance of an array of resonators having the same total POA. This section explores the validation of a 2D "slit" liner COMSOL numerical model which is a 2D simplification of the problem. The results are compared with experimental, DNS and semi-empirical models reported in the literature [92][69].

5.3.1 Model assumptions and geometry

The numerical model reproduces a NASA Langley Research Center (LaRC) experimental set-up which consists of a long impedance tube over a slit liner having a facesheet 0.04 inches thick, an aperture 0.05 inches wide, POA=2.5%, and a cavity depth of 6 inches. The NASA LaRC experimental set-up schematic in Figure 5.4 shows the Normal Incidence Tube (NIT) and the slit liner geometry. The dashed line marks the flanged tube termination over the sample facing sheet.

The numerical model geometry is a 2D representation of the experiment, with the inlet condition representing pure tone plane waves in the duct. Acoustic waves impinge on the slit liner which reflects and absorbs part of the sound waves. Figure 5.5 shows a not-to-scale schematic of the numerical model showing the location of the modelling planes and of the virtual microphone pressure taps, identified by p_1 and p_2. The duct length is $h = 609mm$. Four different planes are identified by red lines, at which the spatial average values of pressure and velocity were obtained, in order to calculate the impedance by using the methods described in Section 5.1.

If the incident sound wave impinging on the resonator is of sufficiently large amplitude, non-linear effects will cause vortex shedding near the aperture for specific excitation frequencies (as shown in Figure 2.10). Two dimensional FEM is used to perform a relatively inexpensive high fidelity DNS calculation. If the appropriate assumptions are

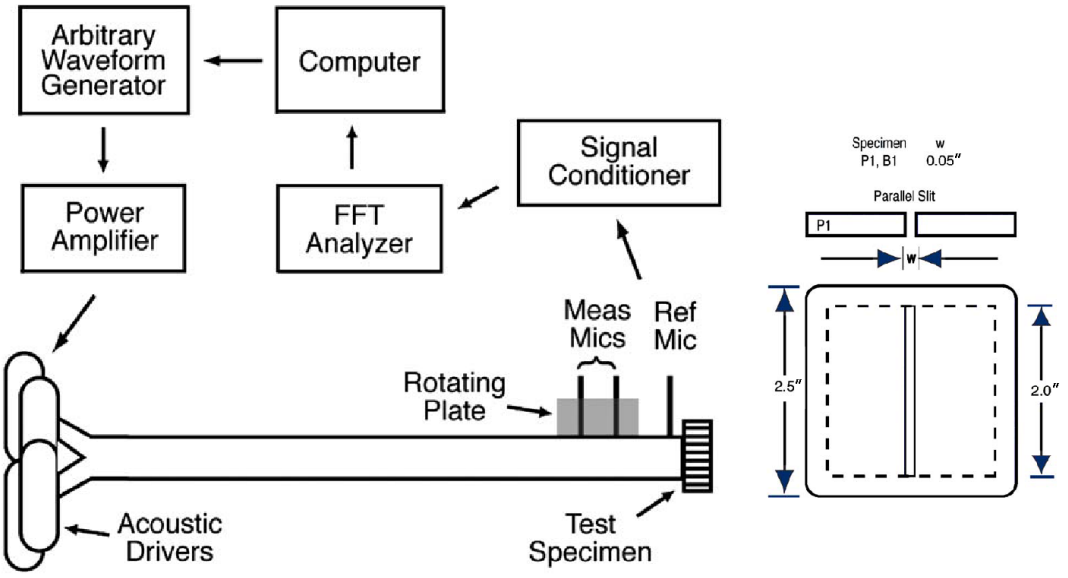

Figure 5.4: NASA LaRC normal incidence tube with instrumentation and a cross section on the tube showing the dashed area where the tube flange touches the single slit liner cell 6 inches deep. Adapted from Tam, 2005[92].

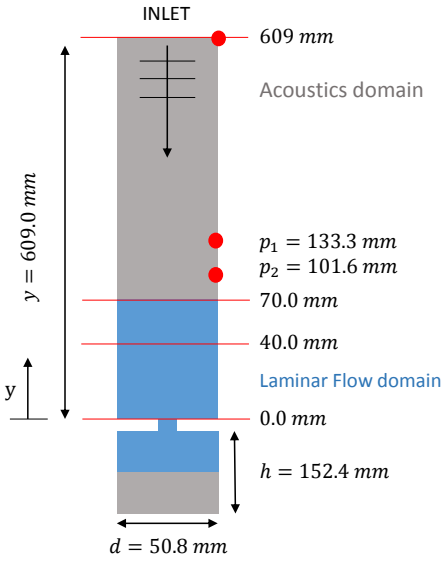

Figure 5.5: Slit liner multiphysics model geometry.

made, Low Reynolds numbers are expected near the hole[92]. Therefore, the Navier Stokes Equation derived in Equation 2.103 can be fully resolved by the FEM model to describe the fluid dynamics of the air near the resonator hole.

Two domains were assigned in the COMSOL model with different physics, in order to reduce the computational cost. A laminar flow compressible Navier Stokes model was used near the resonator aperture, as identified in blue in Figure 5.5. Away from the resonator aperture linear acoustic propagation was assumed, as it is identified in gray in Figure 5.5. In the acoustic domain the wave equation Equation 2.118 is used. In the laminar flow domain the full unsteady Navier Stokes equations in Equations 2.107 are used.

Pressure and density are linearly related in the acoustic domain, as the amplitudes are assumed to be sufficiently small for non-linear propagation effect to be negligible, so locally [19]

$$\rho = \frac{p}{c^2}. \tag{5.38}$$

High order terms are included, however, in the laminar flow domain near the hole. The density in the laminar flow domain can be expressed as [19]

$$\rho_{NL} = \frac{p}{c^2} - \frac{(\beta - 1)\, p^2}{\rho_0 c^4}, \tag{5.39}$$

where ρ_{NL} is the local non-linear density fluctuation, ρ_0 is the air density, and $\beta = 1.2$ is a non-linear coefficient. COMSOL uses a Non-linear Constant Newton iterative method to solve a non-linear system of partial differential equations at each time step. The maximum number of iterations is 6 at each time step, and a MUMPS solver is used. The models are calculated at the ambient temperature and pressure conditions $T = 293.15$ K, P=101325 Pa, which provides an air density of $\rho_0 = 1.2056$ kg/m^3 and speed of sound of $c = 343.20$ m/s.

5.3.2 Boundary conditions

From the Navier Stokes equation, the terms on the right hand side of the equations can be seen as forces $\mathbf{f}$ acting on a mass of air observing

$$\rho \frac{D\mathbf{u}}{Dt} = -\nabla p + \mu \nabla^2 \mathbf{u}. \tag{5.40}$$

So,

$$\mathbf{f} = -\nabla p + \mu \nabla^2 \mathbf{u}. \tag{5.41}$$

The boundary located at 70.0 mm above the liner surface couples the acoustic domain with the laminar flow domain in the COMSOL model. The coupling between physics

is valid as long as vorticity is small at the boundary. The variation of pressure from the acoustics domain can be approximated as a normal force acting on the area of the boundary on the laminar flow domain side, for small displacements $\mu\nabla^2\mathbf{u} \approx 0$, so the inlet condition for the laminar flow region can be approximated as [19]

$$\mathbf{f} = -\nabla p. \tag{5.42}$$

The velocity is calculated on the laminar flow domain by using this linearisation. The pressure on the acoustic domain is calculated by using the density calculated at the boundary with the laminar flow domain that is used to solve the wave equation.

The impedance tube walls and the resonator cavity walls are considered to be rigid with a slip condition, meaning that no boundary layer is formed on these walls. However, the facing sheet is considered rigid, with a no slip boundary condition, where the full Navier Stokes equations are solved.

The inlet located at the top of the virtual impedance tube is defined as a moving membrane that generate plane waves and absorbs the reflected waves, meaning that no plane waves travelling up the tube are reflected at this boundary.

The inlet excitation, defined as a pure tone waveform, can be expressed as,

$$p_I = Asin(\omega t + ky), \tag{5.43}$$

where A is the pressure amplitude, ω is the pure tone angular excitation frequency, t is time, and k the wave number travelling on the y direction.

5.3.3 Mesh

The excitation frequency defines the wave length used to construct an unstructured 2D mesh composed of triangular elements located in regions of varying refinement. Eight elements over the tube width were used at the virtual impedance tube inlet on the acoustic domain. Ten elements per wave length were used in the acoustic domain along the tube, which is more refined than Tam's DNS model which used 8 elements per wavelength [92]. In the Navier Stokes domain, near the slit, the viscous effect is significant. Therefore, oscillatory flow creates a viscous laminar flow associated with a Stokes layer[92], caused by the incident sound wave that accelerates the fluid through the slit channel. Tam [93] suggests a stokes layer element size to be used in DNS based on White's [101] definition of the viscous wavelength, giving

$$\Delta x_{Stokes} = \frac{1}{8}\sqrt{\frac{4\pi\nu}{f}}. \tag{5.44}$$

This equation defines 8 points per wavelength, considering the wavelength of an oscillatory stokes layer to be

$$\lambda = \sqrt{\frac{4\pi\nu}{f}}. \tag{5.45}$$

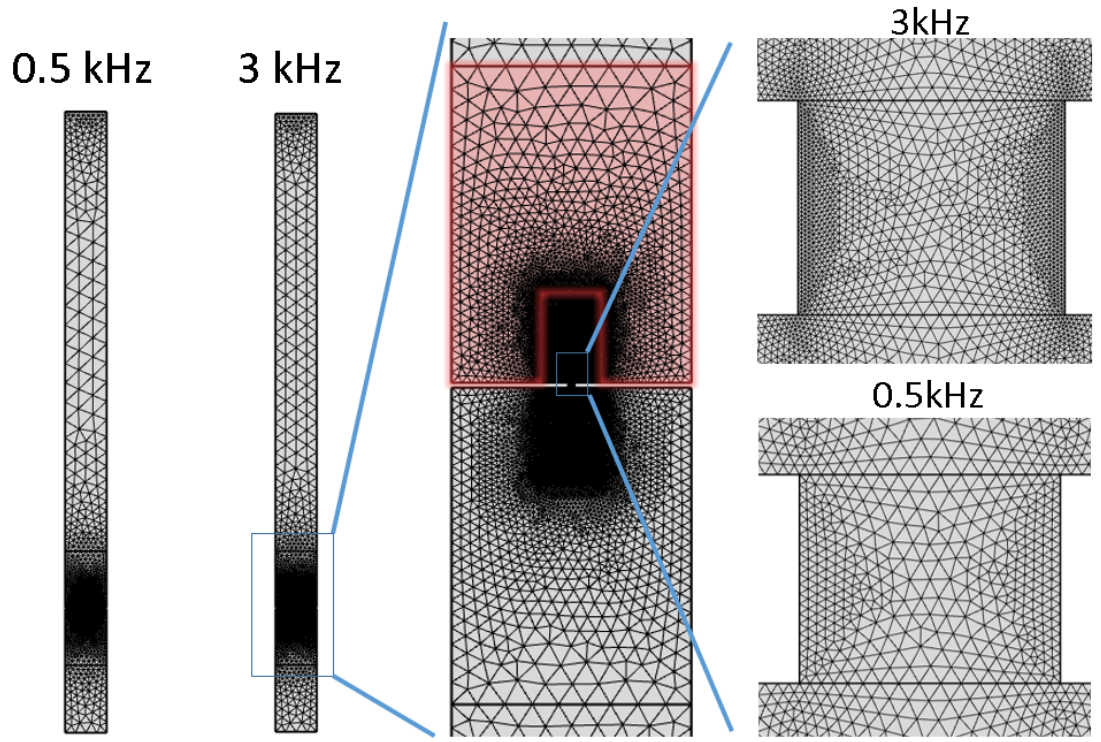

Figure 5.6: Slit liner 2D numerical mesh for 0.5 KHz and 3 kHz.

Figure 5.6 shows two different unstructured mesh sizes generated to solve the FEM model in COMSOL for frequencies at 0.5 KHz and 3 KHz. The expanded sections, highlighted in blue, show the mesh density in the region where the Navier Stokes equations are solved. The minimum and the maximum element sizes defined on the domain near the slit aperture were $\Delta x_{Stokes}/4$ and $\Delta x_{Stokes}/2$ respectively. The red shaded region is a transitional area, where the element size varies from $\Delta x_{Stokes}/4$ until $12\Delta x_{Stokes}$. This red area couples with the acoustics domain located at 70 mm from the slit aperture.

5.3.4 Slit liner model validation

The model solution took 44 hours and 21 minutes to solve for all 50 frequencies shown in red in Figure 5.7, using a 2.80 GHz i7 CPU and 8GB of RAM.

The COMSOL FEM model impedance results for pure tones at 155 dB were compared against experimental data obtained by NASA, DNS results obtained by Tam[92], and the semi-empirical model of Murray[69]. The COMSOL impedance results were calculated by using the FFT method based on the spatial average pressure and velocity over the

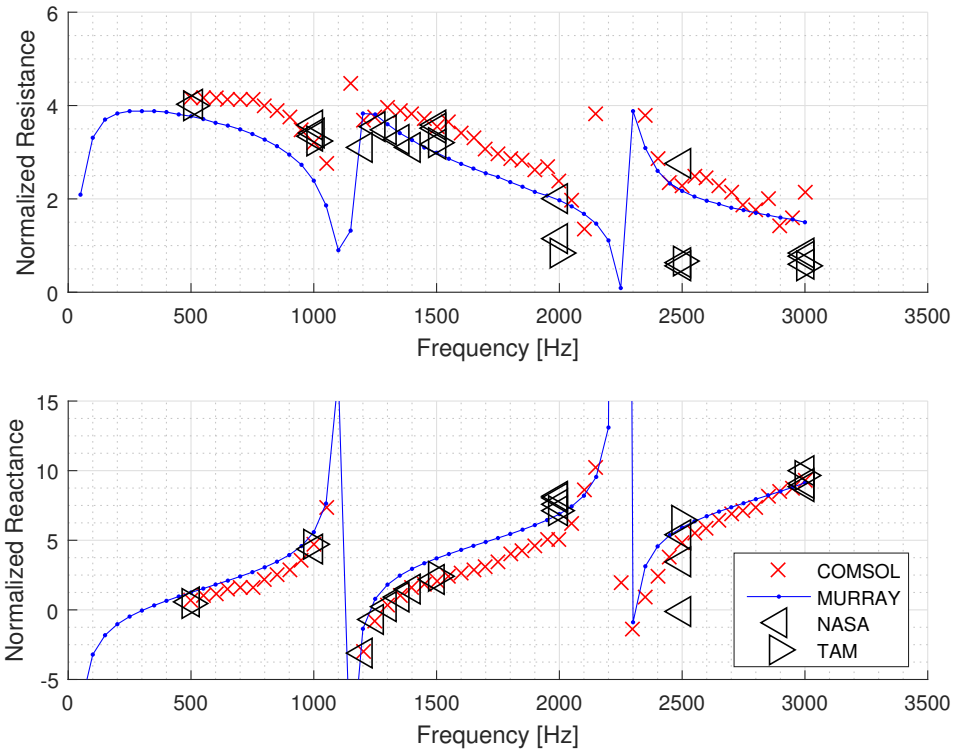

Figure 5.7: 2D Slit liner impedance validation for pure tones at 155 dB. NASA experimental results and Tam DNS results from Tam, 2005[92]. Semi-empirical prediction from Murray, 2012 [69] and COMSOL FEM predictions.

liner surface, described in Section 5.1.4. A discussion about the preferred impedance calculation method will be covered in Section 5.4.

The COMSOL model agrees well with both DNS results from Tam and experimental results at most frequencies and follow the same trend as the semi-empirical model proposed by Murray[69]. Two anti-resonances occur within the analysed frequency range, due to the slit liner cavity depth. It is noted that the experimental repeatability is reduced around the second anti-resonance, especially between 2.0 kHz and 2.5 kHz.

Figure 5.8 illustrates the reflection factor results. The COMSOL FEM model shows reflection magnitude results agree with the experimental and DNS data at lower frequencies, showing small discrepancies from 2.0 to 2.5 kHz which is near the anti-resonance of the liner. However, the differences between reflection coefficient phases are around 5 to 10 degrees for the entire frequency range.

In conclusion, the COMSOL transient 2D FEM slit liner model shows good agreement with the literature data. Physical assumptions, boundary conditions, mesh design criteria and computational time are reasonable to allow use of a personal computer to predict liner impedance by using FEM. An axisymmetric liner model was developed by using

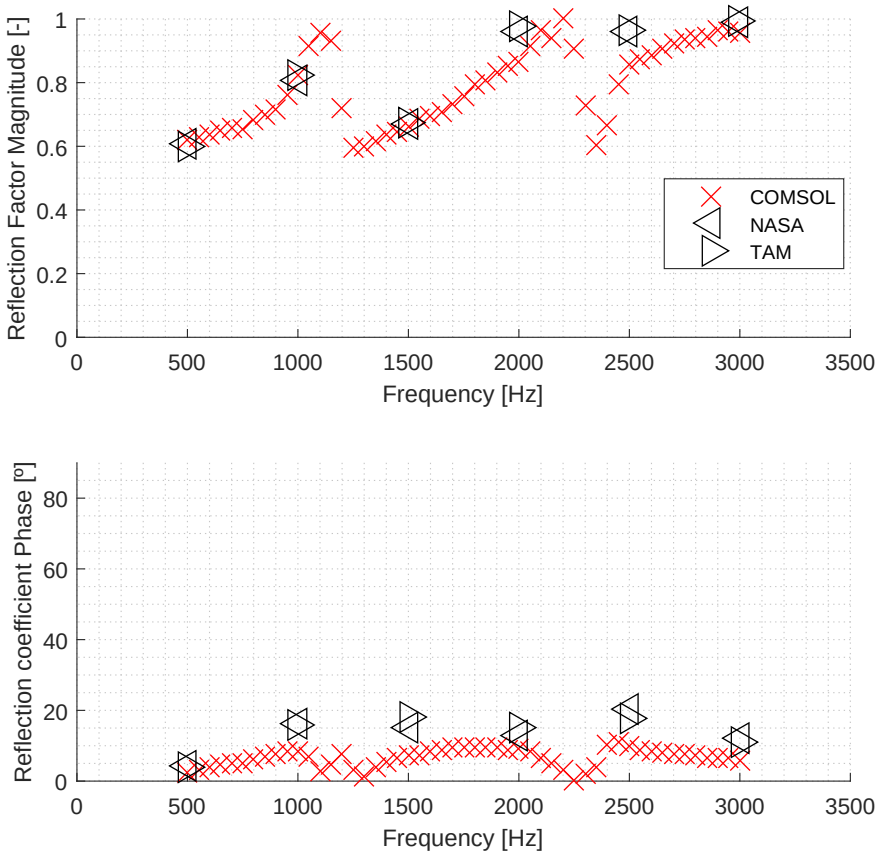

Figure 5.8: Simulation of a 2D Slit liner reflection coefficient for pure tones at 155 dB compared with data from Tam, 2005 [92].

COMSOL in order to reduce the number of elements and computational cost as well as obtain a model that represents a liner with cylindrical holes.

5.4 2D Axisymmetric liner - COMSOL model

The 2D axisymmetric numerical model proposed is based on the same fundamental equations and mesh design criteria used in the slit liner model. The same impedance calculation methods and SPL control algorithm described in section 5.2 were used. The geometry is based on a single hole resonator in an virtual impedance tube. The tube length is 208.2 mm, which is the same length as the PIM illustrated in Figure 2.6. However, the diameter of the model is adjusted in order to maintain the same effective POA as the experimental sample measured.

Four different geometries were simulated, in order to evaluate the impact of the resonator hole shape. A straight hole model was compared to models with three differing hole profiles (small chamfer, convergent-divergent and conical). The hole profiles are shown

on the right hand side of Figure 5.9. The chamfer model contains a chamfer of 1/10th the facing sheet thickness with the same minimum diameter as the straight model hole. The convergent divergent model has the minimum diameter equals the straight model and 45°angle of aperture, the same as the conical model. The straight hole model geometry is shown on the left hand side of Figure 5.9, considering the dotted dashed red line as the axisymmetric axis.

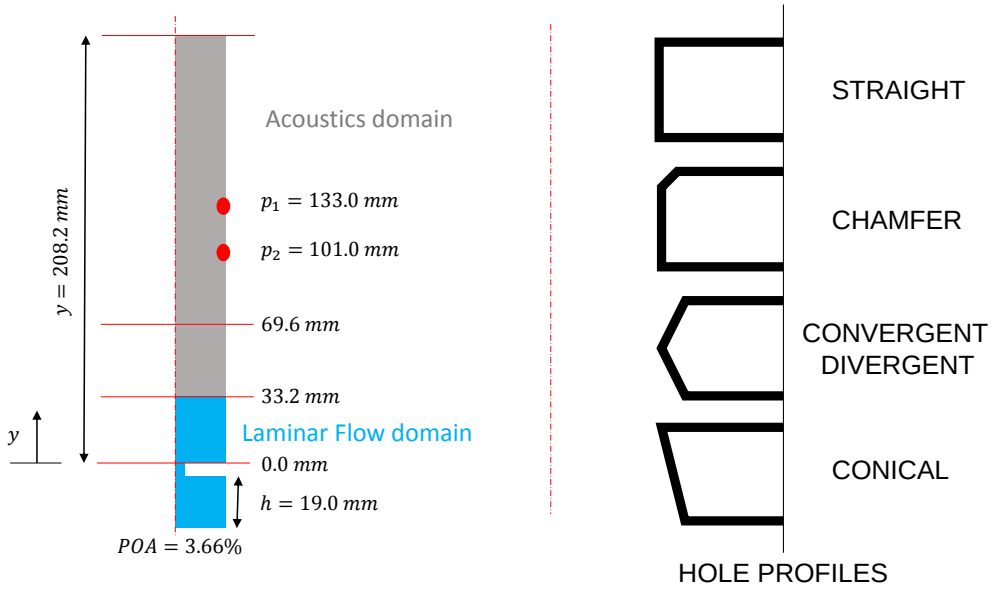

Figure 5.9: 2D liner multiphysics model geometry and hole profiles.

The modelled hole diameter, d, facing sheet thickness, l, and cavity depth, h, are the nominal values of the punched aluminium sample shown on the left hand side of Figure 3.1 (samples provided by Alenia Aermacchi). The virtual pressure taps positions, p_1 and p_2, are located at the same positions as in the PIM in order to replicate the ASTM impedance calculation method. The solid red lines show the positions of the control planes. The dash-doted line represents the axisymmetric axis. The POA used in the model is based on the calculated POA_{eff} defined by Equation 3.15 which was obtained by using pure tone experimental data and TMM on the punched aluminium liner in the sample holder. The computational domain was reduced compared to the slit case by defining a circular hole shape and cylindrical domain with the same POA as the full 2D slit liner. This reduced the computational time by around one order of magnitude.

Other authors have studied Helmholtz resonators also exploring the effect of the hole shape on liner impedance [34][17]. The COMSOL model is an idealised version of the actual liner geometry. Figure 5.10 contains four pictures of cross-sections of punched aluminium SDOF liners. The liners show the facing sheet on the left and the honeycomb on the right of each picture.

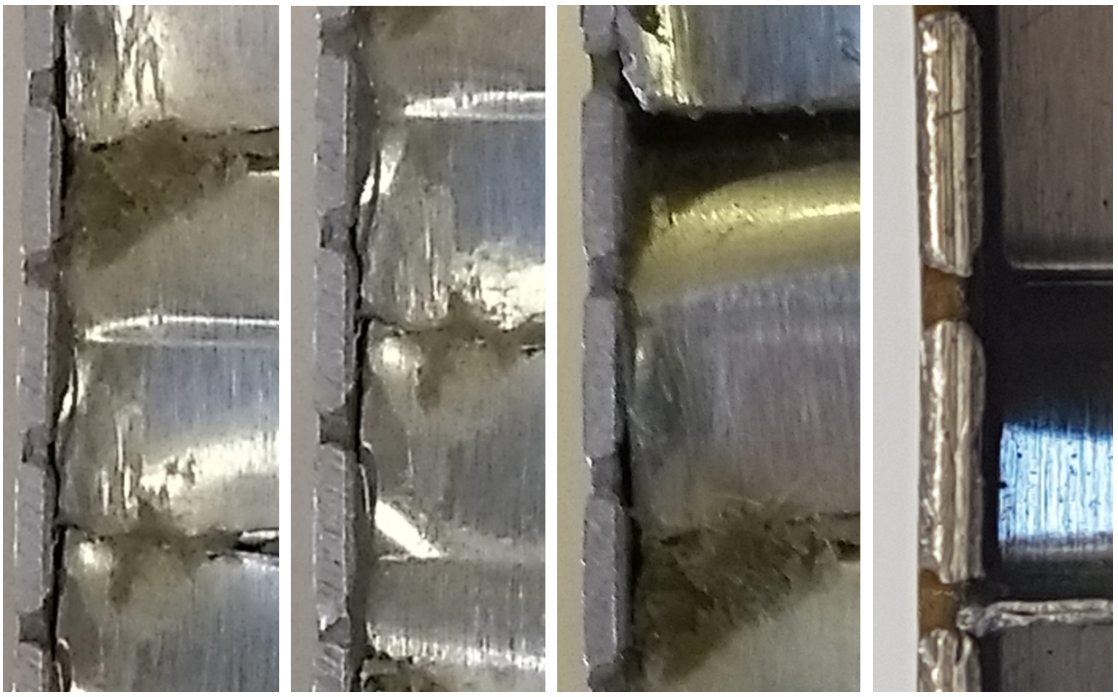

Figure 5.10: Hole shapes of a punched aluminium liner facing sheet cross section having POA=5.18%,d=0.99 mm, l=0.635mm.

It is clear that the holes are not perfectly straight. Some holes look conical and some seem to have small chamfers or rounded edges. Also, the picture on the right hand side shows an alternative punched aluminium liner, not used in the experiments, which has a honeycomb wall in front of a facing sheet hole. This is expected to cause higher resistance due to a decrease of the POA and also by viscous dissipation at the honeycomb walls. Furthermore, alternative manufacturing procedures use adhesive which blocks some of the holes, thereby reducing the effective open area. So, it is possible to have two liners with the same POA but with completely different $POAeff$. Hence, different geometries were modelled in the axi-symmetric model in order to address the effect of such features on the impedance.

5.4.1 Mesh design

The FEM unstructured mesh is composed of triangular elements in the Navier Stokes domain which are smaller than $24\Delta x_{Stokes}$. A variable element Growth Ratio (GR), which corresponds to the multiplication factor of the element size in respect to the adjacent element, was optimized. The mesh design for a pure tone at 2100 Hz is shown in Figure 5.11 as an example for a GR=1.5 in the laminar flow domain. Further refinement by using GR=1.05 was used in order to obtain an improved representation of the vortex near the liner hole. At the rectangular and triangular domains in the hole region, which in fact are axisymmetric volumes, the maximum element size set is Δx_{Stokes}. On the

other adjacent domains the element size grows until $24\Delta x_{Stokes}$ by using the GR as a scale factor until it reaches the acoustics domain.

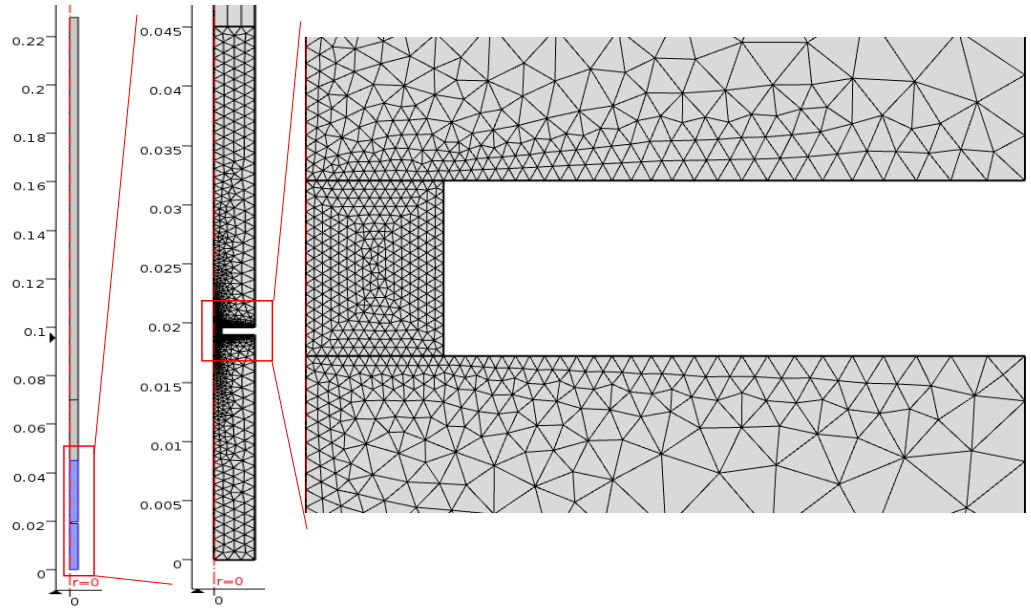

Figure 5.11: Single resonator 2D multiphysics mesh design. Straight model for a single tone excitation at 2100 Hz.

Rectangular elements are used on the acoustics domain, where 20 elements per wavelength are used for pure tone and multiple tone excitation. This means that the mesh is frequency dependent and its resolution is determined by the highest tone frequency component of the excitation signal.

Figure 5.12 shows a comparison of four different meshes created to perform simulations at 2100 Hz for pure tone excitations. All of the geometries used the GR=1.05 criteria and the dimensions are in millimetres.

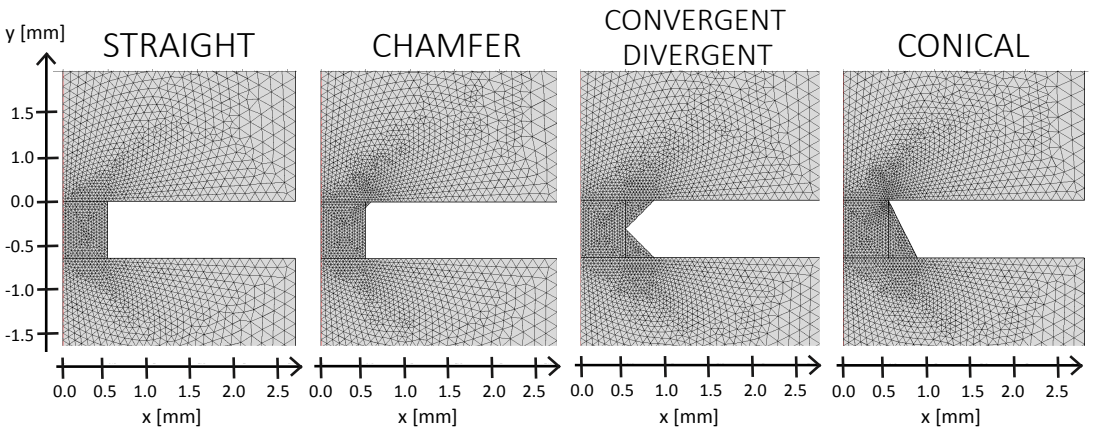

Figure 5.12: Mesh comparison near the hole for different hole geometries and GR=1.05 at 2100 Hz.

Impedance results for pure tones at 155 dB were used to evaluate the mesh convergence. A range of 21 frequencies from 600-5100Hz were calculated one at a time. The simulations were performed on a Dell Precision M4700, 2.80 GHz i7 CPU with 8GB of RAM. The most expensive calculation is in the situation with highest non-linearity and most refined mesh. The time taken to perform the straight hole model calculation for each GR was:

- GR=1.05 -> total solution time = 9h27min,
- GR=1.10 -> total solution time = 5h56min,
- GR=1.30 -> total solution time = 3h55min,
- GR=1.70 -> total solution time = 2h44min.

Figure 5.13 shows the impedances calculated by using the different approaches described in Section 5.1 for a pure tone at 2100 Hz and 155 dB OASPL. The straight hole model was used, that corresponds to the left hand side of Figure 5.12, with GR=1.05. Data was acquired at the probes and planes illustrated in Figure 5.9, where "Mic1" corresponds to P_1 at $x = 133$ mm, and "Mic2" correspond to P_2 at $x = 101$ mm. The result "Liner" corresponds to the spatial average values calculated at $x = 0.0mm$. "Plane 1" corresponds to the spatial average values calculated at $x = 33.2$ mm. "Plane 2" corresponds to the spatial average values at $x = 69.9$ mm. Finally, "Inlet" correspond to the plane at the top of the acoustic domain, $x = 208.2$ mm above the liner surface. Each method is represented by its acronym as named in the titles of each corresponding subsection in section 5.1.

One cycle corresponds to one period of the driving frequency, consequently $T = 1/f = 4.76E^{-4}$ seconds. Two particular methods, FFT(Liner) and FC(Liner) show systematic resistance differences in respect to the other methods. However, all methods agree within $0.2\rho c$ for resistance and reactance. Also, all methods converge after approximately 15 cycles. This means that the sample size of the pressure time history collected at the points excluding the transient solution can be as small as 15 cycles in order to perform the impedance calculation methods. Some methods are more dependent on the sample size then the others, but 15 cycles is shown to be a conservative convergence parameter.

The FFT impedance calculation method on the liner surface, FFT(liner), was chosen as the preferred approach because it shows the lowest impedance variation with number of cycles among all the methods evaluated. This means that after a few cycles this method produces the same results as for a larger time history. The position of the probes strongly influences the precision of the pressure and velocity results due to the standing waves present in the impedance tube. If a virtual microphone or plane is positioned in a zone with minimum total pressures the numerical errors will be more evident, causing errors in the impedance calculated. The convergence of each impedance calculation method was analysed for all of the test cases for different frequencies. The number of cycles

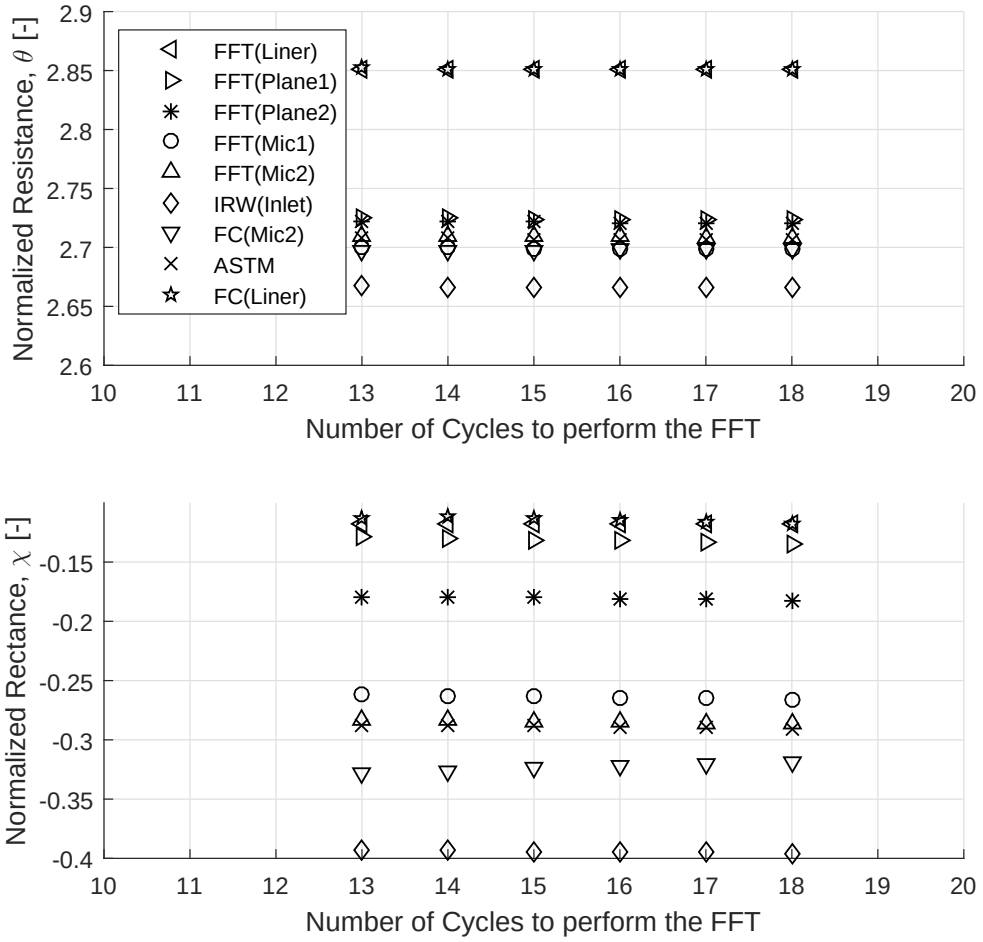

Figure 5.13: Convergence analysis of impedance calculation methods for 2100 Hz pure tone at 155 dB OASPL and GR=1.05.

used to calculate the impedance was varied to check the convergence of each method by using different sample sizes. Only the steady state pressure $\overline{P_p}(t)$ and velocity $\overline{U_p}(t)$ were considered during the impedance calculation.

5.4.2 Pure tone excitation

Several analysis were performed in order to validate the numerical models against experimental data for pure tone (PT) excitations. Different hole geometries (straight hole, 1 side chamfer, convergent-divergent, and conical) were included in the study. The COMSOL numerical predictions were evaluated by comparing them to the punched aluminium SDOF liner in-tube TMM measurements ($POAeff = 3.5\%$). The iterative process described in section 5.2 was used to match the experimental pressure measured at the liner surface with the spatially averaged pressure calculated by the COMSOL models. The

comparisons were made using the liner surface impedance. The facing sheet mass reactance was also extracted by using $m_f = \chi + cot(kh)$, were k is the wave number and h is the cavity depth.

Figure 5.14 shows a comparison of spatially averaged SPLs measured at the sample surface and the COMSOL calculated values for the straight hole model. The tolerance criteria of 0.5 dB used in the SPL control algorithm provided good results at all of the SPLs simulated, as shown in Figure 5.14.

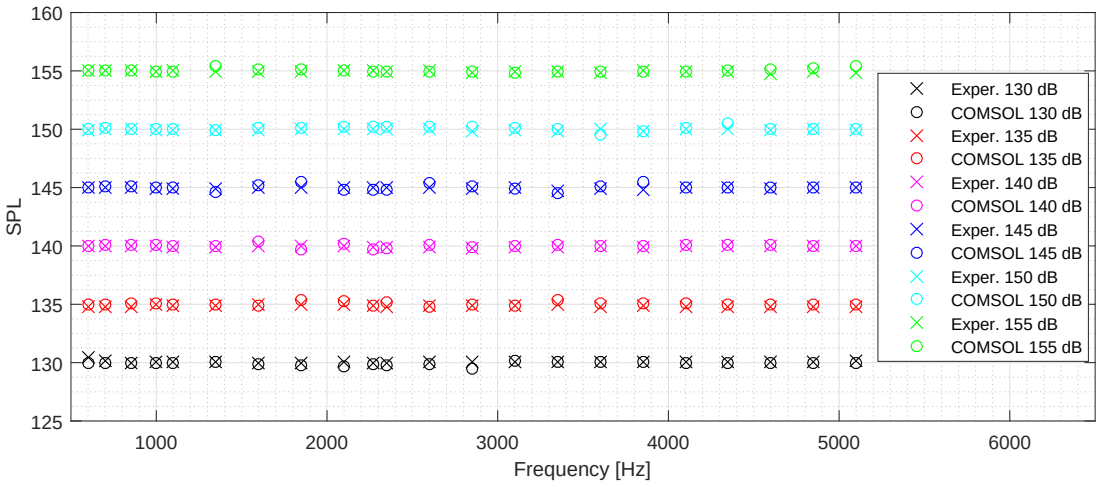

Figure 5.14: SPL Validation: Straight hole COMSOL model against TMM experimental data for the punched aluminium SDOF liner in the sample holder.

Each point on the graph corresponds to one measurement (Exper.) and one numerical simulation (COMSOL). A parametric analysis was performed for 22 pure tone frequencies at 6 different SPLs. Any optimization method could be used instead of the suggested approach, however, 2 or 3 iterations were sufficient to achieve good correspondence between the experimental SPL and the numerical model.

Each combination of pure tone excitation frequency and SPL provide a liner impedance and a reflection coefficient, for which the measured amplitude and phase values could be compared. The calculated reflection coefficient using the FFT(liner) method is shown in Table 5.1.

The reflection coefficient was calculated for each combination of frequency and SPL. This is not the design operating condition of the liner in flight, as the liner is exposed to grazing flow and consequently needs to meet higher resistances. However, it is possible to observe that as the SPL on the pure tone increases, the reflection coefficient decreases, except near the resonant frequency. At high SPL the liner acts as a broadband attenuator with moderate absorption.

Figure 5.15 shows a comparison of normalized resistances from the experimental data and from four different COMSOL numerical models implemented for pure tone (PT)

Table 5.1: Reflection coefficient calculated by COMSOL Straight hole model excited by pure tones.

	SPL aimed [dB]					
Freq [Hz]	130	135	140	145	150	155
600	0.98	0.98	0.97	0.96	0.94	0.90
700	0.97	0.97	0.96	0.94	0.90	0.85
850	0.95	0.95	0.93	0.88	0.83	0.77
1000	0.92	0.91	0.87	0.81	0.73	0.68
1100	0.90	0.87	0.82	0.74	0.66	0.62
1350	0.78	0.72	0.64	0.55	0.50	0.50
1600	0.57	0.48	0.41	0.36	0.37	0.43
1850	0.37	0.26	0.19	0.20	0.30	0.41
2100	0.38	0.24	0.05	0.09	0.26	0.40
2350	0.62	0.47	0.26	0.16	0.26	0.39
2600	0.76	0.65	0.47	0.30	0.29	0.40
2850	0.84	0.77	0.65	0.46	0.35	0.41
3100	0.88	0.84	0.75	0.60	0.45	0.44
3350	0.91	0.89	0.82	0.73	0.55	0.47
3600	0.93	0.91	0.87	0.80	0.65	0.52
3850	0.94	0.93	0.90	0.84	0.76	0.57
4100	0.95	0.94	0.92	0.87	0.80	0.65
4350	0.96	0.96	0.94	0.90	0.84	0.72
4600	0.97	0.96	0.95	0.92	0.87	0.80
4850	0.97	0.96	0.96	0.93	0.89	0.84
5100	0.97	0.97	0.96	0.95	0.91	0.87

excitations. Four different geometries were simulated in order to evaluate the effect of the hole shape on the impedance. Three different OASPLs are presented, where the OASPL measured at the liner surface was compared to the numerical spatial average OASPL in each model and calibrated by using the algorithm to ensure an error of less than 0.5 dB. The resistances of the experimental data for the punched aluminium SDOF sample in the sample holder were obtained by the TMM. The FFT impedance calculation method described in the section 5.1.4 was used to extract the impedances at the liner surface of the numerical models.

The COMSOL resistance predictions follow the trends of the experimental data. In general, the resistance non-linearity is underestimated at low SPL, and over-estimated at high SPL, for each of the modelled hole shapes. However, the COMSOL results clearly demonstrate the importance of hole shape.

At 130 dB OASPL the numerical models show relatively poor agreement with the experimental data. At 140 dB OASPL the straight hole model shows excellent agreement with experimental data. At 150 dB OASPL the convergent-divergent model, shows good agreement with experimental data from 1.0 kHz until 2.0 kHz. In general, the model with a Chamfer on one side shows reasonable agreement with experimental data for different OASPLs.

The experimental resistances from 3.0 kHz to 5.0 kHz at 130 dB and 140 dB gives values that does not correspond to any of the models, which suggests that TMM is not providing reliable results. The relative increase in resistance at high frequencies reduces as SPL

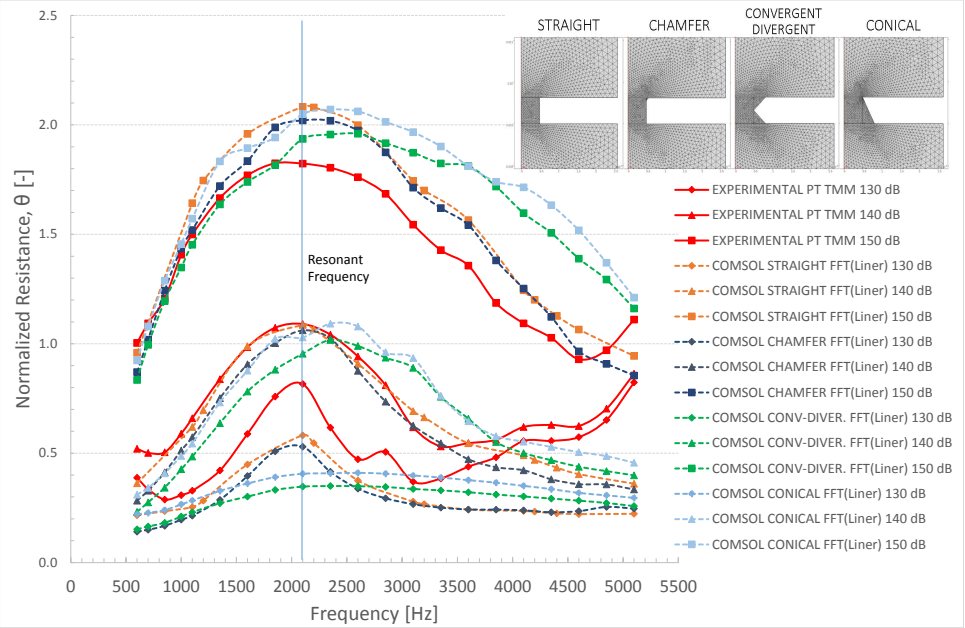

Figure 5.15: Normalized resistance comparison for different geometries of the COMSOL model against experimental data for pure tones at 130 dB, 140 dB and 150 dB OASPL.

increases. This may suggest some gaps in the sample which close off acoustically as the resistance of the gap increases.

The comparisons between the TMM and Dean's *in situ* method shown in Figure 3.27 and Figure 3.28 show a lack of agreement from 3.0 kHz until 5.0 kHz for two different 3D printed samples. This corroborates the hypothesis that the experimental results are questionable in this frequency range.

Figure 5.16 shows the experimental resistance obtained by the TMM at 130 dB compared with the straight hole model results in COMSOL, obtained by using all of the impedance calculation methods described in Section 5.1. All methods show different results for higher frequencies and agree near the resonant frequency. The IRW method (which uses the incident and reflected waves of the inlet to calculate the reflection factor) produced the same behaviour as the experimental result obtained from TMM. It is clear that, at 130 dB, TMM and other impedance calculations produce uncertainties at high frequencies so the data below 3.0 kHz is considered more reliable.

Figure 5.17 shows the same analysis for different impedance calculation methods at 150 dB OASPL. A large increase at high frequencies is observed when the IRW method is used. However, the experimental data show a much reduced increase in resistance compared to the 130dB case, with the increase seen at frequencies above 4.5KHz rather than above 3KHz. The ASTM method is overlaid with FC(Mic2) method and both

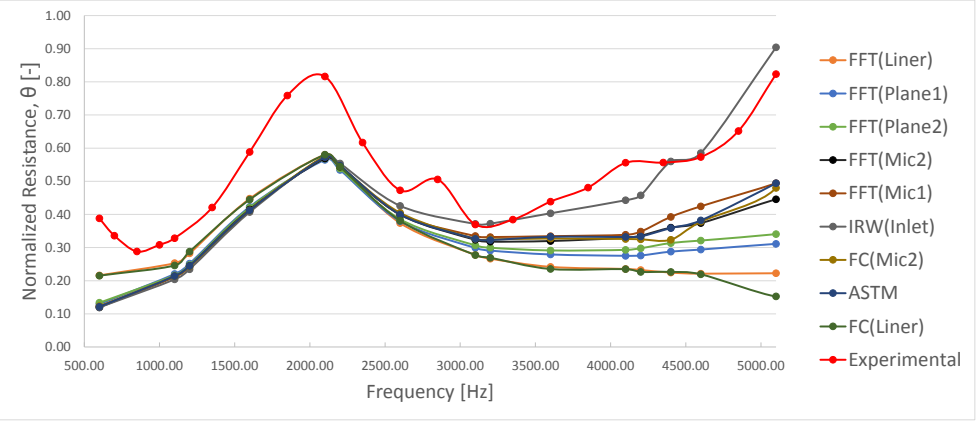

Figure 5.16: Normalized resistances of various impedance calculation methods implemented in the straight hole COMSOL numerical model against experimental data calculated by TMM and measured on a punched aluminium SDOF liner in the sample holder, POA=3.5%, d=0.990 mm, l=0.635 mm, h=19.1 mm, for pure tones at 130dB OASPL.

deviate from experimental results at high frequencies but show similar trends. The majority of the methods shows good agreement from 0.6 kHz up to 2.0 kHz, but diverge at high frequencies. The FFT(Liner) shows the expected trend, so it is likely to be the most reliable method and agrees with FC(Liner).

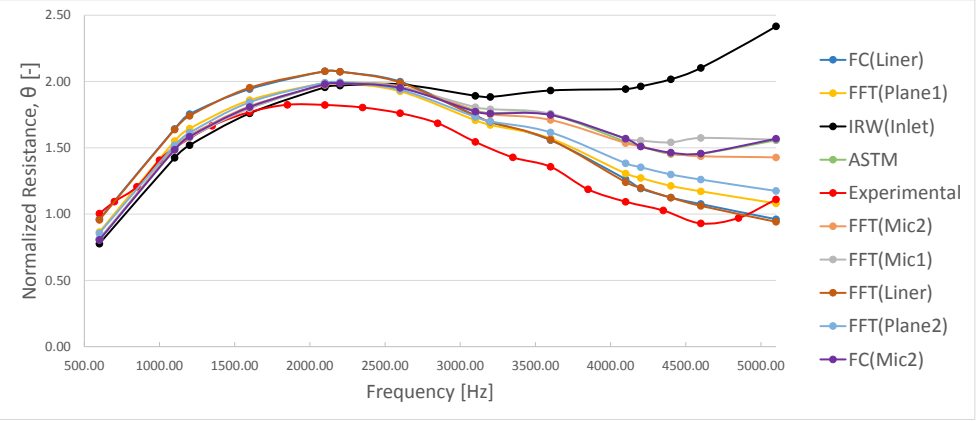

Figure 5.17: Normalized resistances of various impedance calculation methods implemented in straight hole COMSOL numerical model against experimental data calculated by TMM and measured on a punched aluminium SDOF liner in the sample holder, POA=3.5%, d=0.990 mm, l=0.635 mm, h=19.1 mm, for pure tones at 150dB OASPL.

Figure 5.18 shows the reactance predictions for the four different hole geometries simulated in COMSOL model for pure tones at 130 dB OASPL. The straight and chamfer models show good agreement with each other, and with experimental data for frequencies up to 3.0 kHz. The convergent-divergent and conical models show significantly higher

resonant frequencies than the straight and chamfer models which diverge from the experimental results. Higher resonant frequencies is consistent with lower inertance in convergent-divergent and conical models.

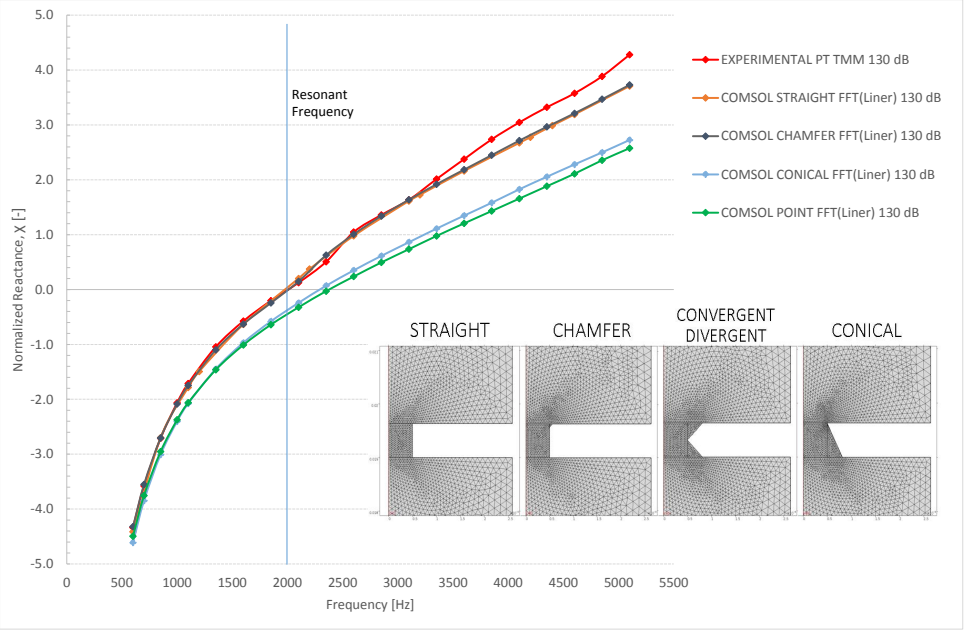

Figure 5.18: Normalized reactance comparison for different geometries of the COMSOL model against experimental data calculated by TMM and measured on a punched aluminium SDOF liner in the sample holder, POA=3.5%, d=0.990 mm, l=0.635 mm, h=19.1 mm, for pure tones at 130dB OASPL.

Figure 5.19 shows the reactance predictions for four different hole geometries simulated in COMSOL for pure tones at 150 dB OASPL. The chamfered model shows excellent agreement with the experimental data up to 3.0 kHz. The straight model shows excellent agreement up to 4.0 kHz.The convergent-divergent and conical models again diverge from the experimental data.

Three main types of flows within and near the hole were observed in the numerical results. The first type occurs for $\omega_0 < 1$ and is characterized by a jet during both inflow and outflow phases of the cycle as observed by Ingard and shown in Figure 2.1.(c). The second type is characterized by a pulsation that causes strong vortex shedding for excitations near the resonant frequency $\omega_0 \approx 1$, as observed in Figure 2.1.(b). The third type occurs at higher frequencies $\omega_0 > 1$ where the velocity magnitudes are smaller but interact more with the walls of the hole creating increased localized shear stresses, as observed in Figure 2.1.(a).

When the pressure outside the resonator is higher than the pressure inside the cavity, the sound wave accelerates the fluid particles through the hole from outside into the liner cavity. If the geometry of the hole is symmetric, the jet changes direction during the other half cycle when the pressure difference reverses, showing the same behaviour

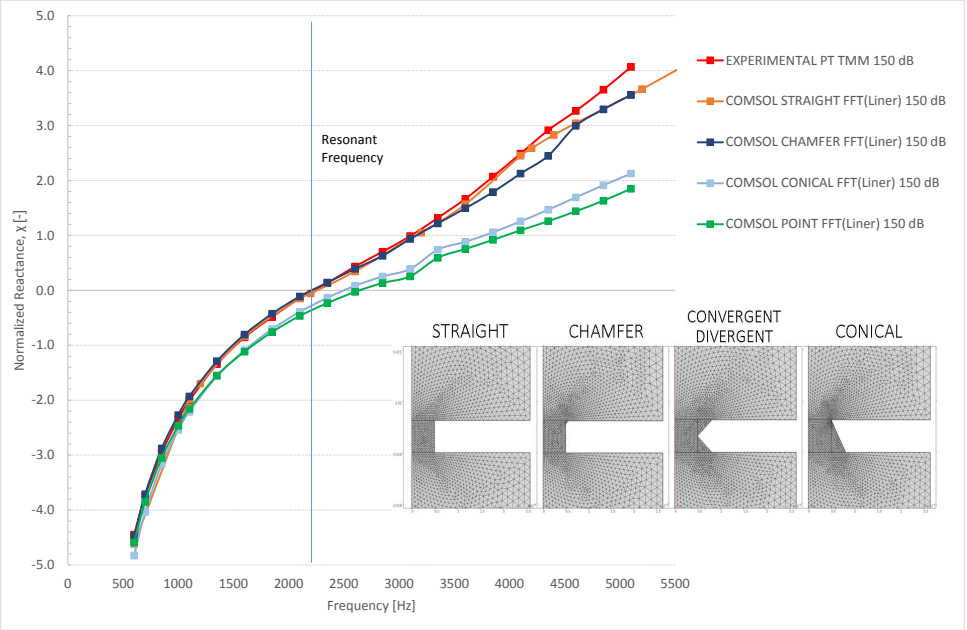

Figure 5.19: Normalized reactance comparison for different geometries of the COMSOL model against experimental data calculated by TMM and measured on a punched aluminium SDOF liner, POA=3.5%, d=0.990 mm, l=0.635 mm, h=19.1 mm, for pure tones at 150dB OASPL.

outside the resonator. The particle displacement in the hole also depends on this pressure difference, and on the excitation frequency.

Figures 5.20 and 5.21 show the vorticity magnitude field, and axial velocity field for the four different hole geometries. The gross parameters of these three models are those for the punched aluminium SDOF liner, POA=3.5%, d_{min}=0.990 mm, l=0.635 mm, h=19.1 mm; apart from the hole shape. The same time frames were selected for the upper and lower plots. The outward jet ejection is shown in Figure 5.20. The inward jet ejection is represented in Figure 5.21. A pure tone excitation at 600 Hz and 130 dB SPL was simulated in all cases. The vorticity magnitude is displayed on a logarithmic scale in 1/s and the axial velocity is represented in m/s.

Significant differences in the velocity and vorticity fields can be seen depending on the pulsating jet direction. Sharp edges at the exit plane causes flow acceleration and larger vortices that are ejected away from the hole. Chamfered edges on the exit plane cause smaller vortices near the hole and more flow reversal at the entrance to the hole. Sharp edges on the entrance plane cause a pronounced *vena contracta*, however, chamfered edges at the entrance plane causes lower axial velocity components.

A jet with high velocity in the core is observed when the excitation frequency approaches the resonant frequency of the resonator, $w \approx 1$, as shown in Figure 5.22. Five stream lines are used to identify the trajectory of the fluid particles on the entrance plane of the liner hole. The velocity profile on the hole creates a shear layer that extends beyond

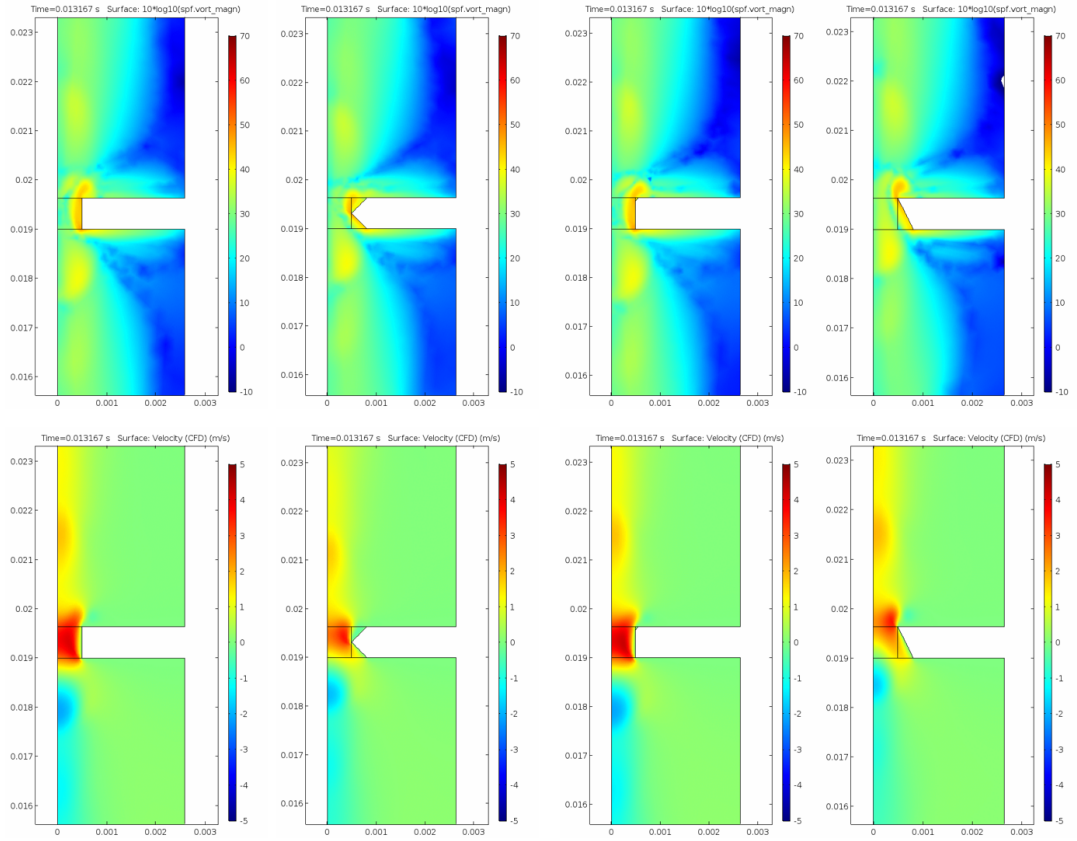

Figure 5.20: Vorticity (top) and axial velocity (bottom) fields of different model geometries during the jet ejection (outward the resonator) for a pure tone at 600 Hz and 130 dB OASPL.

the hole edges and creates a vortex ring that is convected away from the resonator hole. The flow field near the resonator aperture contains flow reversal during both the inflow and outflow periods, in order to maintain mass conservation. The conical model shows a narrow jet with more transverse velocity components, that cause larger vortices that are convected more efficiently than for the other hole shapes. The sharp edge model shows a *vena contracta* and higher vorticity magnitudes near the hole walls, suggesting that the shear stresses due to the boundary layer and flow reversal are stronger in that region.

5.4.3 Axisymmetric model validation

Zhang & Bodony investigated the acoustic liner response to high SPL excitation with and without grazing flow by using Direct Numerical Simulation (DNS)[102][103][104]. A benchmark case will be covered in this section, which compares the proposed COMSOL model, the 1D semi-empirical time domain model proposed, the DNS results obtained by Zhang & Bodony, NASA experimental results, and semi-empirical predictions in the frequency domain by Murray & Astley [69]. Table 5.2 details the liner geometry used in this benchmark study.

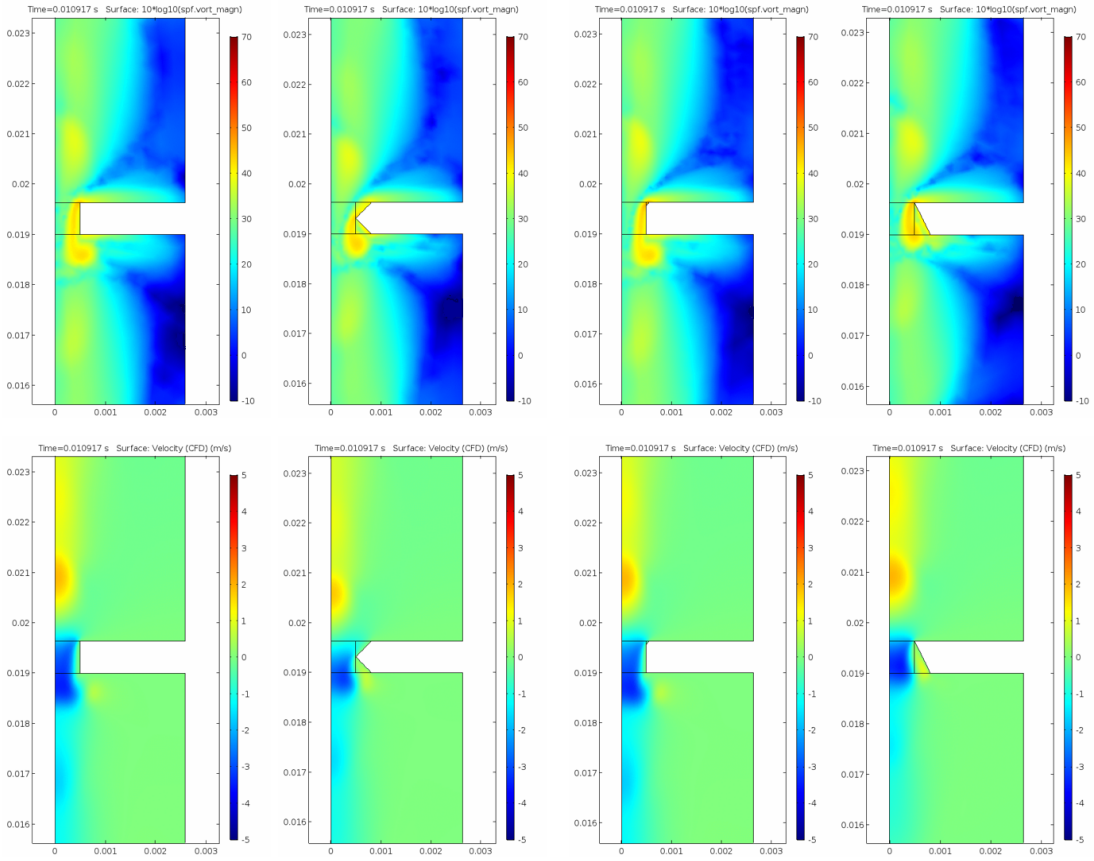

Figure 5.21: Vorticity and axial velocity fields of different model geometries during the jet ejection (inward from the resonator) for a pure tone at 600 Hz and 130 dB OASPL.

Table 5.2: Benchmark liner geometry. Adapted from: Zhang & Bodony, 2011[102].

Parameter	**symbol**	**value and unit**
Aperture diameter	d	0.99 mm
Facesheet thickness	l	0.64 mm
Cavity depth	h	38.10 mm
Hexagonal cavity edge length	a	5.49 mm
Percentage of open area (POA)	σ	6.4%

Since each honeycomb cavity has several apertures on a SDOF liner, it can be modelled as an array of equally spaced resonators that do not interact with each other [38]. Only one resonator modelled with the same POA of the entire liner can be modelled in order to simplify the problem without grazing flow. The perforated plate hole walls are straight and perpendicular to the liner surface in this study. The 3D DNS model proposed by Zhang & Bodony is composed by a hexagonal resonator cavity. The 2D model in COMSOL is composed of an axi-symmetric cylindrical resonator cavity, which significantly reduces the degrees of freedom in comparison to the 3D model.

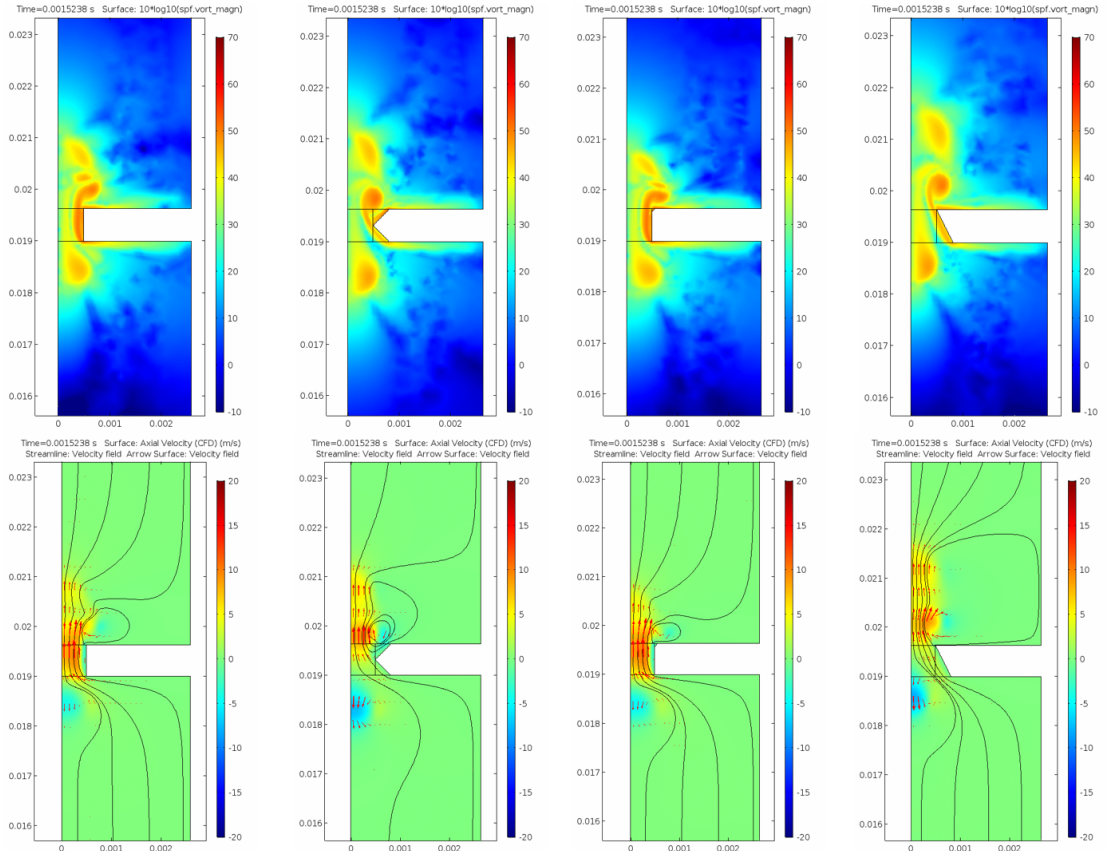

Figure 5.22: Vorticity (top) and velocity (bottom) comparisons among different model geometries for a pure tone at 2100 Hz and 130 dB OASPL. Arrows represent the velocity directions and relative magnitudes.

The normalized impedance results for 130 dB pure tone excitation are shown in Figure 5.23. They are multiplied by the liner porosity σ for consistence with the results published by Zhang & Bodony. It can be seen in the top graph that COMSOL resistance shows good agreement with Zhang & Bodony DNS results, however, both models diverge from the experimental data as the frequency increases. The proposed 1D model agrees with experimental resistance data at 1.5 kHz and 3.0 kHz but disagrees with the experimental results at 2 kHz and 2.5 kHz. The semi-empirical resistance prediction agrees with the COMSOL predictions at all frequencies.

COMSOL reactance predictions are in agreement with the experimental results at 1500 Hz and 2000 Hz, however, both DNS and COMSOL diverge from the experimental results at higher frequencies. The 1D proposed model shows reasonable resistance results at 1500Hz and 3000 Hz, however it disagrees with the experimental results at intermediate frequencies. Again, the semi-empirical reactance prediction agrees with the COMSOL prediction.

Only Zhang & Bodony DNS predictions are available at 3 kHz for high SPLs up to 160dB, as in Figure 5.24. Although the COMSOL and Zhang & Bodony DNS models show reasonable agreement at 130 dB, the COMSOL model predicts lower resistances

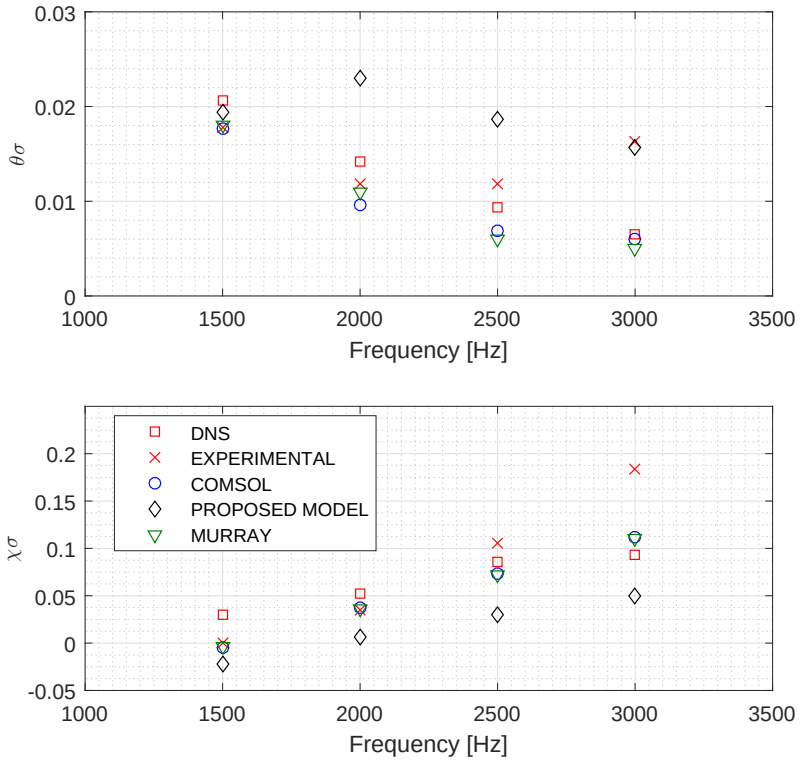

Figure 5.23: Pure tone validation of the COMSOL model and 1D proposed model for a liner with POA=6.4%, d=0.99 mm, l=0.64 mm, h=38.10 mm, at 130dB. Experimental and DNS data from Zhang & Bodony, 2011 [102].

and higher reactances than DNS at high SPLs. The 1D semi-empirical model agrees reasonably well with the COMSOL resistance predictions, but shows lower reactance predictions than the DNS and COMSOL models. The semi-empirical prediction agrees with the COMSOL predictions.

Figure 5.25 shows the vorticity fields on the edge of the resonator aperture for 1500 Hz and 3000 Hz pure tone excitation at 130 dB. Figures 5.25.(a) and (b) are the vorticity magnitude snapshots during the outflow process of DNS and COMSOL models at 3000 Hz respectively and an incident SPL of 130 dB. The vortex structures captured by the COMSOL model are of similar size and magnitude to the Zhang & Bodony DNS simulation.

The acoustic flow creates a shear layer near the wall, which is the main dissipation mechanism at 3.0 kHz as shown in Figures 5.25.(a) and (b). Figures 5.25.(c) and (d) are the vorticity snapshots during the outflow process of the DNS and COMSOL models at 1500 Hz respectively, a frequency near the resonance frequency of this sample, with higher acoustic velocity than at 3 kHz. Both modelling approaches clearly show two distinctive shear layers, one at the wall and one located away from the wall, meaning that in this time step there is flow reversal on the hole creating the vortex. The flow direction is upwards at the center of the aperture, and downwards near the edges of the

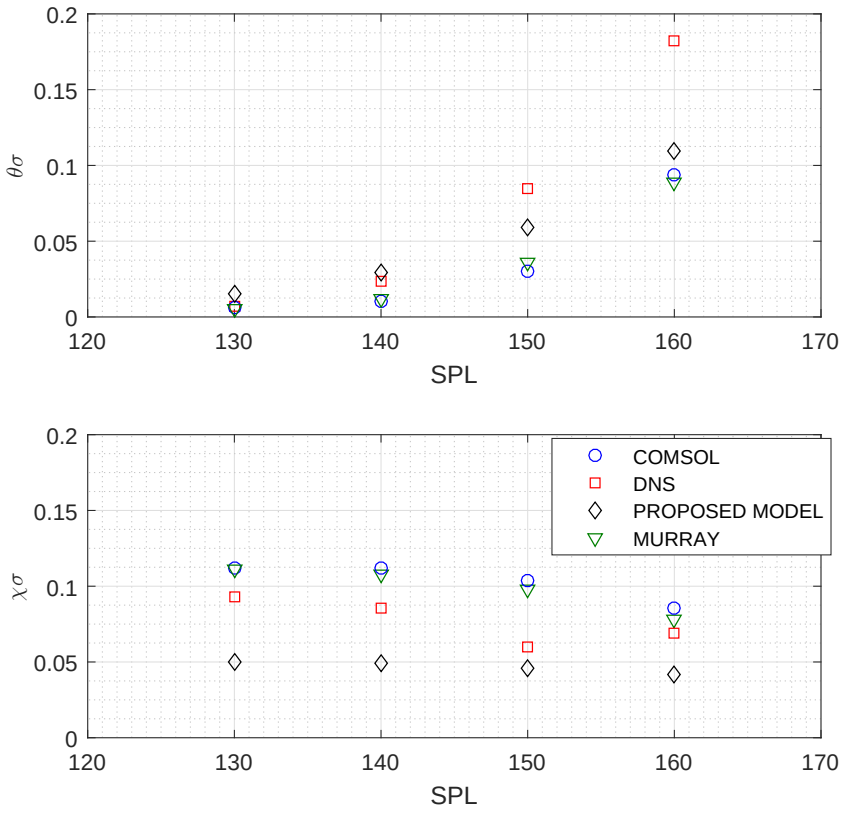

Figure 5.24: Pure tone COMSOL model, 1D proposed model, DNS and Experimental impedances for a liner with POA=6.4%, d=0.99 mm, l=0.64 mm, h=38.10 mm, at 3.0 kHz. DNS data from Zhang & Bodony, 2011 [102].

aperture. This additional shear layer occurs during a limited period of time in each cycle, and it is more pronounced for $\omega_0 \approx 1$.

A finer mesh is essential to observe the details in the fields calculated by the numerical model, costing computational time but allowing better understanding of the physical mechanisms. The element growth ratio was used to control the refinement near the aperture. A comparison between three different growth ratios is shown in Figure 5.26 for 5100Hz excitation at 155 dB. The vorticity magnitude is plotted in a logarithmic scale. It is clear that a second shear layer is formed in the aperture and that the magnitude and size of the vortex ring and the shear layers are comparable. The vortex size becomes smaller as the excitation frequency increases above the resonant frequency $\omega > 1$, showing velocity profiles with lower magnitudes and consequently lower kinetic energy. Pure tones at high frequencies $\omega >> 1$ causes localized vorticity, which reduces the resistance and increases the inertance.

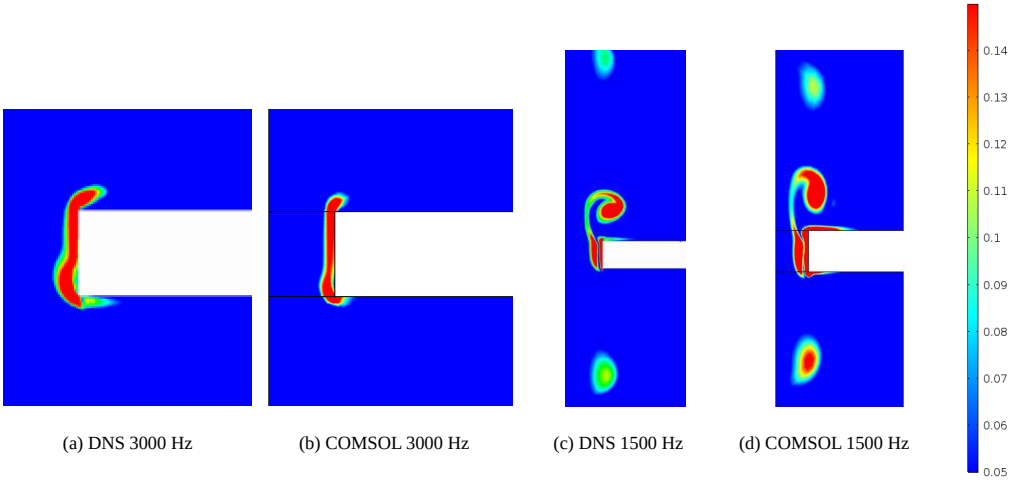

Figure 5.25: COMSOL and Zhang & Bodony DNS [102] pure tone normalized vorticity magnitude $|\omega d/c|$ for a liner with POA=6.4%, d=0.99 mm, l=0.64 mm, h=38.10 mm, at 130dB.

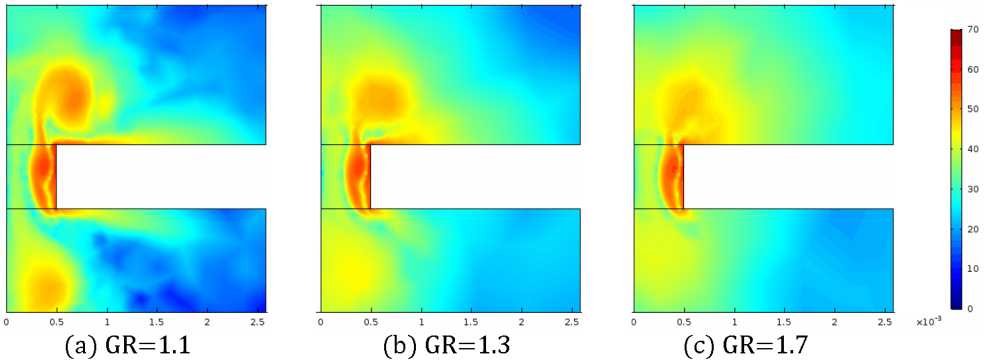

Figure 5.26: COMSOL pure tone vorticity magnitude due to the element growth ratio for pure tone at 5100Hz and 155 dB.

5.5 Preliminary Conclusions

Different impedance calculation techniques were implemented in order to calculate the FEM numerical impedances by using COMSOL & MATLAB. A simplified 2D axisymmetric model was calibrated to simulate the same OASPL as the measured value over the liner surface and allow direct comparisons with the data obtained. The COMSOL & MATLAB models show reasonable agreement with DNS for a 2D slit liner [92] and a 3D circular aperture liner [102] used as benchmark studies. The use of a 2D axisymmetric model significantly reduces the computational time to perform the FEM calculations, permitting the creation of several analyses at different frequencies, SPLs and geometries.

Different hole shapes were considered in order to evaluate the sensitivity of the results to hole shape and the results were compared to the experimental data collected for a punched aluminium SDOF liner. Preliminary results show that convergent-divergent

chamfers on both leading and trailing edges cause a reduction in resistance at low frequencies ($\omega_0 < 1$) when compared to a straight hole with the same minimum diameter. The conical model also show significant reduction in resistance at low frequencies. The reactance of the conical and convergent-divergent models are lower than the straight model and also do not match the experimental data.

Vortex shedding is the main mechanism of dissipation at high SPLs. It occurs more readily for excitation with frequency components near the resonant frequency. A reduction in vortex shedding occurs as the frequency, reactance, and impedance modulus increase, leading to lower acoustic velocities for this cavity depth. The amount of vorticity is a function of the hole wall shape, where sharp edges narrow the *vena contracta* and chamfered edges causes more instabilities due to increased transverse components of velocity. Localized vortices stay closer to the hole when chamfers are present and are pushed away from the hole when straight edges are used. This effect causes the end correction to become smaller as the vortex takes the kinectic energy away from the hole and consequently leads to greater dissipation and acoustic resistance.

Chapter 6

Multiple tone liner response

The preceding chapters have shown that acoustic liner impedance can be successfully predicted for pure tone excitation by using either analytical, experimental or numerical techniques. It was also shown from experimental data presented in Chapter 3 that multiple tone excitation at non-linear SPLs significantly alters the liner impedance. The challenge is to be able to predict the impedance in the presence of multiple tones, of similar amplitude. The presence of two tones at a fundamental and a harmonic frequency is a signal typically experienced by installed aero engine liners. It leads to complicated flow patterns within a perforate hole as the flow is being driven simultaneously by two different frequencies. To the authors' knowledge, no method exists for accurately predicting impedance under this type of signal, so this represents the primary goal of this work.

The impedances of a punched aluminium SDOF liner and two 3D printed liners with low porosity were measured for even harmonically related combinations of tones. The objective of this chapter is to discuss straight hole COMSOL model impedance results in the presence of multiple tone excitations, by using the 2D axi-symmetric numerical model described in chapter 5. The straight hole model was chosen as it provided an acceptable representation of the measured panel non-linear impedance.

The numerical results were compared to experimental data and analysed in order to obtain semi-empirical predictions for multiple tone excitation. Multiple tone signals used in the COMSOL models mimicked the signals used in the experiments. The combination of two harmonically related tones are composed of a fundamental tone and and the first even harmonic twice the frequency of the fundamental.

6.1 Signal characteristics

Figure 6.1 shows analytical multiple tone signals in the time domain for a combination of relative phases and amplitudes for two frequency components at 600 Hz and 1200 Hz, in order to graphically evaluate the pressure signals that impinge on the punched SDOF perforate liner surface. The graphs in the left hand column contain the pressure traces of two frequency components at the same amplitude of 632 Pa (SPL_1=SPL_2=150 dB), so $\Delta SPL = SPL_1 - SPL_2$=0. The centre column graphs contain the pressure traces of signals with more energy (150 dB) within the fundamental (600 Hz) in comparison to the harmonic (1200 Hz, 200 Pa, 140 dB), so ΔSPL=10dB. The right hand side graphs contain the pressure traces with more energy within the harmonic (1200 Hz) at 150 dB, in comparison with the fundamental (600 Hz) at 140 dB, consequently ΔSPL=-10dB. The phase between frequency components of the multiple tone signals was progressively varied by 90° in each row of Figure 6.1.

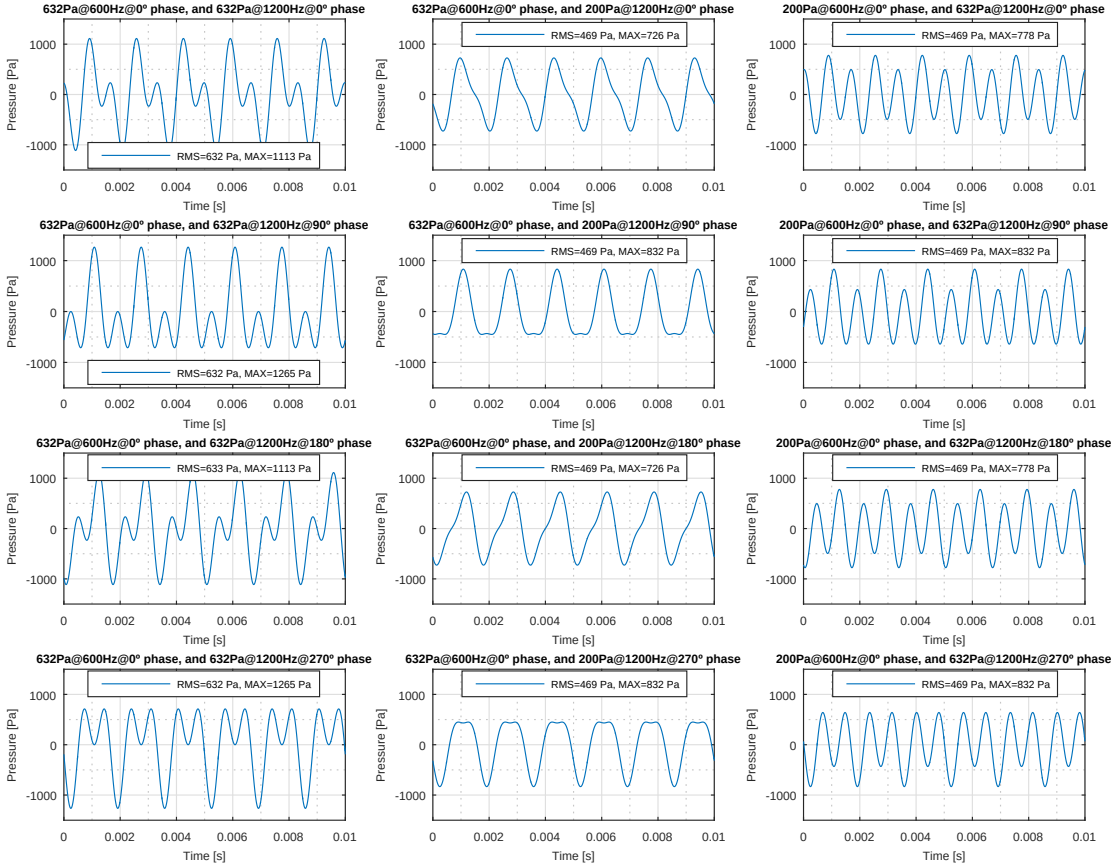

Figure 6.1: Analytical multiple tone signals for 600 Hz and 1200 Hz, with varying relative amplitude and phase between tones.

The variations in the relative amplitude and phase of the tones cause peak level variations (MAX), however, the RMS values are fixed for a given set of amplitudes with varyiing phases. The RMS and MAX values are also maintained if either the fundamental or the

harmonic is the dominant tone for the same OASPL, but the RMS is higher if both tones have the same SPL, consequently the OASPL is higher.

The objective of this analysis was to evaluate if the time dependent signal variations caused by a phase mismatch may cause a significant impedance variation. The impact of varying phase is discussed in section 6.3. Also, a secondary objective was to evaluate the contribution of each frequency component to the impedance changes when compared with pure tone excitation.

The ΔSPL obtained from the multiple tone impinging wave will be discussed as it drives the nonlinear interaction at the liner surface. These signals were applied to the liner samples and also used in the 2D axi-symmetric model, where the SPL difference between frequency components at the liner surface can be written as

$$\begin{aligned} \Delta SPL &= SPL_1 - SPL_2 \\ &= 20\log\left(\frac{\langle P_1\rangle}{P_0}\right) - 20\log\left(\frac{\langle P_2\rangle}{P_0}\right) \\ &= 20\left[\log\left(\frac{\langle P_1\rangle}{P_0}\right) - \left(\frac{\langle P_2\rangle}{P_0}\right)\right] \\ \Delta SPL &= 20\log\left(\frac{\langle P_1\rangle}{\langle P_2\rangle}\right) \end{aligned} \tag{6.1}$$

where $\langle P_1\rangle$ and $\langle P_2\rangle$ are the RMS pressure magnitudes spatially averaged over the liner surface of the fundamental and harmonic tones.

The relative amplitude between impinging tones was chosen to be within 10 dB because it was observed in the experimental data for different liner samples that for values of $|\Delta SPL|$>10dB the multiple tone impedance results approach the relative pure tone excitation result for the tone with greater SPL.

Figure 6.2 shows measured TMM impedances of the sample holder punched aluminium SDOF liner sample inserted on the sample holder ($POAeff$=3.5%) for varying incident signals; multiple tones, pure tones (PT), and white noise (BB) are plotted. The multiple tone signals have zero phase difference. Figure 6.2.(a) and (c) show the fundamental tone impedance for 135 dB and 150 dB OASPL respectively. Figure 6.2.(b) and (d) show the harmonic tone impedances for 135 dB and 150 dB OASPL respectively. ΔSPL=10dB corresponds to the multiple tone F>H, ΔSPL=0dB corresponds to the multiple tone F=H and ΔSPL=-10dB corresponds to the multiple tone H>F.

The impedance results of the punched aluminium SDOF liner are similar to those for S1 and S2, which are the 3D printed samples, as shown in Figures 3.29, 3.30. The difference in SPL between the frequency components for a BB signal is small, around ΔSPL=0dB and the SPL of each frequency component is significantly lower than the SPL of a pure tone signal.

The BB and PT impedances show reasonable agreement at 135 dB OASPL, as shown in Figure 6.2.(a). On the other hand, the BB resistance diverge from the PT values at 150

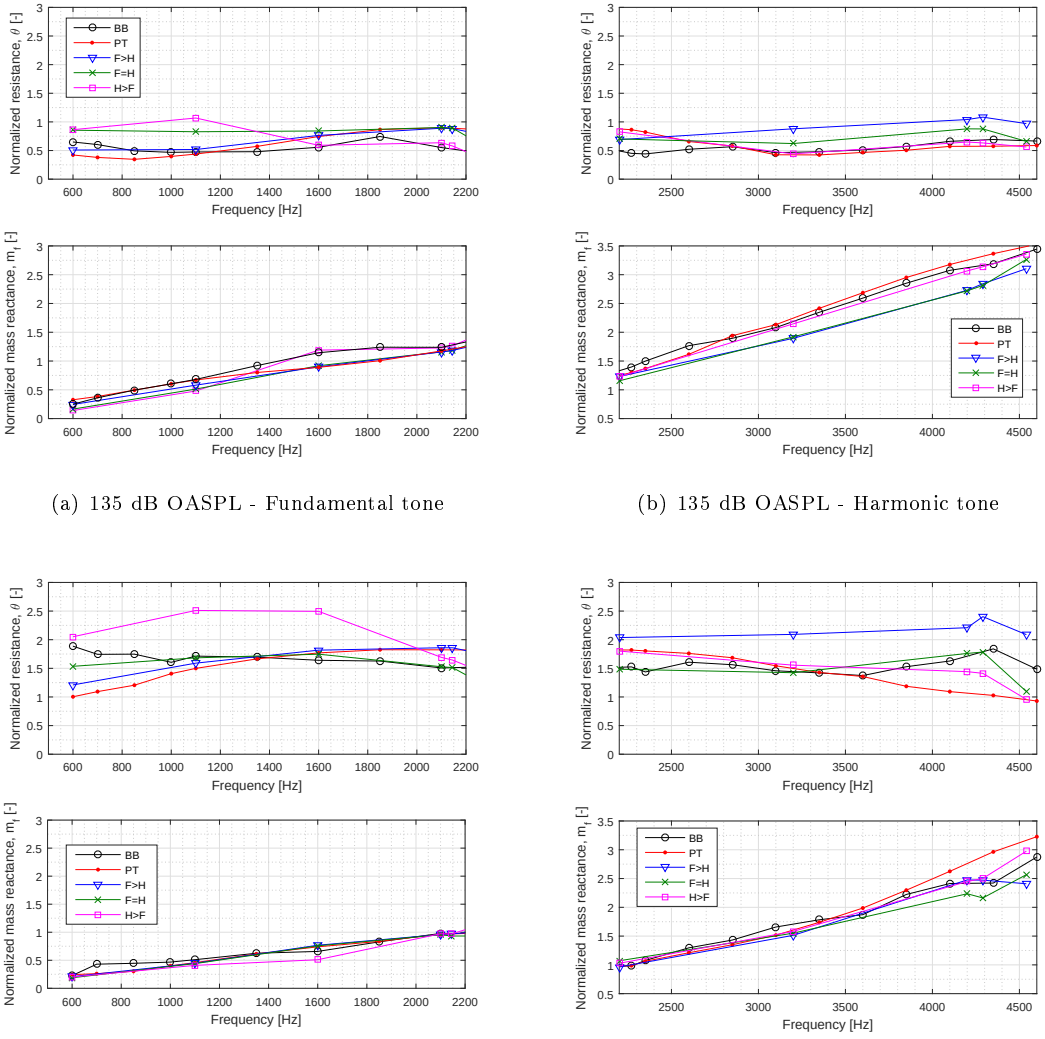

(a) 135 dB OASPL - Fundamental tone

(b) 135 dB OASPL - Harmonic tone

(c) 150 dB OASPL - Fundamental tone

(d) 150 dB OASPL - Harmonic tone

Figure 6.2: Punched aluminium SDOF liner TMM impedance in the sample holder ($POAeff$=3.5%)for different signals. BB - White noise, PT - pure tone, F>H - multiple tone with fundamental input level 10 dB higher than the harmonic, F=H - multiple tone with both tones at the same input level, H>F - multiple tone with the harmonic input level 10 dB higher than the fundamental.

dB, as shown in Figure 6.2.(b). This is expected as at 150 dB all of the incident energy is carried at a single frequency.

The impedance response changes dramatically when the incident signal contains multiple tones. When a second tone is present, the resistance of the fundamental increases as the energy in the harmonic also increases, and vice-versa. This resistance trend is evident even at the relative low OASPL of 135 dB, and it is accentuated at 150 dB OASPL. It is also seen even when tone levels are equal.

In general, the resistance is more sensitive to the multiple tone signal than the reactance. However, the mass reactance is also affected by the introduction of a multiple tone source.

In general, the mass reactance reduces for the fundamental when the harmonic carries additional energy, and vice-versa.

In conclusion, the multiple tone effect is both frequency and ΔSPL dependent for a non-linear perforated SDOF liner. For frequencies away from the resonant frequency the resistance of the fundamental increases when more energy is carried in the harmonic for $\omega_0 < 1$. The resistance of the harmonic increases when more energy is present in the fundamental for $\omega_0 > 1$. The mass reactance shows a reduced change in the presence of multiple tones, but, in general, it reduces in tandem with an increase in resistance.

6.2 COMSOL model validation for multiple tones

The straight hole model was selected to perform the multiple tone predictions because it was shown in the previous chapter that this hole geometry provided good agreement with experimental data for a pure tone source. The FFT(Liner) method applied to the straight hole geometry showed the best agreement with the experimental data calculated by TMM, compared to the other impedance calculation methods. The 2D axisymmetric COMSOL model was used to model the multiple tone experiment for the punched aluminium SDOF liner in the sample holder. The impedance was modelled as a function of pressure amplitude difference between frequency components, $\Delta SPL = SPL_1 - SPL_2$. Zero phase difference was applied between the tones. The numerical results were then compared with experimental data.

The multiple tone signals contain frequency components within a range from 0.5-5.0 kHz. This frequency range relates to the fan blade passing frequency and its first harmonic for small and large engines commonly installed in commercial aircraft.

The spatially averaged pressure simulated by the COMSOL model at the liner surface for the strongest tone was calculated and compared to the error criteria. The impinging wave amplitude was iterated until it matched the experimental pressure measured at the same position using the TMM. In the case of both tones having the same incident amplitude, SPL_1, which corresponds to the fundamental tone, was adjusted to match the experimental data. The values of SPL_1 at the liner surface for both the experimental and the COMSOL model are plotted for each frequency, in the presence of the harmonic at the same incident amplitude (F=H) in Figure 6.3. Both tones of the excitation signal applied in the experimental and in the numerical COMSOL model are in phase. The OASPL was allowed to vary in order to match the measured spatially averaged pressure, related to the fundamental (SPL_1) at the virtual surface of the model, with the experimental data.

Despite the fact that the fundamental tone SPL, SPL_1, was modelled with good accuracy, the SPL of the harmonic, SPL_2, predicted by the COMSOL model shows less good

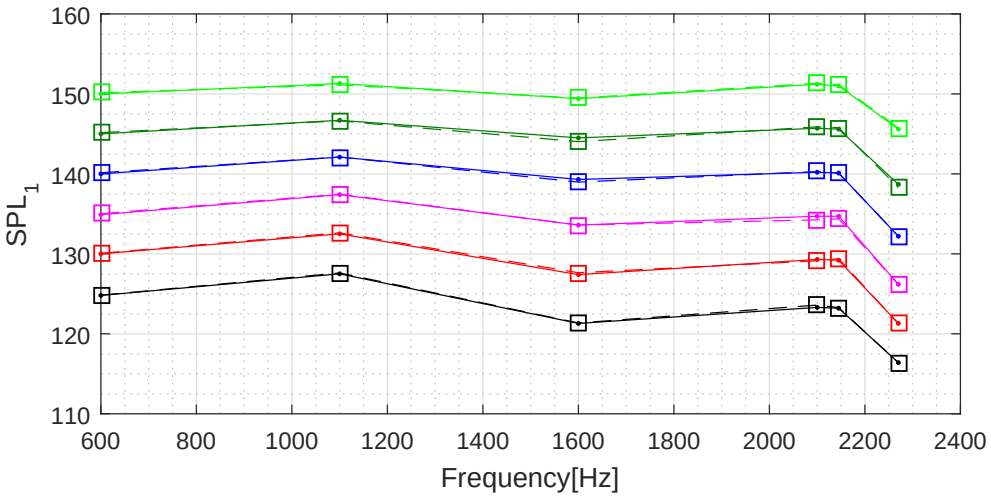

Figure 6.3: SPL_1 calculated at the liner surface for a multiple tone signal with the same amplitude in each tone (F=H, $\Delta SPL = 0$ dB) and zero phase, at 6 distinct OASPLs and frequencies. The experimental data is the solid line with dots on the data points, COMSOL is the dashed line with squares.

agreement with experiment, with an error up to 5 dB as shown in the Figure 6.4. The maximum difference between experimental and numerical results is about 7 dB at high frequencies, where the experimental data shows more uncertainties due to the use of the TMM. The experimental SPL for the harmonic also lies below the COMSOL value in the region of the panel resonance (2200 Hz). The reason for these discrepancies requires further study.

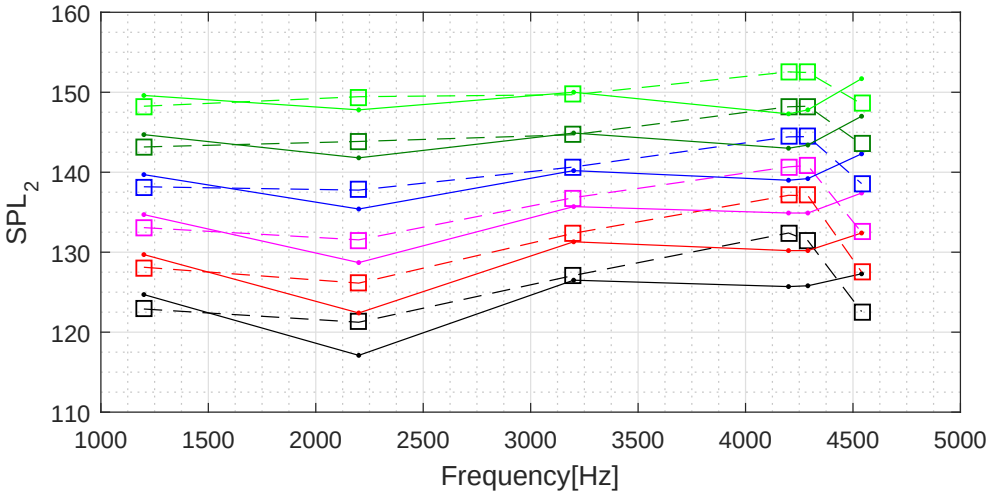

Figure 6.4: SPL_2 comparisons of two tones with the same amplitude (F=H, $\Delta SPL = 0$ dB) and zero phase, at 6 distinct OASPLs and frequencies. Experimental data is the solid line with dots on the data points, COMSOL is the dashed line with squares.

The time domain pressure and velocity of each test case was observed at a number of

different points in the numerical domain of the COMSOL axi-symmetric model. The incident, reflected and total pressures were evaluated at the inlet (impedance tube excitation boundary), corresponding to the loudspeaker position on the physical portable impedance tube.

Figure 6.5 illustrates the time domain pressure traces for a signal composed of tones at 2145 Hz and 4290 Hz, at SPL_1=151 dB and SPL_2=152 dB respectively. It is noted that the analytical expression used to create the input waveform in the COMSOL model is overlaid by the incident wave, showing that there is no reflection at the inlet. The wave fronts take 1.2 ms to go from the inlet to the liner surface and then to be reflected back to the inlet. The transient solution lasts for less than 1 ms at this frequency, and the steady state total pressure is shown after approximately 2 ms.

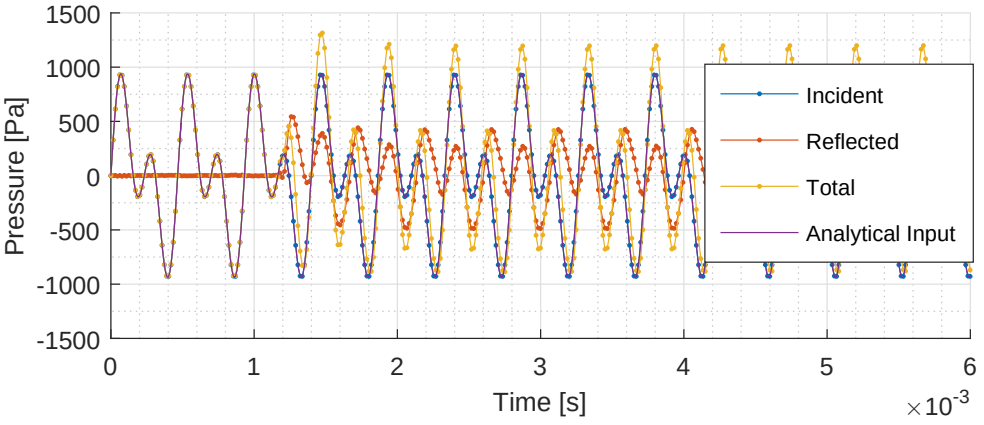

Figure 6.5: Pressure time trace at the inlet of the straight model in COMSOL using multiple tones at 2145 Hz and 4290 Hz, and same relative amplitude of excitation. SPL_d = 151 dB at 2145 Hz.

The spatially averaged pressure over the liner surface in the COMSOL model is plotted in Figure 6.6 for two tones at 2145 Hz and 4290 Hz at SPL_1=151 dB and SPL_2=152 dB respectively. The time step used provides 10 points per period for the highest frequency component, which is T=1/4290 s in this case, giving the time step of Δt =2.33E-5 s. The numerical solutions converged for all the test cases, showing stable steady state results. The RMS value of pressure was calculated in order to obtain the OASPL at the liner surface.

The spatially averaged velocity at the liner surface is plotted in Figure 6.7 for the same case as for the previous spatially averaged pressure plot (Figure 6.6). The RMS value of velocity was calculated from the time trace.

The impedance spectra of the liner exposed to a multiple tone signal can be calculated using the pressure and velocity spectra. The spectra of pressure, velocity, resistance and reactance of the numerical solution can be compared with the experimental data. It is noted that low levels of excitation at frequencies other than the specified excitation

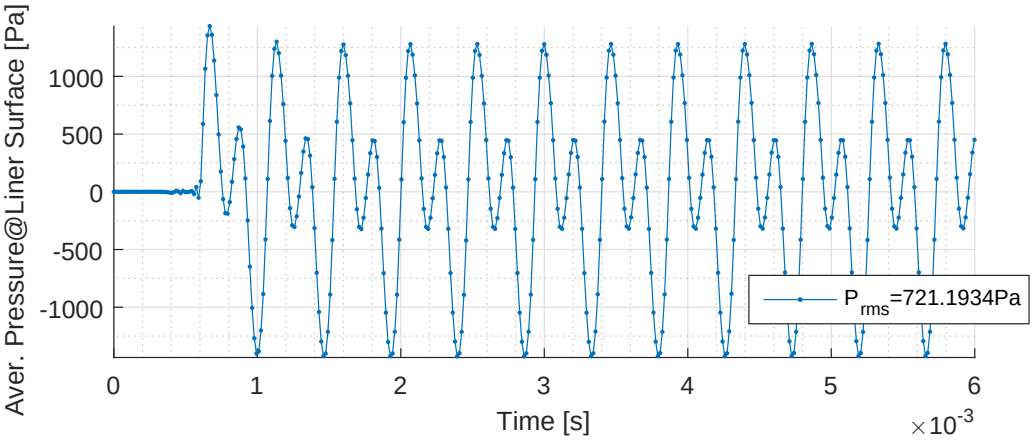

Figure 6.6: Spatially averaged pressure at the liner surface for the straight hole model using multiple tones at 2145 Hz and 4290 Hz, and the same relative amplitude of excitation. SPL_1 = 151 dB at 2145 Hz and SPL_1 = 152 dB at 4290 Hz.

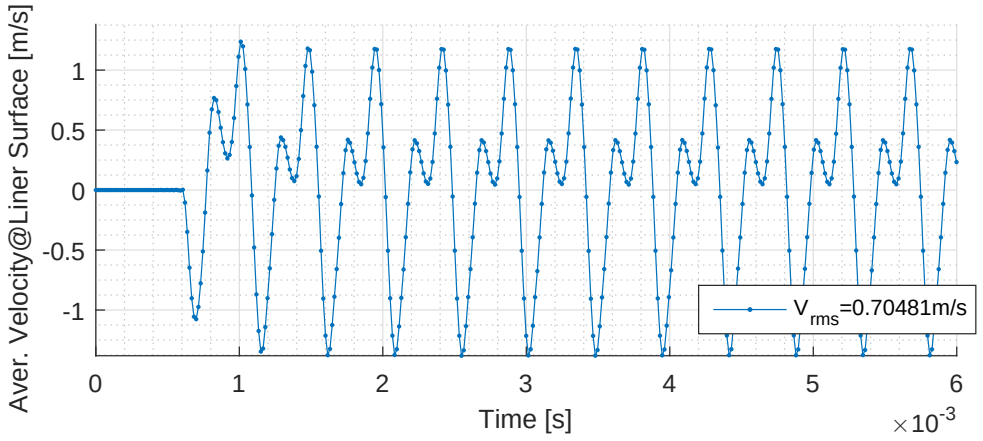

Figure 6.7: Spatially averaged velocity at the liner surface for the straight hole model using multiple tones at 2145 Hz and 4290 Hz, and the same relative amplitude of excitation. SPL_1 = 151 dB at 2145 Hz and SPL_1 = 152 dB at 4290 Hz.

frequencies lead to erratic values of impedance. Therefore, only the impedance values calculated at the excitation frequencies were compared with experimental data.

Figure 6.8 shows the OASPL for each multiple tone signal calculated in the straight hole COMSOL model. Each group of three bars in Figure 6.8 correspond to the OASPLs of three signals (F>H, F=H, F<H), composed of two harmonically related tones. The simulated OASPLs are within the tolerance of 0.5 dB for all combinations of frequencies and $\Delta SPLs$ simulated. The majority of the test cases produce good agreement with experimental data for the punched aluminium SDOF liner.

Figure 6.9 shows the straight hole COMSOL numerical resistance and the associated experimental resistance for three types of excitation signals that contain multiple tones.

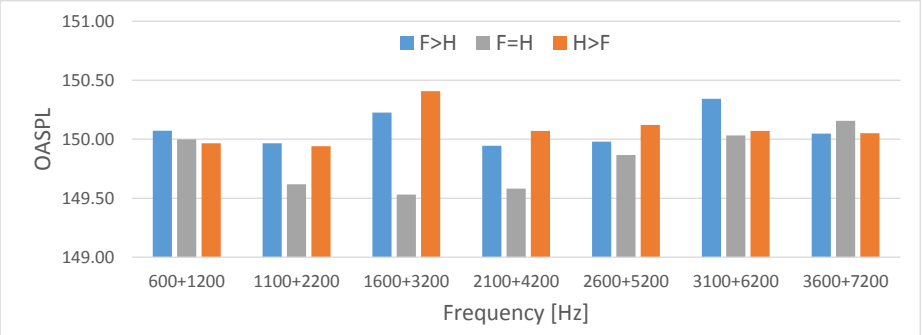

Figure 6.8: Multiple tone OASPLs calculated on the liner surface of the straight hole COMSOL model for all the combinations of frequencies and amplitudes between tones simulated.

The first type of signal is composed of tones at 600 Hz and 1200 Hz. The second type of signal is composed of tones at 1100 Hz and 2200 Hz. The third type of signal is composed of tones at 2100 Hz and 4200 Hz. The amplitude between frequency components of the incident wave was varied for each signal; F>H ΔSPL = 10 dB, F=H ΔSPL = 0 dB, and H>F ΔSPL = -10 dB (F=fundamental, H=harmonic). There are large measured and predicted changes to the resistance for a fixed OASPL with varying tonal content. In general, there is very good agreement between the COMSOL and experimental resistance results and trends for the majority of signals, apart (e.g. poorest agreement is at 4200 Hz for the H>F signal).

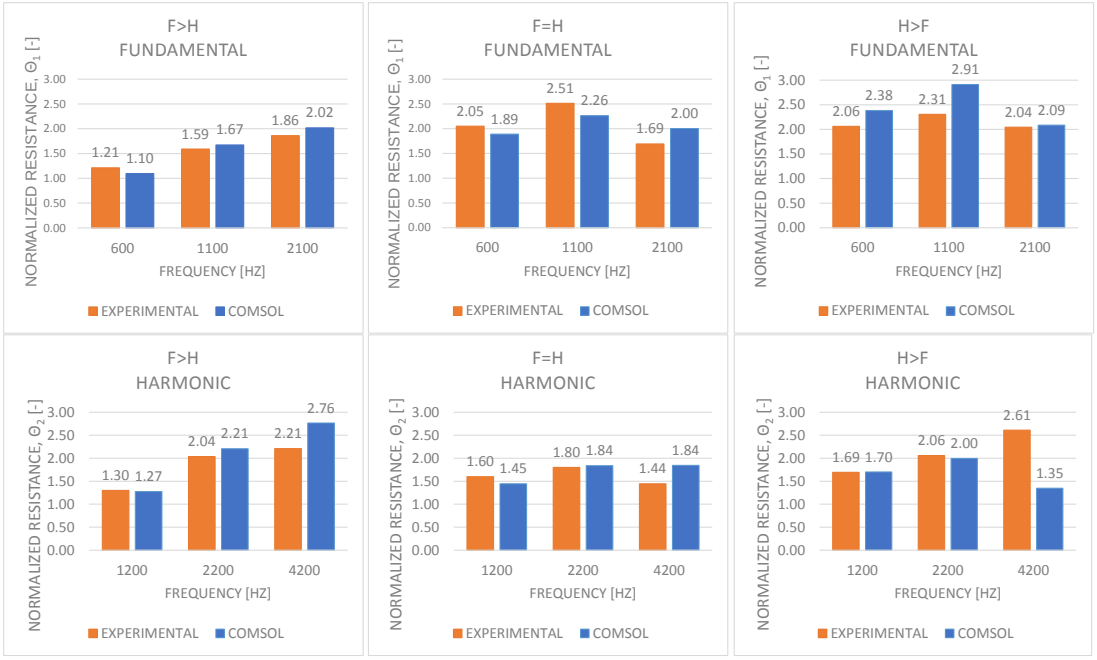

Figure 6.9: Multiple tone resistances of the straight hole COMSOL model compared against experimental TMM punched aluminium SDOF liner in the sample holder using two even harmonically related tones at approximately 150 dB OASPL. Top, fundamental tone resistances; bottom, harmonic tone resistances.

Figure 6.10 shows the straight hole COMSOL reactance and the experimental reactance for the same combinations of frequency and amplitude as shown in Figure 6.9. The COMSOL model reactances show excellent agreement with the experimental reactances. The resonant frequency of the liner occurs at 2200 Hz. Varying the tone SPL content does not provide significant changes to the reactance, suggesting that the non-linear effect arising from changes of tone energy for a fixed OASPL is most evident in the resistance, and negligible for reactance. However, it is noted that for high amplitude pure tones around the resonance frequency, the mass inertance is gradually reduced as the SPL is increased (see Figures 3.12 and 3.20).

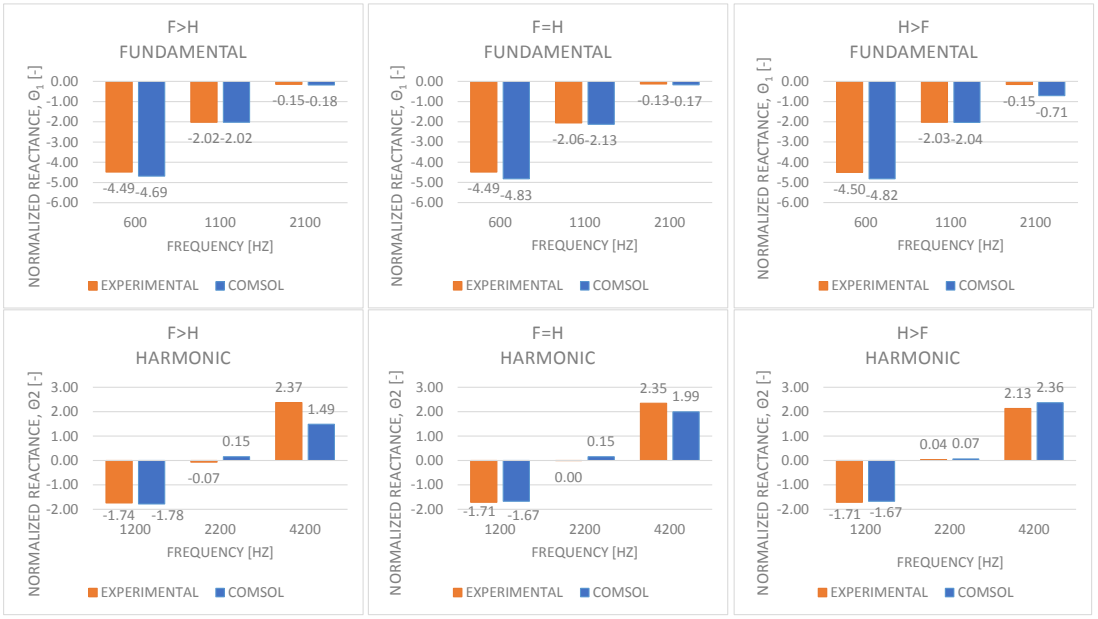

Figure 6.10: Multiple tone reactances of the straight hole COMSOL model compared against experimental data (TMM, punched aluminium SDOF liner in tube) using two even harmonically related tones at approximately 150 dB OASPL. Top, fundamental tone reactances; bottom, harmonic tone rectances.

The COMSOL resistance predictions are very promising. Both pure tones and multiple tones predictions capture the complex response of a highly non-liner liner, providing a platform for improved understanding and prediction of a liner response to a typical aero engine signal with multiple tone content.

6.3 Effect of varying the relative phase between tones

Multiple tone signals composed of two harmonically related tones with different relative phases were evaluated by using the 2D axi-symmetric COMSOL model presented in the previous sections. The relative phase between frequency components of the excitation signal was varied in separate models and compared in order to evaluate the phase effect on the liner response.

Figure 6.11 shows the resistance, reactance, and velocity results of the numerical chamfered model at different OASPLs. The resistance, velocity and reactance results for the fundamental at 600Hz and the harmonic at 1200Hz are plotted in Figure 6.11. Three different relative phases between tones were chosen: 0°, 180° and 270°. The simulations show minimal variations for different phases between frequency components, suggesting that the time dependent RMS value of pressure and velocity determine the resistance and reactance of the liner. This conclusion remains valid for multiple tone combinations at higher frequencies.

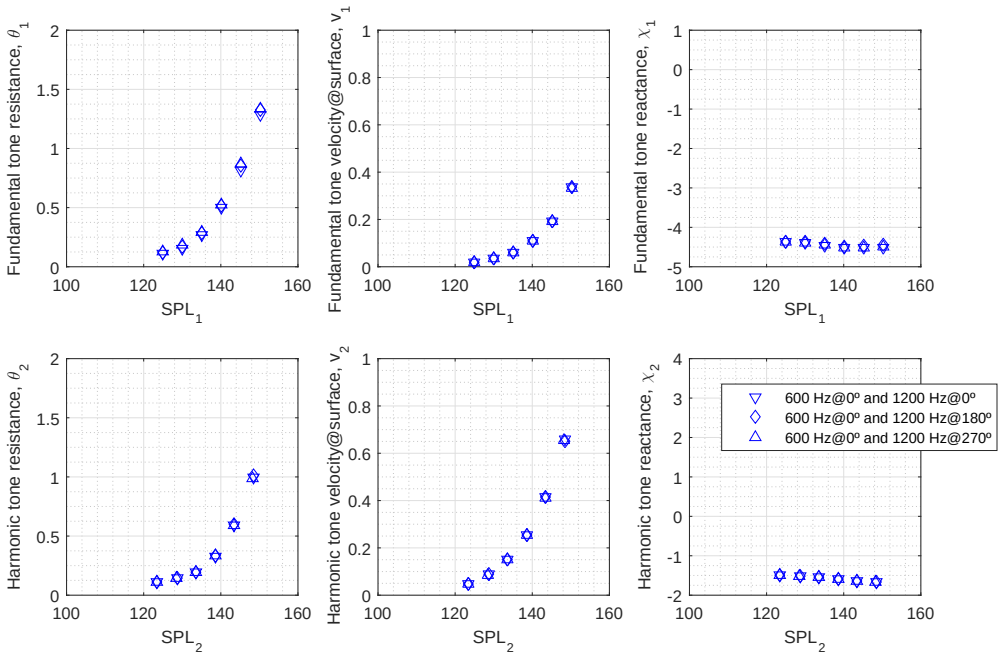

Figure 6.11: Chamfer COMSOL model resistance, reactance and velocity at the liner surface simulations using multiple tone signals having the fundamental (600 Hz) and harmonic (1200 Hz) tones at the same amplitude and varying the relative phase between them.

Figure 6.12 shows the results of multiple tones at 2145 Hz and 4290 Hz, noting that 2145 Hz is near the resonance frequency of the liner. At the highest SPLs there is a variation in resistance at the fundamental and harmonic frequencies, but the deviations do not exceed $0.25\rho c$.

6.4 Liner resistances using multiple tones

Seven different multiple tones composed of two frequency components were simulated using the straight hole COMSOL model. The frequency of the fundamental tone of each signal varied from 600 Hz until 3600 Hz in 500 Hz steps. The even harmonic of these signals was varied in amplitude in order to evaluate the effect of the harmonic

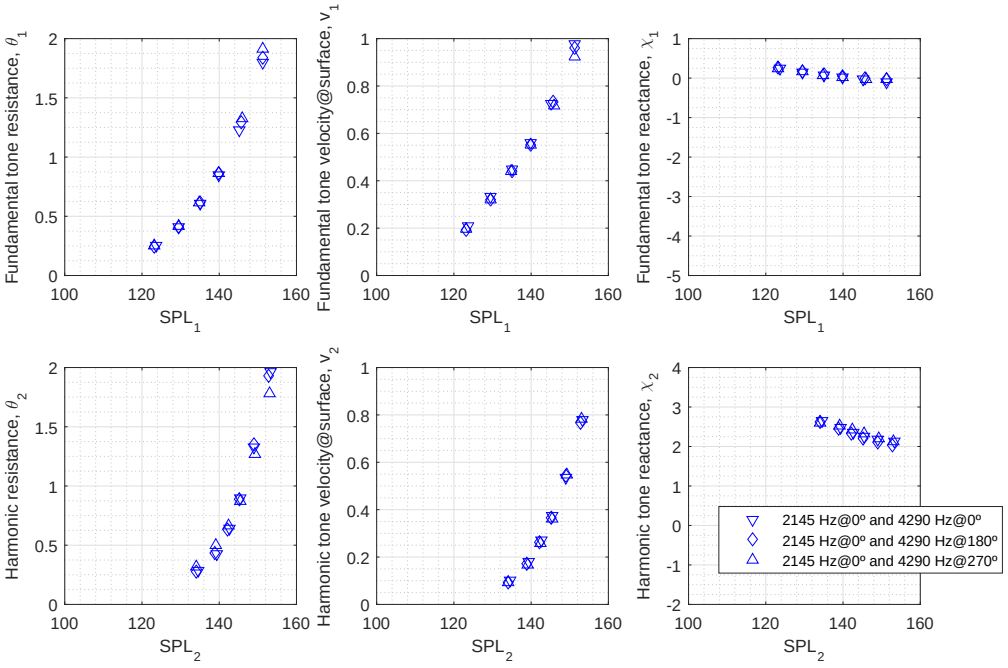

Figure 6.12: Chamfer COMSOL model resistance, reactance and velocity at the liner surface results using multiple tone signals having the fundamental (2145 Hz) and harmonic (4290 Hz) tones at the same amplitude and varying the relative phase between them.

tone ΔSPL on the liner impedance. The resistances calculated at the fundamental and harmonic tones for each multiple tone signal were normalized by the resistances calculated at the same frequencies using pure tone excitation. This comparison allows the evaluation of the relative resistance change due to the effect of the addition of an even harmonically related tone.

Figure 6.13 shows the resistance ratios for multiple tone and pure tone responses at the fundamental tones that were simulated using the COMSOL model, at 150 dB OASPL. The F>H bars on the left hand side show that if the fundamental tone is 10 dB higher than the harmonic, as expected the resistances for multiple tone excitation approach the resistances for pure tone excitation at all frequencies. For F=H and H>F, an increase in resistance of the fundamental is predicted for low frequencies and a decrease in resistance is predicted at high frequencies for the fundamental, due to the presence of the harmonic tone at the same amplitude of the fundamental (150 dB). As the amplitude of the harmonic increases, the multiple tone effect is more evident, causing higher resistances at low frequencies and low resistances at high frequencies. It may be that this multiple tone effect on resistance is correlated with the resonant frequency of the liner, which is around 2200 Hz. Ultimately, in order to confirm this, simulations would need to be performed for a liner with alternative resonance frequency.

The resistances simulated for multiple tones, and evaluated at the harmonic, show almost

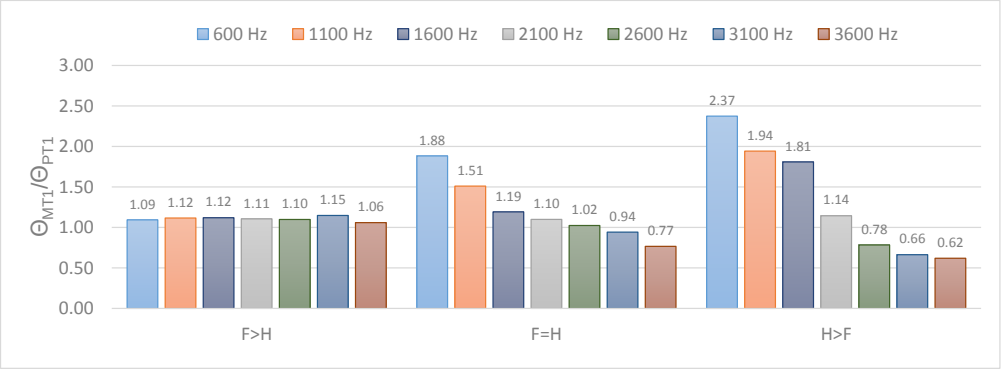

Figure 6.13: Straight hole COMSOL model resistances for multiple tone excitations normalized by the resistances for pure tone excitations at the fundamental for 150 dB OASPL. F>H - excitation signal with fundamental 10 dB higher than the harmonic, F=H - fundamental with the same level of the harmonic, H>F - fundamental 10 dB lower than the harmonic.

the reverse behaviour to that observed for the fundamental. The harmonic resistance predictions are shown in Figure 6.14. The impedances near the resonant frequency, at 2200 Hz, are practically the same for pure tone or multiple tone excitations. The resistance decreases at low frequencies as the energy at the fundamental frequency increases (F>H). However, the resistance increases for F>H at high frequencies. As expected, the H>F case shows values that approach the pure tone resistance values, when the harmonic is 10 dB higher than the fundamental.

These studies confirm that the presence of a harmonically related tone has a significant and progressive impact on the liner resistance of both the fundamental and harmonic tones. The evidences were measured and the simulations agree with these findings as shown in Figure 6.9.

6.5 Proposed resistance correction for multiple tones

The numerical results for multiple tone excitation shown in Figures 6.13 and 6.14 were used to correlate the resonant frequency of the liner ω_0 and the amplitude difference between tones, ΔSPL, with the resistance ratio between the multiple tone and pure tone excitations. These normalized factors were chosen in order to clearly represent the relative differences between multiple tone and pure tone resistances. An expression that adjusts the impedance calculated using a pure tone prediction model was developed in order to account for the presence of significant multiple tone excitation.

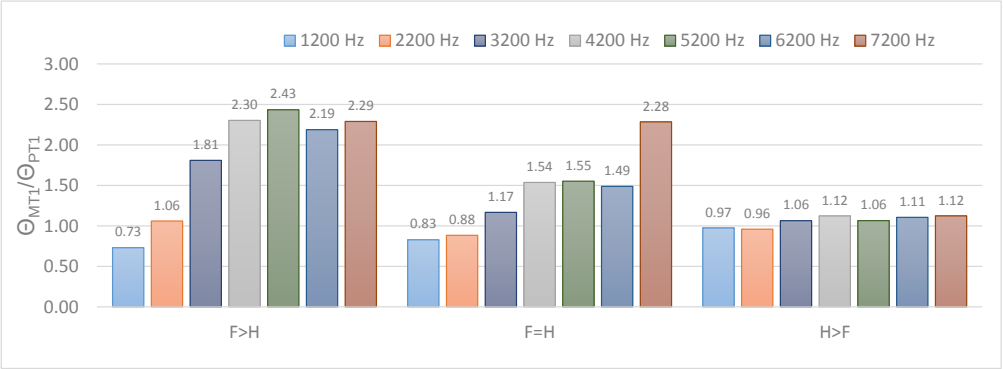

Figure 6.14: Straight hole COMSOL model resistances for multiple tone excitations normalized by the resistances for pure tone excitations at the harmonic for 150 dB OASPL. F>H - excitation signal with fundamental 10 dB higher than the harmonic, F=H - fundamental with the same level of the harmonic, H>F - fundamental 10 dB lower than the harmonic.

Figure 6.15 shows the resistance ratios between multiple tone and pure tone excitations at a given frequency relative to the normalized frequency ω_0 =2200 Hz, where ω_0 approximates te resonance frequency. It is recognized that the resonance frequency changes with SPL and tonal content, but it may be considered second order for the purposes of this exercise. A semi-empirical fit was applied in order to provide a correction to the pure tone impedance predicted by traditional liner impedance models. The fit is plotted in Figure 6.15 with the correspondent equations and correlation coefficients.

It is clear from the numerical results shown in Figure 6.15, as it was clear in the experimental data shown in Figure 3.20 and also in Figure 3.21, that the resistance of a frequency component is strongly influenced by the pressure amplitude of other harmonically related tone. Considering the SPL difference between the fundamental and harmonic tones as $\Delta SPL = SPL_1 - SPL_2$, if this difference is higher than 10 dB $|\Delta SPL| > 10$, the nonlinear interaction between tones will be small, as the response of the liner at a given frequency is dominated by the SPL at that frequency. Consequently, the resistance of the highest tone will be similar to the resistance of a pure tone excitation, so that $\theta_{MT}/\theta_{PT} \approx 1$. On the other hand, if the SPL difference is below 10dB ($|\Delta SPL| < 10$), then the non-linear interaction is strong and it will affect the impedance in both tones.

Considering a multiple tone excitation so that SPL_1 is the spatial average sound pressure level of the fundamental tone at the liner surface, and SPL_2 is the spatial average sound pressure level of the first even harmonic at the liner surface, it is possible to predict the resistance of each frequency component using the following proposed equation

$$\frac{\theta_{MT}}{\theta_{PT}} = \pm\frac{\Delta SPL - 10}{20}\ln(\omega_0) + C_1, \tag{6.2}$$

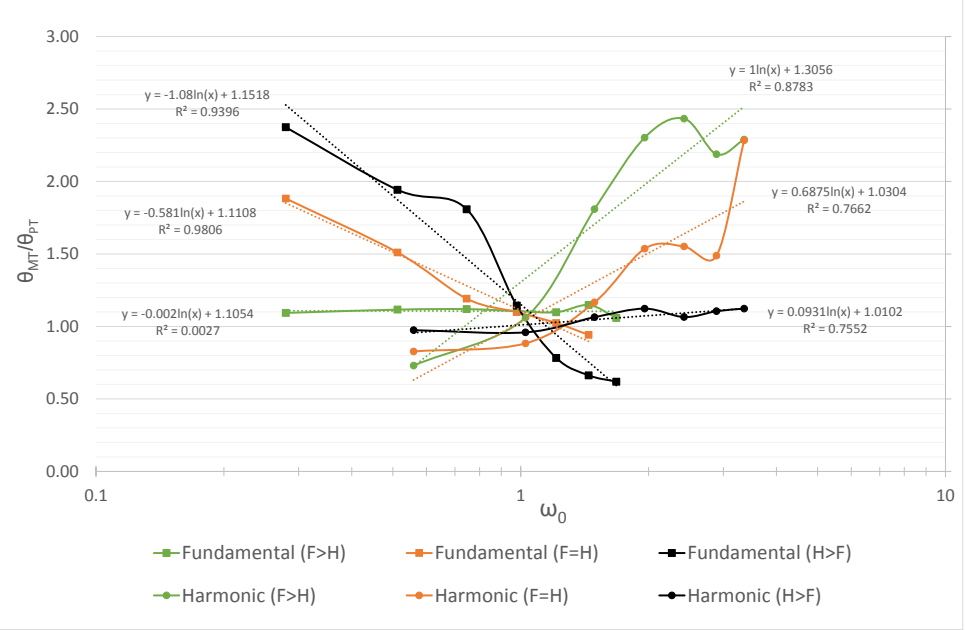

Figure 6.15: Resistance ratio of a COMSOL numerical result between MT and PT excitations for a liner with POA=3.5 %, d=0.990 mm, l=0.635 mm, h=19.100 mm. Green solid lines - F>H, Orange solid lines - F=H, Black solid lines - H>F. Squares are the fundamental resistance ratios, and circles are the harmonic resistance ratios. Dotted lines are the curves fitted to perform a semi-empirical analysis.

where the sign $\pm$ is positive for $\omega_0 < 1$, and negative for $\omega_0 > 1$. $\Delta SPL = SPL_1 - SPL_2$ when $\omega_0 < 1$, or $\Delta SPL = SPL_2 - SPL_1$ when $\omega_0 > 1$. The coefficient C_1 is approximately equal to 1. Observe that this equation is valid only for harmonically-related tones in the nonlinear regime of liner excitation within $|\Delta SPL| < 10$.

By using Equation 6.1, Equation 6.2 can be written in terms of two frequency components with root mean square pressures P_1 and P_2 as

$$\begin{aligned} \frac{\theta_{MT}}{\theta_{PT}} &= \pm\frac{\Delta SPL-10}{20}\ln(\omega_0) + C_1 \\ &= \pm\frac{20\log\left(\frac{\langle P_1\rangle}{\langle P_2\rangle}\right)-10}{20}\ln(\omega_0) + C_1 \\ \frac{\theta_{MT}}{\theta_{PT}} &= \pm\left(\log\left(\frac{\langle P_1\rangle}{\langle P_2\rangle}\right) - 1/2\right)\ln(\omega_0) + C_1 \end{aligned} \tag{6.3}$$

The logarithmic regressions produce different slopes depending on the sound pressure level difference between frequency components of the signal. The curves are also frequency dependent. The resistance at the fundamental tone will be higher than the PT resistance for $\omega_0 < 1$ in a presence of an even harmonic with significant energy (H>F). On the other hand, the resistance at the fundamental tone will be lower than the PT

resistance for $\omega_0 > 1$ when the harmonic has more energy (H>F). The opposite behaviour occurs at the harmonic, where the resistance will be higher than the PT resistance when $\omega_0 > 1$ and the fundamental has more energy (F>H), and the resistance of the harmonic will be lower when $\omega_0 < 1$ using the same signal (F>H).

This fit provides a reasonable first order correction to the pure tone resistance predicted at either tone for a given combination of multiple tone amplitudes at high SPLs. The application of the proposed correction for experimental data collected for the punched aluminium SDOF liner by using the TMM, is in Figure 6.16. It is possible to observe quite good agreement that may be improved by using a quadratic fit rather than a linear fit to the measured data. Also, it is likely that the resonance frequency changes with the frequency content of the signal.

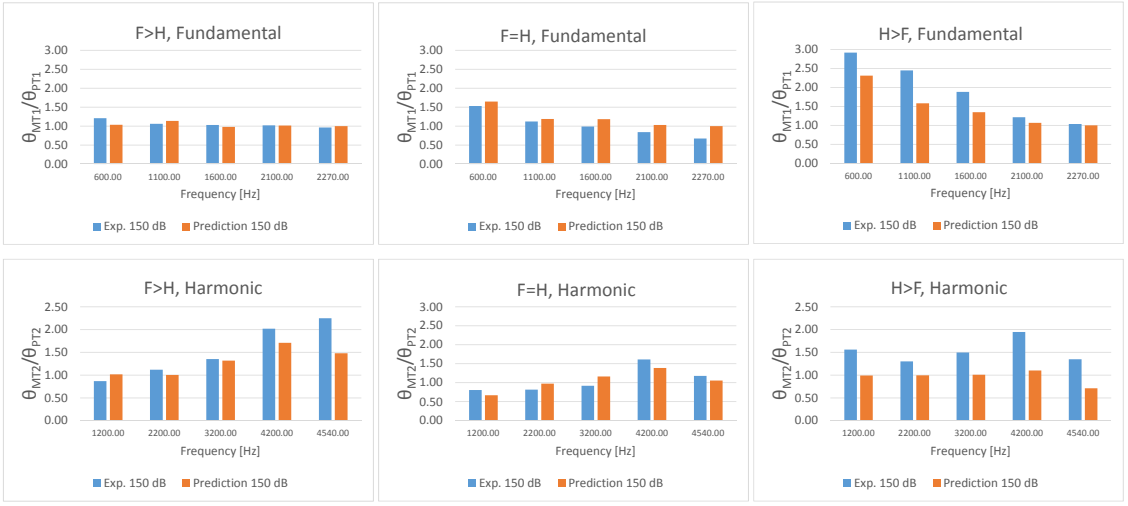

Figure 6.16: Validation of the proposed semi-empirical correction for multiple tone resistance based on pure tone experimental data, using three signals (F>H, F=H, H>F) with different ΔSPL at 150 dB OASPL.

Chapter 7

Conclusions and Future Work

This chapter summarizes the research outcomes, the main conclusions related to the findings, and suggests future work.

7.1 Summary of outcomes

Acoustic liners are used in aircraft engine nacelles to attenuate fore and aft propagating noise in the inlet, bypass, and core ducts. Liner impedance models are needed to allow the definition of liner constructions which most closely match the optimum impedance for maximum attenuation in each duct. While previous experimental and theoretical work has led to the development of good quality impedance models for pure tone, and fully random sources, the non-linear response of these liners to combinations of tones containing high SPLs at the frequencies seen in aero engine ducts is not well understood.

This thesis has reported on experimental and theoretical work to measure and model the response of SDOF perforate liners to high amplitude multiple tones. Initial studies confirmed the highly non-linear response of these liners to pure tone signals. Impedance measurements made using an impedance tube, the in-situ technique, and an eduction rig, were used to develop a time domain impedance 1d semi-empirical model.

A COMSOL DNS time domain model was constructed. This 2D FEM model for a slit liner was compared with literature data (Tam/NASA [92]) for pure tones. An improved 2D axi-symmetric FEM model was then validated against the experimental data, along with other DNS data in the literature (Zhang & Bodony [102]) and a liner semi-empirical prediction model [69] for pure tone signals. The model was refined to run significantly faster than 3D DNS models, while retaining excellent accuracy and agreement with other prediction models proposed. It was also used to evaluate the significant influence of hole shape on non-linear impedance, showing the high sensitivity of the liner impedance to the hole profile.

As stated, the main goal of this thesis was to investigate the response of aero engine liners to multiple tone signals. The COMSOL model was used to model the complex flow patterns within perforate sheets for multiple tone signals. The model predictions were again validated against experimental data. The modelling showed that the large variation in acoustic resistance of each tone is a function of the relative tone amplitude and their frequencies. Finally, the COMSOL results were used to develop a semi-empirical correction to tone resistance to account for the presence of multiple tones.

7.2 Specific technical conclusions

The main conclusions can be itemized and summarized as:

- **The edge effect using impedance tube techniques**

  Flanged experiments using impedance tubes over liner panels are important to allow quality control. The main advantages are the flexibility to test different parts of the same panel and evaluate the blockage as well as localized impedance values. The disadvantages are related to the edge effect that degrades the impedance measurement precision, especially at low frequencies, as discussed in Chapter 3, and illustrated in Figures 3.10 and 3.11. In tube measurements using sample holders can be used to reduce the edge effect and obtain better impedance results at low frequencies. However, the disadvantages include sample destruction and it might cause different $POAeff$ which strongly affects the liner resistance.

- **Discharge coefficient frequency dependence**

  The procedure to obtain the $POAeff$ was described and it was used to obtain the frequency dependent discharge coefficient for the punched aluminium SDOF liner using measurements from the flanged and in-tube set-ups. The data was used to refine the description of the mass reactance and aided the development of a proposed 1D semi-empirical model for liner impedance. The frequency dependence of the discharge coefficient could be visually evaluated for different pure tones using the COMSOL 2D axi-symmetric model.

- **The importance of obtaining the effective percentage of open area**

  A single resonator hole impedance can be calculated using an impedance model and then multiplied by the $POAeff$ in order to obtain a value corresponding to the liner impedance. This may be normalized by the characteristic impedance of air. This liner normalized impedance corresponds to the spatially averaged values of pressure and velocity over the liner surface and usually differs from the impedance predicted using the geometric POA. This was shown in Chapter 3, where the same sample experimented using FTMM and TMM shown significant changes in resistance, as observed in Figure 3.11 and Figure 3.12. It was also found that the

non-linearity is also a function of the hole geometric profile, by experimenting two similar 3D printed samples with almost identical geometric features produced by alternative prototyping techniques.

- **3D printing prototyping challenges to produce liner samples**

  3D printed samples production is technically challenging in terms of geometry tolerances and finishing process. Good tolerances were achieved comparing the nominal and produced features, that allow an evaluation about the quality of laser sintering and photopolymerization processes. The perforated plate thickness was the most difficult parameter to control, followed by the *POA* which is related to the diameter of the holes. Laser sintering was shown to produce hole diameters with good accuracy, in contrast to photopolymerization that required drilling. The correct design of a support structure to hold the 3D printed sample while printing is critical to obtain good quality samples.

- **Limitations of in-tube impedance techniques (*in situ* x TMM)**

  Similar 3D printed ABS samples were produced in order to compare the *in-situ* and the TMM experimental techniques simultaneously, which is an innovative approach to the problem. A dedicated sample holder was developed to allow *in-situ* instrumentation. The *in situ* and TMM experimental techniques agree only for a limited bandwidth from approximately 1.5 kHz until 4.0 kHz. The agreement degrades at high frequencies. This may be due to non perfect sample installation in the impedance tube or reduced accuracy of the Kulite microphone calibration at high frequencies. This requires further study.

- **Sound wave frequency content implications on impedance**

  The impedance of the SDOF liners evaluated was shown to be a strong function of the signal content. The impedance response to varying types of broadband signal was shown to differ from pure tone results at the same OASPLs. Above a certain OASPL, the odd harmonic dominance over even harmonics is reversed for a SDOF liner. The even harmonics interact and there is exchange of energy, causing impedance values that are difficult to predict with current liner impedance models (Figure 3.18). This can be investigated further using the developed 2D axi-symmetric model in COMSOL.

- **Effects of even harmonics on liner impedance**

  Multiple tones were evaluated using two even harmonically related tones for a number of liner samples and amplitude combinations between frequency components. A significant resistance change from the pure tone value was observed for different samples and for various signals, both experientially and numerically. The reactance also varied due to multiple tone excitation, but to a lesser degree. It was shown in

Figure 3.30 and 3.31, that non-linear interaction occurs from low to high frequencies, and vice-versa. The impedance change is related to the relative amplitude of the dominant tones, and to the resonant frequency of the liner.

- **Grazing flow effect and eduction technique limitations**

  The grazing flow has a very significant impact on liner impedance in aircraft engines. The approach condition of an aircraft was simulated at UFSC rig for pure tone excitations and grazing flows up to 0.26 Mach. Different impedance eduction techniques were performed and cross validated with *in-situ* measurements performed on a punched aluminium SDOF liner. The experimental eduction techniques show limitations in terms of frequency range, SPL and Mach number. However the educed impedance show reasonable agreement with *in-situ* measurements [88]. Also, the *in-situ* results with and without grazing flow at the UFSC rig show reasonable agreement with the proposed 1D model as seen in Figures 4.17, 4.18, and 4.19.

- **1D semi-empirical model implementation and validations with and without grazing flow**

  The proposed 1D semi-empirical model was improved using the assumptions from time domain models developed by other authors[78][20][7]. The end correction description was simplified in order to be expressed in terms of the Strouhal number, and the frequency dependent discharge coefficient. The Rice description of the non-linear term related to the velocity was shown to agree with experimental data for the punched aluminium SDOF liner. This was incorporated into the proposed 1D model with excellent agreement at different SPLs, as shown in Figure 4.10 (Mach 0) and subsequent graphs in Chapter 4.

- **2D COMSOL model implementation and validations**

  A slit liner 2D model and an axi-symmetric COMSOL model showed good agreement with experimental and DNS data available in the literature [102]. The validation emphasises the innovative approach by using a model with two domains, that solve different equations that describe the physics near and far from the liner perforate hole. The FEM model solves the full Navier Stokes Equations but remains computationally efficient. The model provides accurate results in comparison with literature data and other semi-empirical models. The flexibility and the speed of the model allow the evaluation of different liner geometries and multi-tonal harmonic signals faster than costly 3D DNS models.

- **Effect of the hole profile**

  The 2D axi-symmetric model developed in COMSOL & MATLAB was used to evaluate different hole profiles for pure tone excitations at various frequencies and SPLs. The impedance sensitivity to the hole profile showed that this evaluation is

critical, in order to correctly design acoustic liners at high SPLs. The frequency content of the impinging sound wave changes the velocity profile at the hole leading and trailing edges. The velocity profile is also dependent on the hole profile. In general, chamfered edges and conical sections alter the resonant frequency of the liner and reduce the inertance, which is desirable in terms of broadband attenuation. The flow velocity and vorticity fields are similar for all hole profiles. However, it was observed that a divergent hole exit creates local vortex rings that are shed and stay close to the hole edge. Straight edges accelerate the fluid creating a more distinct *vena contracta* than the divergent hole exits at the frequencies analysed.

- **Effect of phase between multiple tone frequency components on liner impedance**

  The phase between multiple tone frequency components alters the peak magnitude of the pressure waves for an incoming sound wave. The RMS pressure is phase independent, and there is only small change in impedance due to phase difference near the resonance at high SPL, as shown in Figure 6.12.

- **Multiple tone experimental findings, numerical predictions and proposed corrections**

  A proposed semi-empirical correction of pure tone resistance to obtain multiple tone resistance was developed and based on COMSOL numerical predictions. The correction is frequency dependent and linked to the resonant frequency of the liner. It uses the relative amplitude between two even harmonically related tones to calculate a value that can be multiplied by the pure tone resistance in order to obtain the predicted multiple tone liner impedance at the tones evaluated.

7.3 Future Work

The list of suggestions below aim to guide future studies on this topic, in order to explore the effect of multiple tone excitation in liner impedance even further, and allow better understanding about the physical phenomena. The suggestions are:

- Explore the effects of grazing flow with multiple tones in SDOF liners;
- Explore the effects of odd harmonics in SDOF liners at high SPLs;
- Explore the complex flow patterns and energy dissipation mechanisms for pure tone and multiple tone excitation;
- Explore the impact of bias flow on acoustic impedance for pure tone and multiple tone excitation;
- Explore the non-linear multiple tone impedance of 2DOF liner;

- Develop a simplified description of the end correction based on the inverse of Strouhal number;
- Incorporation of the ΔSPL between multiple tone frequency components in a SDOF liner impedance model.

Appendix A

Impedance meter datasheet

Specifications – Portable Impedance Tube WA-1599-W-005

FREQUENCY RANGE
Tube: 500 Hz to 6.4 kHz

ZERO ABSORPTION
(calculated in 1/3-octave bands)
50 Hz to 4 kHz: < 4%
5 kHz to 6.3 kHz: < 10%

¼″ CONDENSER MICROPHONE CARTRIDGE TYPE 4187
To optimise the measurement accuracy of the microphones have a non-removable protection grid that forms an airtight front cavity. This gives a coupling between the tube and the microphones that is well-defined with respect to phase
Open-circuit Sensitivity (250 Hz): 4 mV/Pa (–48 ± 3 dB re 1 V/Pa)
Capacitance (250 Hz): 6.4 pF, typical
Frequency Response Characteristic (Flush-mounted) ± 1 dB: 1 Hz to 8 kHz
Polarization Voltage: 200 V

PREAMPLIFIER
Type 2670-W-012

ENVIRONMENTAL SENSORS
Integrated sensors measure temperature pressure and relative humidity

LOUDSPEAKER
Max. RMS Power: 50 W at 20°C (68°F)
Impedance: 8 Ω
Diameter: 35 mm (1.38″)

OPERATION
Sound source activation and status indicator integrated in handle

DIMENSIONS
Tube Inner Diameter: 29 mm (1.14″)
Tube Length: 208.2 mm (8.2″)

ASSEMBLED DIMENSIONS (EXCL. CABLE)
356.5 × 184 × 150 mm (14 × 7.2 × 5.9″)

WEIGHT (WITHOUT ACCESSORIES)
4.2 kg (9 lb. 4 oz.)

Specifications – Impedance Meter Program WT-9888

System Requirements

WT-9888 is a software application for use with PULSE LAN-XI System
- The PC requirements for PULSE LAN-XI System Type 3160 must be fulfilled
- FFT & CPB Analysis Type 7700-N2 or FFT Analysis Type 7770-N2 must be installed
- PULSE Material Testing Type 7758-N must be installed

Application Projects

WT-9888 includes a number of predefined application projects for material testing

Measurement

Measurements are based on the two-microphone transfer-function method as described in the ISO 10534–2 and ASTM 1050–98 standards. A group or batch of measurements can be made in a project and measurements from previous projects can be imported into the current project
- Measurement with broadband, pure-tone, or user-defined source
- Automated pass/fail impedance Quality Control routine for use by non-acoustic specialists
- Impedance spectra for broadband OASPLs up to 150 dB
- Perform automated tracking of Resonance Frequency variation with Pure Tone SPL for non-linear materials
- Option for non-linear resistance versus velocity characteristic (pure - tone or broadband up to 150 dB OASPL)

MEASUREMENT TUBES
WT-9888 supports WA-1599 and all tube setups included in Impedance Measurement Tubes Types 4206 and 4206-A and up to three user-defined tube setups in a single project

FFT ANALYSIS
Measurements in WT-9888 are based on FFT analysis
Parameters
- Baseband and Zoom: 50 – 6400 lines
- Frequency Span: 1.56 Hz – 25.6 kHz (tube dependent)
- Centre Frequency Resolution: 1 mHz
- Averaging Mode: Linear, Exponential and Peak hold
- Number of Averages: 1 – 100000

SIGNAL GENERATION
Waveforms: Sine, Random and Pseudo-random
Level: Fixed, Level automation

POST-PROCESSING
Post-processing can be performed on the following results:
- Absorption coefficient
- Reflection coefficient
- Normalised impedance
- Normalised admittance

Individual measurements can be post-processed as follows:
- Averaging of multiple individual results
- Automated procedure for calculation of the distance from the sample to the acoustic centre of microphones
- Calculation of the pressure at the sample facing sheet
- Combining measurements from two different tubes
- Combining measurements from multiple measurements to create resistance versus test level analysis at selected frequency
- Combining measurements from multiple measurements to create resistance versus test level analysis at selected frequency at surface of test object.
- Extraction of 1/n-octave centre frequency information
- Acoustic pressure and acoustic velocity spectra at sample surface
- Calculation of non-linear resistance variation with acoustic velocity (for broadband, pure-tone or user-defined source)
- In-tube sample holder for flanged tube correction routine

RESULTS
WT-9888 offers a large number of task-dependent intermediate and final result types.
Channel Calibration
Sound pressure level at each microphone position
Signal-to-Noise Ratio
Signal-to-Noise Ratio (SNR) at each microphone position
- As measured
- User-defined SNR threshold level

Sound Pressure Level at each Microphone Position
- With generator off (background noise)
- With generator on

Transfer Function Calibration
- Calibrator factor
- Coherence
- Transfer function H1, H2 and H3
- Sound pressure level at each microphone position and at facing sheet

Measurements
- Absorption coefficient
- Acoustic resistance as a function of acoustic velocity (pure-tone or broadband)

- Acoustic velocity as a function of frequency
- Coherence
- Corrected transfer function
- Normalized impedance ratio
- Normalized admittance ratio
- Reflection coefficient
- Resistance vs. test level at selected frequency at surface of test object
- Sound pressure level at each microphone position
- Transfer function

REPORTING
- Integrated reporting with Microsoft® Word
- Automated export of data to Microsoft® Excel®

Ordering Information

Type 9737

PULSE Impedance Meter System Type 9737 includes the following:
- WT-9888: Impedance Meter Program
- Type 7758-N: PULSE Material Testing Program
- Type 7770-N2: PULSE FFT Analysis, 2-channel license
- Type 3160-A-042: Generator, 4/2-ch. Input/Output Module LAN-XI, 51.2 kHz (Mic, CCLD,V)
- WA-1599-W-005: Portable Impedance Tube (500 Hz – 6.4 kHz, max. 150 dB SPL) including:
  – Power Cable, 10 m (32.8 ft.)
  – 2 × Microphone Type 4187 with Preamplifier Type 2670-W-012
  – 5 × WS-4929-W-002: Flat Flange for machining to curved surface
  – WB-3592: Power Amplifier
  – AO 0087-D-002: BNC Cable, 0.2m (0.66 ft.) (cable between Type 3160-A and WB-3592 input)
- WE-0214-W-005: Carrying Case for Type 9737 System to carry all elements of the system (except the lap-top computer) plus optional Pistonphone, Sound Calibrator and accessories. WE-0214-W-005 is fitted with wheels and an extendable handle
- WP-4808: Hard-wall Calibration Sample (150 × 150 × 10 mm [5.91 × 5.91 × 0.39″]) Aluminium
- WA-1706: Sample Holder
- WQ-2927: 12 m (39.4 ft) Mains Extension Lead incl. four-way mains distributor
- WQ-1245: Mains Adaptor for Europe and USA

Dimensions (Ext.): 625 × 500 × 297 mm (24.5 × 19.5 × 11.7″)
Total Weight:
Full Case: 21.25 kg (46.8 lb.)

OPTIONAL ACCESSORIES

Type 4228	Pistonphone
Type 4231	Sound Calibrator
DP-0775	Adaptor for ¼″ Microphones (for Type 4231)
Type 4206	Impedance Tube Kit (50 Hz – 6.4 kHz)
Type 4206-A	Impedance Tube Kit (100 Hz – 3.2 kHz)

AVAILABLE SPARES

Type 2670-W-012	Short Preamplifier Type 2670 with 10 m (32.8 ft.) cable
Type 4187	¼″ Microphone
WC-0015	Microphone Fixing Knob

REQUIRED SOFTWARE
Microsoft® Windows® 7 SP1 (all editions), Windows® XP Professional (SP3, 32-bit), Windows® 8 (64-bit)
Microsoft® Office 2013 (32-bit), Office 2007 (SP2) or Office 2010 (SP2, 32-bit version only)

Service Products

M1-WT-9888	Impedance Meter Program Software Maintenance and Support Agreement
M1-7758-N	PULSE Material Testing Program Software Maintenance and Support Agreement
M1-7770-N2	PULSE Annual Software Maintenance and Support Agreement

EADQUARTERS: Brüel & Kjær Sound & Vibration Measurement A/S · DK-2850 Nærum · Denmark
lephone: +45 7741 2000 · Fax: +45 4580 1405 · www.bksv.com · info@bksv.com

ıcal representatives and service organisations worldwide

Brüel & Kjær

Appendix B

Technical drawings

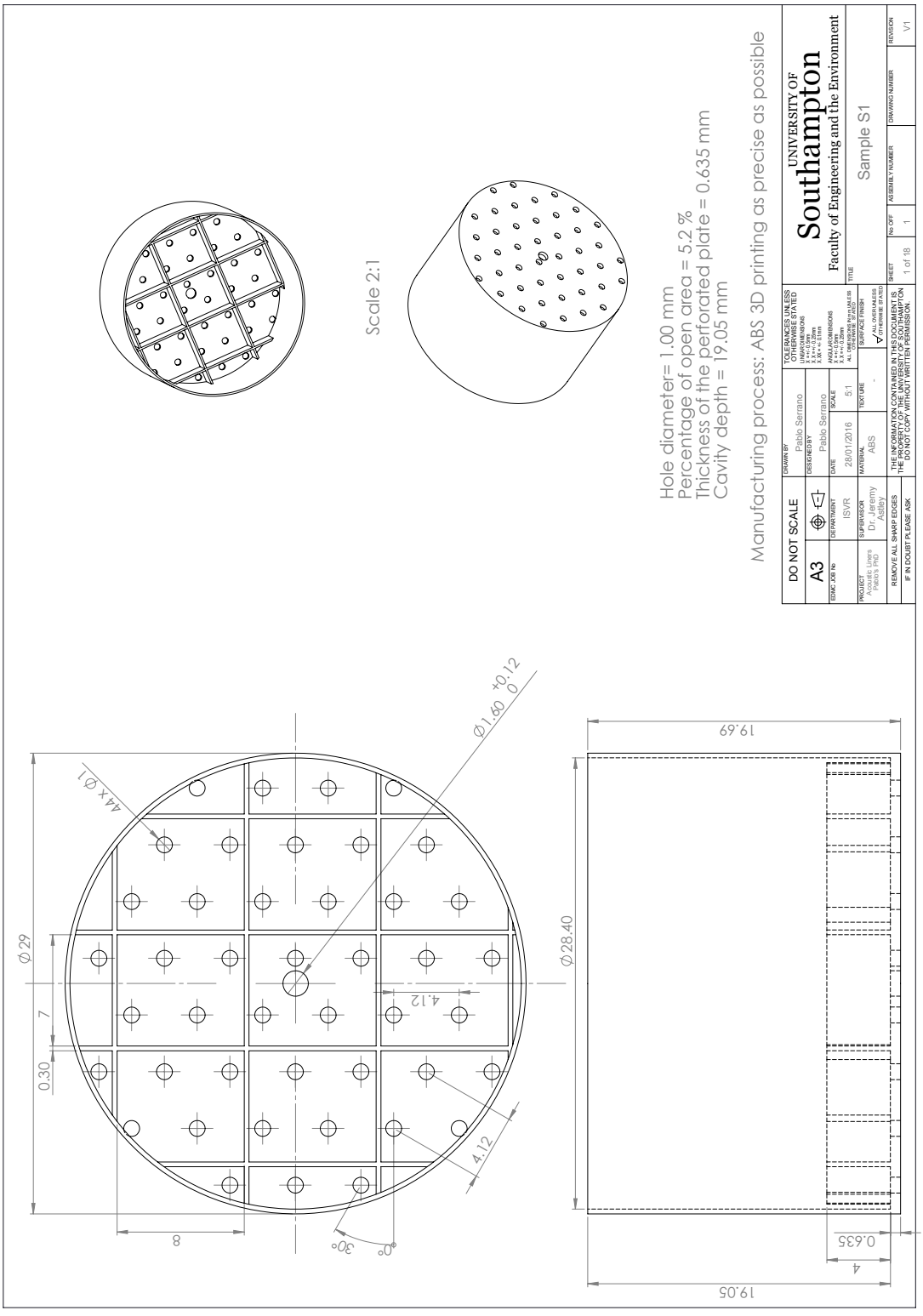
Hole diameter= 1.00 mm
Percentage of open area = 5.2 %
Thickness of the perforated plate = 0.635 mm
Cavity depth = 19.05 mm
Manufacturing process: ABS 3D printing as precise as possible
Scale 2:1
DO NOT SCALE
A3
DRAWN BY
Pablo Serrano
DESIGNED BY
Pablo Serrano
DATE
28/01/2016
SCALE
5:1
MATERIAL
ABS
TEXT ONE
-
TOLERANCES UNLESS OTHERWISE STATED
LINEAR DIMENSIONS
X = +/- 0.5mm
X.X = +/- 0.25mm
X.XX = +/- 0.1mm
ANGULAR DIMENSIONS
X = +/- 0.5°
X.X = +/- 0.25°
4x 4 HOLES
SURFACE FINISHES
ALL SURFACE FINISHES
TO BE 3.2 UNLESS
OTHERWISE STATED
DEPARTMENT
ISVR
SUPERVISOR
Dr. Jeremy Astley
PROJECT
Acoustic Liners
Pablo's PhD
REMOVE ALL SHARP EDGES
IF IN DOUBT PLEASE ASK
THE INFORMATION CONTAINED IN THIS DOCUMENT IS THE PROPERTY OF THE UNIVERSITY OF SOUTHAMPTON
DO NOT COPY WITHOUT WRITTEN PERMISSION
UNIVERSITY OF
Southampton
Faculty of Engineering and the Environment
TITLE
Sample S1
SHEET
1 of 18
No. OFF
1
ASSEMBLY NUMBER
DRAWING NUMBER
REVISION
V1
44x Ø1
Ø1.60 +0.12 0
Ø29
7
0.30
4.12
4.12
8
30°
0°
Ø28.40
19.69
0.635
4
19.05

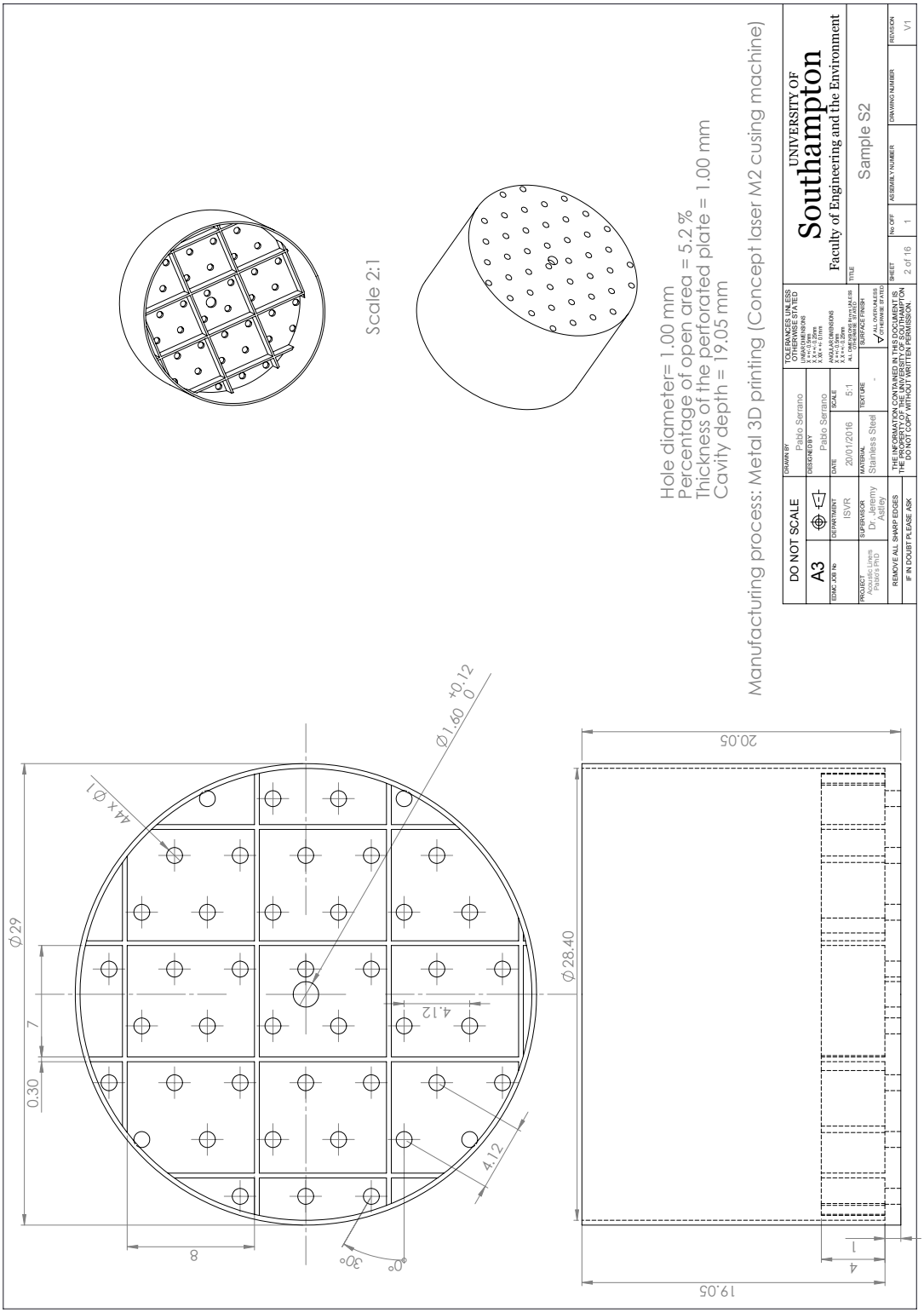
Scale 2:1
Hole diameter= 1.00 mm
Percentage of open area = 5.2 %
Thickness of the perforated plate = 1.00 mm
Cavity depth = 19.05 mm
Manufacturing process: Metal 3D printing (Concept laser M2 cusing machine)
DO NOT SCALE
A3
DRAWN BY Pablo Serrano
DESIGNED BY Pablo Serrano
DATE 20/01/2016
SCALE 5:1
TEXTURE -
SURFACE FINISH
MATERIAL Stainless Steel
DEPARTMENT ISVR
SUPERVISOR Dr Jeremy Astley
PROJECT Acoustic Liners Pablo's PhD
REMOVE ALL SHARP EDGES
IF IN DOUBT PLEASE ASK
TOLERANCES UNLESS OTHERWISE STATED
ANGULAR DIMENSIONS
UNIVERSITY OF Southampton
Faculty of Engineering and the Environment
TITLE
Sample S2
No. OFF 1
ASSEMBLY NUMBER
DRAWING NUMBER
REVISION V1
SHEET 2 of 16
THE INFORMATION CONTAINED IN THIS DOCUMENT IS THE PROPERTY OF THE UNIVERSITY OF SOUTHAMPTON DO NOT COPY WITHOUT WRITTEN PERMISSION
Ø29
0.30
7
44 x Ø1
Ø1.60 +0.12 0
8
4.12
4.12
30°
0°
Ø28.40
20.05
19.05
4
1

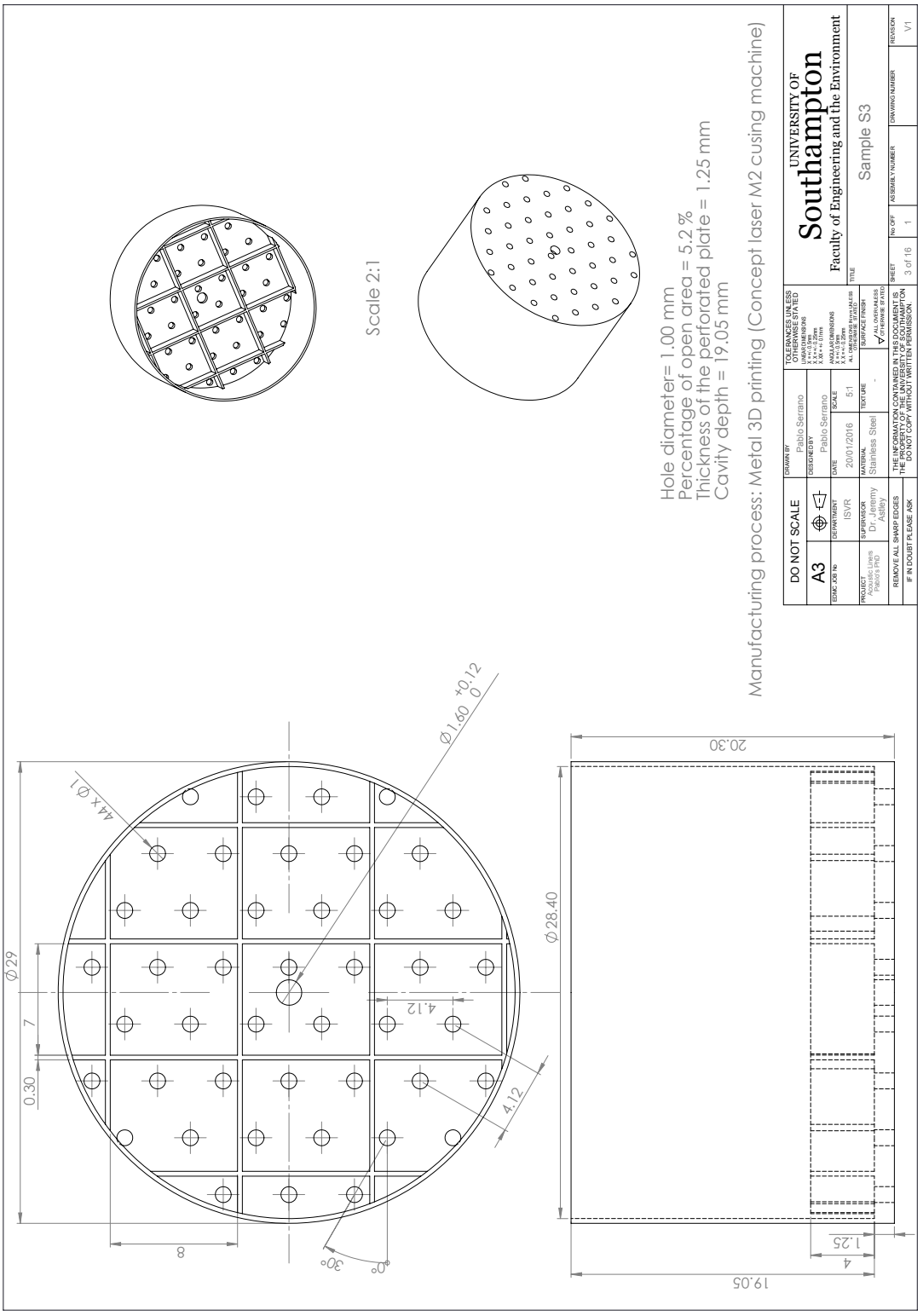
Scale 2:1
Hole diameter= 1.00 mm
Percentage of open area = 5.2 %
Thickness of the perforated plate = 1.25 mm
Cavity depth = 19.05 mm
Manufacturing process: Metal 3D printing (Concept laser M2 cusing machine)
DO NOT SCALE
A3
UNIVERSITY OF Southampton
Faculty of Engineering and the Environment
Sample S3
Pablo Serrano
20/01/2016
Stainless Steel
Dr Jeremy Astley
ISVR
5:1
3 of 16
V1
REMOVE ALL SHARP EDGES
IF IN DOUBT PLEASE ASK
THE INFORMATION CONTAINED IN THIS DOCUMENT IS THE PROPERTY OF THE UNIVERSITY OF SOUTHAMPTON DO NOT COPY WITHOUT WRITTEN PERMISSION
4x Ø1
Ø1.60 +0.12 0
Ø29
Ø28.40
20.30
19.05
4
1.25
8
7
0.30
4.12
4.12
30°
0°

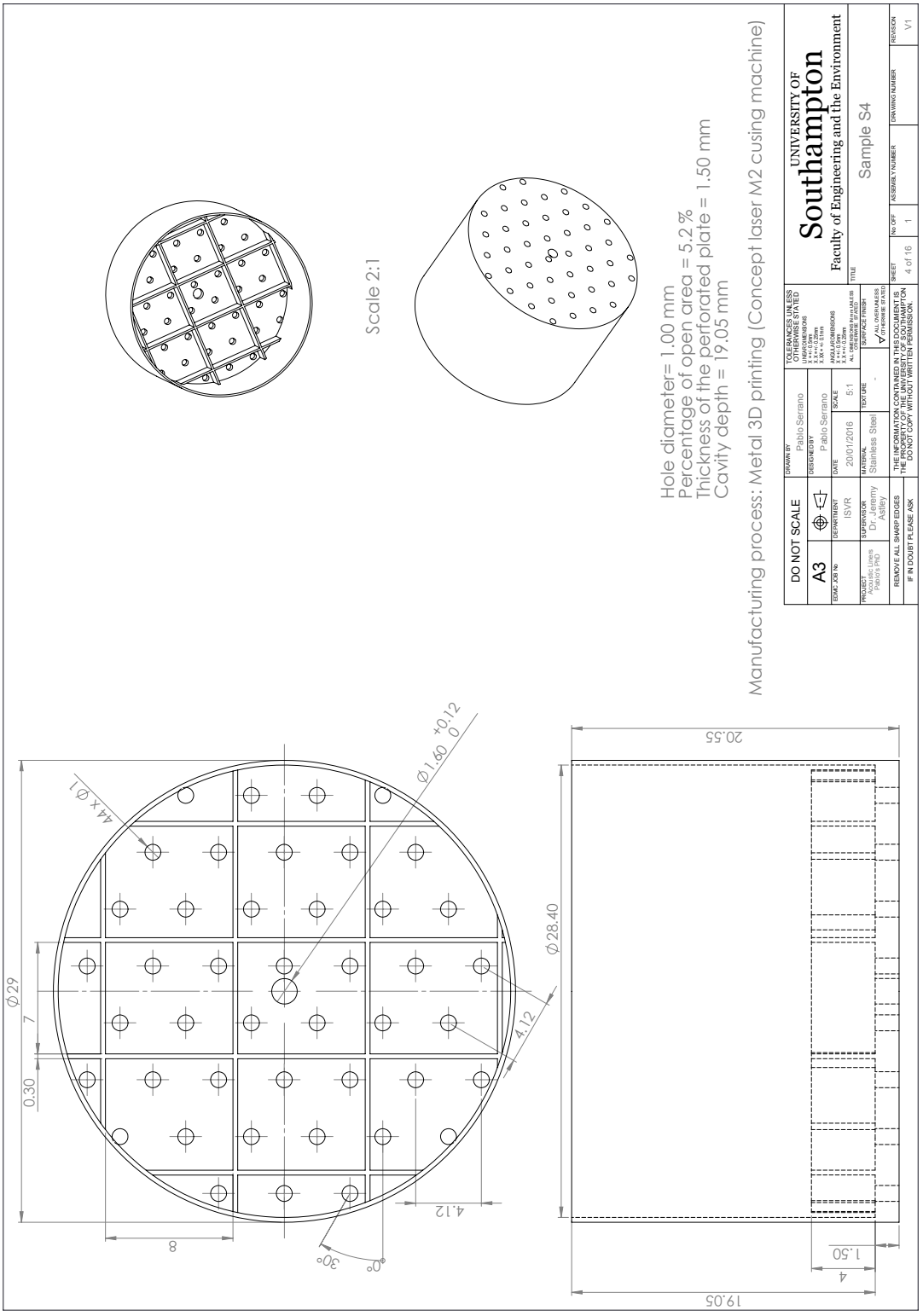
Hole diameter= 1.00 mm
Percentage of open area = 5.2 %
Thickness of the perforated plate = 1.50 mm
Cavity depth = 19.05 mm
Manufacturing process: Metal 3D printing (Concept laser M2 cusing machine)
Scale 2:1
Sample S4
Faculty of Engineering and the Environment
Southampton
UNIVERSITY OF
DO NOT SCALE
A3
DRAWN BY Pablo Serrano
DESIGNED BY Pablo Serrano
DATE 20/01/2016
SCALE 5:1
MATERIAL Stainless Steel
TEXTURE -
SUPERVISOR Dr Jeremy Astley
DEPARTMENT ISVR
PROJECT Acoustic Liners Pablo's PhD
REMOVE ALL SHARP EDGES
IF IN DOUBT PLEASE ASK
THE INFORMATION CONTAINED IN THIS DOCUMENT IS THE PROPERTY OF THE UNIVERSITY OF SOUTHAMPTON DO NOT COPY WITHOUT WRITTEN PERMISSION
SHEET 4 of 16
No OFF 1
ASSEMBLY NUMBER
DRAWING NUMBER
REVISION V1
Ø29
7
0.30
4x Ø1
Ø1.60 +0.12 0
Ø28.40
4.12
4.12
8
30°
0°
20.55
19.05
4
1.50

Hole diameter= 1.00 mm
Percentage of open area = 5.2 %
Thickness of the perforated plate = 2.00 mm
Cavity depth = 19.05 mm
Manufacturing process: Metal 3D printing (Concept laser M2 cusing machine)
Scale 2:1
Sample S5
Faculty of Engineering and the Environment
UNIVERSITY OF Southampton
DO NOT SCALE
A3
Pablo Serrano
20/01/2016
5:1
Stainless Steel
ISVR
Dr. Jeremy Astley
Acoustic Liners Pablo's PhD
THE INFORMATION CONTAINED IN THIS DOCUMENT IS THE PROPERTY OF THE UNIVERSITY OF SOUTHAMPTON AND NOT COPY WITHOUT WRITTEN PERMISSION
REMOVE ALL SHARP EDGES
IF IN DOUBT PLEASE ASK
5 of 16
V1
Ø29
7
0.30
8
4.12
Ø28.40
21.05
19.05
2
4
30°
0°
4x Ø1
Ø1.60 +0.12 0

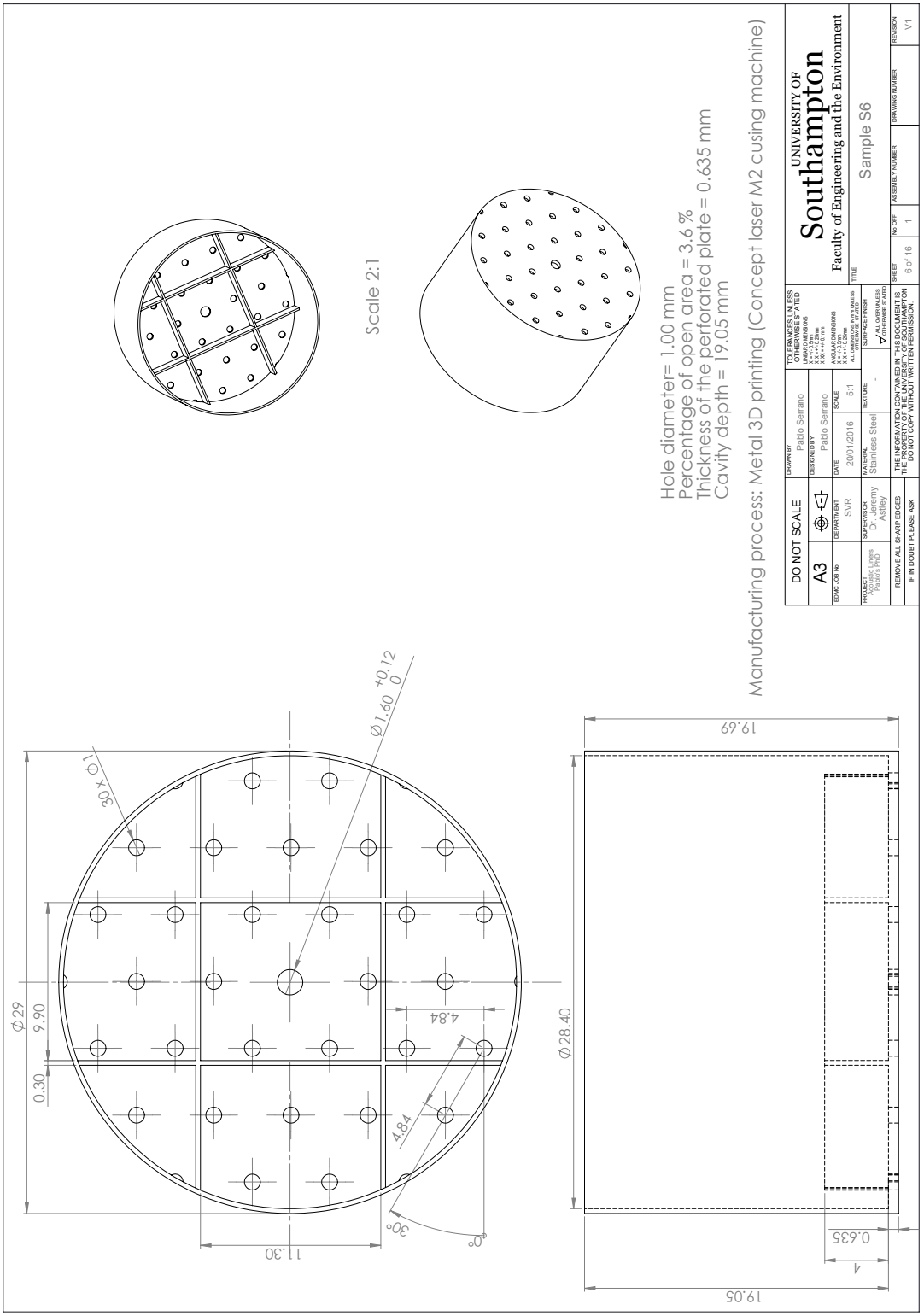
Scale 2:1
Hole diameter= 1.00 mm
Percentage of open area = 3.6 %
Thickness of the perforated plate = 0.635 mm
Cavity depth = 19.05 mm
Manufacturing process: Metal 3D printing (Concept laser M2 cusing machine)
DO NOT SCALE
A3
DRAWN BY Pablo Serrano
DESIGNED BY Pablo Serrano
DATE 20/01/2016
SCALE 5:1
MATERIAL Stainless Steel
TEXTURE -
SURFACE FINISH
TOLERANCES UNLESS OTHERWISE STATED
DEPARTMENT ISVR
SUPERVISOR Dr Jeremy Ashley
PROJECT Acoustic Liners Pablo's PhD
University of Southampton
Faculty of Engineering and the Environment
Sample S6
No. OFF 1
ASSEMBLY NUMBER
DRAWING NUMBER
REVISION V1
SHEET 6 of 16
REMOVE ALL SHARP EDGES
IF IN DOUBT PLEASE ASK
THE INFORMATION CONTAINED IN THIS DOCUMENT IS THE PROPERTY OF THE UNIVERSITY OF SOUTHAMPTON DO NOT COPY WITHOUT WRITTEN PERMISSION
30 x Ø1
Ø1.60 +0.12 0
Ø29
9.90
0.30
11.30
4.84
4.84
30°
0°
Ø28.40
19.69
19.05
4
0.635

Scale 2:1
Hole diameter= 1.00 mm
Percentage of open area = 7.1 %
Thickness of the perforated plate = 0.635 mm
Cavity depth = 19.05 mm
Manufacturing process: Metal 3D printing (Concept laser M2 cusing machine)
Ø29
8.60
0.30
Ø1.60 +0.12 0
60 x Ø1
3.38
3.38
30°
0°
8.10
Ø28.40
19.69
19.05
0.635
4
DO NOT SCALE
A3
DRAWN BY Pablo Serrano
DESIGNED BY Pablo Serrano
DATE 20/01/2016
SCALE 5:1
MATERIAL Stainless Steel
TOLERANCES UNLESS OTHERWISE STATED
LINEAR DIMENSIONS
X.X +/- 0.5mm
X.XX +/- 0.25mm
X.XXX +/- 0.1mm
ANGULAR DIMENSIONS
X.X +/- 0.25mm
ALL SURFACES TO BE FREE FROM BURRS AND SHARP EDGES UNLESS STATED OTHERWISE
TEXT ARE
SURFACE FINISHES
ALL SURFACES 3.2 UNLESS OTHERWISE STATED
University of Southampton
Faculty of Engineering and the Environment
TITLE
Sample S7
DEPARTMENT ISVR
SUPERVISOR Dr Jeremy Astley
PROJECT Acoustic Liners Pablo's PhD
EDAC JOB No
REMOVE ALL SHARP EDGES
IF IN DOUBT PLEASE ASK
THE INFORMATION CONTAINED IN THIS DOCUMENT IS THE PROPERTY OF THE UNIVERSITY OF SOUTHAMPTON AND NOT COPY WITHOUT WRITTEN PERMISSION
SHEET 7 of 16
No. OFF 1
ASSEMBLY NUMBER
DRAWING NUMBER
REVISION V1

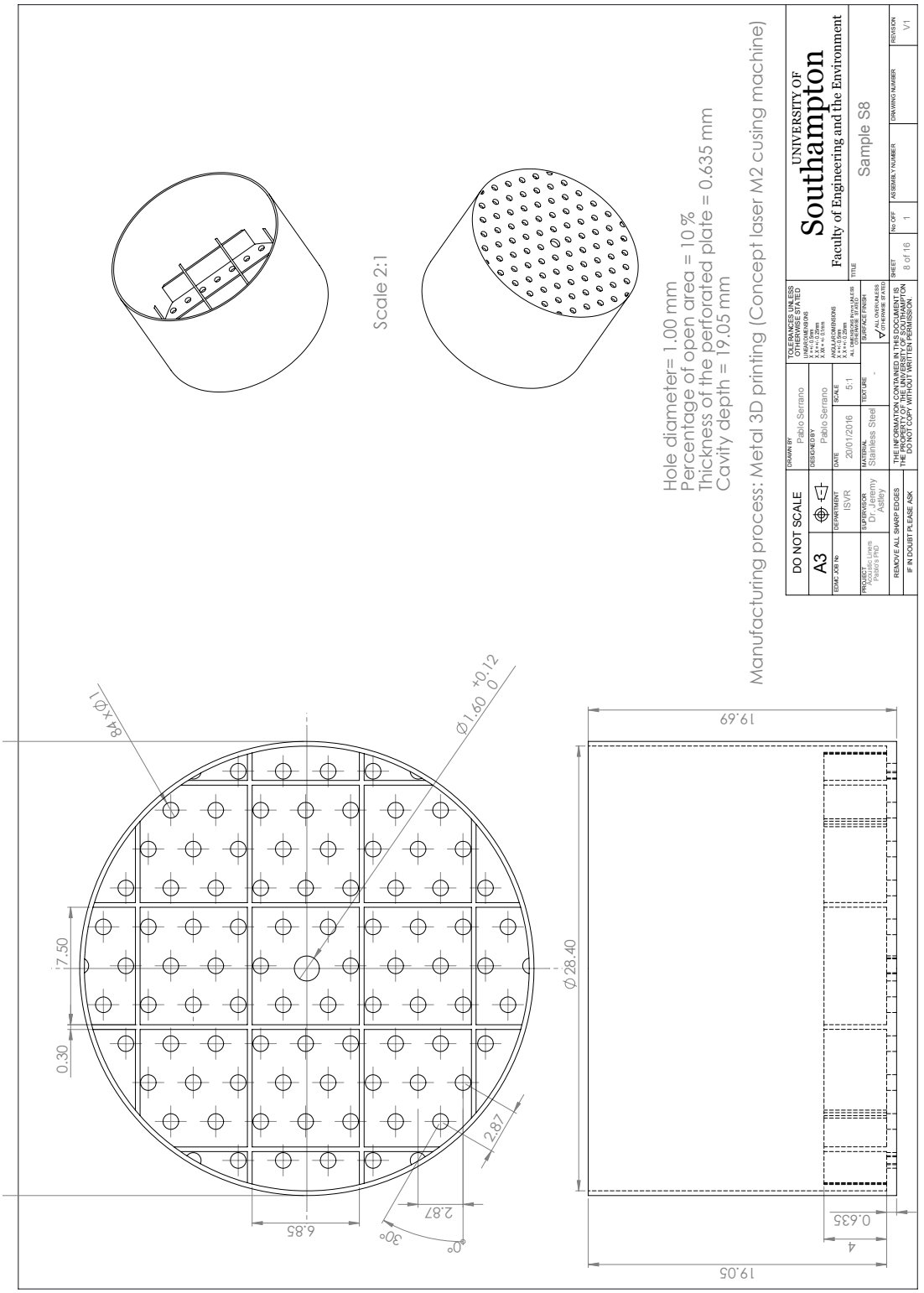
Scale 2:1
Hole diameter= 1.00 mm
Percentage of open area = 10 %
Thickness of the perforated plate = 0.635 mm
Cavity depth = 19.05 mm
Manufacturing process: Metal 3D printing (Concept laser M2 cusing machine)
DO NOT SCALE
A3
DRAWN BY Pablo Serrano
DESIGNED BY Pablo Serrano
DATE 20/01/2016
SCALE 5:1
TEXTURE -
MATERIAL Stainless Steel
SURFACE FINISH
TOLERANCES UNLESS OTHERWISE STATED
DEPARTMENT ISVR
SUPERVISOR Dr Jeremy Astley
PROJECT Acoustic Liners Pablo's PhD
UNIVERSITY OF Southampton
Faculty of Engineering and the Environment
Sample S8
No. OFF 1
ASSEMBLY NUMBER
DRAWING NUMBER
REVISION V1
SHEET 8 of 16
REMOVE ALL SHARP EDGES
IF IN DOUBT PLEASE ASK
THE INFORMATION CONTAINED IN THIS DOCUMENT IS THE PROPERTY OF THE UNIVERSITY OF SOUTHAMPTON DO NOT COPY WITHOUT WRITTEN PERMISSION
19.69
19.05
Ø28.40
Ø1.60 +0.12 0
8xØ1
7.50
0.30
6.85
2.87
2.87
30°
0°
0.635
4

Scale 2:1
Hole diameter= 1.00 mm
Percentage of open area = 19.3 %
Thickness of the perforated plate = 0.635 mm
Cavity depth = 19.05 mm
Manufacturing process: Metal 3D printing (Concept laser M2 cusing machine)
Ø29
9
0.30
162 x Ø1
Ø1.60 +0.12 0
7.70
2.13
2.13
30°
0°
Ø28.40
19.69
19.05
4
0.635
DO NOT SCALE
A3
DRAWN BY Pablo Serrano
DISCHEDBY Pablo Serrano
DATE 20/01/2016
SCALE 5:1
MATERIAL Stainless Steel
TEXT ONE
TOLERANCES UNLESS OTHERWISE STATED
LINEAR DIMENSIONS
X = +/- 0.5mm
X.X = +/- 0.25mm
X.XX = +/- 0.1mm
ANGULAR DIMENSIONS
X = +/- 1 DEGREE
X.X = +/- 0.25mm
ALL 4 ADJACENT EDGES TO BE TOLERANCED TO ±0.1mm UNLESS STATED OTHERWISE
SURFACE FINISHES
ALL SURFACES TO BE 1.6µm UNLESS OTHERWISE STATED
REMOVE ALL SHARP EDGES
IF IN DOUBT PLEASE ASK
THE INFORMATION CONTAINED IN THIS DOCUMENT IS THE PROPERTY OF THE UNIVERSITY OF SOUTHAMPTON AND NOT COPY WITHOUT WRITTEN PERMISSION
PROJECT Acoustic Liners Pablo's PHD
SUPERVISOR Dr Jeremy Astley
EDAC JOB No
DEPARTMENT ISVR
UNIVERSITY OF Southampton
Faculty of Engineering and the Environment
TITLE
Sample S9
SHEET 10 of 16
No OFF 1
ASSEMBLY NUMBER
DRAWING NUMBER
REVISION V1

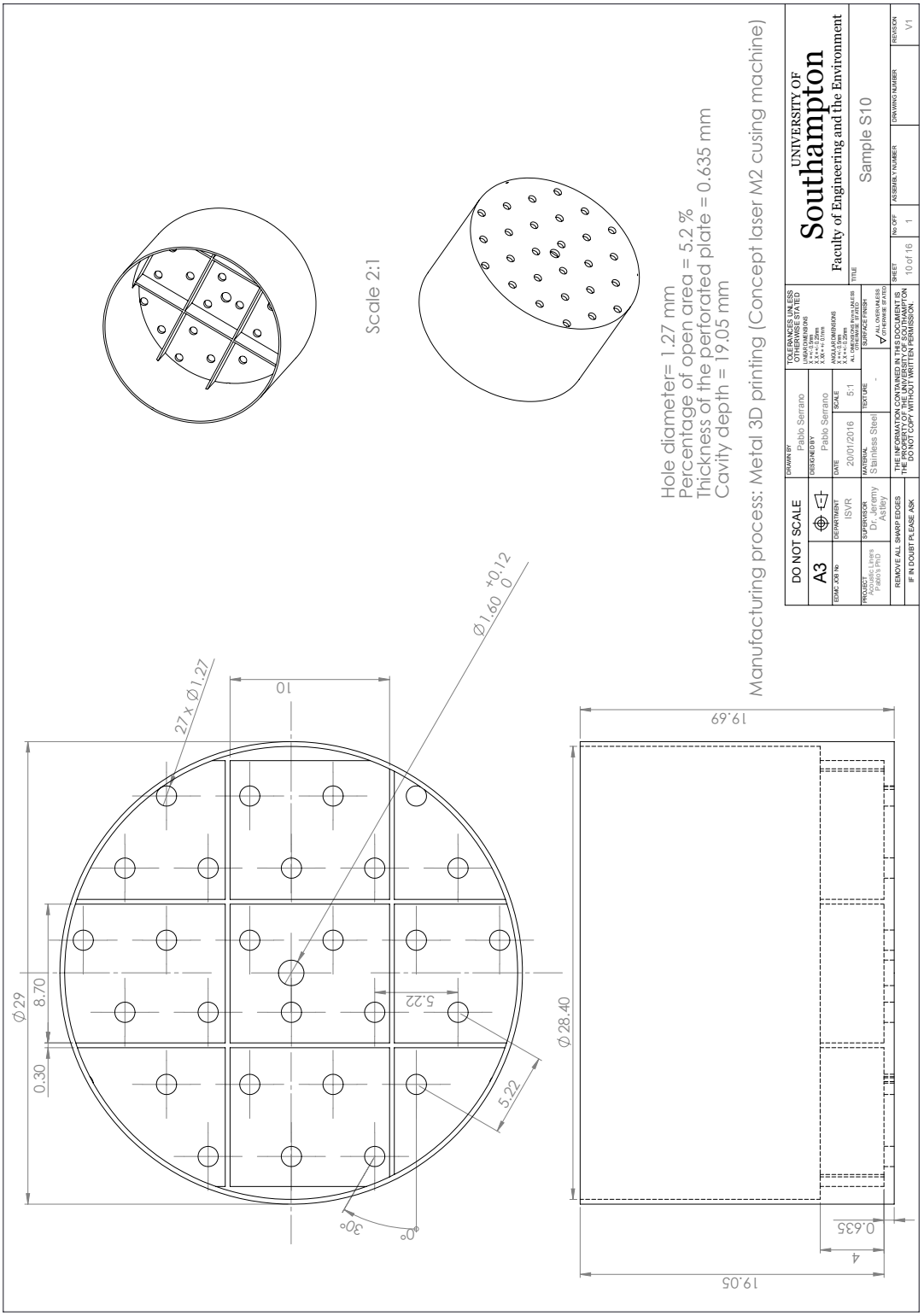
Hole diameter= 1.27 mm
Percentage of open area = 5.2 %
Thickness of the perforated plate = 0.635 mm
Cavity depth = 19.05 mm
Manufacturing process: Metal 3D printing (Concept laser M2 cusing machine)
Scale 2:1
Sample S10
Faculty of Engineering and the Environment
DO NOT SCALE
A3
Patalo Serrano
20/01/2016
5:1
Stainless Steel
ISVR
Dr Jeremy Astley
Patalo's PhD
27x Ø1.27
10
Ø1.60 +0.12 0
Ø29
8.70
0.30
5.22
5.22
30°
0°
Ø28.40
19.69
19.05
4
0.635

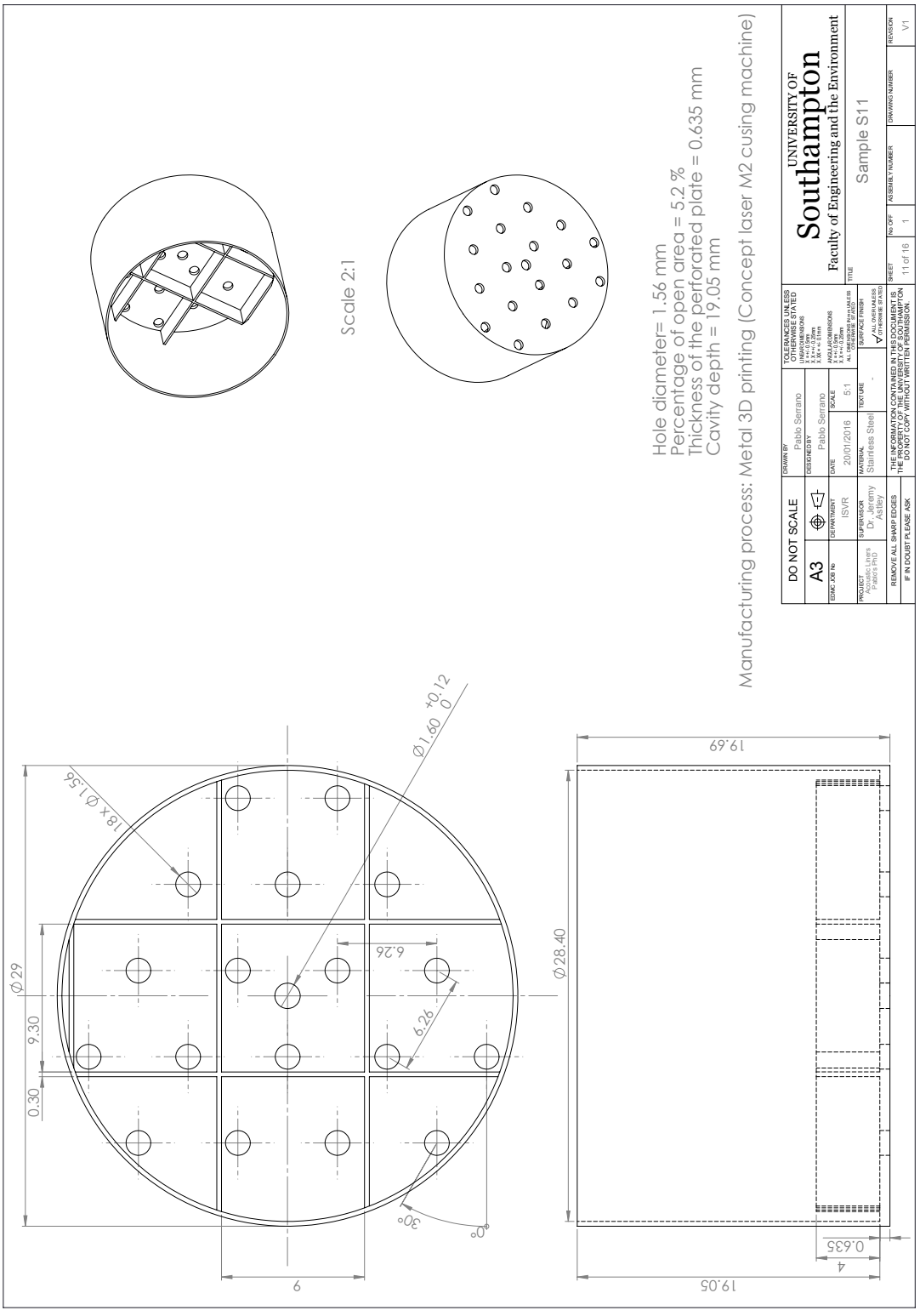
Scale 2:1
Hole diameter= 1.56 mm
Percentage of open area = 5.2 %
Thickness of the perforated plate = 0.635 mm
Cavity depth = 19.05 mm
Manufacturing process: Metal 3D printing (Concept laser M2 cusing machine)
DO NOT SCALE
A3
DRAWN BY
Pablo Serrano
DESIGNED BY
Pablo Serrano
DATE
20/01/2016
SCALE
5:1
MATERIAL
Stainless Steel
TEXT ORE
TOLERANCES UNLESS OTHERWISE STATED
SURFACE FINISH
ALL EDGES BREAK
UNLESS STATED
SUPERVISOR
Dr Jeremy Astley
DEPARTMENT
ISVR
PROJECT
Acoustic Liners
Pablo's PhD
REMOVE ALL SHARP EDGES
IF IN DOUBT PLEASE ASK
THE INFORMATION CONTAINED IN THIS DOCUMENT IS THE PROPERTY OF THE UNIVERSITY OF SOUTHAMPTON
DO NOT COPY WITHOUT WRITTEN PERMISSION
SHEET
11 of 16
No OFF
1
ASSEMBLY NUMBER
DRAWING NUMBER
REVISION
V1
UNIVERSITY OF
Southampton
Faculty of Engineering and the Environment
TITLE
Sample S11
Ø29
9.30
0.30
18 x Ø1.56
Ø1.60 +0.12 0
6.26
6.26
30°
0°
9
Ø28.40
19.69
19.05
4
0.635

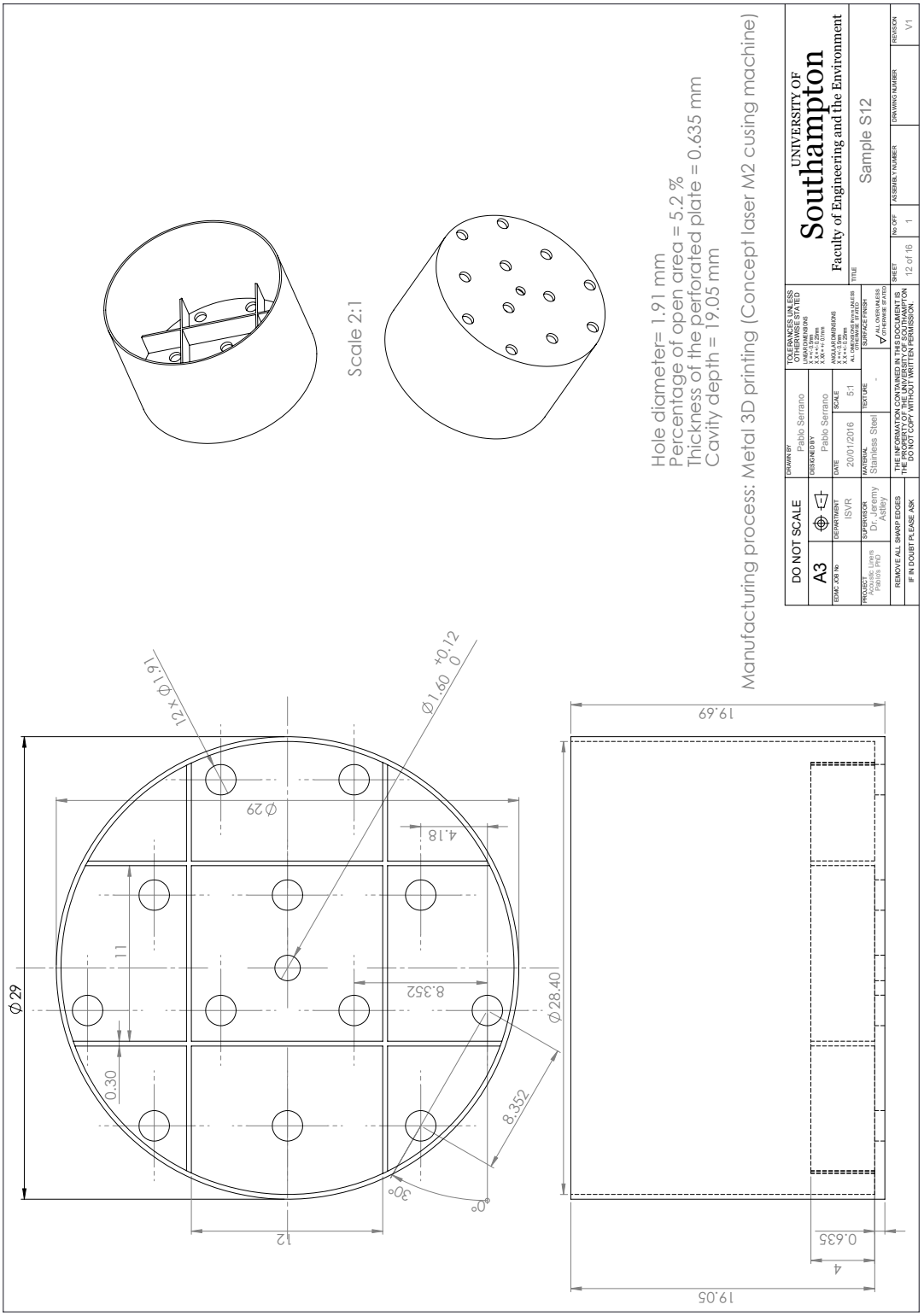
Hole diameter= 1.91 mm
Percentage of open area = 5.2 %
Thickness of the perforated plate = 0.635 mm
Cavity depth = 19.05 mm
Manufacturing process: Metal 3D printing (Concept laser M2 cusing machine)
Scale 2:1
Ø29
Ø28.40
Ø1.60 +0.12 0
12 x Ø1.91
19.69
19.05
8.352
4.18
11
0.30
12
0.635
4
30°
0°
DO NOT SCALE
A3
DRAWN BY Pablo Serrano
DESIGNED BY Pablo Serrano
DATE 20/01/2016
SCALE 5:1
TEXTURE -
MATERIAL Stainless Steel
DEPARTMENT ISVR
SUPERVISOR Dr Jeremy Ashley
PROJECT Acoustic Liners Pablos PhD
TOLERANCES UNLESS OTHERWISE STATED
ANGULAR DIMENSIONS
SURFACE FINISH
REMOVE ALL SHARP EDGES
IF IN DOUBT PLEASE ASK
THE INFORMATION CONTAINED IN THIS DOCUMENT IS THE PROPERTY OF THE UNIVERSITY OF SOUTHAMPTON DO NOT COPY WITHOUT WRITTEN PERMISSION
UNIVERSITY OF Southampton
Faculty of Engineering and the Environment
TITLE Sample S12
No. OFF 1
ASSEMBLY NUMBER
DRAWING NUMBER
REVISION V1
SHEET 12 of 16

Manufacturing process: Drilling
DO NOT SCALE
A3
DRAWN BY
Pablo Serrano
DESIGNED BY
Pablo Serrano
DATE
20/01/2016
SCALE
2:1
MATERIAL
Stainless Steel
TEXT ONE
-
TOLERANCES UNLESS OTHERWISE STATED
LINEAR DIMENSIONS
X = +/- 1mm
X.X = +/- 0.1mm
X.XX = +/- 0.01mm
ANGULAR DIMENSIONS
X.X = +/- 0.25mm
ALL SURFACES TO BE FREE FROM BURRS AND SHARP EDGES UNLESS OTHERWISE STATED
SURFACE FINISH
ALL SURFACES 3.2 UNLESS OTHERWISE STATED
PROJECT
Acoustic Liners
Pablo's PhD
SUPERVISOR
Dr. Jeremy Ashley
REMOVE ALL SHARP EDGES
IF IN DOUBT PLEASE ASK
THE INFORMATION CONTAINED IN THIS DOCUMENT IS THE PROPERTY OF THE UNIVERSITY OF SOUTHAMPTON
DO NOT COPY WITHOUT WRITTEN PERMISSION
University of Southampton
Faculty of Engineering and the Environment
TITLE
In-situ back plate
SHEET
14 of 16
No OFF
1
ASSEMBLY NUMBER
DRAWING NUMBER
REVISION
V1
Ø1.80 +0.20 0
Ø1.72 +0.10 -0.10
7.25
Ø28.80 +0.10 -0.10
3
//
//

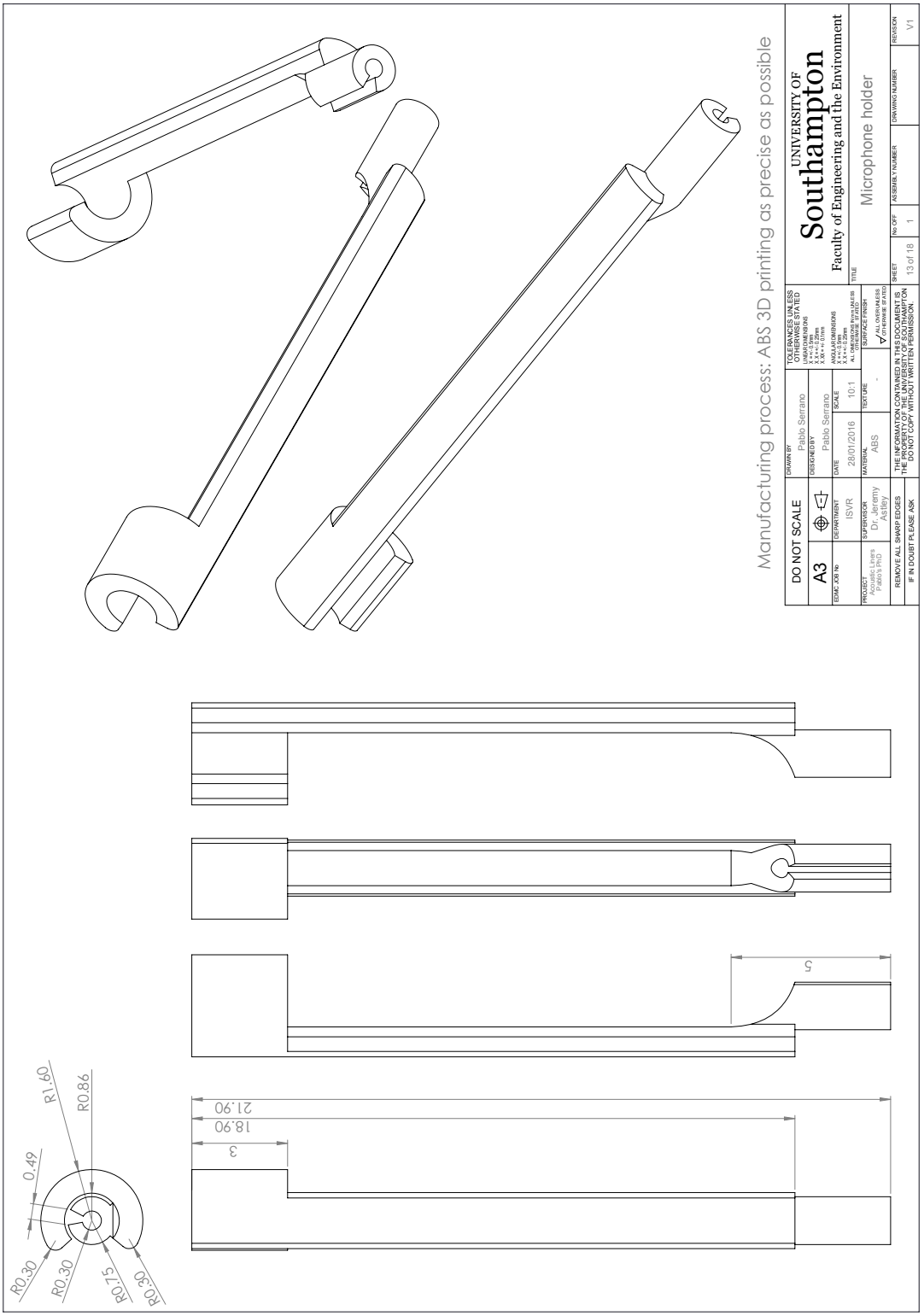
Manufacturing process: ABS 3D printing as precise as possible
DO NOT SCALE
A3
DRAWN BY
Pablo Serrano
DESIGNED BY
Pablo Serrano
DATE
28/01/2016
SCALE
10:1
MATERIAL
ABS
TEXTURE
-
SURFACE FINISH
ALL DIMENSIONS IN MILLIMETRES
UNLESS OTHERWISE STATED
TOLERANCES UNLESS OTHERWISE STATED
DEPARTMENT
ISVR
SUPERVISOR
Dr Jeremy Ashley
PROJECT
Acoustic Lines
Pablo's PhD
REMOVE ALL SHARP EDGES
IF IN DOUBT PLEASE ASK
THE INFORMATION CONTAINED IN THIS DOCUMENT IS THE PROPERTY OF THE UNIVERSITY OF SOUTHAMPTON DO NOT COPY WITHOUT WRITTEN PERMISSION
UNIVERSITY OF
Southampton
Faculty of Engineering and the Environment
TITLE
Microphone holder
No. OFF
1
ASSEMBLY NUMBER
SHEET
13 of 18
DRAWING NUMBER
REVISION
V1
5
21.90
18.90
3
R1.60
R0.86
0.49
R0.30
R0.30
R0.75
R0.30

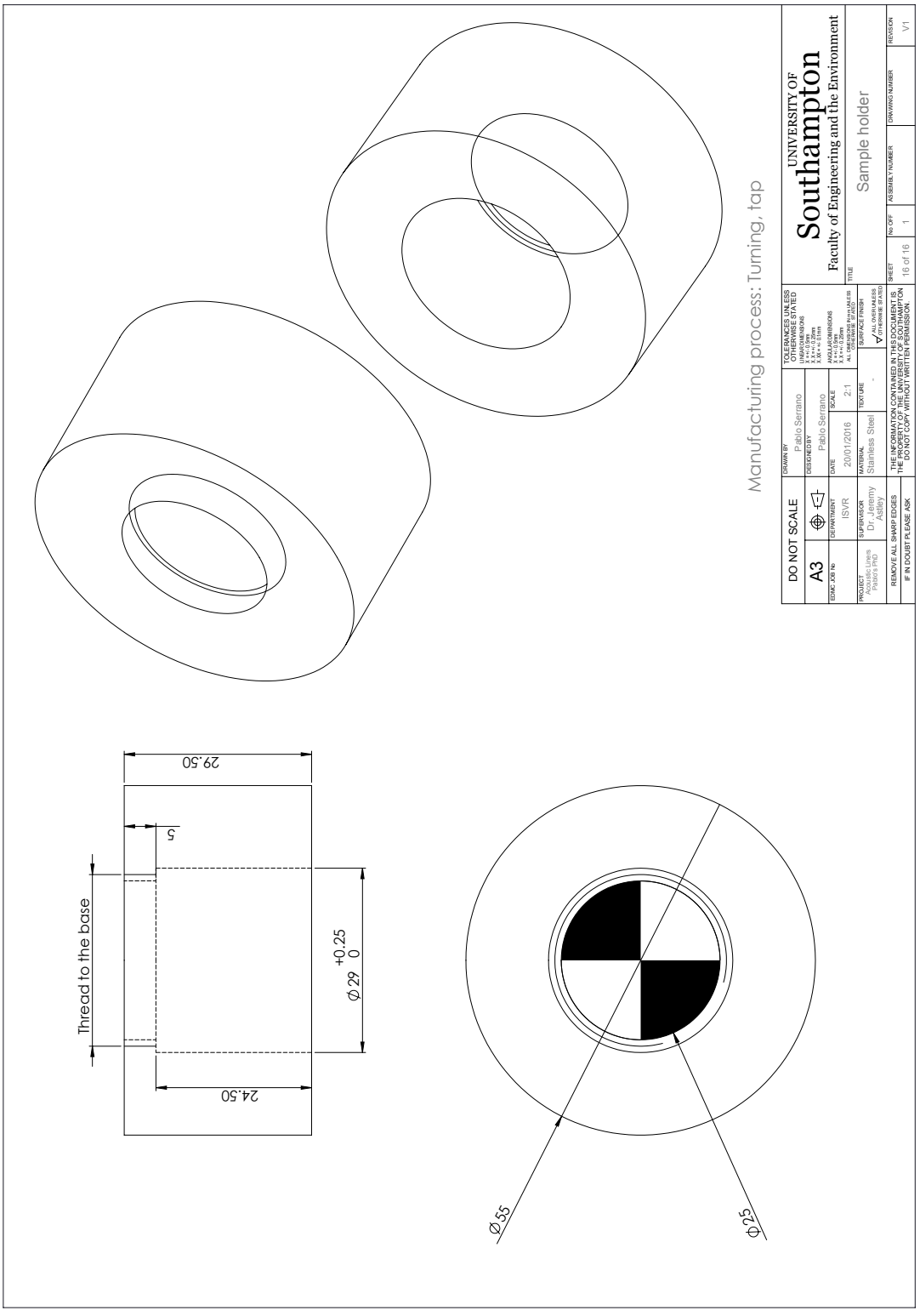
Manufacturing process: Turning, tap
29.50
5
Thread to the base
24.50
Ø29 +0.25 0
Ø55
Ø25
DO NOT SCALE
A3
DRAWN BY
Pablo Serrano
DESIGNED BY
Pablo Serrano
DATE
20/01/2016
SCALE
2:1
MATERIAL
Stainless Steel
TOLERANCES UNLESS OTHERWISE STATED
UNLESS OTHERWISE STATED
ANGULAR DIMENSIONS
TEXT SIZE
SURFACE FINISH
UNLESS OTHERWISE STATED
University of Southampton
Faculty of Engineering and the Environment
TITLE
Sample holder
SHEET
16 of 16
No. OFF
1
ASSEMBLY NUMBER
DRAWING NUMBER
REVISION
V1
PROJECT
Acoustic Liners
Pablo's PhD
SUPERVISOR
Dr Jeremy Astley
DEPARTMENT
ISVR
EDAC JOB No
REMOVE ALL SHARP EDGES
IF IN DOUBT PLEASE ASK
THE INFORMATION CONTAINED IN THIS DOCUMENT IS THE PROPERTY OF THE UNIVERSITY OF SOUTHAMPTON
DO NOT COPY WITHOUT WRITTEN PERMISSION

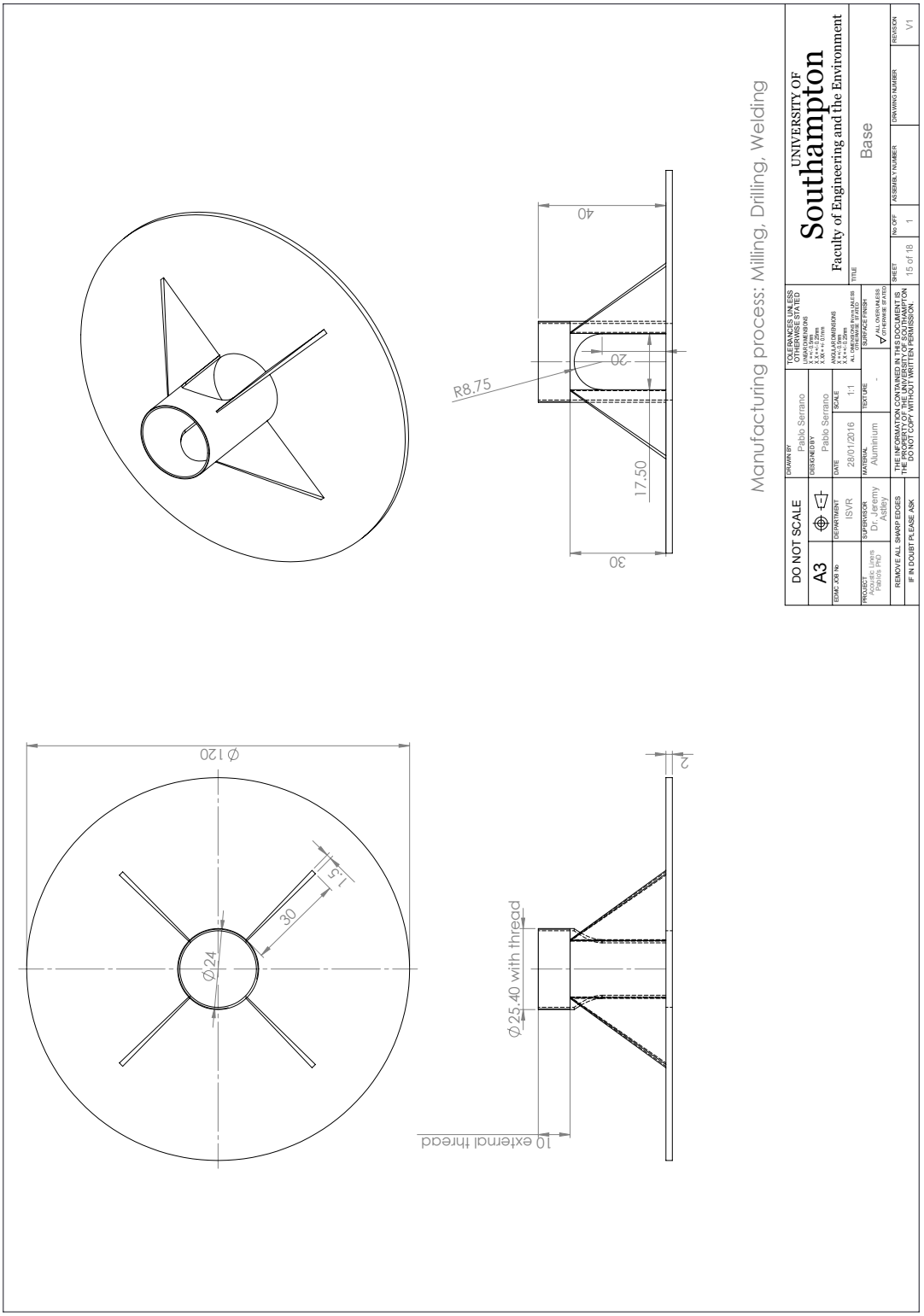
Manufacturing process: Milling, Drilling, Welding
R8.75
40
20
17.50
30
Ø 120
Ø24
30
15
Ø 25.40 with thread
10 external thread
2
DO NOT SCALE
A3
DRAWN BY
Pablo Serrano
DESIGNED BY
Pablo Serrano
DATE
28/01/2016
SCALE
1:1
TOLERANCES UNLESS OTHERWISE STATED
ANGULAR DIMENSIONS
SURFACE FINISH
TEXTURE
-
MATERIAL
Aluminium
DEPARTMENT
ISVR
SUPERVISOR
Dr Jeremy Astley
PROJECT
Acoustic Lines
Pablos PhD
REMOVE ALL SHARP EDGES
IF IN DOUBT PLEASE ASK
THE INFORMATION CONTAINED IN THIS DOCUMENT IS THE PROPERTY OF THE UNIVERSITY OF SOUTHAMPTON DO NOT COPY WITHOUT WRITTEN PERMISSION
SHEET
15 of 18
No. OFF
1
ASSEMBLY NUMBER
DRAWING NUMBER
REVISION
V1
UNIVERSITY OF Southampton
Faculty of Engineering and the Environment
Base

Assembly - Scale 1:2
Sample (S1 to S12)
Microphone Holder
Microphone (MIC062)
Back Plate
Sample holder
Microphone Holder
Microphone (MIC062)
SECTION B-B
SCALE 1 : 1
Ø 120
Ø 55
64.69
B
B
DO NOT SCALE
A3
DRAWN BY
Pablo Serrano
DESIGNED BY
Pablo Serrano
DATE
28/01/2016
SCALE
1:1
TOLERANCES UNLESS OTHERWISE STATED
LINEAR DIMENSIONS
X = +/- 0.5mm
X.X = +/- 0.25mm
X.XX = +/- 0.1mm
ANGULAR DIMENSIONS
X = +/- 0.5°
X.X = +/- 0.25°
4 = +/- 0.083°
TEXT ONE
SURFACE FINISHES
ALL SURFACES
OTHERWISE STATED
University of Southampton
Faculty of Engineering and the Environment
TITLE
Impedance meter In-situ assembly
SHEET
18 of 18
No. OFF
1
ASSEMBLY NUMBER
DRAWING NUMBER
REVISION
V1
EDAC- JOB No
DEPARTMENT
ISVR
SUPERVISOR
Dr Jeremy Astley
PROJECT
Acoustic Liners Pablo's PhD
MATERIAL
REMOVE ALL SHARP EDGES
IF IN DOUBT PLEASE ASK
THE INFORMATION CONTAINED IN THIS DOCUMENT IS THE PROPERTY OF THE UNIVERSITY OF SOUTHAMPTON DO NOT COPY WITHOUT WRITTEN PERMISSION

Bibliography

[1] M. Å bom. Measurement of the scattering-matrix of acoustical two-ports. *Mechanical Systems and Signal Processing*, 5(2):89–104, 1991.

[2] M. e. a. Adib. Novel Aircraft-noise technology review and medium- and long-term noise reduction goals. Technical report, International Civil Aviation Organization, Montréal, 2014.

[3] J. F. Allard and N. Atalla. *Propagation of Sound in Porous Media - Modelling Sound Absorbing Materials*. Wiley, 2009.

[4] G. W. Bielak, J. W. Premo, A. S. Hersh, and L. R. Center. *Advanced turbofan duct liner concepts*. National Aeronautics and Space Administration, Langley Research Center, 1999.

[5] D. T. Blackstock. *Fundamentals of physical acoustics*. Wiley-interscience, Austin, Texas, 2000.

[6] H. Bodén. Experimental Investigation of Harmonic Interaction Effects for Perforates. *11th AIAA/CEAS Aeroacoustics Conference*, May 2005.

[7] H. Bodén. The effect of high level multi-tone excitation on the acoustic properties of perforates and liner samples. *18th AIAA/CEAS Aeroacoustics Conference*, 2012.

[8] H. Bodén. Acoustic properties of perforates under high level multi-tone excitation. *19th AIAA/CEAS Aeroacoustics Conference*, May 2013.

[9] H. Bodén and J. Fritzell. A study of high level tonal and broadband random excitation for acoustic liners. In *AIAA Conference*, pages 1–28, Stockholm, Sweden, 2017. AIAA.

[10] H. Bodén, Y. Guo, and H. B. Tözün. Experimental Investigation of Nonlinear Acoustic. *12th AIAA/CEAS Aeroacoustics Conference*, May 2006.

[11] H. Boden, L. Zhou, J. A. Cordioli, A. A. Medeiros, and A. Spillere. On the effect of flow direction on impedance eduction results. *22nd AIAA/CEAS Aeroacoustics Conference*, pages 1–15, 2016.

[12] U. Bolt, R.H., Labate, S., Ingard. The Acoustic Reactance of Small Circular Orifices. *Journal of the Acoustical Society of America*, 21(2):94–97, 1949.

[13] G. J. Borse. *Numerical methods with MATLAB: A resource for scientists and engineers*. International Thomson Publishing, 1996.

[14] Brüel & Kjær. Portable Impedance Meter System Type 9737 User Manual, 2012.

[15] Brüel & Kjær Aerospace. PULSE Material Testing - PULSE Application Type 7758 - WT 9713 User Manual, 2017.

[16] S. Busse-Gerstengarbe, F. Bake, L. Enghardt, and M. G. Jones. Comparative Study of Impedance Eduction Methods, Part 1: DLR Tests and Methodology. *19th AIAA/CEAS Aeroacoustics Conference*, pages 1–13, May 2013.

[17] F. Caeiro, C. Sovardi, K. Förner, and W. Polifke. Shape optimization of a Helmholtz resonator using an adjoint method. *International Journal of Spray and Combustion Dynamics*, 9(4):394–408, 2017.

[18] J. Carbajo, J. Ramis, L. Godinho, P. Amado-Mendes, and J. Alba. A finite element model of perforated panel absorbers including viscothermal effects. *Applied Acoustics*, 90:1–8, Apr. 2015.

[19] COMSOL Multiphysics. Comsol Multiphysics Reference Manual. pages 1–1262, 2013.

[20] A. Cummings. Transient and multiple frequency sound transmission through perforated plates at high amplitude aiaa. *AIAA journal / NASA 9th Aeroacoustics Conference*, 1984.

[21] A. Cummings. The Effects of Grazing Turbulent Pipe-Flow on the Impedance of an Orifice. *Acustica*, 61:233–242, 1986.

[22] P. Davidson. *Turbulence: An introduction for Scientists and Engineers*. Oxford University Press, 2004.

[23] W. De Roeck and W. Desmet. Indirect acoustic impedance determination in flow ducts using a two-port formulation. In *15th AIAA/CEAS Aeroacoustics Conference*. AIAA, Miami, USA, 11-13 May 2009, 2009.

[24] P. D. Dean. An In-situ Method of Wall Acoustic Impedance Measurement in Flow Duct. *Journal of Sound and Vibration*, 34(1):97–130, 1974.

[25] T. Elnady. *Modelling and characterization of Perforates in Lined Ducts and Mufflers*. PhD thesis, doctoral dissertation. Dept. Aeronautical and Vehicle Eng., Royal Institute of Technology, Stockholm, 2004.

[26] T. Elnady and H. Boden. On the modelling of the acoustic impedance of perforates with flow. *9th AIAA/CEAS Aeroacoustics Conference*, pages 1–39, May 2003.

[27] T. Elnady and H. Boden. An inverse analytical method for extracting liner impedance from pressure measurements. *10th AIAA/CEAS Aeroacoustics Conference*, 2004.

[28] T. Elnady, H. Boden, and B. Elhadidi. Validation of an Inverse Semi-Analytical Technique to Educe Liner Impedance. *AIAA journal*, 47(12):2836–2844, 2009.

[29] W. Eversman. Effect of local impedance variation and non-linearity on multiple tone attenuation. In *16th AIAA/CEAS Aeroacoustics Conference*, page 3825, 2010.

[30] FAA. Federal Aviation Regulations (FARS, 14 CFR). Part 36 - Noise Standards: Aircraft type and airworthiness certification. Appendix G., 2002.

[31] F. Fahy and J. Walker. *Advanced Applications in Acoustics, Noise and Vibration.* Taylor & Francis, 2004.

[32] P. Ferrante, W. D. Roeck, W. Desmet, and N. Magnino. Back-to-back comparison of impedance measurement techniques applied to the characterization of aeroengine nacelle acoustic liners. *Applied Acoustics*, 105:129–142, 2016.

[33] M. d. A. S. Ferrari. *Modeling of Passive Acoustic Liners from High Fidelity Numerical Simulations.* Doctorate thesis, University of California, 2011.

[34] K. Förner, J. Tournadre, P. Martinez-Lera, and W. Polifke. Scattering to Higher Harmonics for Quarter Wave and Helmholtz Resonators. In *22nd AIAA/CEAS Aeroacoustics Conference*, Aeroacoustics Conferences. American Institute of Aeronautics and Astronautics, may 2016.

[35] M. F. Hamilton, D. T. Blackstock, and Others. *Nonlinear acoustics.* Academic press, San Diego, 1998.

[36] A. S. Hersh, B. E. Walker, and J. W. Celano. Helmholtz resonator impedance model, part 1: nonlinear behavior. *AIAA journal*, 41(5):795–808, 2003.

[37] B. Howerton, M. Jones, and J. Buckley. Development and Validation of an Interactive Liner Design and Impedance Modeling Tool. *18th AIAA/CEAS Aeroacoustics Conference*, Jun 2012.

[38] U. Ingard. On the Theory and Design of Acoustic Resonators. *The Journal of the Acoustical Society of America*, 25(6):1037–1061, 1953.

[39] U. Ingard. Nonlinear Attenuation of Sound in a Duct. *Journal of the Acoustical Society of America (JASA)*, 43:167–168, 1968.

[40] U. Ingard and H. Ising. Acoustic Nonlinearity of an Orifice. *Journal of the Acoustical Society of America (JASA)*, 42(February 1967):6–17, 1967.

[41] U. Ingard and S. Labate. Acoustic Circulation Effects and the Nonlinear Impedance of Orifices. *Journal of the Acoustical Society of America (JASA)*, 22(2):211–218, 1950.

[42] ISO. ISO-10534-2. Acoustics - Determination of sound absorption coefficient and impedance in impedance tubes. Part 2: Transfer-function method, 1998.

[43] X. Jing, S. Peng, X. Sun, J. Xiaodong, P. Sen, S. Xiaofeng, X. Jing, S. Peng, and X. Sun. A straightforward method for wall impedance eduction in a flow duct. *The Journal of the Acoustical Society of America*, 124(1):227–234, Jul 2008.

[44] M. G. Jones, B. M. Howerton, and E. Ayle. Evaluation of Parallel-Element, Variable-Impedance, Broadband Acoustic Liner Concepts. *18th AIAA/CEAS Aeroacoustics Conference*, pages 1–17, 2012.

[45] M. G. Jones and P. E. Stiede. Comparison of methods for determining specific acoustic impedance. *The Journal of the Acoustical Society of America*, 101(5):2694, 1997.

[46] M. G. Jones, M. B. Tracy, W. R. Watson, and T. L. Parrott. Effects of liner geometry on acoustic impedance. In *Proc. 8th AIAA/CEAS Aeroacoustics Conference and Exhibit*, 2002.

[47] M. G. Jones, W. R. Watson, and D. M. Nark. Effects of flow profile on educed acoustic liner impedance. *16th AIAA/CEAS Aeroacoustics Conference*, 2010.

[48] M. G. Jones, W. R. Watson, M. B. Tracy, and T. L. Parrott. Comparison of Two Acoustic Waveguide Methods for Determining Liner Impedance. *7th AIAA/CEAS Aeroacoustics Conference*, 2001.

[49] M. G. Jones, W. R. Watson, M. B. Tracy, and T. L. Parrott. Comparison of two acoustic waveguide methods for determining liner impedance. *AIAA Journal*, 2266, 2001.

[50] H. F. Kilian. Nonlinear Aeroacoustic Characterization of Resonators. *PHD Thesis*, (November), 2017.

[51] J. KOOI and S. SARIN. An experimental study of the acoustic impedance of Helmholtz resonator arrays under a turbulent boundary layer. *7th Aeroacoustics Conference*, Oct 1981.

[52] U. Kurze and H. Allen. Influence of Flow and High Sound Level on the Attenuation in a Lined Duct. *The Journal of the Acoustical Society of America (JASA)*, 49(5), 1971.

[53] T. Luong, M. S. Howe, and R. S. McGowan. On the Rayleigh conductivity of a bias-flow aperture. *Journal of Fluids and Structures*, 21(8):769–778, 2005.

[54] D.-y. Maa. Potential of microperforated panel absorber. *Journal of the Acoustical Society of America (JASA)*, 104(July 1998):2861–2866, 1998.

[55] B. Magliozzi, D. B. Hanson, and R. K. Amiet. Propeller and Propfan Noise. In H. H. Hubbard, editor, *Aeroacoustics of Fight Vehicles. Volume 1: Noise Sources*, chapter 1, page 64. National Aeronautics and Space Administration, Langley Research Center, 1991.

[56] C. Malmary, S. Carbonne, Y. Auregan, and V. Pagneux. Acoustic impedance measurement with grazing flow. *AIAA Paper*, 2193:2001, 2001.

[57] Z. Masson, P. G. Serrano, A. A. Medeiros, J. A. Cordioli, D. C. dos Reis, and F. M. Catalano. Desenvolvimento de sistema de controle, aquisição e processamento de sinais para bancada de medição de impedância acústica de liners com escoamento. In *VIII Congresso nacional de engenharia mecânica*, Uberlândia, Brazil, 10-15th August, 2014.

[58] MathWorks. MATLAB. Version 2015b. 2015.

[59] A. McAlpine and M. Fisher. On the prediction of "buzz-saw" noise in acoustically lined aero-engine inlet ducts. *Journal of Sound and Vibration*, 265(1):175–200, Jul 2003.

[60] A. A. Medeiros. *Implementação e validação numérica de método de determinação de impedância acústica com incidência rasante e na presença de fluxo*. Final year project of undergraduation degree, Universidade Federal de Santa Catarina, 2013.

[61] A. A. Medeiros. *On the modelling and characterization of acoustic liners under grazing flow*. Masters thesis, Departamento de Engenharia Mecânica, UFSC, 2015.

[62] A. A. Medeiros and J. A. Cordioli. Evaluation of three impedance eduction methods for acoustic liners under grazing flow. *Euro Noise*, 2015.

[63] A. A. Medeiros, Z. Masson, P. G. Serrano, D. C. dos Reis, and J. A. Cordioli. Comparison of mode-matching and two-port formulations for acoustic impedance eduction of liners under grazing flow. In *Forum Acusticum*, volume 2014, 2014.

[64] T. H. Melling. The acoustic impendance of perforates at medium and high sound pressure levels. *Journal of Sound and Vibration*, 29(1):1–65, 1973.

[65] P. M. Morse and K. U. Ingard. *Theoretical Acoustics*. McGraw-Hill New York, 1968.

[66] R. Motsinger and K. R.E. Design and Performance of Duct Acoustic Treatment. In H. H. Hubbard, editor, *Aeroacoustics of Fight Vehicles. Volume 2: Noise Control*, chapter 14, page 182. National Aeronautics and Space Administration, Langley Research Center, Hampton, Virginia, 1991.

[67] M. L. Munjal. *Acoustics of ducts and mufflers with application to exhaust and ventilation system design*. Wiley New York (NY) et al., 1987.

[68] P. Murray, P. Ferrante, and A. Scofano. The Influence of Aircraft Nacelle Acoustic Panel Drainage Slots on Duct Attenuation. *13th AIAA/CEAS Aeroacoustics ...*, pages 1–20, 2007.

[69] P. B. Murray and R. J. Astley. Development of a single degree of freedom perforate impedance model under grazing flow and high SPL. *18th AIAA/CEAS Aeroacoustics Conference*, June 2012.

[70] P. B. Murray, P. Ferrante, and A. Scofano. Manufacturing process and boundary layer influences on perforate liner impedance. *AIAA Paper*, pages 1–17, 2005.

[71] P. Mustafi. *Improved turbofan intake liner design and optimization*. PhD thesis, University of Southampton, 2013.

[72] M. K. Myers. On the acoustic boundary condition in the presence of flow. *Journal of Sound and Vibration*, 71(3):429–434, 1980.

[73] D. M. Nark, M. G. Jones, D. L. Sutliff, E. Ayle, and F. Ichihashi. Improved broadband liner optimization applied to the advanced noise control fan. In *20th AIAA/CEAS Aeroacoustics Conference*, 2014.

[74] T. L. Parrott and M. G. Jones. Parallel-element liner impedances for improved absorption of broadband sound in ducts. *Noise Control Engineering Journal*, 43(6):183–195, 1995.

[75] J. Primus, E. Piot, and F. Simon. An adjoint-based method for liner impedance eduction: Validation and numerical investigation. *Journal of Sound and Vibration*, 332(1):58–75, 2012.

[76] E. R. Rademaker and E. A. Demmenie. In-situ acoustic impedance measurements on air-injected liners under grazing flow. Technical report, National Aerospace Laboratory NLR, Amsterdam, Netherlands, 2004.

[77] J. W. S. Rayleigh. The theory of sound, vol. 1. *New York: McMillan*, 34, 1945.

[78] E. J. Rice. Model for the acoustic impedance of a perforated plate liner with multiple frequency excitation. Technical report, NASA Technical Memorandum, Cleveland, Ohio, 1971.

[79] C. Richter, F. Thiele, X. Li, and M. Zhuang. Comparison of time-domain impedance boundary conditions by lined duct flows. *AIAA Paper*, 2527:2006, 2006.

[80] S. W. Rienstra. Impedance models in time domain, including the extended Helmholtz resonator model, 2006.

[81] S. W. Rienstra and A. Hirschberg. *An Introduction to Acoustics*. S.W. Rienstra and A. Hirschberg, Eindhoven University of Technology, 2004.

[82] S. W. Rienstra and D. K. Singh. An asymptotic model for non-linear Helmholtz resonator of finite depth. *22nd AIAA/CEAS Aeroacoustics Conference*, pages 1–17, 2016.

[83] L. Santana, W. De Roeck, P. Ferrante, and W. Desmet. Two-Port Indirect Acoustic Impedance Eduction in Presence of Grazing Flows. In *17th AIAA/CEAS Aeroacoustics Conference (32nd AIAA Aeroacoustics Conference)*, Portland, USA, 05-08 June 2011, 2011.

[84] B. H. A. Schuster. A Comparison of Ensemble Averaging Methods Using Dean's Method for In-Situ Impedance Measurements. *18th AIAA/CEAS Aeroacoustics Conference (33rd AIAA Aeroacoustics Conference)*, pages 4–6, June 2012.

[85] P. G. Serrano. Desenvolvimento de uma bancada de determinação da impedância acústica na presença de escoamento tangencial. Master's thesis, Departamento de Engenharia Mecânica, UFSC, 2014.

[86] P. G. Serrano, J. A. Cordioli, A. A. Medeiros, and F. M. Catalano. Development of an acoustic impedance eduction test rig under grazing flow. *7th Forum Acusticum*, 2014.

[87] P. G. Serrano, G. Gabard, P. B. Murray, and R. J. Astley. Non-linear interaction of multiple tones on perforated liners. In *22nd AIAA/CEAS Aeroacoustics Conference*. AIAA, Lyon, France, 30 May - 01 Jun 2016, May 2016.

[88] P. G. Serrano, A. M. Spillere, J. A. Cordioli, P. B. Murray, and R. J. Astley. Comparisons between eduction and insitu measurement procedures for aero engine liner impedance. In *23rd AIAA/CEAS Aeroacoustics Conference*, AIAA AVIATION Forum, page 19. American Institute of Aeronautics and Astronautics, jun 2017.

[89] F. Simon. Long Elastic Open Neck Acoustic Resonator for low frequency absorption. *Journal of Sound and Vibration*, 421:1–16, 2018.

[90] A. M. N. Spillere, A. A. Medeiros, P. G. Serrano, and J. A. Cordioli. Cross-validation of a new grazing flow liner test rig using multiple impedance eduction techniques. *ICSV22, Florence, Italy, 12-16 July 2015*, 2015.

[91] R. Sugimoto, J. Astley, and P. Murray. Low frequency liners for turbofan engines. *20th International Congress on Acoustics, ICA*, (August):1–4, 2010.

[92] C. Tam, H. Ju, M. Jones, W. Watson, and T. Parrott. A computational and experimental study of slit resonators. *Journal of Sound and Vibration*, 284(3-5):947–984, Jun 2005.

[93] C. K. Tam, H. Ju, and B. E. Walker. Numerical simulation of a slit resonator in a grazing flow under acoustic excitation. *Journal of Sound and Vibration*, 313(3-5):449–471, Jun 2008.

[94] C. K. W. Tam and L. Auriault. Time-domain impedance boundary conditions for computational aeroacoustics. *AIAA Journal*, 34(5):917–923, May 1996.

[95] C. K. W. Tam, K. A. Kurbatskii, K. K. Ahuja, and R. J. Gaeta. A numerical and experimental investigation of the dissipation mechanisms of resonant acoustic liners. *Journal of sound and vibration*, 245(3):545–557, Aug 2001.

[96] C. K. W. Tam and K. A. Kurbatskii. Microfluid Dynamics and Acoustics of Resonant Liners. *AIAA Journal*, 38(8):1331–1339, aug 2000.

[97] W. R. Watson and M. G. Jones. Validation of a new procedure for impedance eduction in flow. In *16th AIAA/CEAS Aeroacoustics Conference, Stockholm, Sweden*, 2010.

[98] W. R. Watson and M. G. Jones. A Comparative Study of Four Impedance Eduction Methodologies Using Several Test Liners. Technical report, NASA Langley Research Center, Reston, Virginia, 2013.

[99] W. R. Watson, M. G. Jones, and C. H. Gerhold. Implementation and Validation of an Impedance Eduction Technique. Technical report, NASA Langley Research Center, Virginia, 2011.

[100] W. R. Watson, M. G. Jones, and D. M. Nark. Impedance Eduction in Ducts with Higher-Order Modes and Flow. In *Proceedings of the 15th AIAA/CEAS Aeroacoustics Conference*, 2009.

[101] F. M. White. *Viscous Fluid Flow*. McGraw-Hill, 3rd editio edition, 2006.

[102] Q. Zhang and D. J. Bodony. Numerical Simulation of Two-Dimensional Acoustic Liners with High-Speed Grazing Flow. *AIAA Journal*, 49(2):365–382, Feb 2011.

[103] Q. Zhang and D. J. Bodony. Direct numerical simulation and analytical modeling of locally reacting, single degree of freedom acoustic liners with turbulent grazing flow. *20th AIAA/CEAS Aeroacoustics Conference*, 2014.

[104] Q. Zhang and D. J. Bodony. Effects of the turbulent grazing flow over the impedance prediction of a single-orifice helmholtz resonator. In *22nd AIAA/CEAS Aeroacoustics Conference*, Lyon, France, 2016.

[105] L. Zhou and H. Bodén. Experimental investigation of an in-duct orifice with bias flow under medium and high level acoustic excitation. *International journal of spray and combustion dynamics*, 6(3):267–292, 2014.